Interactions of Ribonuclease 1 with the Cell Surface

By

Chelcie H. Eller

A dissertation submitted in partial fulfillment of

the requirements for the degree of

Doctor of Philosophy

(Biochemistry)

at the

UNIVERSITY OF WISCONSIN–MADISON

2014

Date of final oral examination: 12/8/2014

The dissertation is approved by the following members of the Final Oral Committee:
Ronald Raines, Professor, Biochemistry and Chemistry
Thomas Martin, Professor, Biochemistry
Michael Cox, Professor, Biochemistry
Margaret Clagett-Dame, Professor, Biochemistry
Anna Huttenlocher, Professor, Medical Microbiology & Immunology and Pediatrics

Table of Contents

List of Figures

List of Tables

List of Schemes

List of Abbreviations

ε	extinction coefficient
6-FAM	6-carboxyfluorescein
6-TAMRA	6-carboxytetramethylrhodamine
AMP	antimicrobial peptide
ANG	angiogenin
ATCC	American Type Culture Collection
BODIPY	4,4-difluoro-4-bora-3a,4a-diaza-s-indacene
BRB	bovine brain ribonuclease
BSA	bovine serum albumin
BSR; BS–RNase	bovine seminal ribonuclease
CHO	Chinese hamster ovary
CPP	cell-penetrating peptide
cSBL	sialic acid-binding lectin from *Rana catebeiana*
Da	dalton
ddH_2O	distilled, deionized water
DEFIA	2',7'-diethylfluorescein-5-iodoacetamide
DMF	dimethylformamide
DMSO	dimethylsulfoxide
DNA	deoxyribonucleic acid
DOPC	1,2-dioleoyl-sn-glycero-3-ethylphosphocholine
DSF	differential scanning fluorimetry
dsRNA	double-stranded ribonucleic acid
DTNB	5,5’-dithiobis(2-nitrobenzoic acid)
DTT	dithiothreitol

ECP	eosinophil cationic protein; RNase 3
EDN	eosinophil-derived neurotoxin; RNase 2
EDTA	ethylenediaminetetraacetic acid
EtOH	ethanol
exRNA	extracellular ribonucleic acid
FBS	fetal bovine serum
FIC	fractional inhibitory concentration
FPLC	fast performance liquid chromatography
GAG	glycosylaminoglycan
h	hour
HCl	hydrochloric acid
HeLa	human epithelial cervical adenocarcinoma
HEPES	2[4-(2-hydroxyethyl)-l-piperazinyl]ethanesulfonic acid
HPLC	high-performance liquid chromatography
HSQC	heteronuclear single quantum coherence (or correlation)
HUVEC	human umbilical vein endothelial cells
IC_{50}	half maximal inhibitory concentration
IPTG	isopropyl-1-thio-ß-D-galactopyranoside
k_a	kinetic association rate constant
k_{cat}	first-order enzymatic rate constant
k_d	kinetic dissociation rate constant
K_d	equilibrium dissociation constant
kDa	kilodalton
K_i	inhibitor dissociation constant
K_M	Michaelis constant

λ_{em}	emission wavelength
λ_{ex}	excitation wavelength
LB	Luria–Bertani medium
LL-37	human antimicrobial peptide of the cathelicidin family
MALDI–TOF	matrix-assisted laser desorption/ionization–time-of-flight
MCF-7	human mammary epithelial adenocarcinoma
MES	2-(2*N*-morpholino)ethanesulfonic acid
MEOH	methanol
MIC	minimum inhibitory concentration
min	minute
mRNA	messenger ribonucleic acid
NaCl	sodium chloride
NaOH	sodium hydroxide
nt	nucleotide
NTB	2-nitro-5-thiobenzoate
OD	optical density
ONC	Onconase®, *Rana pipiens* homolog of RNase 1; ranpirnase
OVS	oligo(vinylsulfonic acid)
PBS	phosphate-buffered saline
PC	phosphatidylcholine
PCR	polymerase chain reaction
PDB	protein data bank
PEG	polyethylene glycol
p*I*	isoelectric point
pK_a	log of the acid dissociation constant

poly(A:U)	polyadenylic–polyuridylic acid
poly(C)	polycytidylic acid
poly(I:C)	polyinosinic–polycytidylic acid
PS	phosphatidylserine
ptRNase	pancreatic-type ribonuclease
RI	ribonuclease inhibitor
RMSD	root-mean-square deviation
RNA	ribonucleic acid
RNAi	ribonucleic acid interference
RNase	ribonuclease
RNase 1	human pancreatic-type ribonuclease 1
RNase A	bovine pancreatic-type ribonuclease A
s	second
SSEA-4	stage-specific embryonic antigen-4
ssRNA	single-stranded ribonucleic acid
SDS–PAGE	sodium dodecyl sulfate-polyacrylamide gel electrophoresis
t	time
TB	terrific broth medium
TBBEC	transformed bovine brain endothelial cell
TLR	Toll-like receptor
T_m	Temperature at the midpoint of the thermal transition between folded and unfolded protein
Tris	2-amino-2-(hydroxymethyl)-1,3-propanediol
UV	ultraviolet
Z	net molecular charge (Arg + Lys – Asp – Glu)

Acknowledgements

Dedicated to my dad, Teddy L. Eller,
for being an inspiration –
both as an inquisitive scientist
and as an altruistic and courageous person

The work that follows may have been performed by hands, but its conception would not have been possible without the following Raines Lab members—past and present: Dr. Cindy Chao, Dr. Mike Palte, Dr. Greg Ellis, Dr. Rex Watkins, Dr. Nadia Sundlass, Dr. Joelle Lomax, and Trish Hoang (Ph.D. in training). But really the entire Raines Lab has contributed to this work—with input from a wide range of expertise and insight during group meetings. I also would like to acknowledge Ron Raines, my advisor, for giving me the opportunity to work in a lab with some of the brightest and most creative minds I've ever met. Further, I've also had complete free rein over my project to take it in any direction that I saw interesting.

I've been fortunate to have great support during this time from friends both inside and outside the department. They were available to provide an ear if I needed to talk, a hug for support, a buddy for running, a friend to drink with, or just be there for fun.

And most importantly, I need to thank my family for all of their continual support. My parents have been amazing role models, reminding me that a good scientist also needs to be a good person—kind and passionate. My father, Ted, was especially instrumental for piquing my interest in science. We would watch the science channel together and read *Popular Mechanics*. He always sought out the latest knowledge in space discovery, biology, and electronic devices.

He will always be an inspiration to me. My mother, Cathy, has also been a role model all my life as the strong leader of the family. She has been supportive during my entire thesis work as a rock to lean on during hard times. And my siblings (Holly, Crystal, Adam, and Jess) were my best friends growing up. They have always been interested in listening to my work and provided continual motivation by asking when I would get out of school and get a real job. Combined, I am grateful to all my supportive friends (colleagues or otherwise) who provided the fuel that I needed to get though the marathon that is a Ph.D.

INTERACTIONS OF RIBONUCLEASE 1

WITH THE CELL SURFACE

Chelcie H. Eller

Under the supervision of Professor Ronald T. Raines

at the University of Wisconsin–Madison

Pancreatic-type ribonucleases encompass a diverse and unique family of secreted endoribonucleases, specific to vertebrates. In essence, these enzymes cleave the phosphodiester bonds within RNA molecules. This enzymatic function contributes to diverse processes such as gene regulation, digestion, and immune function. Particularly, as the roles of RNA expand, so do the potential roles of RNases. Specifically, one member of this superfamily, RNase 1, has been presumed to function as a digestive aid due to its homology to bovine RNase A. This prototype of the family was used to establish many biochemical properties associated with RNases—including catalytic mechanism and rates, conformational stability, and three-dimensional structure. Yet, little work has explored functional roles beyond digestion.

Recent observations suggest a more expansive role of human RNase 1. This enzyme circulates in blood and appears to activate chemokine release. Particularly, these observations highlight the constant exposure of cell exteriors to pancreatic-type ribonucleases. The prerequisite cell-surface interactions could illuminate biological roles of RNase 1 as well as provide potential exploitations for therapeutic purposes.

The work, herein, characterizes the interactions of pancreatic-type RNases with cell-surface glycans and determines the biological ramifications of these interactions. Specifically, I compare

these properties between RNase 1 and RNase A, and I find that these proteins diverge in several regards. Moreover, I shed light on the biological implications of these interactions as well as potential means of exploitation for therapeutic purposes.

In CHAPTER 1, I review the current knowledge about pancreatic-type RNases including biochemical characterization, biological roles, and therapeutic potential. Specifically, I will discuss the known interactions of RNases to cell-surface molecules and indicate how these interactions could regulate the function of circulating RNases.

I challenge the inference that the human homolog shares many biochemical properties with RNase A in CHAPTER 2. Through comparison of RNase 1 and three homologous bovine RNases, I find that RNase 1 shares more functional properties with bovine brain RNase than with RNase A. Additionally, RNase 1 is shown to be secreted actively and taken up into endosomes upon stimulus with antigenic RNA—a process presumably mediated through tight interactions with cell-surface glycosaminoglycans. This work exposes new potential endogenous functions as well as some action of therapeutic RNases.

In CHAPTER 3, I utilize a glycan array screen to identify the interactions between RNase 1 and a neutral cancer antigen, Globo H. Characterization of this interaction *in vivo* indicates that this cell-surface binding interaction influences the cytotoxicity of RNase variants. Further, I structurally characterize this interaction to identify residues of RNase 1 that bind to Globo H. Moreover, this interaction is specific for RNase 1 over RNase A, further illustrating the disparities between these homologous proteins.

In CHAPTER 4, I characterize the binding affinity of monoclonal antibodies to globo-series glycans, Globo H and SSEA-4. These cancer-associated antigens are currently undergoing clinical trials as cancer vaccine targets. Hence, knowledge of the specificity of these monoclonal

antibodies toward their epitope and potential cross-reactivity is critical. I show that, indeed, these antibodies are specific for their cognate antigens with little cross-reactivity toward glycans within the globo-series family.

Finally in CHAPTER 5, I conclude my work and discuss preliminary data into new studies of human RNase 1. Biochemical studies could reveal the basis for the striking pH optimum, multivalent binding affinities, and factors that contribute to lipid bilayer disruption. Additionally, I provide the first evidence of an innate immune function in which RNase 1 acts synergistically with human antimicrobial agents to kill relevant microbes. Finally, I provide a system to examine the evolution of biochemical properties of RNases from amphibians to reptiles to mammals.

Chapter 1

Introduction: Pancreatic-Type Ribonucleases

1.1 Overview

The central dogma of biology posits that the role of RNA was mainly as an intermediate between the genetic code encrypted by DNA and the functional machinery of proteins.[1] This elegant notion described the flow of information whereby DNA is copied into messenger RNA using transcription machinery, then subsequently decoded into protein by translational machinery. However, this simplistic model was upended with the discovery of non-coding RNA including micro RNA, small nuclear RNA, small nucleolar RNA, small interfering RNA, and long non-coding RNA.[2] Indeed, of the 75% of the genome that is transcribed, only ~1.2% is responsible for protein coding. The remaining ~73.8%—long thought of as "junk" DNA—is now realized to encode these essential non-coding RNAs. Rather than acting as an intermediate, these RNAs operate with larger protein complexes to regulate gene transcription, mature RNA, and splice out introns.[3-7] Further functional analysis now implicates RNAs in a range of roles, including cell communication, gene regulation, clotting, and homeostasis. As such, dysregulation of these RNAs has been associated with a myriad of disease states.

Regulation of RNA is, therefore, of extreme importance. The primary method of RNA regulation occurs through a balance of upregulation via synthesis/stabilization and downregulation by degradation. The synthesis is controlled by transcriptional machinery, and stability is often conferred through protein•RNA interactions. Conversely, the degradation of RNA occurs by the catalysis of enzymes known as ribonucleases (RNases).[8]

RNases hydrolyze the phosphodiester bond of RNA and are found in all branches of the tree of life. Broadly, RNases are categorized by cleavage of RNA either at the ends (exo) or in the middle (endo) of the biomolecule. Within this extremely diverse enzymatic family, many intracellular endo/exoRNases exhibit energy-dependent, sequence-specific RNA cleavage as part

of large complexes. These enzymes can process and mature RNAs,[9] turnover RNA in lysozymes,[10] facilitate the removal of RNA overhangs as part of the transcriptional machinery,[11] remove the poly(A) tails for mRNA destabilization and turnover,[12] and excise introns as part of the spliceosome.[13]

One unique family of endoribonucleases exists solely within vertebrates as a secreted protein with energy-independent, high non-specific activity. This family, known as the pancreatic-type ribonucleases (ptRNases) or RNase A superfamily, is one of the most highly studied group of enzymes. Herein, I review the unique properties of ptRNases (specifically, those in the RNase 1 subfamily) that include the thoroughly studied biochemical characteristics, lesser known biological roles, and newly discovered therapeutic potential. The function of endogenous or therapeutic RNases within the body relies initially on interactions with the cell-surface. Therefore, I will discuss the components of the cell surface or the glycocalyx and examine the known interactions of RNases with these compounds.

1.2 Pancreatic-type ribonucleases

ptRNases comprise a diverse family of vertebrate-specific secretory enzymes. This family has been observed in species including mammals, amphibians, and fish. Intriguingly, the ptRNase family is highly evolving with several gene duplication events—making the family a model for evolutionary analysis.[14] For example, gene sequencing has led to the annotation of 13 members in this family (numbered 1–13) in humans, ~25 in mice, 19 in cattle, and ~19 in rats.[15-17] These family members are then further categorized into subfamilies based on function and sequence similarity including: RNase 1 (pancreas), RNase 2 and 3 (eosinophil-associated), RNase 4 and 5 (angiogenin), RNase 6–8, and annotated non-canonical RNases 9–13. Many of

these ptRNases exhibit specific tissue expression and functions (Figure 1.1). Human RNase 1 is expressed in the pancreas, as well as nearly all tissues examined. However, the function assigned historically was as an aid for digestion. RNase 2 and 3 (eosinophil-derived neurotoxin; EDN and eosinophil cationic protein; ECP) are released from granules in eosinophils, a type of white blood cell, when activated by an immune stimulus. These RNases exhibit antimicrobial/antiviral activity, although the mechanism has yet to be determined definitively.[18-20] RNase 4 and 5 promote angiogenesis and neuroprotection through a unique internalization process that is still being determined.[21,22] RNases 6–8 are not as well-studied but appear to exhibit antibacterial effects.[23-25] RNases 9–13 lack many of the shared features of ptRNases and might not even display any catalytic activity. Yet, knock-out experiments indicate that RNase 9 and 10 appear to be important for the maturation of sperm.[26,27] These observations highlight the diversity in roles of the human ptRNases. As ptRNases share a great amount of sequence identity, bovine RNase A has been used as a model enzyme for much of the studies surrounding this family.

1.2.1 Biochemical properties of RNase 1

The original work on ptRNases—specifically the RNase 1 subfamily—was performed on the prototype of the family, RNase A, from bovine pancreas and the homolog to human RNase 1. This protein emerged through opportunistic means. As a byproduct from the beef industry, RNase A was shipped across the world into the hands of chemists, biochemists, and biophysicists. From this pioneering work, RNase A became a model protein for emerging technologies and ushered in the “golden age of biochemistry”.[28] RNase A was the third protein to be crystallized,[29] was instrumental in early development of NMR,[30] and played a pivotal role in understanding protein folding.[31]

From the ensuing several decades of research, over 100 PBD entries and 13 NMR structures have now been determined for RNase A.[i] Structurally, RNase A folds into a canonical kidney bean shape formed from 4-stranded anti-parallel β-sheets and 3 short α-helices with 4 disulfide bonds (Figure 1.2A). These properties contribute to the high thermostability (T_m = 64 °C) as well as acid tolerance.[32] The activity of catalysis toward RNA has measured with a k_{cat}/K_M value that can exceed 10^9 $M^{-1}s^{-1}$—making it one of the most proficient enzymes.[33] Further, the mechanism of hydrolysis of a P–O$^{5´}$ bond was determined and the conserved catalytic triad—His12, His119, and Lys41—was identified (Figure 1.2A). His12 abstracts a proton from the 2´-OH of the ribose ring, thereby allowing transphosphorylation with removal of a proton from His119. Subsequently, His119 removes a proton from a water molecule to enable attack on the 5´-oxygen to regenerate the active site (Figure 1.2B). While not directly involved in proton transfer, Lys41 crucially stabilizes the transition state. This activity has been demonstrated on single-stranded RNA (ssRNA) substrates, with a preference toward cleavage between uridine and adenosine bases.[34-36] Additional pioneering work using NMR spectroscopy determined the active site pK_a's of His12 and His119 to be 6.0 and 6.5, which motivates a pH optimum of 6.2 for RNA hydrolysis.[37] Homologous ptRNases with the exception of RNases 9–13 share the same canonical fold, catalytic triad, and catalytic activity. Therefore, many other properties such as pH optimum and substrates were presumed to be common to the ptRNase family. Particularly, as human RNase 1 exhibits the greatest sequence identity to the bovine homolog; it was presumed that many of the properties of RNase A were specific to all RNase 1 subfamily members.

1.2.2 Biological functions of RNase 1

[i] We reexamine the NMR chemical shifts assigned for the solution structure of RNase A in APPENDIX 1.

While this wealth of biochemical work using RNase A led to 4 Nobel Prizes, the biological function of RNase A was vastly underappreciated. As this enzyme was purified in massive amounts from bovine pancreas, the assumption reigned that homologs of RNase 1 were merely digestive enzymes needed to break down ingested ssRNA.[38] Indeed, the biochemical properties of RNase A—high stability, acid tolerance, acidic pH optimum, high activity, and pancreatic expression—predict a role within the harsh milieu of the gut. Likewise, high expression of RNase 1 in the pancreas supported the conclusion that the human homologue also primarily acted as a digestive enzyme. As the other members of the ptRNase superfamily exhibited specific tissue expression or robust cellular activities like angiogenesis or antimicrobial activity, little work sought to probe the role of RNase 1 in the body.

The fate of all ptRNases begins with translation in the endoplasmic reticulum. Upon passage through the Golgi, some ptRNases can become glycosylated. Ultimately a signal peptide—which is later removed—leads to secretion. This export suggests a primary role outside of the cell. In fact, the cytosol of every cell contains an inhibitor to RNases, aptly named ribonuclease inhibitor (RI). This protein guards the cell by sequestering any RNase that may enter into the cell with an astounding femtomolar affinity (0.12×10^{-15}M).[39,40] Indeed, if an RNase enters a cytosol lacking RI to inhibit its activity, mere picomoles of the RNase A are toxic to the cell.[41]

While RNase A in bovine may primarily act in ruminant digestion, several recent observations have led to speculation for addition functions of RNase 1 in humans. Indeed, RNase 1 expression has been detected in nearly all tissues, with particularly high protein secretion from endothelial tissues.[42] This accounts for the circulation of RNase 1 throughout the body via blood plasma at concentrations of 400 ng/mL (or ~20 nM)—potentially the only nuclease in plasma.[43-45] Interest further piqued in RNase 1 when changes in RNase plasma levels

were observed in multiple pathological conditions, such as degenerative diseases, infections, autoimmunity, cancer, and tissue injury.[46-50] While no unique correlation emerged as a useful biomarker, this suggested that RNase 1 played a role in inflammation. Within the last decade, one study sought to identify specific inflammatory cytokines released by immature dendritic cells, which are immune cells that activate the adaptive immune response, upon exposure to RNase 2, EDN. EDN was compared against RNase 1—intended as a negative control. Surprisingly, the authors found that RNase 1 also induced the release of inflammatory cytokines from dendritic cells that led to activation of the adaptive immune response.[51] Additionally, RNase 1 appears to show distinct enzymatic activity against double-stranded RNA (dsRNA)—a feature unique to some ptRNases. Presumably, positively-charged residues of RNase 1 destabilize the dsRNA to access the single strand for hydrolysis. [52,53] Combined, these observations indicate the RNase 1 is in the blood, likely interacting with immune cells with broader substrate targets than originally thought for the enzymes of this superfamily.

In fact, the recent discovery of extracellular RNA (exRNA) indicates that RNA circulates in bodily fluids, including plasma, urine, saliva, and semen.[54-56] These RNAs are suspected to play a role in cellular communication,[57,58] immune response,[59] clotting,[60] and homeostasis. Additionally, these nucleic acids appear to be markers of several cancers, as well as organ destruction including that of brain, liver, and heart.[54,61-63] As RNase 1 appears to be the only non-specific RNase that can target both ssRNA and dsRNA in the blood, this enzyme could regulate exRNA degradation.[64,65] Therefore, RNase 1 may not only promote digestion, but may exhibit additional functions depending on the tissue or context—an intriguing possibility that has been historically overlooked.

1.2.3 Therapeutic potential of RNase 1

Another striking feature of some ptRNases—specifically identified via a frog homolog, Onconase or ONC—was the ability to cause apoptosis in various human cancer cells.[66-68] ONC, when applied intravenously, reduced xenographed tumors in mice;[69,70] thereby, prompting clinical trials as a cancer therapeutic.[71] Several of the attributes of RNases—high thermostability, high activity, facile purification, and high amenability to modification—make for an appealing candidate for targeted protein therapies. Moreover, RNases are naturally endocytosed into cells owing to the net positive charge of these small proteins—a barrier that typically restricts cytosolic drug therapies. Thus, the putative pathway of ptRNase-mediated cytotoxicity relies on initial cell-surface binding, internalization, and translocation from endosomes. Once inside the cell, cytotoxic RNases cleave RNA leading to cell death. Mammalian ptRNases bind to and are sequestered by RI in an evolutionarily conserved manner.[72] Therefore, the cytotoxicity of ONC was attributed to the extremely low affinity to mammalian RI. However, renal toxicity has limited the efficacy of this protein therapy.[73,74]

In order to circumvent this renal toxicity, efforts turned to manipulating non-toxic mammalian RNases with lowered affinity for human RI.[ii] These variants disrupt the electrostatic interactions between the binding interface between the two proteins (some key residues shown in red in Figure 1.2A).[7,8] In fact, insertion of a few point mutations results in active variants that reduce the binding affinity to RI by 10^6-fold and result in IC_{50} values ranging from 0.1–10 μM.[7-9] This toxicity appears to be selective to cancer cells and reduces tumor mass in mouse models.[75-77] As a result, variants of the human RNase 1 are undergoing clinical trials as a chemotherapeutic

[ii] Further information about the engineering of such therapeutic ptRNases and the assays to measure the cytotoxic effect on cancerous cells is described in APPENDIX 2.

agent. Intriguingly, it remains unclear what specific properties instill toxicity in cancer cells over non-cancerous cells—as all cells contain RI. It is postulated that specific cell-surface molecules could potentially alter the internalization or the translocation efficiency of cytotoxic RNases, thereby conferring cancer specificity. Indeed, cancer cells exhibit many altered cell-surface markers[78] and variable rates of endocytosis.[79]

Interestingly, RNase 1 may even possess an endogenous mechanism to evade RI. One of the key residues within the inhibitor binding site—Asn88—is one of 3 naturally *N*-glycosylated sites of RNase 1. This glycosylation site within the RI binding interface is distinct to human RNase 1 compared to RNase A. Presumably appending a large branched carbohydrate at this position would be a steric hindrance for binding to RI—thereby targeting cancer cells endogenously. Fascinatingly, aberrations in glycosylation of RNase 1 have been observed in cancer,[42] and particularly increased glycosylation of Asn88 appears to be a biomarker for pancreatic cancer.[80] Whether engineered or naturally RI-evasive, therapeutic RNases must be able to localize to cell-surface of cancer cells to facilitate internalization.

1.3 ptRNases at the cell surface

While the biochemical studies of RNase A have provided an abundance of characterization of the shared properties among some of the ptRNases, the emerging biological role and therapeutic potential of RNase 1 raise many questions as to how this enzyme functions within the context of the body. As either an endogenous protein or an exogenous chemotherapeutic agent, circulating ptRNases are readily exposed to cell surfaces. Therefore, understanding the interactions of RNases with the cell surface could reveal cell types that are influenced by RNase 1.

1.3.1 Specific interactions of ptRNases with cell-surface molecules

Typically, internalization is thought to occur through a receptor-mediated process. Early studies found that the antitumor amphibian RNase from *Rana catebeiana*, sialic acid-binding lectin (cSBL), possessed two binding sites for sialic acids.[81] These sites are responsible for binding to a 180-kDa molecular mass glycoprotein found on a variety of human tumor cells. Further removal of sialic acids reduced the ability of cSBL to agglutinate these tumor cells.[82] Conversely, homologous amphibian ONC from *Rana pipiens* exhibites low affinity to sialic acids. Yet, saturable, nanomolar binding affinities were determined for glioma cells.[83] Still, a receptor has yet to be identified, and ONC internalization occurred in a non-saturable manner into HeLa cells.[84] Human RNase 5, ANG, also bound to smooth muscle cells in a saturable manner, indicating a specific receptor.[85] Yet, RNase A and RNase 1 exhibited non-saturable cellular internalization. Therefore, while some RNases may contain surface-receptor binding sites to particular cell types, it was difficult to draw shared conclusions from homologous RNases. Potentially RNase 1 members bound in a non-specific manner. However, this saturation for RNase 1 was not screened against different cell types. Without a receptor, cellular uptake of cationic RNases was predicted to be largely dominated by electrostatic interactions with the negatively charged cell surface.

1.3.2 Electrostatic contributions between ptRNases and cell-surface molecules

Extensive work has shown that electrostatic interactions on proteins and peptides contribute to much of cell-surface localization.[86,87] RNase A binds to sulfated cell-surface mimics such as heparin *in vitro*, and work *in vivo* indicated that sulfated glycans contribute to cellular uptake.[88]

Indeed, if the biosynthesis of these glycans were diminished, then RNase A internalization was reduced. However, ONC internalization appeared less dependent on particular glycans.[88] Likewise, increasing overall protein charge correlates to the cellular internalization of RNase 1.[89] Therefore it appeared that both RNase A and RNase 1 internalization was mediated by non-specific interactions with negatively charged molecules.

As RNase uptake did not appear to be driven by receptor-mediated endocytosis, further analysis led to the conclusion that RNase A internalization occurs through multiple internalization pathways (Figure 1.3). In fact, RNase A uptake could be reduced using inhibitors to dynamin, clathrin, or macropinocytosis via actin filaments—indicating trafficking through these pathways. Reduction of caveolar-mediated endocytosis or depletion of cholesterol and phosphoinositide 3-kinase had no effect.[90] However, due to the homotypic fusion events within the endosomal and recycling pathways, there are many endocytic pathways that are ill-defined. Indeed, RNase A uptake was still observed even with combined inhibition of both dynamin-mediated endocytosis and macropinocytosis—indicating the potential uptake through clathrin- and caveolin-independent pathways. These methods of internalization overlap those observed for cationic peptides, again suggesting a mechanism that relies on electrostatic interactions.[90]

The different mechanisms of ONC and RNase A highlight the variation in binding to cell-surface components and internalization pathways of homologous RNases despite their all having a positive net charge. In fact, simple analyses of the affinity of human, bovine, and amphibian RNases to a heparin column indicates interesting discrepancies. RNase 1 (charge +6) binds the column more tightly than does RNase A (charge +4). However, ONC (charge +5) does not bind the resin at physiological pH. This dichotomy suggests that more specific interactions confer heparin binding rather than overall charge. In fact, mutagenesis of charged residues on ONC

showed that specific charged patches rather than total charge affected internalization and cytotoxicity.[91] Computational analysis determined that mammalian RNases exhibit cationic charge clustering that allows for certain faces to dock onto a negatively charged surface. [iii] Conversely, ONC evenly distributes its cationic charge such that low binding results. Subsequent *in vitro* assays monitoring the affinity of RNases to negatively charged liposomes corroborated these *in silico* analyses. [92]

Together, these observations indicate variations between homologous RNases and raise the question as to whether there exist specific interactions between cell-surface molecules. Specifically, as human RNase 1 has burgeoning proposed functions, are there further disparities between RNase A and RNase 1 in terms of cell-surface interactions? More importantly, what are the biological ramifications of these cell-surface interactions? In order to identify potential interactions and the ensuing biological response, we must understand the composition and role of the extracellular coating on cells, or "*glycocalyx*".

1.4 Glycocalyx of the endothelium

The endothelium includes the cells that line the interiors of blood and lymphatic vessels and serves as the interface between tissue and circulating fluid. Therefore, circulating RNases most likely interact with this particular cell type. The exact width of the glycocalyx ranges from 0.5 – 1.2 μm and increases width as a function of vasculature diameter.[93] While it is simpler to view this layer as a static picture, the reality is a dynamic breathing mesh that is constantly shedding and being replaced.[94]

[iii] In order to parse out inherent differences, molecular modeling and *in vitro* binding assays were employed to compare how RNase 1, RNase A, and ONC dock onto a negatively-charged surface as described in APPENDIX 3.

The membrane is a complex network of proteins and lipids decorated with varying degrees of branched carbohydrates. Studying this network has been difficult due to the heterogeneity of the carbohydrates. For example, while approximately 9 different monosaccharides exist as building blocks, permutations result in over 20,000 different individual and characterized mammalian glycans. This complexity rises in part from chemical modification of carbohydrate monomers, variation in glycosidic linkages, and different protein or lipid anchors. However, the components of the glycocalyx can be categorized into the following groups: proteoglycans, glycosaminoglycans, glycoproteins, and glycolipids (Figure 1.4).[94]

1.4.1 Components of the glycocalyx

Proteoglycans, or glycosylated proteins, make up the backbone of the glycocalyx. These proteins can be inserted into the plasma membrane by transmembrane domains. Alternatively, some are secreted and interact transiently with other components to support glycocalyx structures. Examples of such anchored proteoglycans include syndecans and glypicans. Examples of secreted proteoglycans include mimecans, perlecans, biglycans, decorins, and versicans. These proteins are post-translationally modified with negatively charged glycosaminoglycan (GAG) side chains attached to Ser, typically in the sequence Ser-Gly-X-Gly.

Glycosaminoglycans are linear polymers of carbohydrates made of repeating disaccharides of uronic acid and hexosamine. The modification on these two components dictate the classification into heparan sulfate (HS), chondroiton sulfate (CS), dermatan sulfate (DS), keratin sulfate (KS), and hyaluronic acid (HA). Modifications of the basic units include sulfation and/or (de)acetylation. All are negatively charged—with the exception of HA—and range from 10–100 kDa in size. The most abundant GAG is heparan sulfate which can be from 50–90% of total

proteoglycan, but this amount can vary based on stimuli such as that from chemokines. CS is the next most abundant GAG. The charged GAGs are assembled in the ER and appended onto proteins in the Golgi. HA is the only GAG not linked onto a protein. Rather, it is assembled in the cytosol into a large 10^4-kDa polymer and exported out to the glycocalyx. This molecule– lacking any modifications— is charge-neutral, and forms a viscous gel in aqueous solution. It is held to the glycocalyx by interactions with binding partners such as CDC37/P32. GAGs are surrounded by many water molecules and thus occupy an enormous hydrodynamic volume. These molecules bind and regulate chemokines, cytokines, growth factors, morphogens, enzymes, and adhesion molecules. Additionally, pathogenic microorganisms take advantage of these molecules as means of adhering to target host cells.

Glycoproteins are, similarly, proteins that are co/post-translationally modified with oligosaccharides. However, these proteins are appended with carbohydrates that are typically branched and include more diverse monosaccharides, often without repeating patterns. These appendages are either linked on the core protein at an amide nitrogen of asparagine (*N*-glycosylated) or at an hydroxyl oxygen on hydroxylysine, hydroxyproline, serine, or threonine (*O*-glycosylated). Examples include selectins (E and P), integrins, and immunoglobulins.

Glycolipids are molecules wherein a carbohydrate (containing one or more monosaccharide) is attached via a glycosidic linkage to a hydrophobic moiety. These molecules are categorized by the type of lipid tail. Classification includes glycoglycerolipid (one or more glycerol residues), glycophosphatidylinositol (a phosphatidylinositol), and glycosphingolipids (attached to a sphingoid or a ceramide). The main glycolipids on the cellular exterior include the latter, glycosphingolipids. These glycans are further classified as neutral or acidic based on the charges appended onto the sugar monomers. These linear or branched glycans are built in a processive

manner whereby monomers are added onto a growing chain by glycosyltransferases in the Golgi, then subsequently trafficked to their final destination.

1.4.2 RNases interactions with glycocalyx components

As mentioned *vide supra*, cSBL bound to sialic acids on a glycoprotein receptor while mammalian RNases appeared to bind to negatively-charged components. Specifically, reduction of glycosyltransferases responsible for anionic GAGs or enzymatic removal of sialic acids reduced RNase A internalization—indicating internalization via HS, CS, and sialic acids.[88,90] Further, examination of RNase A uptake found that removal of glucosphingolipids, via D-threo-PPMP inhibitor, had no effect on internalization. However, protease treatment reduced cellular uptake by RNase A by 80%. Likewise ONC saw a 50% reduction in internalization upon protease treatment. This concluded that anionic proteoglycans influenced uptake rather than anionic glycolipids.[88] While RNase 1 is known to bind heparin columns and cell internalization correlates to protein charge,[89] analysis as described above were not performed using RNase 1. As the possible biological roles for RNase 1 expand, this necessitates a thorough investigation of specific cell-surface binding interactions.

1.4.3 Functions of the glycocalyx: Beyond a barrier

As cell-surface interactions are being identified, important questions still remain about the implications of cellular binding. Classically, the components of the glycocalyx act as a barrier to protect the interior of the cell by repelling negatively-charged molecules and restricting access of molecules greater than 70 kDa. However, the glycocalyx defines the cell physiology and regulates a myriad of cell responses. The variations of the glycocalyx act as an identifier to

localize particular antigens and factors to cell types, mediate cell-cell contact, and discriminate from “self versus non-self”. These molecules also act in many cellular functions as receptors for chemokines, cytokines, coagulation agents, and growth factors.[94,95] For example, selectins are involved in leukocyte recruitment.[96] The burgeoning roles of integrins include cell-cell contacts, immune function, and binding growth factors that trigger signal transduction via intracellular kinases.[97] Many cell-surface interactions are facilitated by multiple binding sites, and this multivalency allows for tight affinity through several weaker interactions. However, defining these many interactions remains difficult. As RNase A interacts with GAGs and sialic acids, does this specificity target internalization to some cell types over others, or to cancerous versus non-cancerous cells?

1.4.4 Dysregulation of the glycocalyx in cancer

While the glycocalyx is important for normal cellular function, changes (either increases or decreases) in expression have been observed in the onset of cancers. This coupling is not surprising, as the glycocalyx is involved in immune recognition, cell–cell contact, and regulation of growth factors—properties often altered upon tumorigenicity.[78] Particularly, cancer cells often exhibit more anionic cell-surface charge.[98] This observation supports the cancer cell specificity of therapeutic RNases. Moreover, comparison of cancerous versus non-cancerous cells has also identified glycans that are specifically overexpressed in some cancers. These are classified as tumor-associated cancer antigens (TACA). Examples of these antigens include the Globo H, polysialic acid, Lewis y, fucosyl GM1, Tn, and sialyl Tn. Typically these glycans have limited expression in non-cancerous cells.[78] The advancement of carbohydrate synthesis has led to the development of glycans as the basis for immune therapy. Ideally, a synthesized antigen moiety

can be appended to other antigenic compounds to be applied as a vaccine. The injected molecule would activate the immune system to begin manufacturing antibodies against these antigens. This approach relies on the glycan being specific to cancer cells compared to normal cells, and relies on the high affinity and specificity for the antibody to the glycan.[iv] As several of these antigens have been associated with the fatal process of metastasis, there is much excitement about being able to halt a tumor from relocating. In fact, several vaccines are currently in clinical trials to treat the most aggressive cancers, including breast, prostate, cervical, and lung. Therefore, therapeutic RNases could target cancer cells through either increased anionic glycans or specific tumor antigens.

1.5 Understanding cell-surface interactions for insight into RNase biology

In light of recent observations about RNase 1 in terms of its location in the plasma and potential as a cancer therapeutic, it is important to understand how this protein interacts with components of the cell surface. Although electrostatic interactions play a large role, they cannot explain the discrepancies that have been observed among homologous species. Particularly, what specific or nonspecific interactions lead to the binding of RNase 1 to cells and how do these interactions interplay with cellular physiology? In order to shed light on these questions, I use a combination of glycan array-screening, enzymology, structural analysis, and cell biology.

In CHAPTER 2, I explore new biochemical properties that distinguish RNase 1 from RNase A and illuminate the true functional homolog, bovine brain RNase, BRB. I show that RNase 1 has distinct pH optimum and activity toward dsRNA. Additionally, I show that the

[iv] Examination of the affinity and specificity of the globo-series glycan family members, Globo H and SSEA-4, to their cognate monoclonal antibodies is determined in CHAPTER 4.

affinity of RNase 1 and BRB for heparan sulfate and chondroitin sulfate likely contribute to greater cellular uptake, particularly in endothelial cells. Functionally, RNase 1 and BRB are released from endothelial cells by viral RNA mimics, further implicating a role of RNase 1 in innate immunity.

In CHAPTER 3, I utilize a glycan array screen to identify the interactions between RNase 1 and a neutral cancer antigen, Globo H. Characterization of this interaction *in vivo* indicates that this cell-surface binding interaction influences the cytotoxicity of RNase variants. Further, I structurally characterize this interaction to identify residues of RNase 1 that bind to Globo H. Moreover, this interaction is specific for RNase 1 over RNase A further illustrating the growing disparities between the homologous proteins.

In CHAPTER 4, I characterize the binding affinity of monoclonal antibodies for two globo-series glycans, Globo H and SSEA-4. These cancer-associated antigens are currently undergoing clinical trials as cancer vaccine targets. Hence, knowledge of the specificity of these monoclonal antibodies toward their epitope and potential cross-reactivity is important. I show that, indeed, these antibodies are specific for their cognate antigens with little cross-reactivity toward glycans within the globo-series family.

Finally in CHAPTER 5, I conclude my work and discuss preliminary data and potential new avenues in the chemistry and biology of RNase 1. Particularly, NMR spectroscopy could reveal the precise basis of the shifted pH optimum of RNase 1 to illuminate disparity from RNase A. Additionally; I propose experiments to determine the affinity of RNase 1 toward multivalent liposomes and to explore how this affinity effects translocation across a lipid bilayer. Finally, I provide the first evidence that RNase 1 acts synergistically with human antimicrobial agents as a toxin to relevant microbes.

Ultimately, fully understanding the biological interplay of RNase 1 requires working in an organism. While these powerful experiments are currently being pursued in my laboratory, my work begins to indicate how RNase 1 exhibits properties beyond that presumed from the classic studies of RNase A and could be playing a role in immune function, blood clotting, antimicrobial activities, and cancer cell-specific toxicity.

Figure 1.1

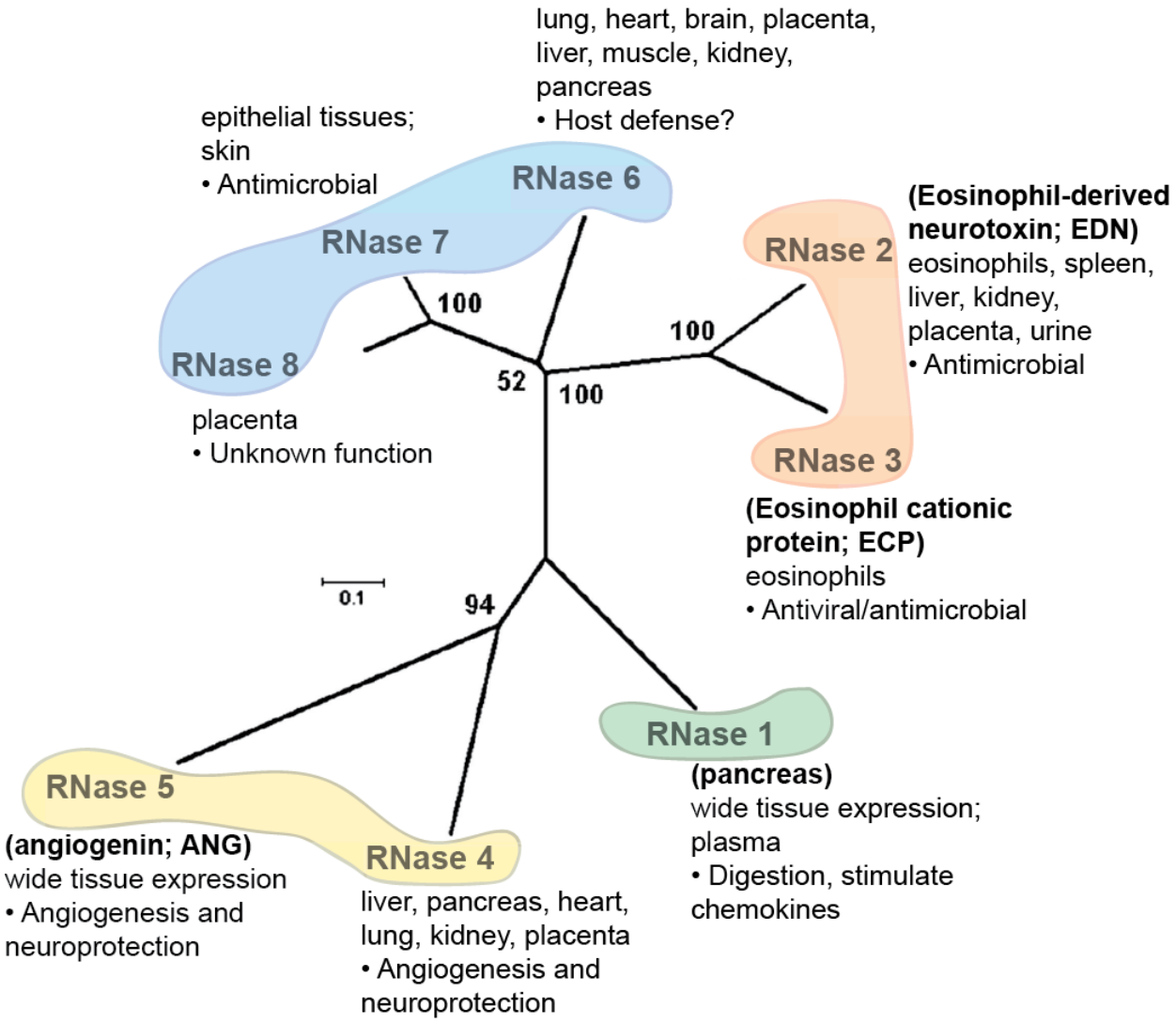
lung, heart, brain, placenta, liver, muscle, kidney, pancreas
• Host defense?
epithelial tissues; skin
• Antimicrobial
RNase 6
RNase 7
RNase 8
placenta
• Unknown function
100
52
100
100
94
0.1
RNase 2
(Eosinophil-derived neurotoxin; EDN)
eosinophils, spleen, liver, kidney, placenta, urine
• Antimicrobial
RNase 3
(Eosinophil cationic protein; ECP)
eosinophils
• Antiviral/antimicrobial
RNase 1
(pancreas)
wide tissue expression; plasma
• Digestion, stimulate chemokines
RNase 5
(angiogenin; ANG)
wide tissue expression
• Angiogenesis and neuroprotection
RNase 4
liver, pancreas, heart, lung, kidney, placenta
• Angiogenesis and neuroprotection

Figure 1.1 Unrooted phylogenetic tree of canonical human pancreatic-type ribonucleases Genetic analysis of the eight human ptRNases indicates evolutionary relationships. These can be divided into four related groups as indicated by the enclosed shapes. Tissue expression and potential functions are listed for each RNase. Analysis performed using the neighbor-joining method with Poisson-corrected distances (2000 bootstrap replications). Bootstrap percentages indicated on interior branches. Figure amended from (ref. 99).

Figure 1.2

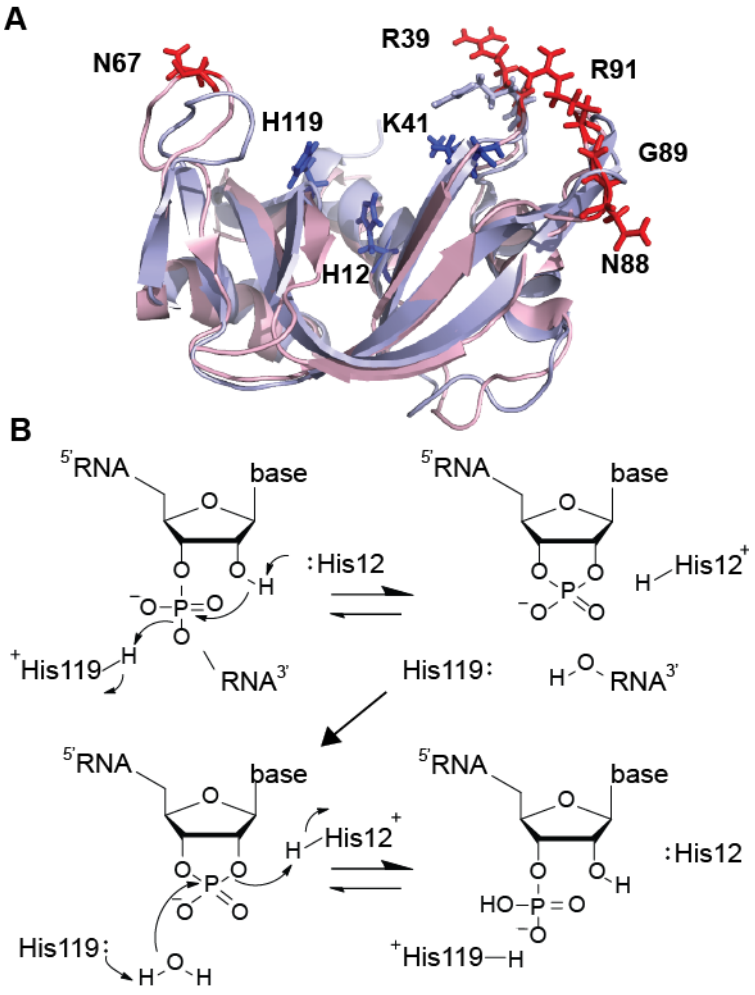
A
N67
R39
R91
H119
K41
G89
H12
N88
B
5'RNA
base
:His12
His12+
His119
RNA3'
His119:
5'RNA
base
His12+
:His12
His119:
His119—H

Figure 1.2 Structural features and catalytic mechanism of ptRNases

A. Backbone structure alignment of RNase 1 (light red) and RNase A (light blue) indicates the high structural similarity (PDB 2K11 and 5RSA, respectively) of ptRNases. The conserved catalytic triad of RNase 1 is highlighted in dark blue to indicate the active site. The RI-binding sites of RNase 1 are shown in dark red. When bound to the inhibitor, ribonucleic activity is completely abolished. *B.* Mechanism of RNA hydrolysis by RNase 1 and RNase A. His12 activates the 2´-OH of the ribose ring to displace the $^{3'}$RNA. His119 abstracts a proton from water to regenerate the active site. Figure amended from (ref. 28).

Figure 1.3

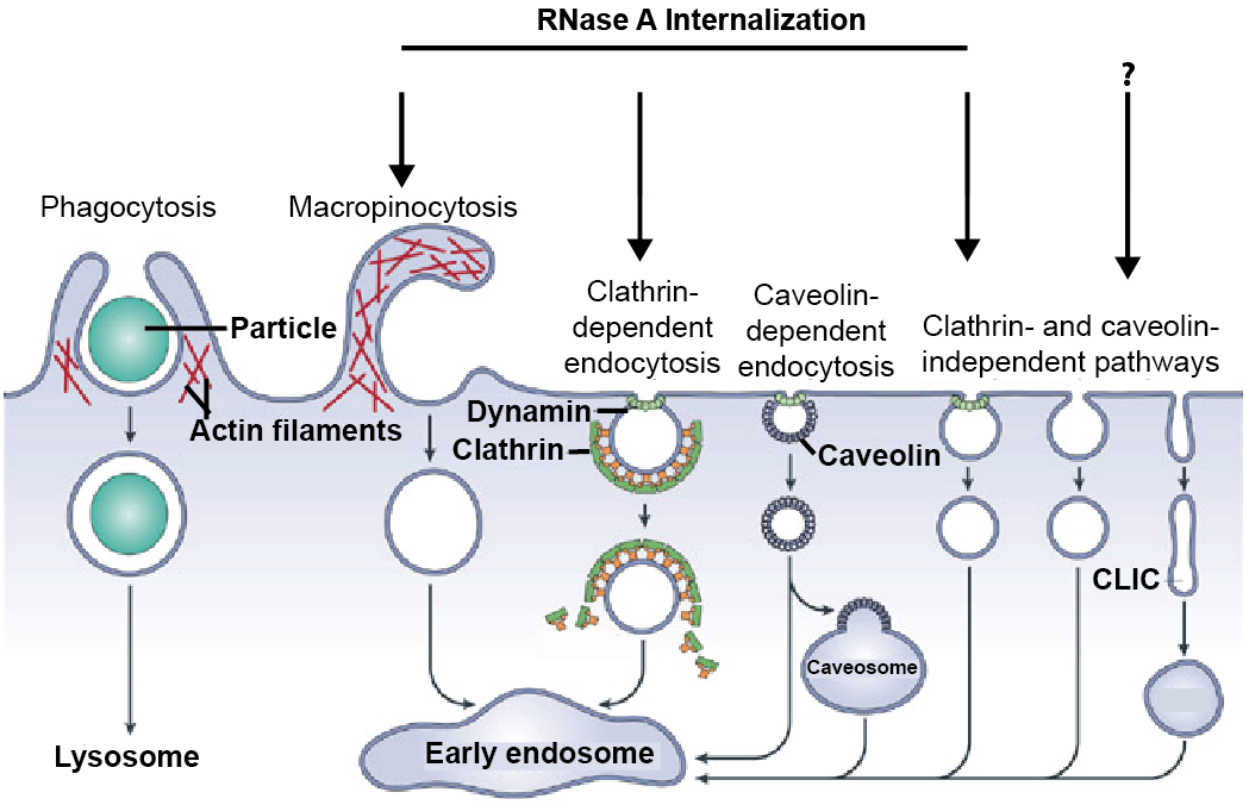
RNase A Internalization
?
Phagocytosis
Macropinocytosis
Clathrin-dependent endocytosis
Caveolin-dependent endocytosis
Clathrin- and caveolin-independent pathways
Particle
Actin filaments
Dynamin
Clathrin
Caveolin
CLIC
Caveosome
Lysosome
Early endosome

Figure 1.3 Pathways for cellular internalization utilized by ptRNases

Cartoon representation of the major pathways of cellular entry and the routes used by ptRNases. Phagocytosis and macropinocytosis are the uptake of large particles and fluid, respectively, that requires rearrangement of actin filaments. Endosomal uptake can require proteins like dynamin (GTPase), clathrin (coat protein), and caveolin (structural protein). Yet some internalization can take place in the absence of all these structural elements to become encapsulated in clathrin- and caveolin-independent carriers (CLIC). Internalization of RNase A was shown to be partially dependent on macropinocytosis and dynamin- and clathrin-dependent endocytosis as shown by the arrows. Figure amended from (ref. 100 and 90).

Figure 1.4

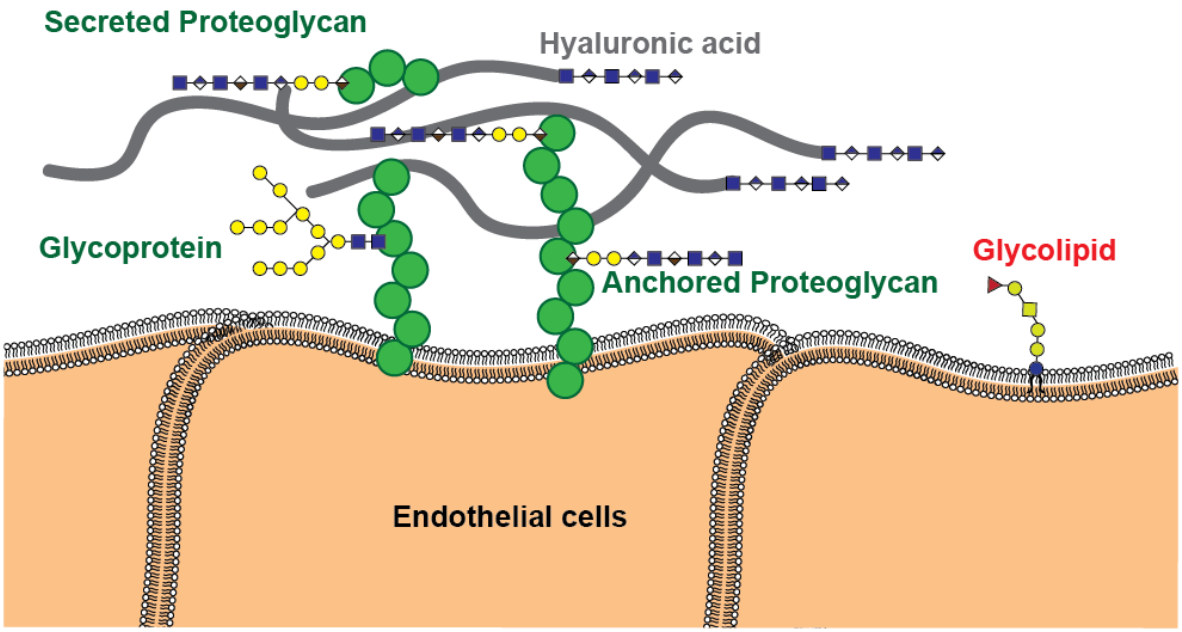
Secreted Proteoglycan
Hyaluronic acid
Glycoprotein
Anchored Proteoglycan
Glycolipid
Endothelial cells

Figure 1.4 Composition of the endothelium glycocalyx

Cartoon representation of the major constituents of the glycocalyx (not drawn to scale). Proteoglycans are appended with linear GAG chains and either anchored in the membrane or secreted. Hyaluronic acid is the only soluble GAG but interacts with many cell-surface constituents. Glycoproteins contain *N*- or *O*-linked branched glycosylation. Glycolipids are lipids modified with branched or unbranded carbohydrate chains. Figure amended from (ref. 94).

Chapter 2

Bovine Brain Ribonuclease is the Functional Homolog of Human RNase 1

Contribution:

I performed the double-stranded RNA assays, heparin binding, BODIPY conjugation, and cell biology experiments on the ribonucleases provided to me except for the pH vs activity profile as well as provide contributions to the text.

This chapter was prepared for publication as:
Eller, C.H.*, Lomax, J.E.*, Raines, R.T. Bovine Brain Ribonuclease is the Functional Homolog of Human Ribonuclease 1. *Journal of Biological Chemistry* (2014) 289, 25996 - 26006
*(Authors contributed equally to this work)

Abstract

Mounting evidence suggests that human pancreatic ribonuclease (RNase 1) plays important roles *in vivo*, ranging from regulating blood clotting and inflammation to directly counteracting tumorigenic cells. Understanding of these putative roles has been pursued with continual comparisons of human RNase 1 to bovine RNase A, an enzyme that appears to function primarily in the ruminant gut. Our results imply a different physiology for human RNase 1. We demonstrate distinct functional differences between human RNase 1 and bovine RNase A. Moreover, we characterize another RNase 1 homolog, bovine brain ribonuclease, and find pronounced similarities between that enzyme and human RNase 1. We report that human RNase 1 and bovine brain ribonuclease share high catalytic activity against double-stranded RNA substrates, a rare quality among ribonucleases. Both human RNase 1 and bovine brain RNase are readily endocytosed by mammalian cells, aided by tight interactions with cell-surface glycans. Finally, we show that both human RNase 1 and bovine brain RNase are secreted from endothelial cells in a regulated manner, implying a potential role in vascular homeostasis. Our results suggest that brain ribonuclease—not RNase A—is the true bovine homolog of human RNase 1, and provide fundamental insight into the ancestral roles and functional adaptations of RNase 1 in mammals.

2.1 Introduction

Pancreatic ribonuclease (RNase)[4] 1 is a small, secreted, RNA-degrading enzyme conserved in mammals. Its biological purpose is unknown. Until recently, all assumptions about its physiology were based on studies of a well-known bovine homolog, RNase A. This protein is secreted primarily from the bovine exocrine pancreas, and is believed to degrade mRNA from symbiotic bacteria in the rumen, a harsh environment with a normal pH range of 5.8–6.4 and temperatures from 38–42 °C.[38,101] Indeed, RNase A seems well-suited for this role, possessing extremely high catalytic activity against single-stranded (ss)RNA at acidic pH, as well as remarkable thermostability and acid-tolerance.[28]

Studies of RNase 1 in other species suggest a biological function apart from digestion. Observations in rats demonstrated that RNase 1 levels do not change following periods of fasting or consumption, as with other digestive enzymes.[102] In humans, pancreatectomy does not affect circulating RNase 1 levels,[103] and we now recognize the primary source of RNase 1 in human blood to be the vascular endothelium.[104] Recent work suggests that RNase 1 degrades extracellular RNA, potentially regulating hemostasis, inflammation, and innate immunity.[44,64,105-107] Data *in vitro* [40,108] and *in vivo* [59,76,109] have implicated human RNase 1 as having an endogenous anti-cancer function, and clinical trials for a variant of this enzyme are underway.[110,111] Taken together, these data imply a much broader physiological role for mammalian RNase 1 than digestion.

The discrepancies between bovine RNase A and mammalian homologs might reside in the peculiar evolution of RNase 1 in ruminants. Whereas most mammals possess a single *RNASE1* gene, evolutionary analyses predict that bovine *RNASE1* underwent two major gene duplication events around 30 million years ago, resulting in paralogous genes encoding three distinct

proteins: RNase A, seminal ribonuclease (BSR), and brain ribonuclease (BRB). Intriguingly, BSR naturally dimerizes upon folding, whereas all other homologs exist as monomers. Orthologs of these three ribonucleases have been identified in many ruminant species. Although many BSR genes show pseudogene features (including stop-codon insertion, loss of catalytic residues, or loss of dimerization), BRB genes do not, implying a necessary function for the BRB protein.[112-114]

Of the three bovine ribonucleases, only BRB is not well characterized. Apart from classic work on RNase A,[28] D'Alessio, Matoušek, and others have established that BSR possesses interesting biological functions not associated with digestion.[115,116] Indeed, BSR has cytotoxic, aspermagenic, and immunosuppressive activity, likely related to the need to protect sperm cells from the female immune system. BSR is, however, only expressed in the seminal vesicles and testes of *Bos taurus*, limiting the potential to extrapolate its functions and properties to other mammalian RNase 1 homologs. In contrast, BRB (which was named for its initial discovery and purification from bovine brain)[117,118] is expressed not only in brain, but in all tissues examined, including endometrium, lymph node, small intestine, liver, and kidney.[16] The widespread expression pattern of BRB closely resembles that for human and mouse *RNASE1* genes.[119] Further, phylogenetic analyses imply that BRB is evolutionarily older than both RNase A and BSR, suggesting greater similarity to the ancestral form of RNase 1 in ruminants.[120] RNase A shares greater overall sequence identity with human RNase 1 than does BRB (Table 2.1). Nevertheless, conclusions based on sequence similarity are not nearly as powerful or as precise as those based on protein function.

We have performed the first detailed biochemical characterization of BRB. Our data upend the relationship between human RNase 1 and bovine RNase A; instead, the true functional

homolog of human RNase 1 in the cow appears to be BRB. Moreover, our findings support the hypothesis that mammalian RNase 1 is not merely a digestive enzyme, but rather an evolutionarily honed vascular regulator.

2.2 Methods

2.2.1 Equipment

All fluorescence and absorbance measurements were made with a Tecan M1000 fluorescence plate reader, unless stated otherwise. All data were fitted and analyzed with the program Prism 5 (GraphPad), unless stated otherwise.

2.2.2 Cloning, expression, and purification of proteins

DNA fragments encoding human RNase 1, P19C human RNase 1, and H12A human RNase 1; BRB and S19C BRB, RNase A and A19C RNase A; BSR, C31A/C32A mBSR, and P19C/C31A/C32A mBSR; and bovine RI were inserted into the pET22b (Novagen) expression vector for tagless expression in *E. coli* strain BL21(DE3). All mutations were generated using site-directed mutagenesis. Ribonucleases were purified as inclusion bodies, and variants containing a free cysteine residue were labeled with either 2′,7′-diethylfluorescein[121] or BODIPY FL (Molecular Probes) as described.[92] Bovine RI was purified via RNase A-affinity chromatography as described.[122] Dimeric BSR was isolated as a monomer and allowed to dimerize upon refolding as described.[123] Following purification, protein solutions were dialyzed against PBS and filtered prior to use. The molecular mass of each ribonuclease conjugate was confirmed by MALDI–TOF mass spectrometry. Protein concentration was determined by using a bicinchoninic acid assay kit (Pierce) with wild-type RNase A as a standard.

2.2.3 T_m determination

Thermal unfolding of ribonucleases was monitored in the presence of a fluorescent dye using differential scanning fluorimetry (DSF). DSF was performed using a ViiA 7 Real-Time PCR machine (Applied Biosystems) as described.[124,125] Briefly, a solution of protein (30 μg) was placed in the wells of a MicroAmp optical 96-well plate, and SYPRO Orange dye (Sigma Chemical) was added to a final dye dilution of 1:166 in relation to the stock solution of the manufacturer. The temperature was increased from 20 °C to 96 °C at 1 °C/min in steps of 1 °C. Fluorescence intensity was measured at 578 nm, and the resulting data were analyzed with Protein Thermal Shift software (Applied Biosystems). A solution with no protein was used for background correction. Values of T_m were calculated from ∂fluorescence/∂T and are the mean of three independent experiments.

2.2.4 Inhibitor dissociation rate

The equilibrium dissociation rates of the RI·ribonuclease complexes were determined as described.[72,122,126] Briefly, RI and 2′,7′-diethylfluorescein-labeled ribonucleases were mixed in equimolar ratios, and the resulting solution was incubated at 25 °C for 5 min. A 50-fold molar excess of human RNase 1 was added to scavenge dissociated RI. Complex dissociation was measured by monitoring the increasing fluorescence of dissociated ribonuclease over time. Values of K_d are the mean of at least three independent experiments.

2.2.5 pH dependence of enzyme activity

The pH dependence of ribonucleolytic activity with a ssRNA substrate was determined by measuring the initial velocity of cleavage of 6-FAM–dArU$(dA)_2$–6-TAMRA (IDT)[127] (0.2 μM) at pH 4.0–9.0. Assays were carried out in 96-well plates (Corning) at 25 °C in various ribonuclease-free buffers: 0.10 M NaOAc, 0.10 M NaCl (pH 4.0–5.5); 0.10 M BisTris, 0.10 M NaCl (pH 6.0–6.5); 0.10 M Tris, 0.10 M NaCl (pH 7.0–9.0). All assays were performed in triplicate with three different enzyme preparations. Values of optimal pH were calculated by fitting of normalized initial velocity data from solutions of various pH to a bell-shaped distribution. Values of k_{cat}/K_M at the optimal pH were determined from initial velocity data, as described.[127]

2.2.6 Double-stranded RNA degradation

Steady- state kinetic parameters for a double-stranded (ds)RNA substrate were determined by following changes in absorbance upon enzymatic degradation, as described.[128] Poly(A:U) (Sigma Chemical) was dissolved in reaction buffer (0.10 M Tris–HCl, 0.10 M NaCl, pH 7.4) and serially diluted by two-fold in a 96-well plate (Corning). After equilibration at 25 °C, a baseline at A_{260} was established, and the initial substrate concentration was determined using ε_{260} = 6.5 $mM^{-1}cm^{-1}$ for poly(A:U). Ribonucleases were added to solutions of varying substrate concentrations, and after mixing the change in absorbance at 260 nm was monitored over time. Initial reaction velocities were determined by using $\Delta\varepsilon_{260}$ = 3.4 $mM^{-1}cm^{-1}$ for poly(A:U). All assays were performed in triplicate with three different enzyme preparations. Values of V_{max} and K_M were calculated by fitting data to the Michaelis–Menten equation.

dsRNA degradation was also assessed with a stable fluorescent hairpin substrate with the sequence: 5,6-FAM–CGATC(rU)ACTGCAACG GCAGTAGATCG (IDT). This substrate had a

single RNA nucleotide near the fluorophore-labeled 5′ end. The substrate was dissolved in water and annealed by first heating to 95 °C and then cooling slowly to room temperature. A solution of substrate (50 nM) was added to a solution of ribonuclease (1 μM), and the resulting mixture was incubated for 5 min. The reaction was quenched by the addition of 40 units of rRNasin (Promega), and the products were subjected to electrophoresis on a 20% w/v native acrylamide gel at 10 mAmp. Formation of cleavage product was monitored by excitation at 495 nm and emission at 515 nm with a Typhoon FLA 9000 scanner (GE Healthcare), and band density was quantified with ImageQuant software (GE Healthcare). The gel was then incubated in SYBR Gold (Invitrogen) and imaged for total nucleic acid. All assays were performed in triplicate with three different enzyme preparations.

2.2.7 Binding of ribonucleases to glycans

Soluble glycans, including heparin, chondroitin sulfate A, chondroitin sulfate B, and chondroitin sulfate C (Sigma Chemical), were diluted across a 96-well plate in 5-fold dilutions in 1× PBS, pH 7.4. Ribonuclease–BODIPY conjugates were added to a final concentration of 50 nM, and the resulting solutions were incubated for 30 min at room temperature. Polarization was monitored by excitation at 470 nm and emission at 535 nm, and data were normalized to a solution lacking carbohydrate and fitted to a binding isotherm by nonlinear regression.

2.2.8 Liposomal disruption assay

Liposomes were constructed as described[129] using 1,2-dioleoyl-*sn*-glycero-3-ethylphosphocholine (DOPC; Avanti Polar Lipids). Lyophilized lipids were resuspended in 25 mM Tris–HCl buffer, pH 7.0, containing NaCl (80 mM), 8-aminonaphthalene-1,3,6-trisulfonic

acid (12.5 mM), and *p*-xylene bis(pyridinium bromide) (45 mM).[130] The lipid suspension was subjected to five freeze–thaw cycles and extruded through polycarbonate filters to form unilamilar vesicles of diameter ~100–150 nM as determined by dynamic light scattering. Liposomes were diluted to 700 μM and incubated with 5 μM ribonuclease in a 96-well plate. Ribonuclease-induced leakage of the entrapped vesicle content was monitored by measuring the de-quenching of the fluorescence of 8-aminonapthalene-1,3,6-trisulfonic acid over time.[130] Percent leakage was calculated by normalizing to liposome disruption by Triton-X 100.

2.2.9 Cellular internalization of ribonucleases

The uptake of BODIPY-labeled ribonucleases into nonadherent mammalian cells was monitored by flow cytometry, as described.[126] Human K-562 cells were grown in RPMI media (Invitrogen) containing FBS (10% v/v) and pen/strep (Invitrogen). Cells were maintained at 37 °C in 5% CO_2. Cells were plated at 2×10^6 cells/mL in a 96-well plate. Ribonucleases in PBS were added to 5 μM, and the resulting solution was incubated for 4 h. Cells were collected by centrifugation at 1000 rpm for 5 min, washed twice with PBS, exchanged into fresh medium, and collected on ice. The total fluorescence of live cells was measured using a FacsCalibur flow cytometer (BD Bioscience). Fluorescence data between experiments were normalized by calibrating each run with fluorescent beads. Data were analyzed with FlowJo software (Tree Star).

The uptake of BODIPY-labeled recombinant ribonucleases into adherent human umbilical vein endothelial cells (HUVEC) (Lonza) and bovine endothelial bovine brain endothelial cells (TBBEC) (C. Czuprynski, University of Wisconsin–Madison) was monitored with confocal microscopy (Nikon). HUVEC cells were grown in EGM-2 medium (Lonza); TBBEC cells were

grown in RPMI medium containing FBS (10% v/v) and pen/strep (Invitrogen). Cells were maintained at 37 °C in 5% CO_2. Cells were plated at 2×10^6 cells/mL in a 96-well plate. Ribonucleases in PBS were added to 1.25 μM, and the resulting medium was incubated for 4 h. The outer membrane was stained with WGA-594, and the nucleus was stained with Hoechst 33342 (Invitrogen). Cells were then washed 3 times with PBS. Cells were imaged with an Eclipse TE2000-U laser scanning confocal microscope (Nikon) equipped with an AxioCamdigital camera (Carl Zeiss).

2.2.10 Ribonucleolytic assay of conditioned media

After serum starvation for 4 h, cells were treated with PBS or poly(C) (Sigma Chemical), poly(I:C) (InvivoGen), or poly(A:U) (Sigma Chemical) to 25 μg/mL. After 20 min, conditioned medium was collected, and a protease inhibitor cocktail (1×) (Sigma), EDTA (0.10 M), and Triton X-100 (1% v/v) were added immediately. Medium (10 μL) was assayed for ribonucleolytic activity using 6-FAM–dArU$(dA)_2$–6-TAMRA in 0.10 M Tris–HCl buffer, pH 7.4, containing NaCl (0.10 M) as described above.

2.2.11 Zymogram of conditioned media

Conditioned medium obtained as described above was concentrated using 5K MWCO spin concentrators (Corning). Samples were treated with PNGaseF (50 units) (New England Biolabs) in reaction buffer overnight at 37 °C. Samples were diluted with 2× Laemmli buffer (Bio-Rad) and loaded into a polyacrylamide gel (15% w/v) containing poly(C) (Sigma Chemical). Loaded samples were subjected to electrophoresis for 1.5 h at 100 V. Subsequent washing, refolding, and staining with toluidine blue were performed as described.[44,131]

2.2.12 Sequence alignment and phylogenetic tree reconstruction

Protein sequence alignments were made using MUSCLE[132] with manual adjustments. A maximum-likelihood phylogram was generated in MEGA5.2 using the Jones–Taylor–Thornton (JTT) substitution model with uniform site substitution rates[133] and 1000 bootstrap replicates.

2.2.13 Statistical analyses

Numerical data from experiments *in vitro* and *in cellulo* were analyzed by using unpaired and paired *t*-tests, respectively, to determine *p*-values.

2.3 Results

Recombinant BRB had never been characterized prior to our work. Moreover, only preliminary studies had been performed on isolated enzyme.[134,135] To enable relevant comparisons, we also analyzed well known homologs: human RNase 1, bovine RNase A, and both monomeric (mBSR) and dimeric (dBSR) forms of bovine seminal RNase (BSR). Until now, these enzymes had never been compared in a single, controlled study using the same methods and substrates. We chose to include a monomeric form of BSR (C31A/C32A)[123] to establish any differences in biochemical properties conferred by dimerization.

2.3.1 Initial characterizations of BRB

We began our study by analyzing biochemical properties of BRB that had been investigated for its homologs (Table 2.1). Analysis of aligned sequences demonstrated that BRB has less overall sequence identity and similarity to human RNase 1 than to either RNase A or BSR. Yet,

when the divergent, 17-residue C-terminal tail of BRB was excluded from analysis, the ensuing BRBΔ125–141 displayed identity (70%) and similarity (82%) to human RNase 1 as high or higher than those of RNase A and BSR. Like human RNase 1, BRB was found to be less thermostable than either RNase A or BSR. BRB was found to bind tightly to its endogenous inhibitor, bovine RI, similar to other homologous ribonucleases.[72,122,123,136]

2.3.2 Human RNase 1 and BRB show a pronounced shift in catalytic pH optimum

Previous studies have shown that orthologous ribonucleases can exhibit different pH optima for catalysis.[137] Our results reveal similar contrasts. Whereas RNase A had its highest activity at pH 6.1, both human RNase 1 and BRB had their highest activity at pH 7.2 (Figure 2.1A). Additionally, RNase A was ~5-fold more active against ssRNA at optimal pH than was either human RNase 1 or BRB (Figure 2.1B). Interestingly, we also found a distinct shift in pH optimum between monomeric and dimeric forms of BSR: mBSR had its highest activity at pH 6.5, whereas dBSR shows its highest activity at pH 7.1 (Figure 2.1A). Further, we noted a drastic drop in catalytic efficiency for dBSR over its monomeric form (Figure 2.1B).

2.3.3 Human RNase 1 and BRB can degrade double-stranded RNA with high efficiency

Although all pancreatic-type ribonucleases can degrade ssRNA substrates, a small subset display high activity toward dsRNA.[128] We examined the ability of ribonucleases to degrade dsRNA using poly(A:U) as substrate. We found that human RNase 1 degraded this dsRNA substrate with >2000-fold higher efficiency than that of RNase A. Tellingly, we found that BRB degraded poly(A:U) with efficiency ~200-, 7-, and 2-fold higher than those of RNase A, mBSR and dBSR, respectively (Figure 2.2A). The trend for human RNase 1 and dBSR agrees with

previous reports.[53,128,138] An active-site variant, H12A RNase 1, demonstrated little measurable activity against the substrate. We also assessed the ability of RNase B (Sigma Chemical), which is a naturally occurring glycoform of RNase A, to degrade poly(A:U), and found no significant change in activity from RNase A (data not shown).

As the heterogeneous nature of poly(A:U) does not allow for controlled secondary structure, we sought to create a novel dsRNA substrate to confirm our findings with poly(A:U). We designed a simple hairpin containing a single ribonucleotide embedded within a DNA oligonucleotide and labeled on the 5′ end with a fluorophore. Successful cleavage of this ribonucleolytic substrate necessitates unwinding of the DNA duplex formed by the hairpin. We monitored the formation of the fluorescent 6-mer cleavage product of ribonuclease catalysis by electrophoresis using a native polyacrylamide gel (Figure 2.2B). Densitometric analysis of substrate and cleavage products mirrored the same trend observed with the poly(A:U) substrate. Specifically, human RNase 1 demonstrated the most product formation, followed by BRB, then dBSR, mBSR and RNase A (Figure 2.2C). Again, H12A RNase 1 demonstrated little activity.

2.3.4 Human RNase 1 and BRB bind cell-surface molecules and disrupt liposomes

We used fluorescence polarization (FP) to compare the affinity of human and bovine ribonucleases toward common cell-surface glycans. Representative data are shown in Figure 2.3A. We found that both human RNase 1 and BRB had significantly higher affinity for all glycans tested than did either mBSR or RNase A. Average K_d values determined from at least three independent FP experiments are displayed as a heatmap (Figure 2.3B), and show that human RNase 1 and BRB exhibited nanomolar affinity for various carbohydrates.

We sought to determine if the increased affinity of ribonucleases for glycans correlated with their ability to disrupt lipid membranes. We observed significant differences between human RNase 1, BRB, and dBSR as compared to RNase A and mBSR (Figure 2.3C). Still, the rates of liposomal disruption were relatively low compared to enzymes such as lysozyme, which exhibits ~12-fold higher disruption efficiency than human RNase 1 (data not shown). The hydrophobic C-terminal tail did not endow BRB with a marked ability to disrupt liposomes.

2.3.5 Human RNase 1 and BRB readily enter mammalian cells

Next, we determined if greater cell-surface glycan association enhanced the uptake of human RNase 1 and BRB into nonadherent human cells. A representative sample of raw fluorescence data acquired by flow cytometry is shown in Figure 2.4A. Averaged, normalized data from three independent experiments indicated that both human RNase 1 and BRB were internalized into K-562 cells a significantly greater extent than were either mBSR or RNase A (Figure 2.4B).

Human RNase 1 is known to circulate freely in all bodily fluids, including blood.[44,104,139] Hence, we were curious to know if ribonucleases could interact with the vascular endothelium—cells known to play dynamic regulatory roles in host defense and vascular homeostasis.[140] We probed the internalization of ribonucleases into both human and bovine endothelial cells. Interestingly, we found that RNase 1 and BRB were taken up to a far greater extent by both human and bovine endothelial cells than were either mBSR or RNase A (Figure 2.5A and 2.5D).

2.3.6 Human RNase 1 and BRB are released from cells in response to dsRNAs

Previous studies have demonstrated that human RNase 1 is secreted profusely from endothelial cells.[44,104,139] Based on our findings that human RNase 1 and BRB can readily

degrade dsRNA, we hypothesized that extracellular dsRNA in the blood might act as an agonist that promotes RNase 1 secretion. Within 20 min of exposure to the double-stranded RNA substrates poly(I:C) or poly(A:U), conditioned medium from both human and bovine endothelial cells displayed significantly higher levels of ribonucleolytic activity (Figures 2.5B and 2.5E). Surprisingly, this phenomenon did not occur upon exposure to single-stranded RNA [poly(C)], or DNA (data not shown). Zymogram analysis of cell-conditioned media provide a qualitative indication that the increased RNase activity in the samples was due to human RNase 1 and BRB produced by human and bovine endothelial cells, respectively (Figures 2.5C and 2.5F). The ribonucleases secreted by these cells have *N*-linked glycans, which are removed by treatment with PNGaseF.

2.4 Discussion

Mounting evidence suggests that mammalian RNase 1 plays important roles *in vivo*, ranging from regulating blood clotting and inflammation to directly counteracting tumorigenic cells. We believe that progress toward understanding these putative roles has been hindered by continual comparisons of human RNase 1 to bovine RNase A. Although RNase A is perhaps the most important model protein in biological chemistry,[28,141,142] RNase A is the product of but one of three *RNASE1* duplicates in the bovine genome. Its expression is limited *in vivo*, and its evolution is recent. Despite these shortcomings, RNase A has been considered the archetypal RNase 1 enzyme, with its properties ascribed globally to all homologous proteins. Thus, the prevailing view of RNase 1 has been of a digestive enzyme possessing little importance beyond the ruminant gut.

Our data stand in stark contrast to this hypothesis. We find distinct differences between human RNase 1 and RNase A. Moreover, we have characterized an additional bovine variant, bovine brain RNase (BRB), and find pronounced similarities between this unappreciated protein and human RNase 1. We have demonstrated that human RNase 1 and BRB share similar biochemical properties, including strong catalytic activity against double-stranded RNA, as well as the intriguing ability to enter mammalian cells readily. These clustered attributes set human RNase 1 and BRB apart from either BSR or RNase A (Figure 2.6A). Coupled with previous reports of the widespread tissue expression of BRB in cows,[16] our data suggest that BRB—not RNase A—is the true functional homolog of human RNase 1. Moreover, our data support the existence of an important biological role for both human RNase 1 and BRB unrelated to digestion.

Our treatise is consistent with a phylogenetic analysis (Figure 2.6B), which suggests BRB resulted from an earlier genetic duplication than did either BSR or RNase A and thus resembles more closely the ancestral form of RNase 1 in ruminants.[120] Laboratory reconstructions of proposed “ancient” bovine ribonucleases support this claim, showing that “ancestral” forms of bovine RNase 1 display properties more similar to BRB than RNase A, including decreased thermostability and increased activity toward dsRNA.[143,144] Compellingly, the timeline of the divergence of RNase A corresponds to the Oligocene cooling epoch, which resulted in the rise of grasslands and the emergence of ruminant digestion. Hence, RNase A most likely represents a specialized digestive form of RNase 1 that arose simultaneously with foregut fermentation.[114,143] A similar phenomenon is known to have occurred in colobine monkeys, where a secondary form of RNase 1 with distinct properties evolved to participate in ruminant-like digestion.[137] Taken

together, extant evidence indicates that RNase A is not the prototype for mammalian RNase 1 in terms of function.

The question remains: if not digestion, what is the biological purpose of RNase 1? A conclusive answer to this question hinges upon future analysis of *in vivo* models. Still, our work does provide a basis for speculation. The ability of human RNase 1 and BRB to degrade dsRNA is of special interest because of its immunological implications. Most viruses produce dsRNA at some point during their replication. In mammalian cells, dsRNA is a potent antigen recognized by sensors such as Toll-like receptor (TLR) 3, through which dsRNA can trigger the transcription-based antiviral interferon response.[145,146] We found that stimulating endothelial cells with the dsRNA substrate poly(A:U), as well as with the synthetic viral dsRNA analog poly(I:C), increased the secretion of both RNase 1 and BRB significantly, whereas treatment with ssRNA or DNA did not. RNase 1 has been shown to be released spontaneously from endothelial cells upon treatment with various vascular agonists.[44] Potentially, the presence of extracellular dsRNA provides a signal to direct the spontaneous release of stored, latent RNase 1. By degrading antigenic stimulants like extracellular RNAs, RNase 1 could play a crucial role in regulating antiviral immunity and inflammation.

Whereas the potential importance of dsRNA degradation by RNase 1 is clear, the mechanism of catalysis is not. The RNase 1 active site cannot accommodate two nucleic acid strands simultaneously; thus, the putative mechanism invokes the unwinding of the double helix by cationic residues near the enzymic active site. Arg-32[112,128] and Lys-102[53] have been implicated, in particular. Both of these cationic residues are present in human RNase 1 and BRB, but absent in BSR and RNase A. Yet, other residues that could be important for dsRNA degradation by

human RNase 1, including Arg-4, Lys-6, Lys-62, and Lys-74,[53,138] are not found in BRB, leaving unknown the precise basis for dsRNA degradation.

Intriguingly, the Toll-like receptors that respond to ssRNA and dsRNA (TLR7/TLR8 and TLR3, respectively) are all localized within endosomes.[147-149] Our current work demonstrates that both human RNase 1 and BRB internalize into mammalian cells significantly better than do either RNase A or mBSR (Figures 2.4, 2.5A, and 2.5D). We have shown previously that RNase 1 internalization involves endocytosis;[84,88,90] thus, human RNase 1 and BRB might be especially well adapted to enter endosomes, where they could degrade antigenic RNA and regulate signaling cascades. Their increased cellular uptake could hinge upon increased interactions with anionic cell-surface glycans. Indeed, our data show that human RNase 1 and BRB bind much more tightly to an assortment of sulfated glycans, especially heparin, than does RNase A. This interaction is not merely based on Coulomb's law, as mBSR (Z = +9) binds much more weakly than does human RNase 1 (Z = +6). Accordingly, we posit that human RNase 1 and BRB contain putative heparan sulfate-binding motifs. For example, the BBXB motif, where B represents a basic residue, has been shown to be a common heparan sulfate-binding motif in proteins.[150-152] Human RNase 1 and BRB both contain three cationic regions that are similar to a BBXB motif and are absent from both mBSR and RNase A (Figure 2.7). These unique areas of positive charge might account for many of the distinct properties shared by these enzymes, including dsRNA degradation, increased lipid disruption, and enhanced cellular internalization.

An unexpected result from our study is the pronounced divergence in pH optimum for catalysis among ribonucleases (Figure 2.1). We found RNase A to have a pH-optimum of 6.0, a value that closely reflects classic studies[153] and makes RNase A well-suited for the acidic environment of the bovine rumen. Conversely, human RNase 1 and BRB had a pH-optimum of

7.3 and 7.4, respectively, which are close to the pH of many bodily fluids, including blood (pH 7.3). These data correlate with observations that human RNase 1 circulates freely throughout the body in all fluids tested.[119] We speculate that differences in pH-optimum between homologs could be due to slight perturbations in the pK_a values of the two active-site histidine residues. We were surprised to observe a large difference in pH-optimum (~1.3 pH units) for catalysis by the native dimeric form of BSR and the artificial monomer. The dimeric structure of BSR is also necessary for its other putative biological functions, including its immunosuppressive and antitumor activity.[115,136] The dimer is known to swap its N-terminal helices,[154,155] thereby forming a chimeric active site that could have higher histidine pK_a values. Thus, its unique quaternary structure appears to equip BSR for catalysis in the cytosol as well as in bovine seminal fluid, where the typical pH is 6.8–7.2.[156] This functional imperative for a dimeric form could explain the existence of the BSR gene as a pseudogene in species where the cysteine residues required for dimerization have been lost.

Many questions remain regarding the biology of mammalian RNase 1, and BRB in particular. An ongoing mystery is how glycosylation of RNase 1 influences its endogenous functions. Analyses of human tissues and fluids indicate that various tissue sources produce differentially glycosylated forms of RNase 1;[104,157] BRB has also been shown to have *N*-linked glycans that are highly heterogeneous and distinct from those attached to RNase A.[158] We too found secreted ribonucleases that were *N*-glycosylated (Fig. 2.5C and 2.5F). A second perplexity surrounds BRB: what is the purpose of its extended, hydrophobic C-terminal tail? Although all ruminant brain ribonucleases possess a similar tail, the amino-acid sequences of these regions are not conserved, and seem to have arisen through multiple substitutions and deletions.[113,134] The tail is known to be *O*-glycosylated at two sites,[117] but the significance of these oligosaccharide

chains is not known. We speculated that the hydrophobic tail allows BRB to preferentially disrupt lipid membranes, but our data showed that BRB did not have significantly different activity toward liposomes than either human RNase 1 or dBSR (Fig. 2.3C). Previous studies have shown that proline-rich motifs can be associated with facilitating protein–protein interactions, specifically transient interactions such as recruitment of multiple factors.[159] Thus, the proline-rich C-terminal tail of BRB could act as a protein scaffold to recruit other proteins.

In conclusion, we have presented data that establish functional relationships between human and bovine homologs of mammalian RNase 1. Our data provide fundamental insight into the biological role of RNase 1 in mammals, suggesting a physiology not associated with digestion. Further studies, including analyses of mammalian animal models, are necessary for a complete description of the most significant biological functions of RNase 1 in humans and other mammals. Currently, mouse studies probing the therapeutic potential of RNase 1 against various pathologies have utilized RNase A as their treatment of choice.[59,64,105-107,160] We speculate that the use of recombinant human RNase 1, BRB, or mouse RNase 1 would provide a more robust and relevant phenotype. Finally, we note that our understanding of BRB has been hindered by its appellation, which incorrectly implies an association only with the brain, just as our understanding of human RNase 1 has been obfuscated by its undue association with the pancreas.

Acknowledgements

We are grateful to Prof. C.J. Czuprynski (University of Wisconsin-Madison) for providing TBBE cells, and T.T. Hoang for human angiogenin.

Table 2.1 Biochemical properties of human and bovine ribonucleases

Ribonuclease	**MW (kDa)**	***Z*[a]**	**% Identity to RNase 1**	**% Similarity to RNase 1[b]**	**T_m (°C)[c]**	**K_d (fM)[d]**
RNase 1 (*H. sapiens*)	14.7	+6	100	100	55.5 ± 0.5	0.12 ± 0.1
BRB (*B. taurus*)	15.8	+11	61	72	52.2 ± 0.4	0.35 ± 0.21
mBSR (*B. taurus*)	13.7	+9	70	80	60.1 ± 0.5	1.94 ± 0.72
dBSR (*B. taurus*)	27.5	+18	70	80	62[e]	>2 x 10^{9}[f]
RNase A (*B. taurus*)	13.7	+4	68	82	63.9 ± 0.4	0.16 ± 0.12

[a] Value is for the net molecular charge: Arg + Lys – Asp – Glu

[b] For % similarity calculations: K = R; D = E; C = G = H = N = Q = S = T = Y; A = F = I = L = M = P = V = W

[c] Value is the temperature at the midpoint of thermal denaturation, determined by incorporation of a hydrophobic dye and quantitation by differential scanning fluorimetry[125]

[d] Value is for the complex with bovine ribonuclease inhibitor, determined as described[72,122,126]

[e] Value was determined with circular dichroism spectroscopy[161]

[f] Value is for the complex with human ribonuclease inhibitor[136]

ND, not determined

Figure 2.1

A

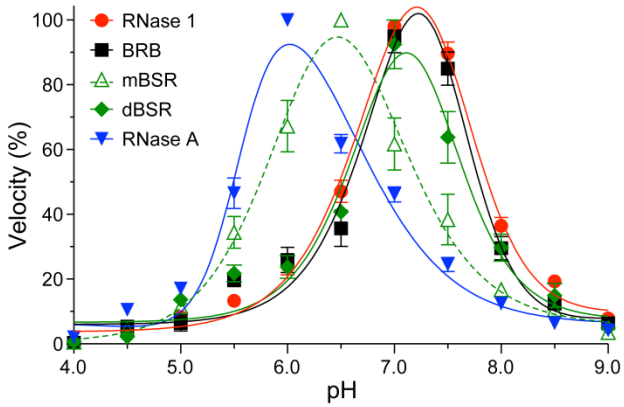

B

	pH Optimum	k_{cat}/K_M (10^6 $M^{-1}s^{-1}$) at pH Optimum
RNase 1	7.3	2.8 ± 1.6
BRB	7.4	2.2 ± 1.4
dBSR	7.2	0.3 ± 0.1
mBSR	6.3	4.9 ± 1.7
RNase A	6.0	11.5 ± 1.5

Figure 2.1 Effect of pH on catalysis on single-stranded RNA cleavage by human and bovine ribonucleases

A. pH–Rate profiles using the normalized initial velocity for cleavage of single-stranded RNA. Values (± SE) are the mean from at least three independent experiments. *B*. pH optima for catalysis as calculated from the data in panel *A*, and values (± SE) of k_{cat}/K_M at that pH.

Figure 2.2

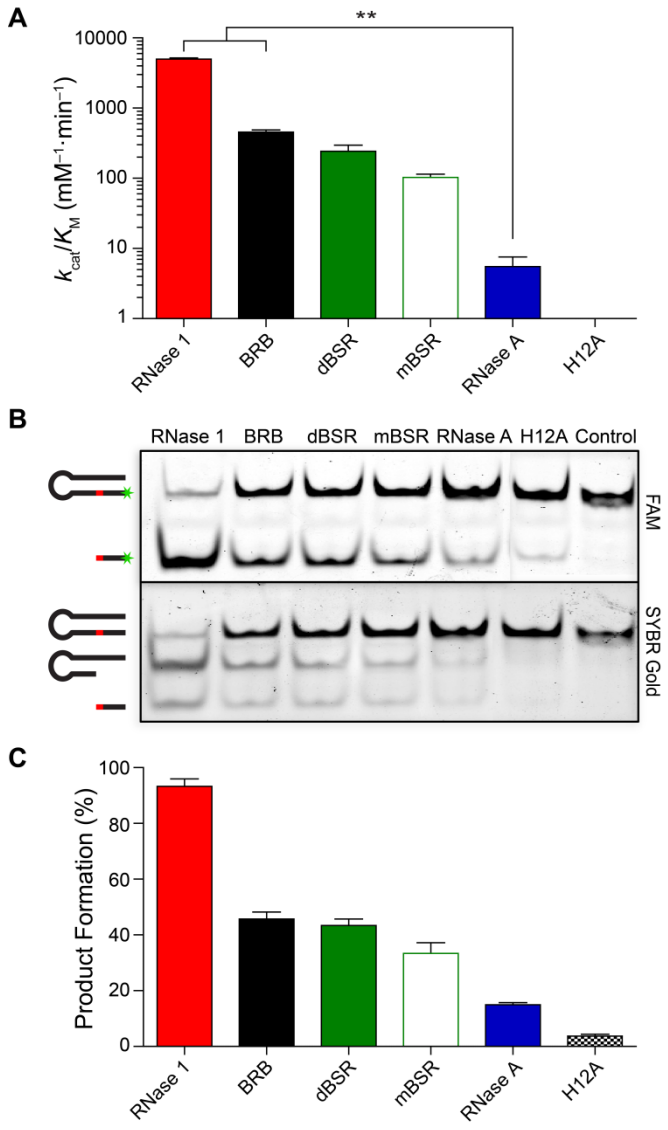
A
**
10000
1000
100
10
1
k_{cat}/K_M (mM^{-1}·min^{-1})
RNase 1
BRB
dBSR
mBSR
RNase A
H12A
B
RNase 1
BRB
dBSR
mBSR
RNase A
H12A
Control
FAM
SYBR Gold
C
100
80
60
40
20
0
Product Formation (%)
RNase 1
BRB
dBSR
mBSR
RNase A
H12A

Figure 2.2 Catalysis of double-stranded RNA cleavage by human and bovine ribonucleases *A*. Values k_{cat}/K_M for the cleavage of poly(A:U). Values (± SE) are the mean from at least three independent experiments. $^{**}p < 0.01$. *B*. Native polyacrylamide gel showing cleavage of a DNA hairpin containing a single RNA residue (red) and labeled on the 5′ end with FAM (green). SYBR Gold enables imaging of all nucleic acids. *C*. Extent of FAM-labeled product formation for the data in panel *B*. Values (± SE) are the mean from four native gels.

Figure 2.3

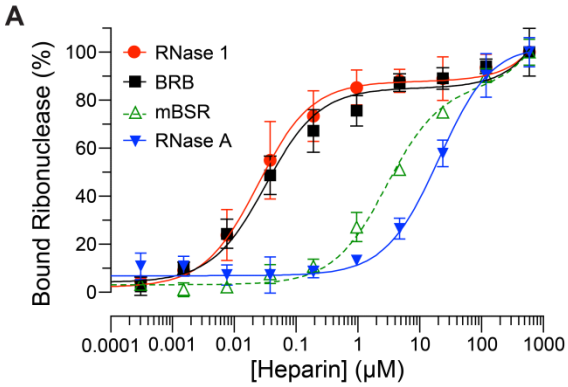

B

Values of K_d for Ribonuclease•Glycan Complexes (μM)

Degree of Sulfation

	Heparin	Chondroitin Sulfate B	Chondroitin Sulfate A	Chondroitin Sulfate C
RNase A	42 ± 3	81 ± 58	120 ± 80	356 ± 22
mBSR	7.9 ± 0.4	55 ± 23	57 ± 1	13 ± 1
BRB	0.064 ± 0.019	2.8 ± 1.4	5.3 ± 0.8	0.47 ± 0.09
RNase 1	0.012 ± 0.003	10 ± 5	7.6 ± 4.8	5.7 ± 0.6

Tighter Binding — Weaker Binding

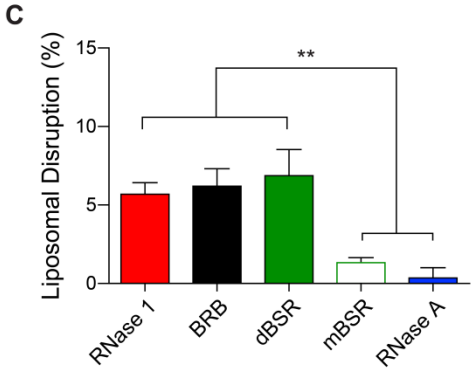

Figure 2.3 Interactions of human and bovine ribonucleases with membranes

A. Representative isotherms for binding of BODIPY-labeled ribonucleases to heparin as determined by fluorescence polarization. *B*. Heatmap indicating the relative affinity for various cell-surface glycans, determined as in panel *A*. Values (± SE) are the mean from at least three independent experiments. Blue tones represent nM affinity; yellow tones represent μM affinity. *C*. Disruption of phosphatidylcholine liposomes by ribonucleases, as measured by the release of an encapsulated dye. Values (± SE) are the mean from at least three independent experiments. $^{**}p < 0.01$.

Figure 2.4

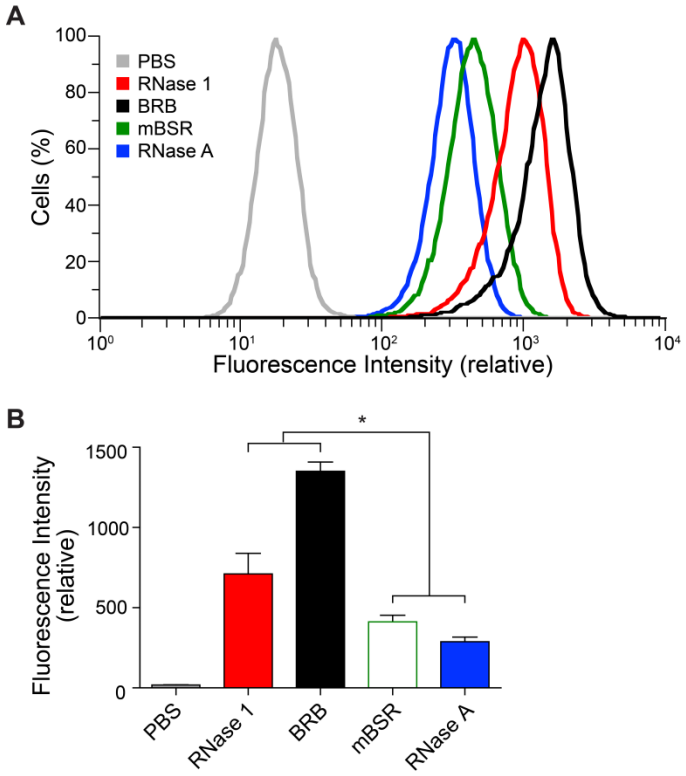
A
100
80
60
40
20
0
Cells (%)
PBS
RNase 1
BRB
mBSR
RNase A
10^0
10^1
10^2
10^3
10^4
Fluorescence Intensity (relative)
B
*
1500
1000
500
0
Fluorescence Intensity (relative)
PBS
RNase 1
BRB
mBSR
RNase A

Figure 2.4 Mammalian cell internalization of human and bovine ribonucleases

A. Representative flow cytometry data for the uptake of BODIPY-labeled ribonucleases into K-562 cells after 4 h. *B*. Values (± SE) are the mean from four independent experiments. *$p < 0.05$.

Figure 2.5

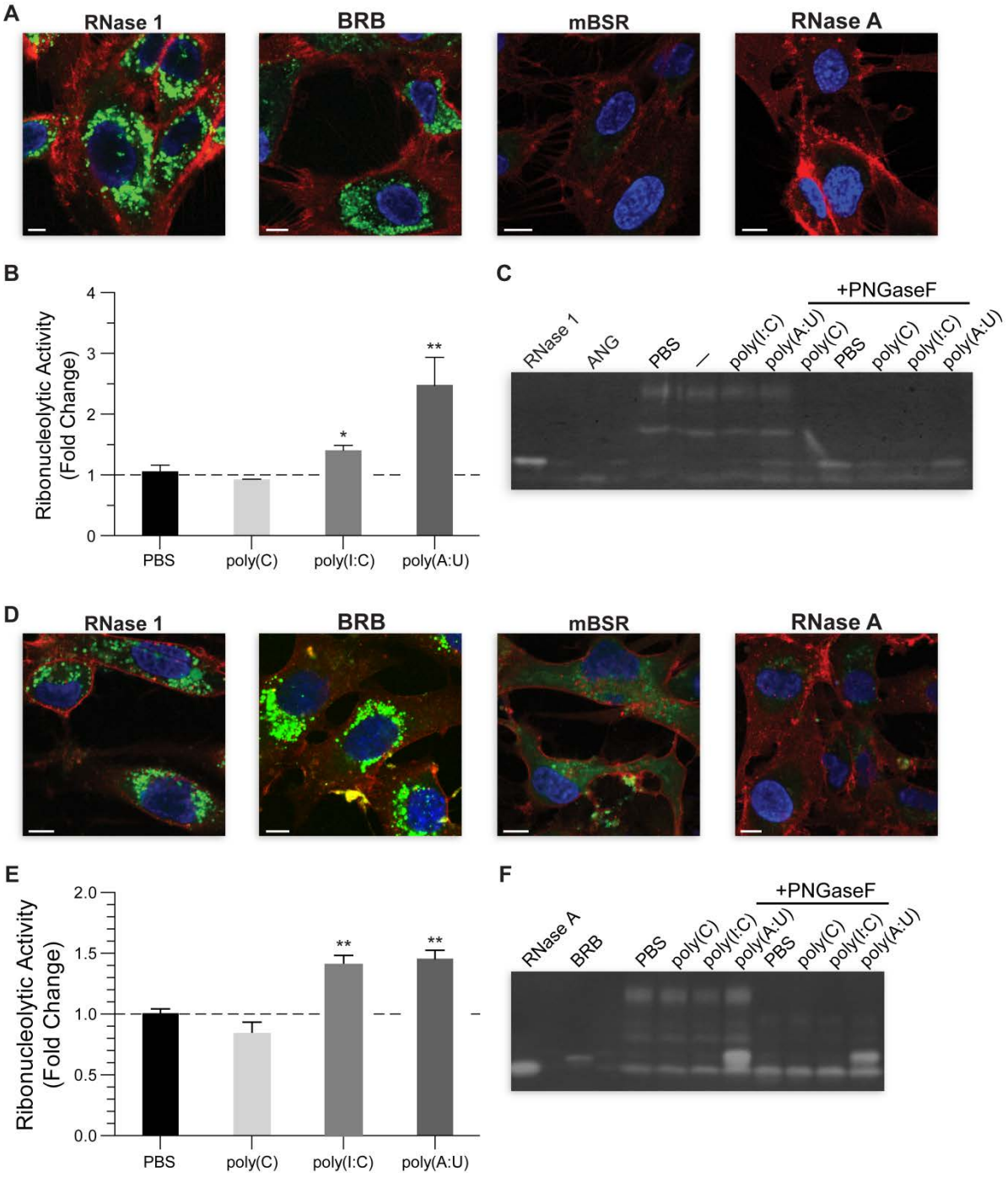
A
RNase 1
BRB
mBSR
RNase A
B
Ribonucleolytic Activity (Fold Change)
PBS
poly(C)
poly(I:C)
poly(A:U)
C
+PNGaseF
RNase 1
ANG
PBS
poly(I:C)
poly(A:U)
poly(C)
PBS
poly(C)
poly(I:C)
poly(A:U)
D
RNase 1
BRB
mBSR
RNase A
E
Ribonucleolytic Activity (Fold Change)
PBS
poly(C)
poly(I:C)
poly(A:U)
F
+PNGaseF
RNase A
BRB
PBS
poly(C)
poly(I:C)
poly(A:U)
PBS
poly(C)
poly(I:C)
poly(A:U)

Figure 2.5 Endothelial cell internalization and release of human and bovine ribonucleases *A–C*, HUVEC cells; *D–F*, TBBEC cells. *A,D*. Cellular internalization of exogenous ribonucleases (1.25 µM) after 4 h. Ribonuclease label: BODIPY (green); outer membrane stain: WGA-594 (red); nuclear stain: Hoechst 33342 (blue). Scale bar: 5 µm. *B,E*. Ribonucleolytic activity of cell-conditioned media after treatment with ssRNA or dsRNA. Values (± SE; $n = 6$) are normalized to basal activity. *$p < 0.05$; **$p < 0.01$. *C,F*. Zymogram of concentrated conditioned medium before or after treatment with the *N*-glycosidase PNGaseF. ANG: human angiogenin.[162]

Figure 2.6

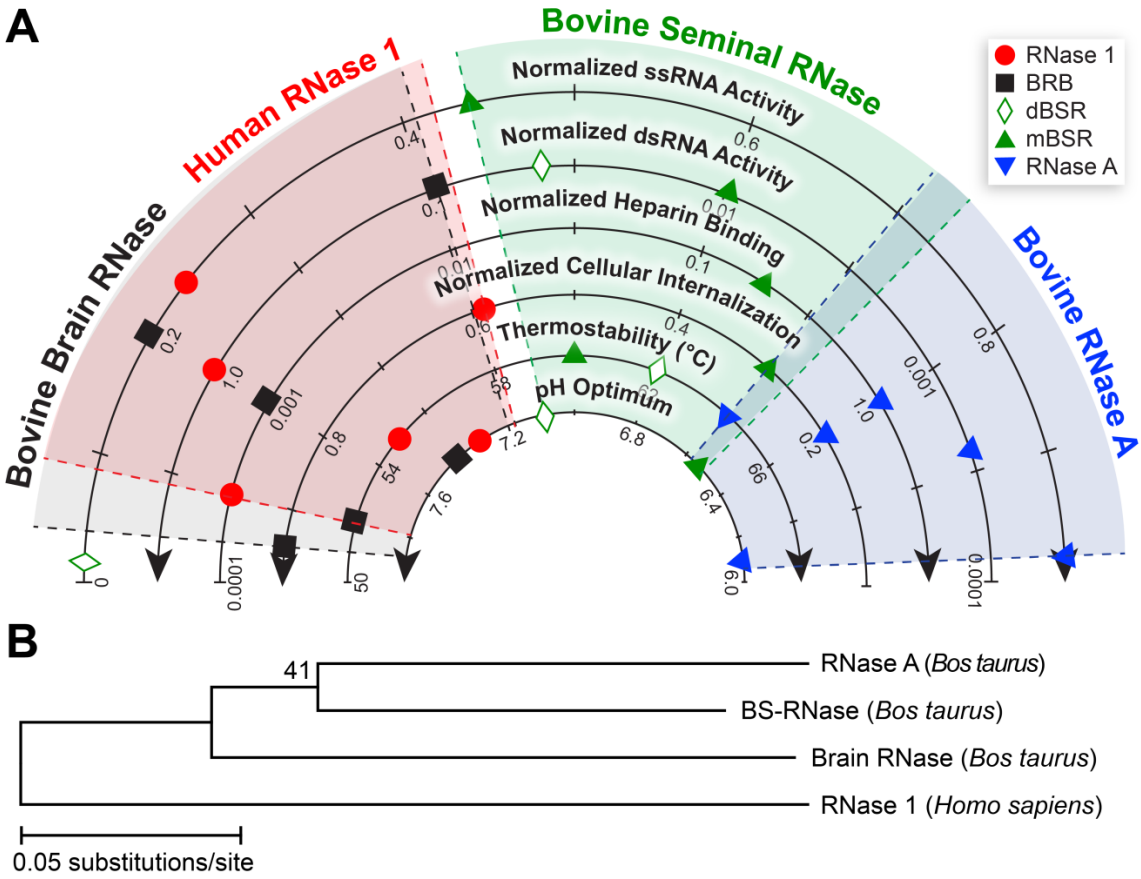
A
Bovine Seminal RNase
Human RNase 1
Bovine Brain RNase
Bovine RNase A
Normalized ssRNA Activity
Normalized dsRNA Activity
Normalized Heparin Binding
Normalized Cellular Internalization
Thermostability (°C)
pH Optimum
RNase 1
BRB
dBSR
mBSR
RNase A
B
41
RNase A (Bos taurus)
BS-RNase (Bos taurus)
Brain RNase (Bos taurus)
RNase 1 (Homo sapiens)
0.05 substitutions/site

Figure 2.6 Schematic summaries of data for human and bovine ribonucleases

A. Schematic representation of normalized biochemical parameters from Table 2.1 and Figures 2.1–2.4. Symbols indicate data obtained from assays; shaded regions indicate the range of all values for a particular ribonuclease. *B*. Phylogram indicating bootstrap values >40.

Figure 2.7

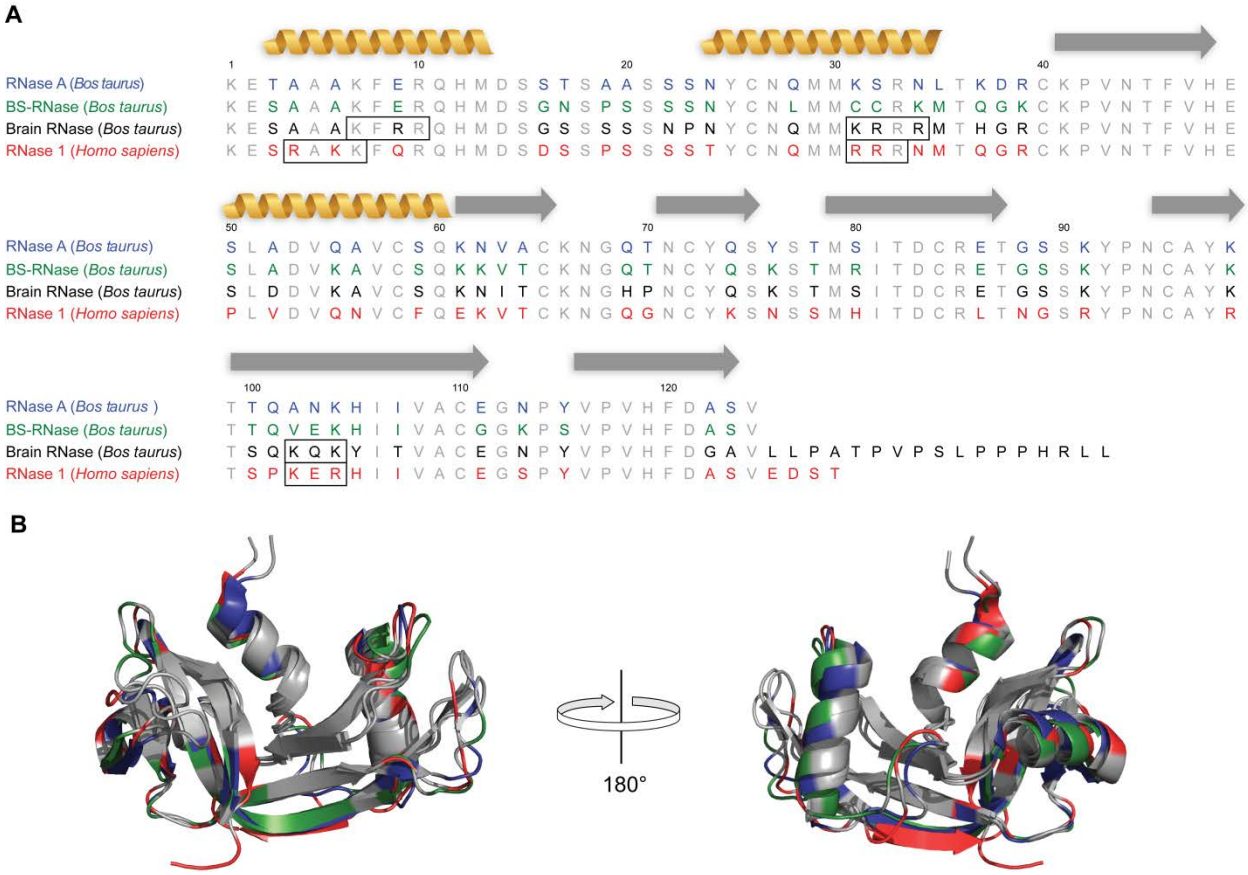
A
RNase A (Bos taurus)
BS-RNase (Bos taurus)
Brain RNase (Bos taurus)
RNase 1 (Homo sapiens)
B
180°

Figure 2.7 Sequence and structural alignment of human and bovine ribonucleases

A. Grey residues indicate residues conserved in all proteins; colored residues indicate divergence. Black boxes indicate putative heparan sulfate-binding domains. Yellow coils denote α-helices; gray arrows denote β-sheets. *B.* Backbone overlay of human RNase 1 (red; PDB entry 1Z7X), mBSR (green; 1BSR), and RNase A (blue; 1FS3).

Chapter 3

Human Ribonuclease 1 Binds to the Human Cancer Antigen Globo H

Contribution:

I performed all the biochemical and cell biology experiments in this chapter except for the collection of the NMR experiments, synthesis of Globo H and SSEA-4, and the glycan array.

This chapter is in preparation for publication as:

Eller, C.H., Chao, T.Y., Singarapu, K.K., Ouerfelli, O., Markley, J.L., Danishefsky, S.J., Raines, R.T. Human Ribonuclease 1 Binds to the Human Cancer Antigen Globo H. In preparation.

Abstract

Pancreatic-type ribonucleases are a highly conserved family of small, cationic, secretory enzymes that catalyze the cleavage of RNA. Recent efforts have endowed ribonucleases from human pancreas (RNase 1) and bovine pancreas (RNase A) with selective cytotoxicity for cancer cells. It is, however, unknown why cancer cells are preferentially vulnerable to these ribonuclease variants. A screen for the binding of RNase A to a large array of human cell-surface glycans revealed strong affinity for anionic glycans and, surprisingly, a neutral hexasaccharide, Globo H, which is a cancer antigen. We found that the affinity of RNase A and RNase 1 for immobilized Globo H is in the low micromolar–high nanomolar range, depending on the pH. We showed that a synthetic inhibitor of Globo H biosynthesis decreases the cytotoxicity of RNase A and RNase 1 variants. Finally, we used heteronuclear single quantum coherence (HSQC) NMR spectroscopy to discover that the residues in RNase 1 that interact with Globo H are distal from the enzymic active site. This work reveals a new interaction that directs a systemic human enzyme to a moiety displayed on cancer cells, and encourages the development of human RNase 1 as a chemotherapeutic agent.

3.1 Introduction

Pancreatic-type ribonucleases (RNases) are small cationic proteins that are secreted by vertebrate cells.[28] Two RNases from human (RNase 1) and bovine (RNase A) are highly efficient catalysts of RNA cleavage. Moreover, when engineered to evade a cytosolic inhibitor protein, RNase 1 and RNase A are endowed with cytotoxicity.[32,89,163,164] The putative pathway of RNase-mediated cytotoxicity involves internalization into the endosomal pathway, translocation into the cytosol, and cleavage of RNA, which leads to apoptosis.

Surprisingly, the cytotoxic activity of RNases is specific for cancer cells, and a variant of RNase 1 is undergoing Phase I clinical trials as a cancer chemotherapeutic agent. The molecular basis for this specificity is unclear. One hypothesis is that the cationic RNases interact with anionic cell-surface moieties to mediate the binding of RNases, and their subsequent internalization and translocation.[88] In fact, RNase A variants bind to the cell membrane in a non-saturable, non-receptor mediated manner.[84] Further, reducing the negative charge on a cell surface by diminishing the biosynthesis of heparan sulfate and chondroitin sulfate decreases net internalization, as does decreasing the positive charge of an RNase.[88,89] Mechanistic studies showed that RNase internalization is analogous to that of cell-penetrating peptides and occurs through both clathrin-coated vesicles and macropinosomes.[90] Given the surface of cancer cells is commonly more anionic due to increases in glycosaminoglycan profile, phospholipid composition, or glycosphingolipid exposure,[78] these data provide some basis for the preferential susceptibility of cancer cells to RNase-mediated cytotoxicity. Still, we suspected that other factors could contribute.

Eukaryotic cells are covered by a glycocalyx—an extensive network of polysaccharides.[165] The glycocalyx serves as a rich source of binding sites for receptors and ligands, as well as

pathogens and toxins. The mammalian glycome is estimated to consist of a few hundred unique glycan structures on glycoproteins and glycolipids.[166] One such glycan is Globo H.

Globo H is a neutral hexosaccharide glycosphingolipid. Globo H, as a glycolipid as well as a glycoprotein, endogenously locates on the outer membrane of epithelial cells, namely mammary, uterine, pancreas, and kidney tissues.[167,168] Yet, immunohistological analyses have detected high expression of Globo H on the outer membrane of tumor specimens from small cell lung, breast, prostate, lung, pancreas, gastric, ovarian, and endometrial tissues.[169] Indeed, overexpression of this tumor antigen correlates to poor prognosis.[170,171] As endogenous expression resides in tissues generally inaccessible to immune system, Globo H has become an attractive vaccine target for epithelial tumors. This approach is further supported by trials indicating that treatment of up to 16 mg of antibody against Globo H, MBr1, in cancer patients resulted in no organ toxicity.[172] Additionally, MBr1 exhibits high affinity and specificity to Globo H over related glycans in this family.[173] As such, vaccine therapies containing synthetic Globo H are now in clinical trials.[174,175] Despite the current therapeutic interest in Globo H, little is known about the functional role of Globo H, and to date, no molecules (other than antibodies) have been determined to interact with this cell-surface glycan.

Herein, we screen an array of immobilized human glycans and find that RNase A interacts strongly with Globo H. We determine the *in vitro* binding affinities of bovine RNase A and human homolog, RNase 1, to Globo H using surface-binding assays. We find that a small-molecule inhibitor of Globo H biosynthesis reduces the vulnerability of cells to cytotoxic variants of RNase A and RNase 1. Further using heteronuclear single quantum coherence (HSQC) NMR spectroscopy, we identify residues of RNase 1 that interact with Globo H enriched in micelles. Together, these data contribute an enhanced understanding of the efficacy

of RNases as cancer chemotherapeutic agents, and suggest a role of human RNase 1 as an endogenous anti-cancer agent.

3.2 Methods

3.2.1 Glycan array

A glycan array was screened for RNase A ligands by the standard procedure of Core H of the Consortium for Functional Glycomics (CFG).[176] The array was version 2.0 and comprises 264 synthetic and natural glycans that are found on human cells. The gycans were amine-functionalized with an amino group and immobilized to *N*-hydroxysuccinimide-activated glass slides.[176] Briefly, RNase A was diluted to a concentration of 200 μg/mL in binding buffer, 20 mM Tris–HCl, pH 7.4, containing NaCl (150 mM), $CaCl_2$ (2 mM) $MgCl_2$ (2 mM), Tween 20 (0.05% v/v), and BSA (1% w/v). Binding of RNase A was detected by using primary antibodies and secondary antibodies labeled with Alexa Fluor® 594 from Life Technologies (Grand Island, NY).[177] Primary antibody against RNase A was used at a concentration of 1 μg/mL. To correct for antibody binding, the antibodies were screened against the array independently, and fluorescence values obtained with antibodies alone were subtracted from those in the presence of RNase A.

3.2.2 Production of RNases: Wild-type, fluorescent conjugations, and [^{15}N] labeled

RNase 1 and RNase A were produced by heterologous expression of their cDNA in *E. coli* strain BL21(DE3) as described previously.[163] To conjugate a fluorescent dye via a maleimide group, a cysteine residue was installed into each ribonuclease by site-directed mutagenesis, and G89C RNase 1, P19C RNase 1, and A19C RNase A were produced in a similar manner. After

purification, the nascent thiol was protected as a mixed disulfide by reaction with 5,5′-dithiobis-(2-nitrobenzoic acid). Prior to conjugation, the nascent thiol in 10 mg of protein was deprotected by the addition of dithiothreitol (4 equiv) from Goldbio (St. Louis, MO). The ribonuclease was separated from excess dithiothreitol by passage through a column of PD-10 desalting resin (GE Healthcare, Pittsburg, PA). The deprotected ribonuclease was reacted with 10 equiv of BODIPY-Fl (Life Technologies) dissolved in aqueous DMSO (10% v/v). While stirring, BODIPY-Fl was added drop wise, and the reaction was allowed to proceed at room temperature for 2 h, then at 4 °C for 4 h. After overnight dialysis into 50 mM AcOH, pH 5.0, purification by chromatography on a cation-exchange resin (GE Healthcare) yielded conjugated RNase. This protein was analyzed by mass spectrometry and SDS–PAGE with imaging by fluorescence scanning and Coomassie staining.

[^{15}N]RNase 1 and [^{15}N]RNase A were also produced in *E. coli* as described previously,[163] except using a double-growth procedure in minimal media containing [^{15}N]NH_4Cl from Cambridge Isotope Laboratories (Andover, MA) after induction with IPTG from Sigma–Aldrich (St. Louis, MO).[178] Growth conditions yielded an average of 15 mg of RNases from 1 L of medium. Protein purification was monitored with SDS–PAGE. The final purified proteins were submitted to the University of Wisconsin Biotechnology Center (Madison, WI) for analysis using matrix-assisted laser desorption/ionization (MALDI) mass spectroscopy to check for homogenous incorporation of ^{15}N. The observed masses of 14790.1 and 13809.2 Da indicated isotope incorporation had been (14790.1 – 14,604)/192 = 96.9% and (13809 – 13681)/172 = 74.4% for RNase 1and RNase A, respectively.

RNases were assayed for catalytic activity by monitoring cleavage of a fluorogenic RNA substrate, 6-FAM–dArUdGdA–6-TAMRA from IDT.[179] Assays were performed in 0.10 M MES

[oligo(vinylsulfonic acid)-free] buffer, pH 6.0, containing NaCl (0.10 M). The addition of RNases yielded a linear increase of fluorescence that can be converted into activity with the equation:

$$k_{\mathrm{cat}}/K_{\mathrm{M}} = \frac{\Delta I/\Delta t}{(I_{\mathrm{max}} - I_0)[\mathrm{RNase}]} \tag{3.1}$$

where $\Delta I/\Delta t$ is the initial reaction velocity, I_{max} is the maximum detected fluorescence after saturating substrate with excess RNase A, and I_0 is the initial background fluorescence after incubation of substrate. Fluorescence labeling or isotopic incorporation had no significant effect on enzymatic activity compared to wild-type with activities as (2.1 ± 1.2) $\mu M^{-1}s^{-1}$ and (31 ± 6) $\mu M^{-1}s^{-1}$ for RNase 1 and RNase A, respectively.

3.2.3 Glycans: Globo H-ceramide, Globo H-BODIPY, Globo H-biotin, SSEA-4-BODIPY, SSEA-4-biotin

Globo H-ceramide, Globo H-BODIPY, and Globo H-biotin were synthesized from Globo H as described.[173,180] SSEA-4-biotin and SSEA-4-azide were provided by the Consortium for Functional Glycomics. Synthesis from SSEA-4-azide yielded SSEA-4-BODIPY as described.[173]

3.2.4 Fluorescence binding assay

Binding between RNases and soluble glycans was monitored by fluorescence polarization of BODIPY-glycan conjugates, SSEA-4 and Globo H, and saturating with RNases. In a 96-well plate, PBS, pH 7.3, containing glycan (25 nM) was incubated with increasing amounts of an

RNase. Additional HSA or BSA was added to maintain a constant concentration of 7.5 μg per well. Additionally non-specific interactions of glycans toward albumin were monitored using increasing concentrations of HSA or BSA (Sigma–Aldrich). After 30 min at 25 °C, polarization was recorded on the M1000 fluorimeter (Tecan Group, Männedorf, Switzerland).

3.2.5 Fluorescence surface-binding assay

Quantification of binding between RNases and immobilized glycans was monitored using a fluorescence surface binding assay. Briefly, a 96-well plate coated in NeutrAvidin (Pierce, Rockford, IL) was washed with 3× PBS then incubated with 10 equiv of Globo H–biotin or SSEA-4–biotin. To reduce non-specific interactions, wells were incubated with aqueous milk (5% v/v) and washed 3× in PBS. RNase–BODIPY conjugates were incubated to equilibrium in PBS, pH 7.4, containing Tween X-100 (0.005% v/v) or 20 mM Tris–HCl buffer, pH 5.0, containing NaCl (130 mM). After 3 washes, the fluorescence of RNase–BODIPY was detected by emission at 530 nm after excitation at 490 nm. Binding isotherms were normalized to the fluorescence from glycan alone, and data were analyzed by non-linear regression fit to the equation:

$$Y = \frac{B_{\mathrm{max}}[\mathrm{RNase}]^h}{\left({K_\mathrm{d}}^h + [\mathrm{RNase}]^h\right)} \tag{3.2}$$

where Y is normalized relative fluorescence (RFU), B_{max} is the maximum percent fluorescence, and h is the Hill coefficient.

3.2.6 Cell culture

MCF-7 human breast cancer cell line (ATCC) was grown in DMEM high glucose from Invitrogen (Carlsbad, CA) containing FBS (10% v/v) and pen/strep (Invitrogen). Cells were maintained at 37 °C in 5% CO_2. Inhibition of fucosyltransferases was performed as described previously using peracetylated 2-fluoro-2-deoxyfucose (F-fucose; 100 μM) in a final concentration of 0.1% v/v DMSO.[181,182] Cells were treated for 3 days with F-fucose prior to treatment with RNases, and control cells were treated with DMSO only.

3.2.7 Confocal microscopy

Cells (1×10^5/well) were plated in an 8-well microscopy slide from Ibidi (Verona, WI). RNase-BODIPY conjugates in serum-free medium were incubated with cells for 4 h. The cell surface was stained with WGA-488 from Life Technologies (Grand Island, NY), or α-Globo H from Enzo (Farmingdale, NY) and secondary goat α-mouse Alexa 594 from Life Technologies. Nuclei were stained with Hoechst 33342 from Life Technologies. Images were captured on Eclipse TE2000-U laser scanning confocal microscope from Nikon equipped with an Axio Camdigital camera from Carl Zeiss.

3.2.8 Cell viability assay

Cells (5000/well) were plated into 96-well plate (Corning, Corning, NY) and grown for 3 days in the presence of F-fucose/DMSO or DMSO (0.1% v/v) alone. Medium was exchanged to serum-free medium, and RNases in PBS were added in increasing concentration and incubated for 44 h. Medium was removed, and cells were incubated in CellTiter 96 MTS reagent from

Promega (Madison, WI) for 2 h. The absorbance was then measured at 490 nm and normalized to that from cells treated with 0.1% v/v DMSO alone (100%) and 1 mM H_2O_2 (0%).

3.2.9 Preparation of samples for ^{15}N-HSQC NMR spectroscopy

Samples were prepared in 600 µL with 100 mM KH_2PO_4 buffer, pH 6.5 or pH 4.7, containing [^{15}N]RNase (250 µM), cetyl trimethylammonium bromide (25 mM; Sigma–Aldrich), and D_2O (10% v/v). Globo H ceramide was first resuspended in $CHCl_3$/MeOH/H_2O 65:35:5. An aliquot of 0.15 µmol (1 equiv compared to the [^{15}N]RNase) was dried under N_2(g) and then under high vacuum for 2 h. The protein micelle buffer solution was added to resuspend the Globo H into micelles.

NMR data were recorded at 25 °C in 8-inch Wilmad glass tubes from Wilmad-Labglass (Vineland, NJ) on the 600 MHz Varian NMR Spectrometer (NMRFAM). ^{15}N-HSQC NMR spectra were measured and peak assignments were made with Sparky using the assignments determined from the solution structure of RNase 1[183] and RNase A.[178] The vector change of chemical shift ($\Delta\Delta\delta$) upon addition of Globo H (1 equiv) was determined with the equation:

$$\Delta\Delta\delta = \sqrt{(\Delta\delta^{1}\mathrm{H})^2 + \left(\left(\tfrac{1}{5}\right)\Delta\delta^{15}\mathrm{N}\right)^2} \tag{3.3}$$

where chemical shifts ($\Delta\delta$) of the ^{1}H and ^{15}N were determined by subtracting the peak chemical shifts of RNase in the absence of Globo H. Chemical shift perturbations ($\Delta\Delta\delta$) were inserted as the β-factor in PDB entry 2k11 and images were made with the program PyMOL from Schrödinger (New York, NY).

3.3 Results

3.3.1 Glycan array screening

RNase A was found to bind to only a few human cell-surface glycans (Figure 3.1; Table 3.1). The structure of those glycans falls into two categories: glycoproteins and unbranched glycans. The glycoproteins bound by RNase A are serum proteins with complex glycan modifications. Human α1-acid glycoprotein (AGP, glycan **1**–**3**) contains various forms of di-, tri-, and tetraantennary sialylated carbohydrate chains; transferrin (glycan **6**) contains two disialylated biantennary glycans; and ceruloplasmin (glycan **4**) possesses bi- and triantennary *N*-glycosidic glycans.[184-186] Each of these glycoproteins is anionic (p*I* 2.7–5.5). Thus, their interaction with RNase A (p*I* 9.3) could have arisen through nonspecific Coulombic interactions.

Several tetrasaccharides and hexasaccharides were also recognized by RNase A. The hexasaccharides Fucα1-2Galβ1-3GalNAcβ1-3Galα1-4Galβ1-4Glcα-Sp9 (glycan **56**) and Neu5Acaα2-3Galβ1-3GalNAcβ1-3Galα1-4Galβ1-4Glcβ-Sp0 (glycan **223**) belong to the globo-series of glycosphingolipids. Glycan **56**, also known as the Globo H antigen, is found on a variety of cells and is the basis for an anti-cancer vaccine in a variety of clinical trials.[187] Glycan **223** represents the Stage Specific Embryonic Antigen 4, SSEA-4, which is expressed briefly during early stages of development and in certain teratocarcinoma cells.[188,189] Surprisingly, RNase A bound only weakly to the pentasaccharide precursor to these molecules, Galβ1-3GalNAcβ1-3Galα1-4Galβ1-4Glc (glycan **127**), but interacted tightly with a similar structure, GalNAcβ1-3Galα1-4Galβ1-4GlcNAcβ-Sp0 (glycan **90**). Together, these results suggest that RNase A recognizes the core tetrasaccharide GalNAcβ1-3Galα1-4Galβ1-4Glc that constitutes all

globo-series glycosphingolipids. Still, the relative fluorescence indicates that RNase A had somewhat higher affinity for the anionic glycoproteins than the globo-series glycans.

Globo H expression has been detected inconsistently in mammals (i.e., highly measured in tissues from rat yet less abundant in tissues from cats and dogs).[190] As such analyses of the globo-series glycolipids have not been characterized in bovine tissues. We assessed bovine mammary gland epithelial cell line (MAC-T) for globo-series glycans, Globo H, SSEA-4, and SSEA-3, but detected no glycan expression using confocal microscopy (data not shown). More thorough studies assessed localization of this glycolipid in human tissue and specifically on human breast cancers. We, therefore, sought to characterize the interaction of the human homolog, RNase 1, and this human glycan.

3.3.2 RNase 1 binds to immobilized Globo H

To characterize the affinity of RNases toward a neutral glycolipid, Globo H (glycan **56**), we initially utilized soluble fluorescence polarization assays (Figure 3.2A). We could not, however, attain saturation, despite adding a 10^5-fold molecular excess. Accordingly, we used a surface-binding assay that mimics the cell surface to quantify binding affinities (Table 3.2). Glycan–biotin conjugates were immobilized on avidin plates and saturated with fluorophore-labeled RNases. We found that RNase 1 bound to Globo H with an affinity of (0.79 ± 0.18) μM (Figure 3.2B). The binding of RNase A to Globo H was significantly weaker with an affinity of (20.9 ± 1.9) μM (Figure 3.2B). We also assessed the affinity of RNase 1 and RNase A toward SSEA-4 (glycan **223**). This glycan shares a pentasaccharide unit with Globo H, yet appeared to bind to RNase A more weakly in the glycan array. We found that immobilized SSEA-4 did indeed bind

RNases weakly with an affinity of (10.2 ± 1.2) μM to RNase 1 and (17.4 ± 1.3) μM to RNase A (Figure S3.3B).

3.3.3 Globo H contributes to RNase-mediated cytotoxicity

As we observed a strong interaction of RNase 1 with Globo H, we sought to search for a biological role for this interaction. Although RNase 1 has been implicated to be involved in immune function and cytokine release,[51,191] a direct effect on cellular pathways has yet to be uncovered. Variants of RNase 1 and RNase A that evade cytosolic RI are selectively toxic to cancer cells. For example, variants of RNase 1 (R39D/N67R/N88R/G89R/R91D or DRRRD) and RNase A (G88R) demonstrate cytotoxicity against human leukemia cells lines with IC_{50} values of 10.8 and 6.2 μM, respectively.[32,89] We therefore sought to determine the effect of reducing cellular Globo H on RNase-mediated cytotoxicity. Recent synthetic strategies created sugar analogs to remodel the cell surface as a tool for studying the roles of glycans.[181,182] These fluorinated transition state inhibitors bind to glycosyltransferases, thereby, blocking the active site. In particular, peracetylated 2-fluoro-2-deoxyfucose (F-fucose), inhibits expression of Globo H on the cell surface of MCF-7 breast cancer cells by blocking the addition of the terminal fucose unit to form Globo H. This technique has been shown to inhibit three of the 14 fucosyltransferases (FUT3/7/8),[182] but had not been tested as an inhibitor of FUT1/2, which are enzymes necessary for the biosynthesis of Globo H.[192] We, therefore, first confirmed that F-fucose did indeed reduce the display of Globo H on the surface of MCF-7 cells by using microscopy and flow cytometry (Figure 3.3A and 3.3B). Then, we assessed the effect of this reduction on the cytotoxicity of RNases. We found that cells with diminished Globo H levels were less vulnerable to cytotoxic RNases (Figure 3.3C).

3.3.4 Binding interface of RNase 1 toward Globo H

Next, we used HSQC NMR spectroscopy to define the binding interface of RNase 1 to micelles enriched in Globo H–lipid. The backbone chemical shifts of RNase 1 exhibited few changes in the presence of zwitterionic CTAB micelles. In contrast, these shifts were perturbed markedly by micelles containing Globo H at 1 equiv relative to RNase 1 (Figure S3.4). These changes in the vector of the chemical shift were calculated by Eq. 3.3 and plotted by residue number (Figure 3.4A). At pH 6.5, we found that major backbone perturbations at residues Tyr92, Phe46, Asn76, Phe120, Ser23, Val47, Val52, and Ser77 (Table 3.3). These perturbations were mapped onto the structure of RNase 1 to depict regions of greatest binding (Figure 3.4B). The perturbations at pH 6.5 were dispersed along the protein, residing mainly in turns and bends (Table 3.3). As RNase 1 is readily endocytosed and glycosylaminoglycans reside in the interior of endosomes,[193] we also monitored the interactions at pH 4.7, which is encountered in endosomes (Figure 3.4C). Interestingly, we found greater overall shifts in perturbations that clustered predominantly to a more polar serine-rich loop region, Ser18–Thr24, as well as at His80 (Figure 3.4D and Table 3.4). Moreover, these sites are regions known to be the most flexible within the structure. As these residues are primarily polar, the interactions are likely due to hydrogen bonding. We determined whether pH altered the affinity of RNase 1 for Globo H and found that in buffer at pH 5.0 the affinity to Globo H was 10-fold weaker with a K_d = (10.7 ± 1.36) μM. Affinity to SSEA-4 was (11.8 ± 1.18) μM—not significantly different than the affinity at pH 7.4 (Figure S3.6A). This potentially suggests that while the binding site of RNase 1 to Globo H are more clustered at low pH, some of the multivalency that confers tighter binding is lost. The affinity of RNase A to immobilized Globo H and SSEA-4 was equally weak at pH 5.0

with K_d = (17.5 ± 1.4) and (19.2 ± 2.0) μM, respectively (Figure S3.6B). We also monitored the perturbations on RNase A using ^{15}N-HSQC NMR spectroscopy. At pH 4.7, we found few residues that were altered (Figure S3.5), consistent with the weak binding observed with *in vitro* assays (Figures 3.2 and Figure S3.3).

3.4 Discussion

We discovered that the major secretory ribonuclease in humans, RNase 1, interacts with a human cell-surface glycan, Globo H, which is also a cancer antigen. We found that RNase 1 binds to this neutral glycan with high nanomolar affinity and binds with regions distal from the active site. Globo H was initially discovered as a tumor associate antigen due to its overabundance on MCF-7 breast cancer cells. These antigens have inspired clinical trials of synthetic constructs containing cancer antigens—including Globo H—to illicit an immune response that targets this antigen. Yet little is known about this glycan or the role it plays on the surface of cells. Further, there are no known proteins, other than antibodies, that bind to Globo H. (The cytosolic protein FKBP-4 was found to interact with globo-series glycan SSEA-4.[194]) We provide evidence that the secreted extracellular RNase 1 interacts with cell-surface glycan Globo H. Interestingly, RNase 1 and RNase A bound only to the immobilized glycans rather than soluble dye-labeled glycans (Figure 3.2A and Figure S3.3A) despite 10^5-fold molar saturation. This observation suggests that RNases require multivalent binding for measurable affinity.

RNases are known to interact with anionic cell-surface glycans. Indeed, sialic acid and heparan sulfate play a role in RNase uptake;[88] the bulk of these studies utilized RNase A. These interactions are manifested primarily through Coulombic forces with cationic side chains of

RNases. Recently, RNase 1 was shown to exhibit more specific heparan binding, potentially mediated through charge clusters.[195] Yet, no specific receptors have been discovered for RNase 1. We provide evidence that human RNase 1 does have a particular cell-surface target. Evidence is mounting that RNase 1 degrades extracellular RNA and, thus, regulates blood clotting, homeostasis, and immunity.[44,195] A cell-surface target—Globo-H—could direct RNase 1 towards an intracellular site of action.

The interaction between RNase 1 and Globo-H could explain some of the cancer cell susceptibility that is observed with engineered cytotoxic RNase variants.[32] Although these variants contain amino-acid substitutions that disrupt binding interface to cytosolic RI,[32,89] both normal and cancerous cells contain RI. One of many alterations that occur during tumorgenicity are changes to cell-surface components.[78] Therefore, uptake and translocation rates could differ between normal and cancerous cells.[79] We found that reducing Globo H on the cell surface reduce the susceptibility of cells to RNases.

Glycosylaminoglycans, like Globo H, reside on the extracellular surface as well as potentially locating to the interior of endosomes.[193] Interestingly, the NMR analyses provided evidence that the RNase 1 has multiple and unique binding sites depending on pH. Strikingly, the regions become more clustered, albeit weaker, at acidic pH. As RNases are readily endocytosed[90] and exhibit high acid tolerance, this clustering of Globo H binding residues could facilitate the translocation of the protein across lipid bilayers.

Interestingly, other targets of the glycan array include sialic acid glycoproteins (Figure 3.1). These proteins include the transporter, α1-glycoprotein, whose role is largely unknown aside from being a useful carrier to improve pharmacokinetics of drugs.[196] Cerruloplasmin is a copper-binding protein that associates with transferrin, an iron-binding protein. Together, these data

indicate that RNase 1 is interacting with additional plasma proteins, likely increasing circulation time by avoiding renal filtration. This observation lends validity to RNases as a protein therapy. Whereas PEGylation also increases circulation time,[197] the addition of lengthy polymers to RNases reduces cellular uptake and enzymatic activity.[198,199]

RNase 1 differs markedly from RNase A in its binding to Globo H. Interestingly, RNase 1 and RNase A share 82% sequence similarity. Yet, within the eight residues of RNase 1 that were perturbed by Globo H micelles, six are shared with RNase A. Only Val52 and Asn76, which are alanine and tyrosine in RNase A, differ. The residues involved in low-pH binding also contained many shared residues (8 of 11). However, the highest binding hit, H80, along with T24 and K102, differed in RNase A to a Ser, Asn, and Ala, respectively. It is possible that all of these residues are necessary for the multivalent binding observed or that these residues contribute to necessary structural arrangement.

Current work has indicated that there are still more differences between the homologous proteins RNase 1 and RNase A.[195] RNase A has dominated the thinking about pancreatic-type ribonucleases because so much seminal work in field of biochemistry was done with this enzyme. As a result the biological function of human RNase 1 has been underappreciated. We found that Globo H is not observable on the surface of a bovine mammary cell line, MAC-T, whereas it is found on human mammary cancer cells. We propose that the interaction of RNase 1 and Globo H evolved for a specific purpose—defense against cancer.

Acknowledgements

We are grateful to M. R. Aronoff for preparing peracetylated 2-fluoro-2-deoxyfucose and to Prof. C. J. Czuprynski for providing transformed (MAC-T) bovine mammary gland epithelial cells. This study made

use of the National Magnetic Resonance Facility at Madison, which is supported by Grant P41 GM103399 (NIH). The human glycan array screen, SSEA-4–azide, and SSEA-4–biotin were provided by the Consortium for Functional Glycomics, which was supported by Grant U54 GM062116 (NIH).

Table 3.1 Top hits from screen of RNase A against human glycan array

Glycan type		Glycan	Glycan Modification
Anionic glycoproteins	1–3	Human α1-acid glycoprotein	Di-, tri-, tetraantennary sialylated
	4	Ceruloplasmin	Bi-triantennary *N*-glycosidic
	5	Transferrin	Two disialylated biantennary
Unbranched glycans	56	Globo H	Fucα1-2Galβ1-3GalNAcβ1-3Galα1-4Galβ1-4Glcβ
	90		GalNAcβ1-3Galα1-4Galβ1-4GlcNAcβ
	223	SSEA-4	Neu5Acα2-3Galβ1-3GalNAcβ1-3Galβ1-4Galβ1-4Glcβ

Table 3.2 Affinity of RNase 1 and RNase A for surfaces of Globo H and SSEA-4

		K_d (μM)	
Glycan	pH	RNase 1	RNase A
Globo H	7.4	0.79 ± 0.18	20.9 ± 1.9
	5.0	10.7 ± 1.4	17.5 ± 1.4
SSEA-4	7.4	10.2 ± 1.2	17.4 ±1.3
	5.0	11.8 ± 1.2	19.2 ± 2.0

Table 3.3 Residues of RNase 1 that interact with Globo H at pH 6.5

$\Delta\Delta\delta$ (ppm)	Residue	Structure[a]
>0.100	Tyr92	t
0.05–0.10	Phe46, Asn76, Phe120	s, b, b
0.03–0.05	Ser23, Val47, Val52, Ser77	b, s, h, b

[a] t, turn; b, bend; s, β-strand; h, α-helix

Table 3.4 Residues of RNase 1 that interact with Globo H at pH 4.7

$\Delta\Delta\delta$ (ppm)	Residue	Structure[a]
>0.100	His80	s
0.05–0.10	Ser21, Ser22, Ser18, Ser23	–, –, –, b
0.03–0.05	Thr24, Arg39, Val47, Asp83	b, b, s, s
	T82, K102	s, s

[a]t, turn; b, bend; s, β-strand, h, α-helix; –, no structure

Figure 3.1

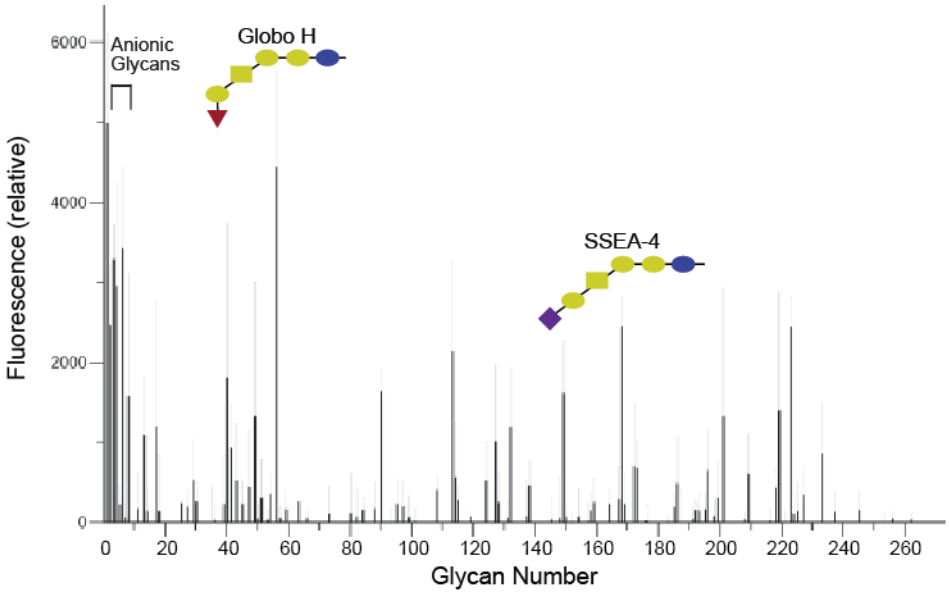
Anionic
Glycans
Globo H
SSEA-4
Fluorescence (relative)
6000
4000
2000
0
0
20
40
60
80
100
120
140
160
180
200
220
240
260
Glycan Number

Figure 3.1 Histogram of glycan binding analysis of RNase A to immobilized human glycan array

The array from CFG (version 2.0) comprises 264 synthetic and natural amine functionalized glycoconjugates that were immobilized to *N*-hydroxysuccinimide-activated glass slides.[176] Binding of RNase A was detected via primary antibodies and secondary antibodies labeled with Alexa Fluor® 594.

Figure 3.2

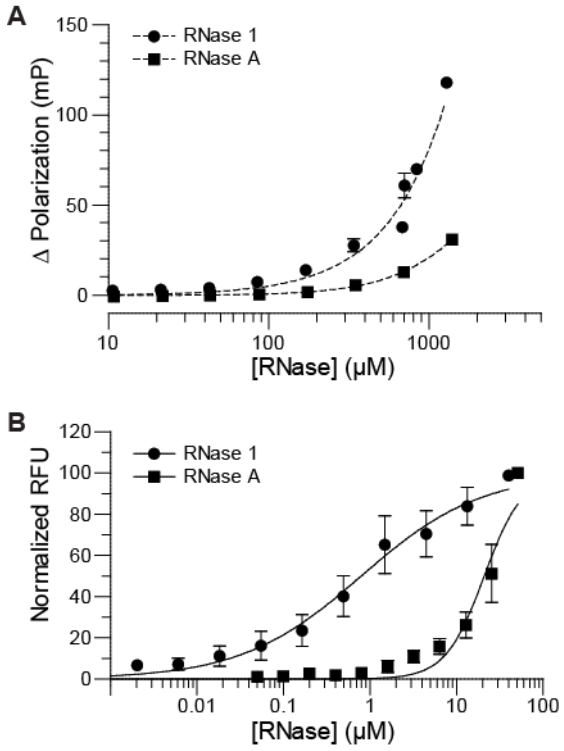
A
RNase 1
RNase A
Δ Polarization (mP)
150
100
50
0
10
100
1000
[RNase] (μM)
B
RNase 1
RNase A
Normalized RFU
120
100
80
60
40
20
0
0.01
0.1
1
10
100
[RNase] (μM)

Figure 3.2 Binding isotherms of RNase A and RNase 1 to soluble- and surface-bound Globo H *A.* Soluble BODIPY–Globo H was incubated with increasing concentrations of RNases and binding events were monitored using fluorescence polarization. *B.* Biotinylated Globo H was immobilized on neutravidin plate and incubated with saturating concentrations of BODIPY–RNases. Relative fluorescence is plotted against concentration, and data fit to non-linear regression, $n = 4$.

Figure 3.3

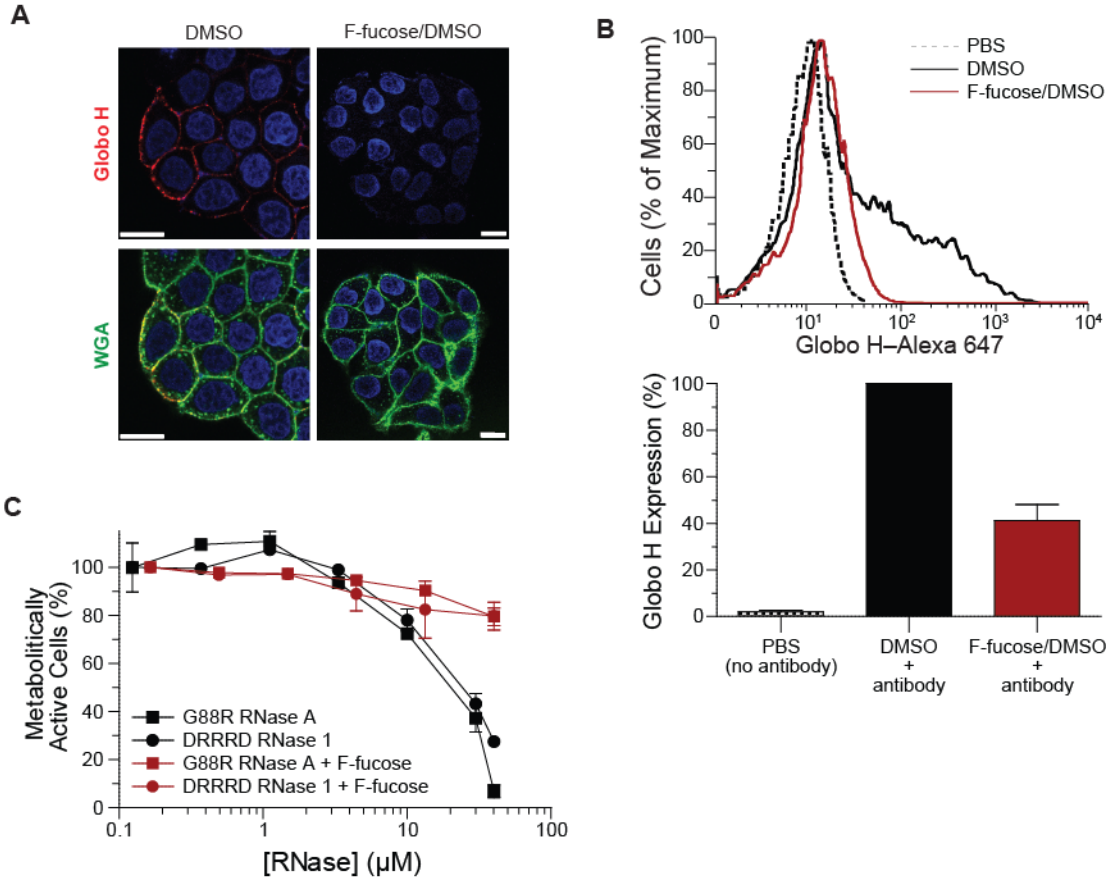
A
DMSO
F-fucose/DMSO
Globo H
WGA
B
PBS
DMSO
F-fucose/DMSO
Cells (% of Maximum)
Globo H–Alexa 647
Globo H Expression (%)
PBS (no antibody)
DMSO + antibody
F-fucose/DMSO + antibody
C
Metabolitically Active Cells (%)
G88R RNase A
DRRRD RNase 1
G88R RNase A + F-fucose
DRRRD RNase 1 + F-fucose
[RNase] (μM)

Figure 3.3 Effect of inhibiting Globo H biosynthesis on the cytotoxicity of RNase A and RNase 1 variants for MCF-7 cells

A. Treatment of MCF-7 cells with F-fucose inhibits Globo H expression as monitored by confocal microscopy. Nuclear stain: Hoechst 33342 (blue); αGH: Alexa-594 (red); outer membrane stain: WGA-488 (green). Scale bar: 5 μm. *B*. Quantification of Globo H expression on MCF-7 cells and its reduction with F-fucose (red) as measured by flow cytometry. *C*. Effect of inhibiting Globo H biosynthesis on RNase-mediated cytotoxicity as measured by assays of cell viability. Cytotoxic variants of RNase 1 (DRRRD) and RNase A (G88R) were added in increasing concentrations and cell viability was normalized to that with untreated cells, $n = 3$.

Figure 3.4

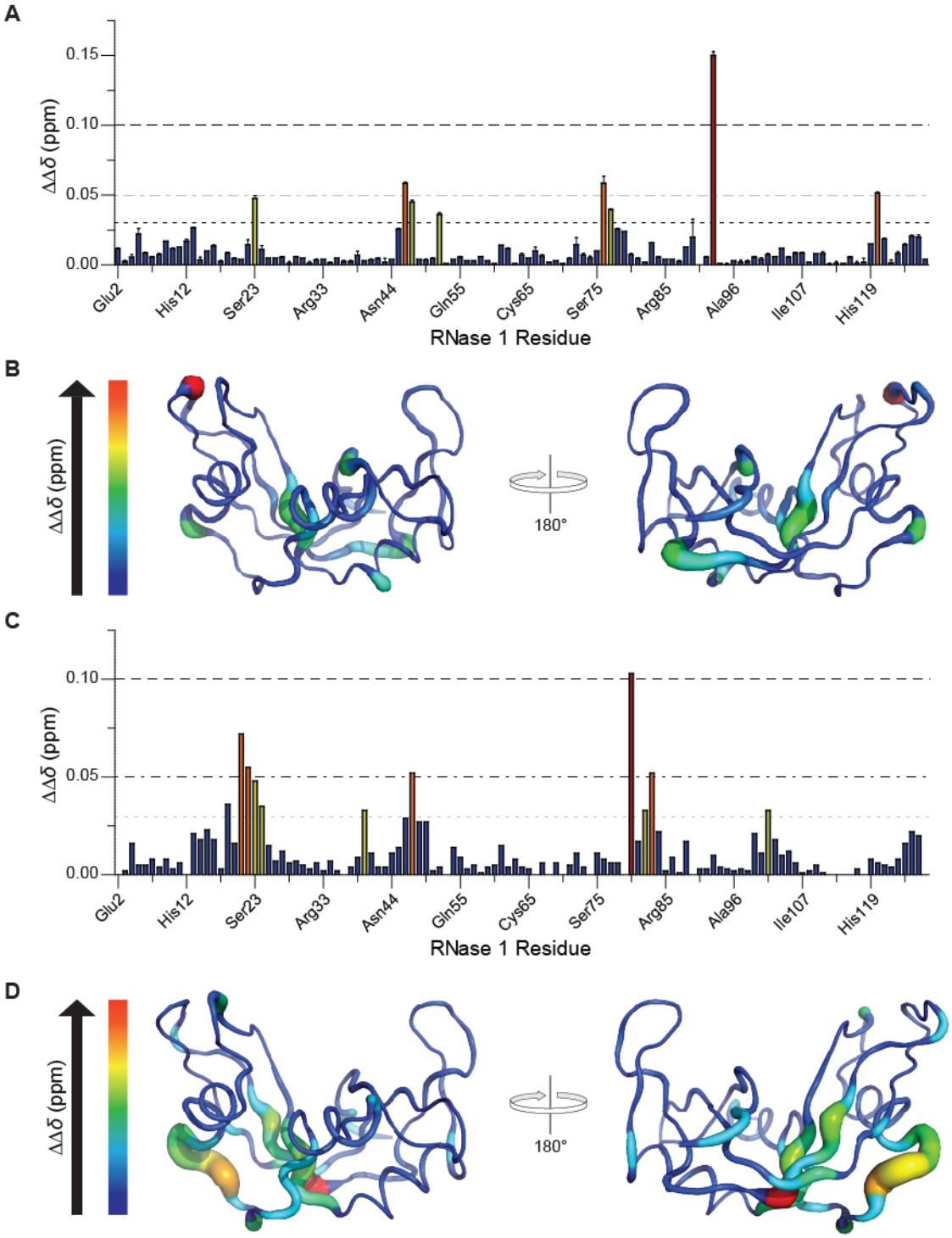
A
0.15
0.10
0.05
0.00
ΔΔδ (ppm)
Glu2
His12
Ser23
Arg33
Asn44
Gln55
Cys65
Ser75
Arg85
Ala96
Ile107
His119
RNase 1 Residue
B
ΔΔδ (ppm)
180°
C
0.10
0.05
0.00
ΔΔδ (ppm)
Glu2
His12
Ser23
Arg33
Asn44
Gln55
Cys65
Ser75
Arg85
Ala96
Ile107
His119
RNase 1 Residue
D
ΔΔδ (ppm)
180°

Figure 3.4 NMR Structure of RNase 1·Globo H binding interface at pH 6.5 and 4.7

A solution of [^{15}N]RNase 1 was prepared in the presence and absence of Globo H-enriched micelles. Chemical shift changes ($\Delta\Delta\delta$ ppm) were calculated as the average of n = 2 from the vector change with Globo H and plotted by residue (*A* and *C*). Changes in chemical shift are inserted as the β-factor in pdb entry 2K11 and displayed with the program PyMOL (*B* and *D*). Backbone regions colored in red and wider indicate greater chemical shift perturbations.

Supplementary Information

S3.1 Materials

All reagent-grade materials were from Sigma–Aldrich (St. Louis, MO) and were used without further purification, except for 2-fluoro-2-deoxyfucose, which was from CarboSynth (San Diego, CA).

S3.2 General experimental

S3.2.1 Solvent removal

The phrase "concentrated under reduced pressure" refers to the removal of solvents and other volatile materials using a rotary evaporator at water aspirator pressure (<20 torr) while maintaining the water-bath temperature below 40 °C. Residual solvent was removed from samples at high vacuum (<0.1 torr). The term "high vacuum" refers to vacuum achieved by mechanical belt-drive oil pump.

S3.2.2 NMR spectroscopy

^{1}H, ^{13}C NMR spectra for all compounds were acquired on Bruker spectrometers in the NMRFAM at the University of Wisconsin–Madison operating at 400 (^{1}H) and 101 (^{13}C) MHz. The chemical shift data are reported in units of δ (ppm) relative to residual solvent or TMS.

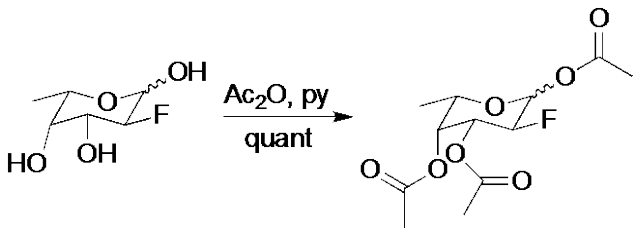

S3.2.3 Peracetylation of 2-fluoro-2-deoxyfucose

Peracetylated 2-fluoro-2-deoxyfucose was prepared from 2-fluoro-2-deoxyfucose by a procedure similar to that described previously.[182] Briefly, 2-fluoro-2-deoxyfucose (10 mg, 0.0602 mmol) was dissolved in pyridine (0.35 mL), and the resulting solution was cooled to 0 °C. Acetic anhydride (0.020 mL, 0.2167 mmol) was added, and the reaction vial was covered in foil and allowed to warm to room temperature overnight. The reaction mixture was then diluted with DCM (5 mL), washed with 1 M HCl (3 × 2 mL), saturated aqueous $NaHCO_3$ (3 mL), and brine (3 mL). The organics were dried over Na_2SO_4(s), concentrated under reduced pressure, and dried by high vacuum to provide a quantitative yield of peracetylated 2-fluoro-2-deoxyfucose (0.0175 g).

^{1}H NMR (400 MHz, $CDCl_3$) α-Anomer, *δ* 6.43 (d, *J*=3.98 Hz, 1H, H-1), 5.42 (td, *J*=10.64, 3.34 Hz, 1H, H-3), 5.37 (d, *J*=3.70 Hz, 1H, H-4), 4.88 (ddd, *J*=49.38, 10.17, 3.97 Hz, 1H, H-2), 4.25 (q, *J*=6.53 Hz 1H, H-5), 2.18 (6H), 2.06 (s, 3H), 1.15 (d, *J*=6.52 Hz, 3H, H-6). β-Anomer, *δ* 5.77 (dd, *J*= 8.05, 4.12 Hz, 1H, H-1), 5.31 (s, 1H, H-4), 5.17 (ddd, *J*=13.34, 9.89, 3.47 Hz, 1H, H-3), 4.64 (dt, *J*=51.81, 8.90 Hz, 1H, H-2), 3.99 (q, *J*=6.50 Hz,1H, H-5), 2.23 (s, 3H), 2.18 (s, 3H), 2.06 (s, 3H), 1.22 (d, *J*=6.44 Hz, 3H, H-6). ^{13}C NMR (101 MHz, $CDCl_3$) α-Anomer (major), *δ* 170.45, 170.23, 169.22, 89.34 (d, *J*=21.62 Hz, C1), 84.36 (d, *J*=190.72 Hz, C2), 71.19 (d, *J*=7.49 Hz, C4), 68.73 (d, *J*=19.1 Hz, C3), 67.26 (C5), 21.08, 20.82, 20.67, 15.88 (C6). HRMS (ESI) calcd. for $C_{12}H_{17}FO_7$ $[M+NH_4]^+$ 310.1297, found 310.1299.

Figure S3.1

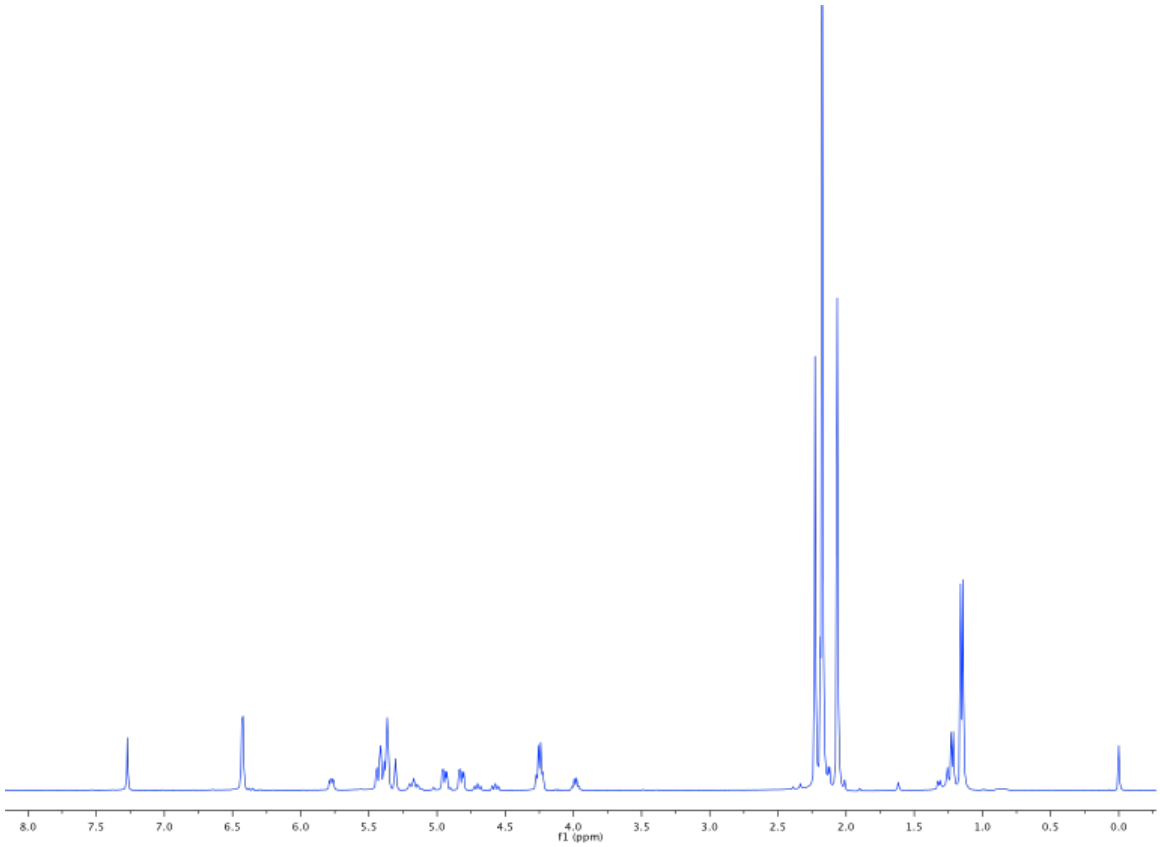

Figure S3.1 ^{1}H NMR spectrum of peracetylated 2-fluoro-2-deoxyfucose

Mixed anomers in $CDCl_3$ spectra recorded on 400 MHz.

Figure S3.2

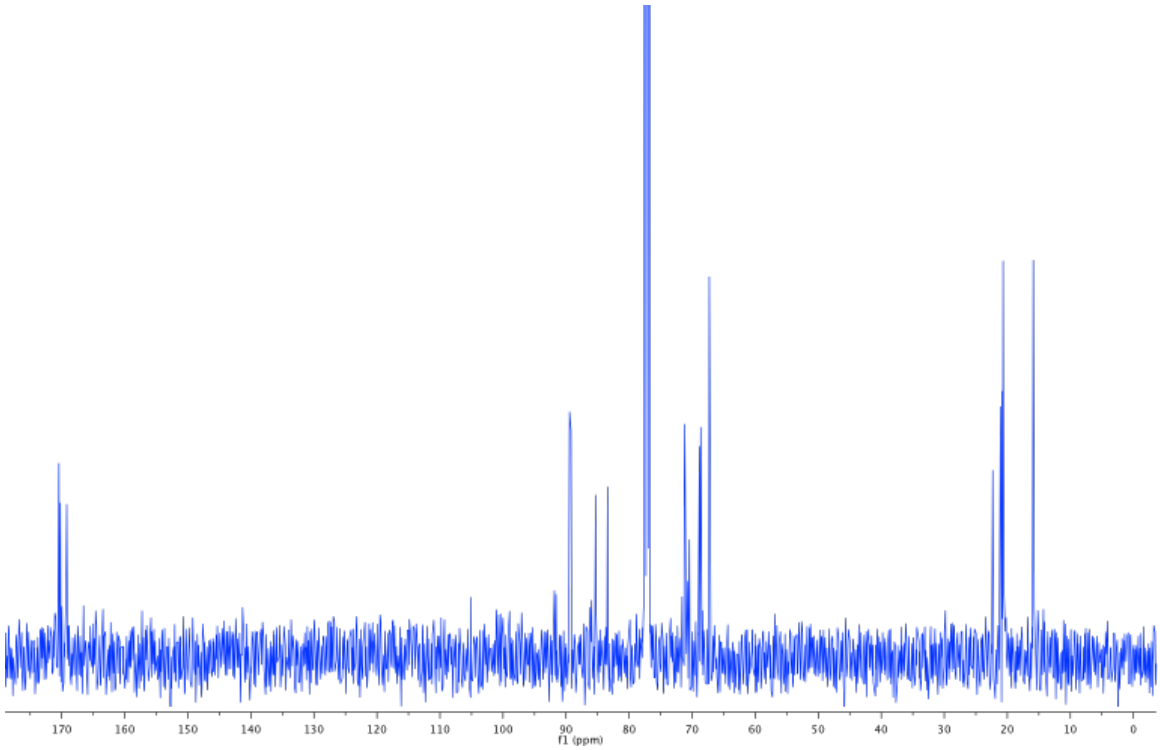

Figure S3.2 ^{13}C NMR spectrum of peracetylated 2-fluoro-2-deoxyfucose

Mixed anomers in $CDCl_3$ spectra recorded on 101 MHz.

Figure S3.3

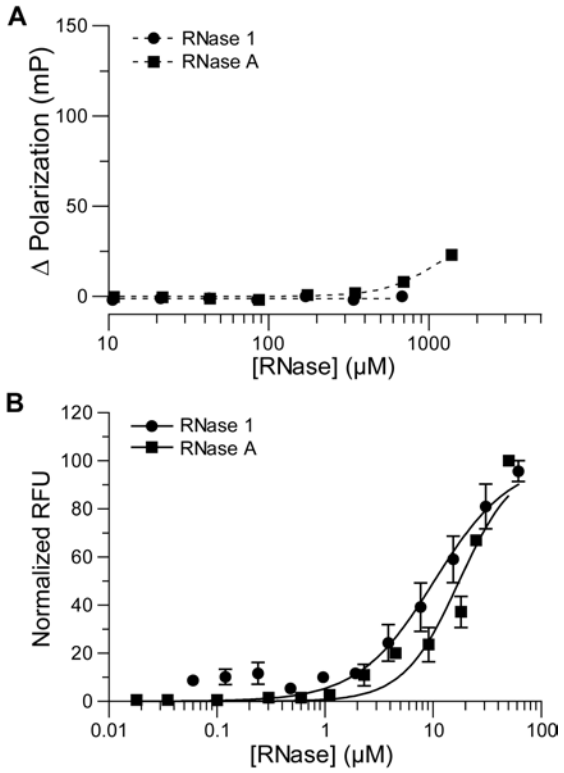
A
RNase 1
RNase A
Δ Polarization (mP)
150
100
50
0
10
100
1000
[RNase] (μM)
B
RNase 1
RNase A
Normalized RFU
120
100
80
60
40
20
0
0.01
0.1
1
10
100
[RNase] (μM)

Figure S3.3 *In vitro* binding isotherms of RNase 1 and RNase A with SSEA-4 at pH 7.4

A. Fluorescence polarization assay for the interaction of RNase 1 and RNase A with soluble SSEA-4-BODIPY. *B.* Surface binding assay for the interaction of RNase–BODIPY conjugates with immobilized SSEA-4–biotin. Fluorescence emission data were fitted by non-linear regression to Eq 3.2 For RNase 1, K_d = (10.2 ± 1.2) μM; for RNase A, K_d = (17.4 ± 1.3) μM.

Figure S3.4

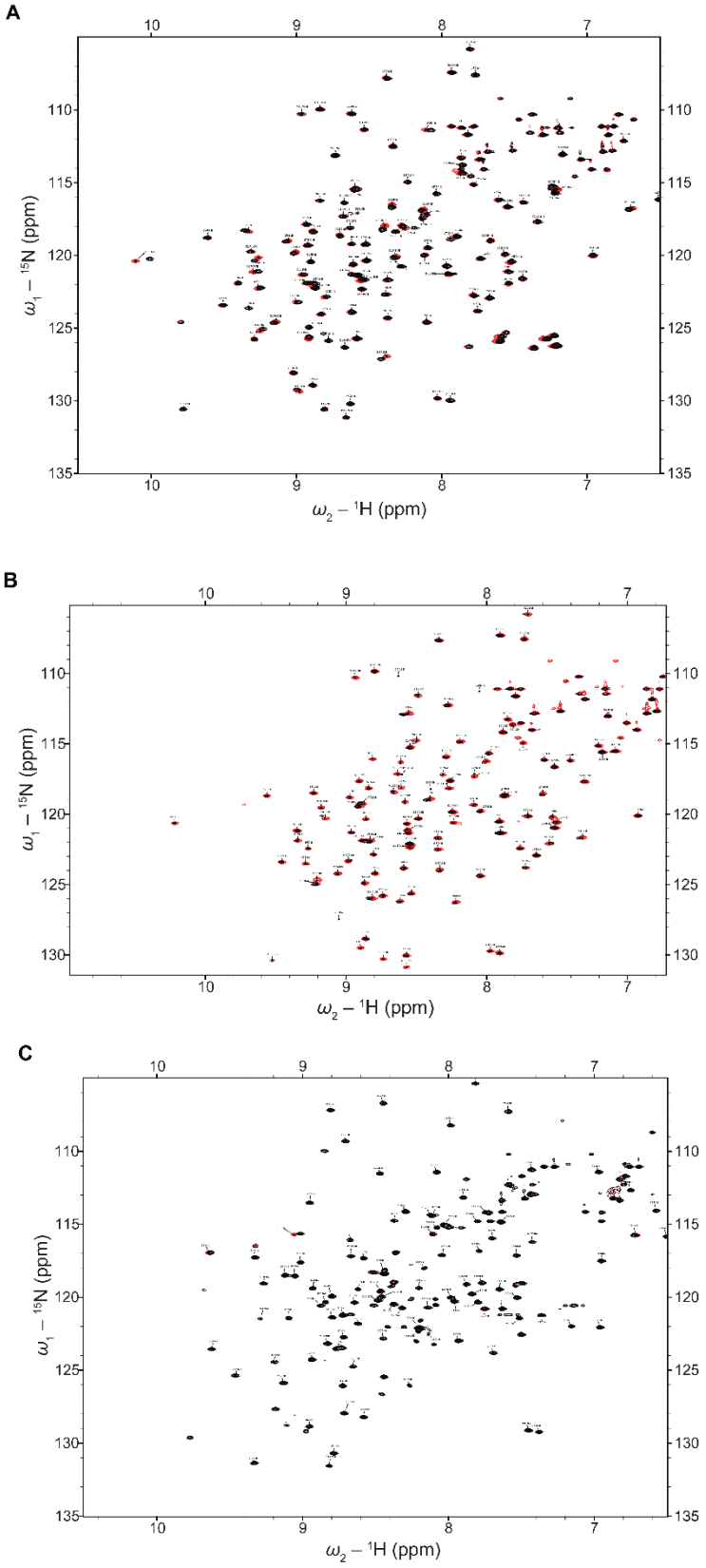

Figure S3.4 2D-HSQC NMR spectra of [^{15}N]RNase 1 and [^{15}N]RNase A in the presence and absence of Globo H-enriched micelles

Spectra are of [^{15}N]RNases (250 μM) in the presence of CTAB micelles (25 mM; black) loaded with Globo H (250 μM; red). *A*. RNase 1 at pH 6.5. *B.* RNase 1 at pH 4.7. *C*. RNase A at pH 4.7. Spectra were recorded at 600 MHz and plotted with the program Sparky.

Figure S3.5

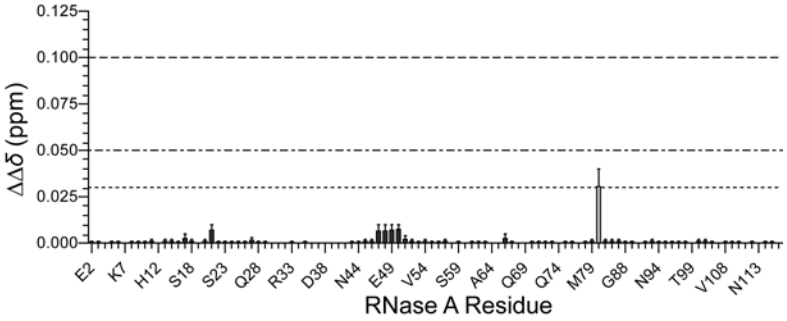
0.125
0.100
0.075
0.050
0.025
0.000
ΔΔδ (ppm)
E2
K7
H12
S18
S23
Q28
R33
D38
N44
E49
V54
S59
A64
Q69
Q74
M79
G88
N94
T99
V108
N113
RNase A Residue

Figure S3.5 Chemical shift perturbations of RNase A in the presence of Globo H micelles at pH 4.7

Chemical shift changes ($\Delta\Delta\delta$ ppm) were calculated as the average value (n = 2) from the vector change in the presence of Globo H (Eq 3.3) and plotted by residue.

Figure S3.6

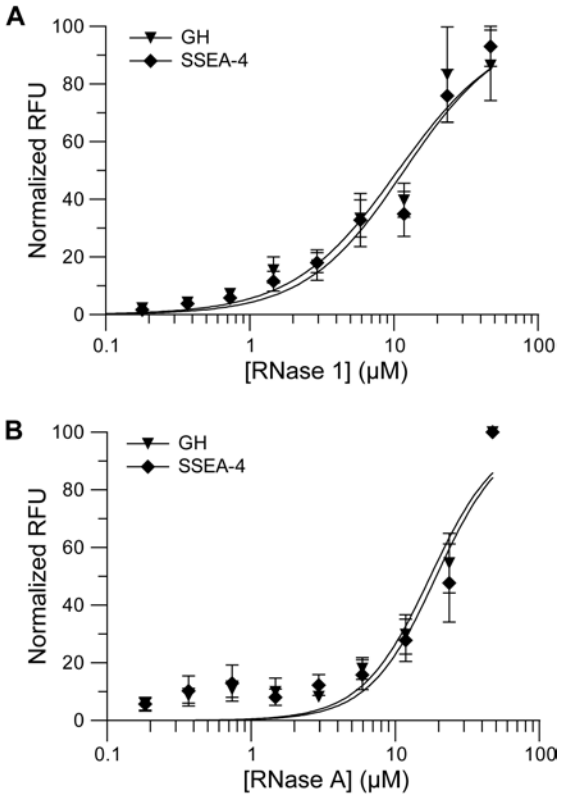
A
GH
SSEA-4
Normalized RFU
100
80
60
40
20
0
0.1
1
10
100
[RNase 1] (μM)
B
GH
SSEA-4
Normalized RFU
100
80
60
40
20
0
0.1
1
10
100
[RNase A] (μM)

Figure S3.6 *In vitro* binding isotherms of RNase 1 and RNase A with immobilized Globo H and SSEA-4 at pH 5.0

RNase–BODIPY conjugates were added to immobilized glycans in 10 mM Tris–HCl buffer, pH 5.0, containing NaCl (130 mM). Data were fitted by non-linear regression to Eq 3.2. *A*. For RNase 1·Globo H, K_d = (10.7 ± 1.4) μM; for RNase 1·SSEA-4, K_d = (11.8 ± 1.2) μM. *B*. For RNase A·Globo H, K_d = (17.5 ± 1.4) μM; for RNase A·SSEA-4, K_d = (19.2 ± 2.0) μM.

Chapter 4

Affinity of Monoclonal Antibodies to Globo-Series Glycans

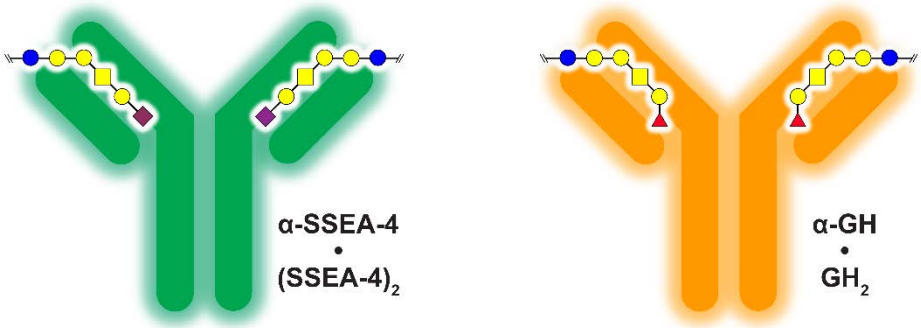

Contribution:

I performed all the experiments except for the synthesis of Globo H-biotin and Globo H-BODIPY (Carbohydrate Synthesis Facility) and SSEA-4-biotin and SSEA-4-azide (Consortium for Functional Glycomics).

This chapter was prepared for publication as:
Eller, C.H., Yang, G., Ouerfelli, O., and Raines, R.T. Affinity of Monoclonal Antibodies for Globo-Series Glycans. *Carbohydrate Research* (2014) 397, 1 - 6

Abstract

Globo-series glycans are human cell-surface carbohydrates that include stem-cell marker SSEA-4 and cancer-cell antigen Globo H. These two hexasaccharides differ only in their terminal saccharide: *N*-acetylneuraminic acid in SSEA-4 and L-fucose in Globo H. Herein, we evaluated the affinity of the monoclonal antibodies α-SSEA-4 and α-GH for the glycans SSEA-4 and Globo H. Using fluorescence polarization, we find that the two monoclonal antibodies have affinity for their cognate glycan in the low nanomolar range, and have negligible affinity for the non-cognate glycan. Using surface plasmon resonance, we find that each cognate affinity is ~20-fold greater if the glycan is immobilized on a surface rather than free in solution. We conclude that the terminal saccharide plays a dominant role in the ability of monoclonal antibodies to recognize these Globo-series glycans and that the extraordinary specificity of these antibodies supports their use for identifying and sorting stem-cells (α-SSEA-4) and as an agent in cancer immunotherapy (α-GH).

4.1 Introduction

4.1.1 Globo-series glycans

Globo-series glycans comprise a group of neutral glycosphingolipids in which a ceramide is linked to a glycan with a root structure of GalNAcβ3Galα4Galβ4Glc.[200,201] Typically, these glycans are retained on the plasma membrane and cluster into lipid rafts.[202] The endogenous function of this glycan family is largely unknown. Their expression does, however, occur during early stages of development and is thought to mediate cell contact and adhesion.[203] Importantly, changes in these glycans are observed throughout differentiation and during tumorigenesis.[169,204] Two notable hexasaccharide members of this family are stage-specific embryonic antigen-4 (SSEA-4) and Globo H (Figure 4.1). These glycans share a common precursor, SSEA-3 (Galβ3GalNAcβ3Galα4Galβ4Glc), but vary in the terminal monosaccharide: β3-linked *N*-acetylneuraminic acid for SSEA-4 and α2-linked L-fucose for Globo H.

4.1.2 SSEA-4, a stem-cell marker

SSEA-4 was discovered using the monoclonal antibody, MC-813-70 (α-SSEA-4), produced by immunization against human embryonic stem cells.[188] Subsequent analyses found expression of this epitope on many stem cell types as well as induced pluripotent stem cells and embryonic carcinoma cells.[205] Although SSEA-4 expression is not required for stem-cell pluripotency, a decrease in expression is observed upon differentiation.[206] In addition the pentasaccharide precursor, SSEA-3, is also used to identify stem cells and is depleted rapidly from the cell surface upon differentiation. Hence, commercial antibodies for both glycans are often used to identify undifferentiated cells.[207] The use of α-SSEA-3 (MC-613) and α-SSEA-4 enables the identification of spontaneous differentiation and the collection of live stem cells.[208,209] Such live-

cell sorting has distinct advantages in stem cell and regenerative therapies,[210] and is not enabled by other known stem-cell markers, such as nuclear transcription factors.[211] More recently, SSEA-4 has been detected on malignant glioma cells,[212] which form the most aggressive and common brain tumors in adults, as well as on breast cancer cells.[213,214] As a result, antibodies against SSEA-4 can illicit complement-dependent cytotoxicity and support the targeting of SSEA-4 in cancer vaccines.

4.1.3 Globo H, a cancer-cell antigen

Globo H was isolated originally from human breast cancer cell line MCF-7.[215] High-level expression of Globo H has been observed on a variety of other cancer cells, including colon, ovarian, prostate, and lung.[213,216] Identification of this cancer-cell antigen was made possible using the antibody MBr1 (α-GH), which was raised specifically against MCF-7 cells.[217] Binding assays using printed microarrays demonstrated that α-GH recognizes the terminal tetrasaccharide moiety with 10-fold less affinity than the intact hexasaccharide, and does not bind to the SSEA-3 precursor of Globo H that lacks the terminal fucose.[218] Endogenous Globo H expression remains in the apical surface of epithelial tissue, an area somewhat inaccessible to the immune system.[218] As such, Globo H is an attractive target for cancer immunotherapy.[219]

Toward this end, chemical synthesis has been used to access the soluble moiety of Globo H on a large scale.[180] Conjugation of Globo H to other cancer-cell antigens, such as GM2, STn, TF, and KLH, can lead to potential vaccines that induce the production of IgM antibodies that direct the immune system to tumor cells.[175,214,220] Such experimental vaccines are undergoing clinical trials for the treatment of metastatic breast, prostate, lung, and ovarian cancers.[221]

The value of SSEA-4 and its antibody in stem-cell identification and therapies, and of Globo H as an epitope for cancer vaccines is unequivocal. Given the similar structures of SSEA-4 and Globo H (Figure 4.1), we sought to determine the specificity of common monoclonal antibodies for each antigen. Investigations of the binding of proteins to cell-surface glycans typically involve printed microarrays, which can provide false-positives and are often less quantitative than other methods.[222] By using using synthetic glycan conjugates, fluorescence polarization, and surface plasmon resonance, we provide a quantitative assessment of the affinity of α-SSEA-4 and α-GH for SSEA-4 and Globo H. Our findings provide guidance for a wide range of investigations in biomedicine.

4.2 Methods

4.2.1 Materials

BODIPY-Fl succinimidyl ester was from Invitrogen (Carlsbad, CA). Dibenzocyclooctyne-amine was from Jena Biosciences (Jena, Germany). β-(azidoethyl)SSEA-4 (Compound No B295, Lot S270-1) and SSEA-4–biotin (Compound No B295, Lot S284-1) were provided by the Consortium for Functional Glycomics (San Diego, CA). β-(4-Pentene-1-yl)Globo H was synthesized as described previously.[174,180] α-SSEA-3 IgM monoclonal antibody (MC-613) and α-SSEA-4 IgG3 monoclonal antibody (MC-813-70) were from Thermo Fisher Scientific (Rockford, IL). α-Globo H IgM monoclonal antibody (MBr1) was from Enzo Life Sciences (Farmingdale, NY). Phosphate-buffered saline (PBS; Ca^{2+}- and Mg^{2+}-free) was from Life Technologies (Grand Island, NY). Bovine serum albumin (BSA), biotin, Tween-20, solvents, and other reagents were from Sigma–Aldrich (St. Louis, MO).

4.2.2 Instrumentation

The identity of synthetic compounds was confirmed by both NMR spectroscopy using a 500 MHz instrument and mass spectrometry using a ULTRAFLEX® III instrument, both from Bruker (Billerica, MA). LC/MS was performed with an LCMS-2020 instrument from Shimadzu (Kyoto, Japan). Fluorescence polarization was recorded on M1000 fluorimeter from Tecan Group (Mannendorf, Switzerland), and data were analyzed with Prism 5 from GraphPad Software (La Jolla, CA). Surface plasmon resonance (SPR) was measured with a ProteOn XPR 36 System using a NLC NeutrAvidin sensor chip from Bio-Rad Laboratories (Hercules, CA).

4.2.3 Synthesis of cyclooctyne–BODIPY

We chose BODIPY as our fluorescent probe.[223] This probe is neutral, and its fluorescence is not sensitive to pH. BODIPY-Fl succinimidyl ester (2.5 mg; 6.4 µmol) was dissolved in 0.23 mL of 0.025 M DMF containing dibenzocyclooctyne-amine (1.1 equiv) and triethylamine (3 equiv). Amide-bond formation was monitored by TLC (10% v/v MeOH in DCM). Upon completion of the reaction, the product was purified by preparative TLC to remove remaining reactants and filtration through cotton using MeOH as the solvent to give 3.5 mg (95%) of cyclooctyne–BODIPY. *m*/*z* 568.4 [calc'd for $C_{32}H_{33}BF_2N_5O_2$ (M+NH_4) 568.5). **^{1}H NMR (500 MHz, CD_3OD)** δ 7.65 (dd, *J* = 7.6, 1.3 Hz, 1H), 7.45 (s, 4H), 7.42 (s, 1H), 7.36 (td, *J* = 7.5, 1.5 Hz, 1H), 7.31 (td, *J* = 7.6, 1.4 Hz, 1H), 7.24 (dd, *J* = 7.5, 1.5 Hz, 1H), 6.96 (d, *J* = 4.1 Hz, 1H), 6.25–6.18 (m, 2H), 5.13 (d, *J* = 14.0 Hz, 1H), 3.70 (d, *J* = 14.0 Hz, 1H), 3.27–3.20 (m, 2H), 3.16–3.07 (m, 2H), 2.50 (s, 3H), 2.47–2.40 (m, 2H), 2.28 (s, 3H), 2.07–1.98 (m, 2H).

4.2.4 Synthesis of SSEA-4–BODIPY

β-(azidoethyl)SSEA-4 (0.25 mg; 0.20 μmol) was dissolved in 2.0 mL of 20% v/v H_2O in MeOH. To this solution was added cyclooctyne–BODIPY (5 equiv). The reaction was allowed to proceed overnight. Upon completion of the reaction as monitored by TLC (20% v/v MeOH in DCM), the reaction mixture was concentrated under reduced pressure, and the residue was suspended in H_2O. Free dye was extracted with ether washes to give 0.34 mg (95%) of SSEA-4–BODIPY. LC/MS *m*/*z* 1779 [calc'd for $C_{77}H_{104}BF_2N_9O_{36}$ (M+H) 1781). **^{1}H NMR (500 MHz, 1:4 CD_3OD/D_2O)** δ 8.50 (s, 1H), 8.24 (d, *J* = 7.8 Hz, 1H), 8.06–7.91 (m, 1H), 7.72–7.16 (m, 9H), 7.09–6.98 (m, 1H), 6.34–6.24 (m, 2H), 6.09 (d, *J* = 7.5 Hz, 1H), 6.01–5.88 (m, 2H), 5.20–3.09 (m, 47H), 2.85–2.77 (m, 2H), 2.62–2.46 (m, 5H), 2.35–2.26 (m, 3H), 2.08–1.97 (m, 6H), 1.91–1.71 (m, 2H), 1.36–1.23 (m, 2H). **^{19}F NMR (400 MHz, CD_3OD)** δ –76.41.

4.2.5 Synthesis of Globo H–BODIPY

To a solution of β-(4-pentene-1-yl)Globo H (52 mg, 29 μmol) and *N*-*tert*-butyl allylcarbamate (34 mg, 0.22 mmol) in dichloromethane (1 mL) was added the Hoveyda I catalyst (15 mg, 18.2 μmol). The resulting mixture was heated to 37 °C for 2 days and then concentrated under reduced pressure, and the residue was purified by flash chromatography on SiO_2 using a linear gradient of hexane/acetone (2:1 to 1:1) as eluent. Five consecutive short-path columns were necessary to give 24 mg (43%) of the desired olefin metathesis product, *N*-Boc-6-amino-4-hexene-1-yl Globo H, as well as 26 mg of starting material.

To a portion of *N*-Boc-6-amino-4-hexene-1-yl Globo H (24 mg) in MeOH (1 mL) was added 10% w/w Pd on C (10 mg). After purging with H_2(g), a balloon containing H_2(g) was applied to the reaction mixture, which was stirred vigorously for 4 h. H_2(g) was replaced with Ar(g). After

filtration through a pre-washed and packed pad of Celite® and concentration, the residue was dissolved in 25% TFA in dichloromethane (1 mL) and stirred for 30 min. The volatiles were removed under reduced pressure and then under high vacuum. The dried residue was dissolved in 1 mL of dichloromethane and successively treated under Ar(g) with DIEA (0.1 mL) and BODIPY–NHS ester (5 mg, 12.8 μmol), and the resulting mixture was stirred in the dark overnight. Solvents were then removed under high vacuum, and the residue was dissolved in MeOH (1 mL), and treated with 20 μL of a solution of NaOMe (25% w/v) in MeOH. Stirring was maintained until LC/MS indicated that the reaction was complete. Neutralization with AcOH and purification by HPLC gave 2 mg of purified product.

LC/MS *m*/*z* 1390 [calc'd for $C_{54}H_{93}N_4O_{32}S$ (M+H) 1390]. **^{1}H NMR (500 MHz, CD_3OD)** δ 7.90 (d, *J* = 9.0 Hz, 1H), 7.44 (s, 1H), 7.01 (d, *J* = 3.8 Hz, 1H), 6.32 (d, *J* = 3.8 Hz, 1H), 6.22 (s, 1H), 5.23 (d, *J* = 4.0 Hz, 1H), 4.93 (d, *J* = 4.0 Hz, 1H), 4.55 (3 d, *J* = 7.5 Hz, 3H), 4.42–4.40 (m, 1H), 4.28–4.30 (m, 4H), 4.14–3.64 (m, 27H), 3.57–3.48 (m, 9H), 3.45–3.44 (m, 1H), 3.38–3.15 (m, 27H), 2.59 (t, *J* = 7.7 Hz, 2H), 2.51 (s, 3H), 2.29 (s, 3H), 2.01 (s, 3H), 1.62–1.58 (m, 2H), 1.50–1.46 (m, 2H), 1.42–1.38 (m, 2H), 1.34–1.29 (m, 2H), 1.24 (d, *J* = 6.5 Hz, 3H). **^{19}F NMR (470 MHz, CD_3OD)** δ –77.01.

4.2.6 Synthesis of Globo H–biotin

(*N*-Boc-6-amino-4-hexene-1-yl)Globo H (42 mg) was dissolved in 1.5 mL of 25% v/v TFA in dichloromethane, and the reaction mixture was stirred for 30 min. Volatiles were removed under reduced pressure, and the residue (42 mg) was used directly in the next step. To a solution of biotin (34 mg, 0.14 mmol) in 0.5 mL NMP were added HATU (52 mg, 0.14 mmol) and

0.3 mL of DIEA. After stirring for 5 min, the deprotected amino alkyl Globo H (42 mg) in 1.5 mL DMF was introduced through a syringe. Stirring overnight, concentration under reduced pressure (cold water bath), and purification by flash chromatography using a linear gradient of MeOH/dichloromethane (2–6% v/v) gave 42 mg of crude β-(6-biotinamido-4-hexene-1-yl)Globo H.

The previous product (42 mg) was dissolved in MeOH (1 mL), and to this solution was added 10% w/w Pd on C (10 mg). After purging with H_2(g), a balloon containing H_2(g) was applied to the reaction mixture, which was stirred vigorously for 2 h. H_2(g) was replaced with Ar(g), and the reaction mixture was filtered through a pre-washed and packed pad of Celite®. After concentration of the filtrate, the residue was purified by flash chromatography using a linear gradient of MeOH/DCM (1–6%) to afford pure protected β-(6-biotinamido-1-hexyloxy)Globo H (38 mg). To this peracetylated biotinamidoalkyl Globo H (38 mg) in 1.2 mL MeOH was added 35 μL of NaOMe (25% w/v) in MeOH, and the resulting solution was stirred until analysis by LC/MS indicated that the deprotection was complete (~4 h). The pH was then brought carefully to neutrality with AcOH, and the product was concentrated under reduced pressure and purified by chromatography on Bio-Gel P-4 Gel from Bio-Rad Laboratories using water as eluent, and lyophilized to give 20.3 mg of β-(6-biotinamido-1-hexyl)Globo H. (LC/MS *m*/*z* 1342 [calc'd for $C_{54}H_{93}N_4O_{32}S$ (M+H) 1342]. ^{1}H NMR (500 MHz, D_2O), δ 5.15 (d, *J* = 3.5 Hz, 1H), 4.82 (d, *J* = 3.1 Hz, 1H), 4.56–4.52 (m, 2H), 4.48–4.39 (m, 3H), 4.36–4.30 (m, 2H), 4.17–4.13 (m, 2H), 4.03 (bs, 1H), 3.96–3.46 (m, 32H), 3.27–3.20 (m, 2H), 3.13–3.08 (m, 2H), 2.92 (dd, *J* = 4.9 Hz, *J* = 13 Hz, 1H), 2.85 (m, 3H), 2.71 (d, *J* = 13 Hz, 1H), 2.19–2.16 (m, 1H), 1.97 (bs, 2H), 1.66–1.13 (m, 16H).

4.2.7 Fluorescence polarization binding assay

The affinity of antibodies for glycans was quantified by monitoring the fluorescence polarization of SSEA-4–BODIPY and Globo H–BODIPY upon addition of α-SSEA-4 and α-GH antibodies. Measurements were performed on 100-μL solutions in the wells of a 96-well plate containing glycan (25 nM) and BSA (7.5 μg) in PBS, pH 7.3. In addition, the affinity of BSA for glycans was determined by monitoring the fluorescence polarization upon addition of BSA. After 30 min at 25 °C, polarization was recorded and values of the equilibrium dissociation constant (K_d) were determined by fitting the data with non-linear regression analysis to the equation:

$$P = \frac{\Delta P[\mathrm{Ab}]^h}{\left(K_\mathrm{d}{}^h + [\mathrm{Ab}]^h\right)} + P_\mathrm{min} \tag{4.1}$$

where P is the average of the measured polarization values, ΔP (= $P_{max} - P_{min}$) is the difference in anisotropy values of bound and free glycan, [Ab] is the total concentration of antibody, and h is the Hill coefficient.

4.2.8 Surface plasmon resonance binding assay

The affinity of antibodies for glycans was also quantified with monitoring the SPR as α-SSEA-4 and α-GH were flowed over Globo H–biotin and SSEA-4–biotin bound to a NeutrAvidin chip. The chip was conditioned with 30-μL injections of 50 mM NaOH and 1.0 M NaCl at a flow rate of 30 μL/min in both vertical and horizontal paths. Running buffer was PBS, pH 7.3, containing BSA (0.1 % w/v) and Tween-20 (0.005% v/v), and the chip surface was

maintained at 25 °C. The surface was labeled in the vertical channel with SSEA-4–biotin or Globo H–biotin at 0.5 μg/mL with a 300-s injection at 30 μL/min. Binding to the chip surface led to an increase of 40–100 RU. One lane was labeled with 0.5 μg/mL biotin. The chip was rotated into the horizontal direction and stabilized with a 30-μL pulse of 1.0 M NaCl at a flow rate of 30 μL/min, followed by 3 pulses of 30 μL buffer at 100 μL/min. Analyte (antibody or buffer) was applied at various concentrations across the horizontal path at 100 μL/min with a dissociation time of 750 s. The surface was regenerated with 30 μL of 0.10 M glycine, pH 1.7, at a flow rate of 30 μL/min. Equilibrium binding isotherms for the binding of α-SSEA-4 and α-GH to their respective glycans were determined by plotting the response unit at equilibrium (RU_{eq}) versus antibody concentration in GraphPad, and fitting the data to eq 4.1. Sensorgrams for the binding of α-SSEA-3 were analyzed with ProteOn software using a kinetic bivalent fit, and values of K_d were calculated by fitting the kinetic data from eight experiments using four different antibody concentrations. All SPR data were assessed for goodness-of-fit using the criteria that the χ^2 values lie between 10% RU_{max} and 10% RU – χ^2.

4.3 Results

Two quantitative solution-based assays were used to characterize the affinity between important human cell-surface glycans and relevant monoclonal antibodies. Fluorescence polarization was used to assess binding in solution, and SPR was used to assess binding on a surface.

4.3.1 Affinity of monoclonal antibodies to globo-series glycans in solution

We used the fluorescence polarization of BODIPY-labeled SSEA-4 and Globo H to monitor binding to a monoclonal antibody, α-SSEA-4. We found that the antibody exhibited high affinity to soluble SSEA-4–BODIPY with K_d = (115 ± 10) nM, h = 1.9 in PBS (Figure 4.2A). [If the Hill coefficient were fixed at h = 2.0, then K_d = (112 ± 6) nM.] We assessed further any non-specific affinity of α-SSEA-4 toward Globo H, which shares five of the six saccharides of SSEA-4. We found that α-SSEA-4 interacts only weakly with Globo H–BODIPY even at nearly micromolar concentrations, indicating that the antibody distinguishes markedly between the terminal *N*-acetylneuraminic acid of α-SSEA-4 and L-fucose of Globo H.

We also assayed the affinity of Globo H–BODIPY to its respective monoclonal antibody, α-GH. We were able to determine a value of K_d = (161 ± 13) nM, h = 4.8 in PBS (Figure 4.2B). [If the Hill coefficient were fixed at h = 2.0, then K_d = (322 ± 88) nM.] In analogy to α-SSEA-4, the affinity of the α-GH antibody was specific for Globo H over SSEA-4.

Finally, we assessed the affinity of SSEA-4–BODIPY and Globo H–BODIPY for BSA. Both glycans demonstrated only weak affinity for BSA (Figure 4.2C) and binding did not achieve saturation. The non-specific binding of Globo H to BSA did appear to be stronger than that of SSEA-4, consistent with the preference of BSA for hydrophobic moieties[224] and the L-fucose of Globo H being more hydrophobic than the *N*-acetylneuraminic acid of SSEA-4.

4.3.2 Affinity of monoclonal antibodies to Globo H and SSEA-4 on a surface

Next, we used a highly sensitive assay based on SPR to measure the affinity of SSEA-4 and Globo H for α-SSEA-4, α-GH, and α-SSEA-3 antibodies. Using a Neutravidin chip and biotinylated SSEA-4 and Globo H, we were able to create two-dimensional surfaces of the

glycans. Flowing an antibody over that surface enabled us to monitor binding from the increase in response units (RU).

We found that α-GH and α-SSEA-4 bound specifically to their respective hexasaccharide antigen (Figure 4.3A and 4.3B). In addition, we found that α-SSEA-3 bound more tightly to SSEA-4 than to Globo H (Figure 4.3C). Plotting RU at saturation versus concentration yielded equilibrium binding isotherms (Figures 4.4A and 4.4B). Fitting these data to eq 4.1 provided K_d values of (7.5 ± 0.4) nM, h = 1.7 for the α-SSEA-4·SSEA-4 complex and (8 ± 3) nM, h = 1.5 for the α-GH·Globo H complex. [If the Hill coefficients were fixed at h = 2.0, then the values of K_d would be (7.3 ± 0.3) nM and (7 ± 2) nM, respectively.]

The measured affinity of the monoclonal antibodies for glycans displayed on a surface exceeds that for soluble glycans by ~20-fold. This discrepancy is likely due to multivalency.[225-228] The antibodies are bivalent, and can bind to two surface-displayed glycans simultaneously with a concomitant increase in affinity. This arrangement could better mimic binding to the surface of a human cell.[227,228]

SSEA-3, while mainly a stem cell marker, has been observed to be overexpressed on teratocarcinoma cells.[188,229] Due to the weaker affinity of α-SSEA-3 for the glycan surfaces, we were able to fit the sensorgrams using a kinetic bivalent fit to each curve (Figure 4.4C), to give K_d values of (18 ± 2) nM for the α-SSEA-3·SSEA-4 complex and (0.5 ± 0.2) μM for the α-SSEA-3·Globo H complex. Thus, α-SSEA-3 has a significant preference for the *N*-acetylneuraminic acid of SSEA-4 than the L-fucose of Globo H.

Prior assessments of the affinity of monoclonal antibodies to glycan antigens used microarray technology. In that way, α-SSEA-4 had been shown to form a complex with SSEA-4 having a K_d value of (4.21 ± 0.26) nM,[230] and α-GH had been shown to form a complex with Globo H having

a K_d value of (0.56 ± 0.129) nM.[218] Our data are consistent with this low nanomolar affinity for surface-displayed glycans, and reveal a high specificity.

4.4 Conclusions

We conclude that the monoclonal antibodies α-SSEA-4 and α-GH bind specifically to their cognate antigens with affinity in the low nanomolar range, both in solution as well as on a two-dimensional surface. Moreover, the antibodies have virtually no cross-reactivity for the non-cognate glycan. These data support the reliability and utility of these monoclonal antibodies for the identification of stem cells and for applications in cancer immunotherapy.

Acknowledgements

We are grateful to Professor S. J. Danishefsky of the MSKCC for his support and encouragement of this work. We thank Dr. N. A. McGrath and M. R. Aronoff of the University of Wisconsin–Madison for advice on the synthesis of SSEA-4–BODIPY. We are grateful to Dr. G. Sukenick, and H. Fang of the MSKCC NMR Analytical Core Facility for help with the acquisition of NMR, MS, and LC/MS data. β-(Azidoethyl)SSEA-4 and SSEA-4–biotin were provided by the Consortium for Functional Glycomics, which was supported by Grant U54 GM062116 (NIH). SPR data were obtained at the University of Wisconsin–Madison Biophysics Instrumentation Facility, which was established with support from the University of Wisconsin–Madison and Grants BIR-9512577 (NSF) and S10 RR013790 (NIH). The Organic Synthesis Core Facility is supported in part by Grant P30 CA008748 (NIH). This work was supported by Grant R01 CA073808 (NIH).

Figure 4.1

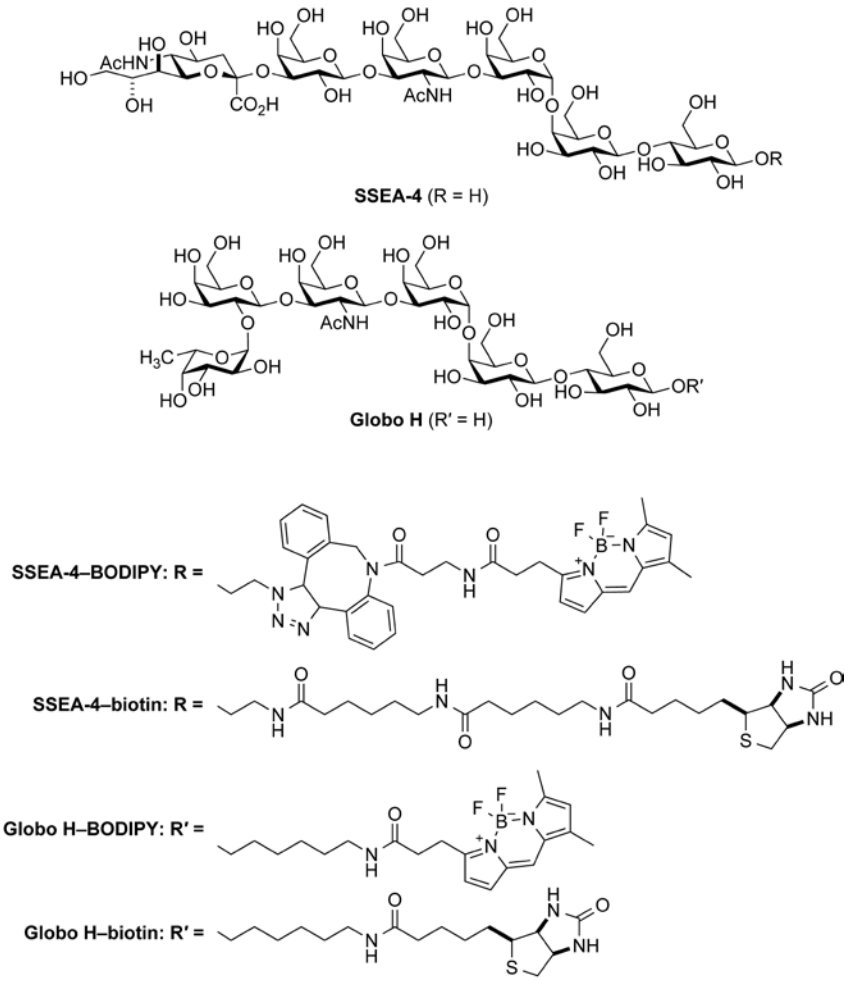
SSEA-4 (R = H)
Globo H (R′ = H)
SSEA-4–BODIPY: R =
SSEA-4–biotin: R =
Globo H–BODIPY: R′ =
Globo H–biotin: R′ =

Figure 4.1 Chemical structures of SSEA-4, Globo H, and their conjugates with BODIPY and biotin

Figure 4.2

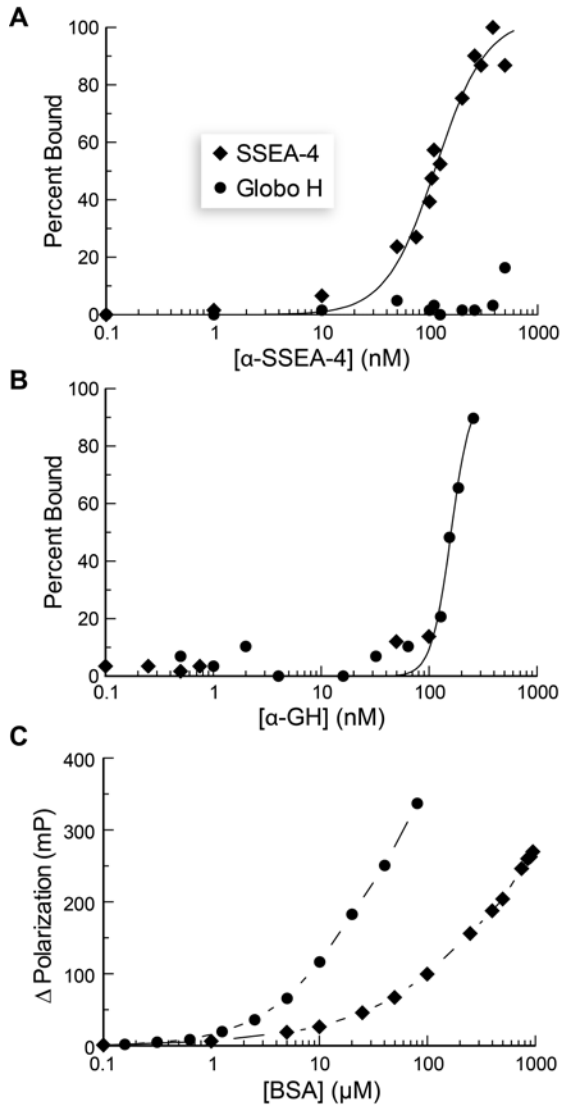
A
Percent Bound
SSEA-4
Globo H
[α-SSEA-4] (nM)
B
Percent Bound
[α-GH] (nM)
C
Δ Polarization (mP)
[BSA] (μM)

Figure 4.2 Representative binding isotherms of monoclonal antibodies to glycans in solution as determined with fluorescence polarization

SSEA-4–BODIPY and Globo H–BODIPY were incubated with increasing concentrations of *A.* α-SSEA-4 or *B.* α-GH in PBS containing BSA, or *C.* BSA in PBS. Polarization was normalized to determine the percent bound at each concentration. Data were analyzed by non-linear regression to Eq 4.1 (n = 3) to give K_d = (115 ± 10) nM for the α-SSEA-4·SSEA-4–BODIPY complex and K_d = (161 ± 13) nM for the α-GH·Globo H–BODIPY complex.

Figure 4.3

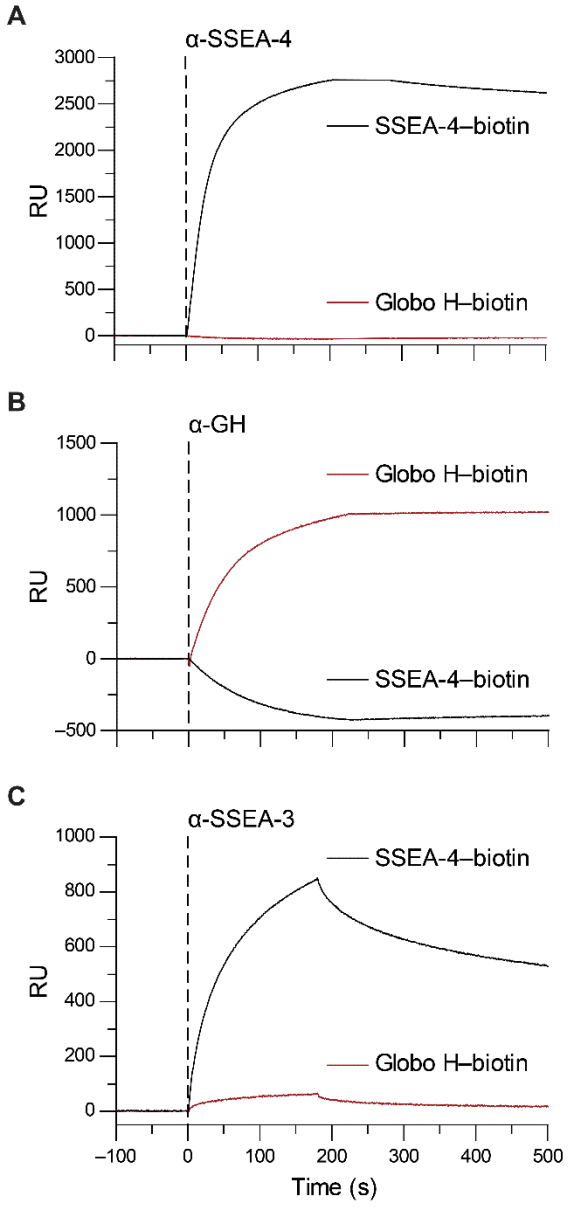
A
α-SSEA-4
3000
2500
2000
1500
1000
500
0
RU
SSEA-4–biotin
Globo H–biotin
B
α-GH
1500
1000
500
0
–500
RU
Globo H–biotin
SSEA-4–biotin
C
α-SSEA-3
1000
800
600
400
200
0
RU
SSEA-4–biotin
Globo H–biotin
–100
0
100
200
300
400
500
Time (s)

Figure 4.3 Specificity of monoclonal antibodies for glycans on a surface as determined via SPR Representative SPR sensorgrams of monoclonal antibodies *A*. α-SSEA-4, *B*. α-GH, or *C*. α-SSEA-3 interacting with Globo H (red) or SSEA-4 (black) immobilized on a NeutrAvidin chip. Antibodies were flowed over the horizontal channels. Curves were referenced to interspots on the horizontal channel to correct for non-specific interactions.

Figure 4.4

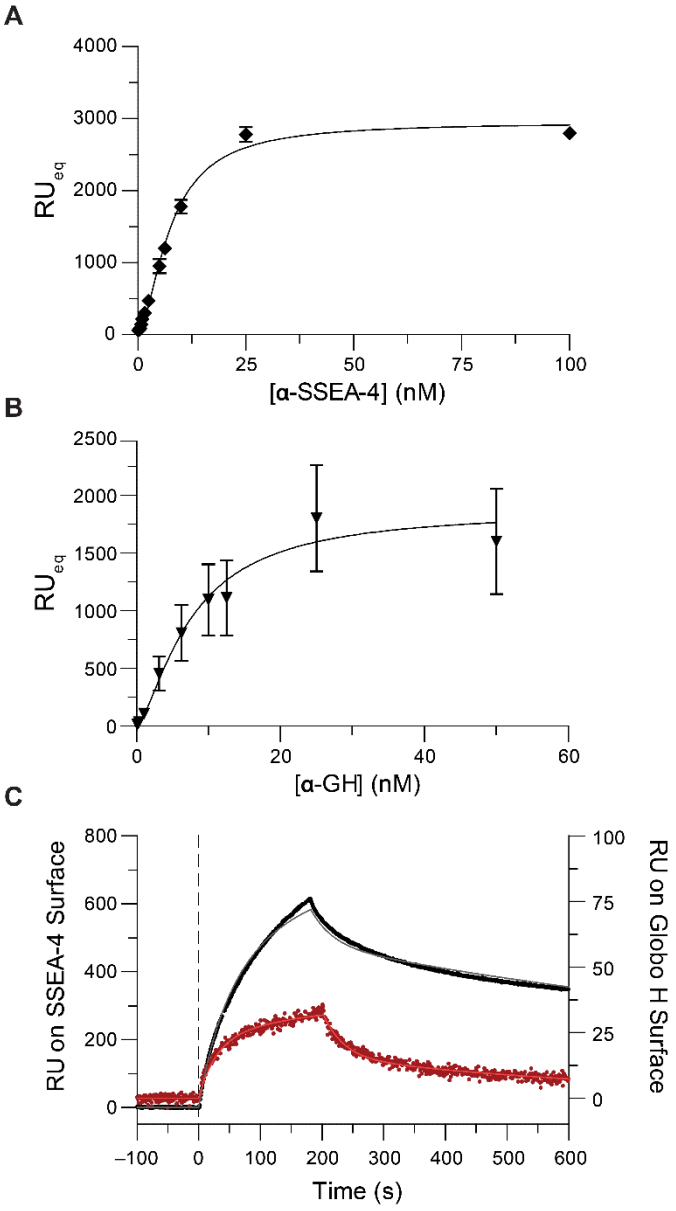
A
4000
3000
2000
1000
0
RUeq
0
25
50
75
100
[α-SSEA-4] (nM)
B
2500
2000
1500
1000
500
0
RUeq
0
20
40
60
[α-GH] (nM)
C
800
600
400
200
0
RU on SSEA-4 Surface
100
75
50
25
0
RU on Globo H Surface
–100
0
100
200
300
400
500
600
Time (s)

Figure 4.4 Affinity of monoclonal antibodies for glycans on a surface as determined via SPR Response units at saturation (RU_{eq}) were recorded for increasing antibody concentrations and *A*. SSEA-4 (K_d = 7.5 ± 0.4 nM) and *B*. Globo H (K_d = 7 ± 4 nM) surfaces. Data were analyzed by non-linear regression to Eq 4.1. *C*. Sensorgram of α-SSEA-3 binding to SSEA-4 (black; K_d = 18 ± 2 nM) and Globo H (red; K_d = 0.5 ± 0.2 μM) surfaces. Data were fitted to a kinetic bivalent binding curve (thin line) with ProteOn software.

Supplementary information

Scheme S4.1

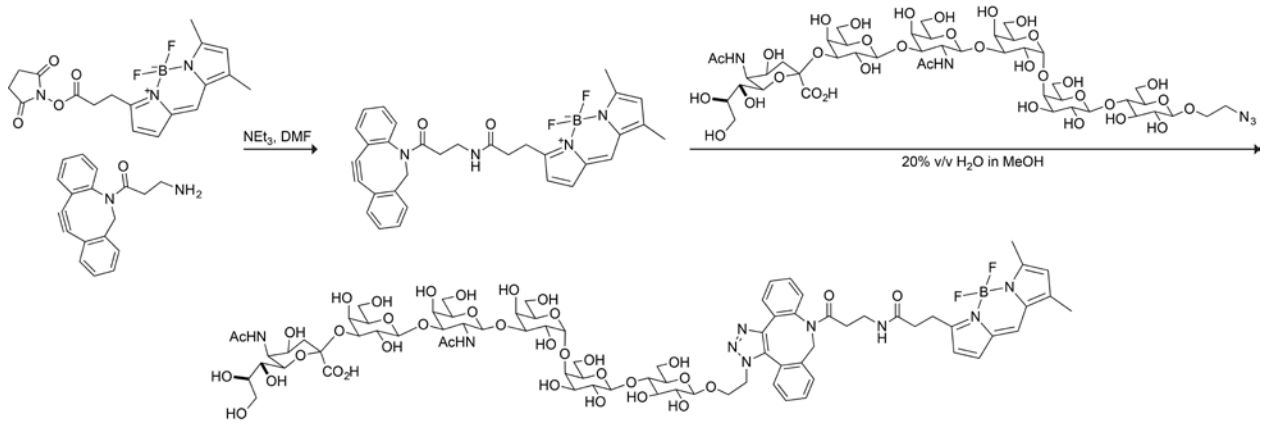

Scheme S4.1 Route for the synthesis of SSEA-4–BODIPY

Scheme S4.2

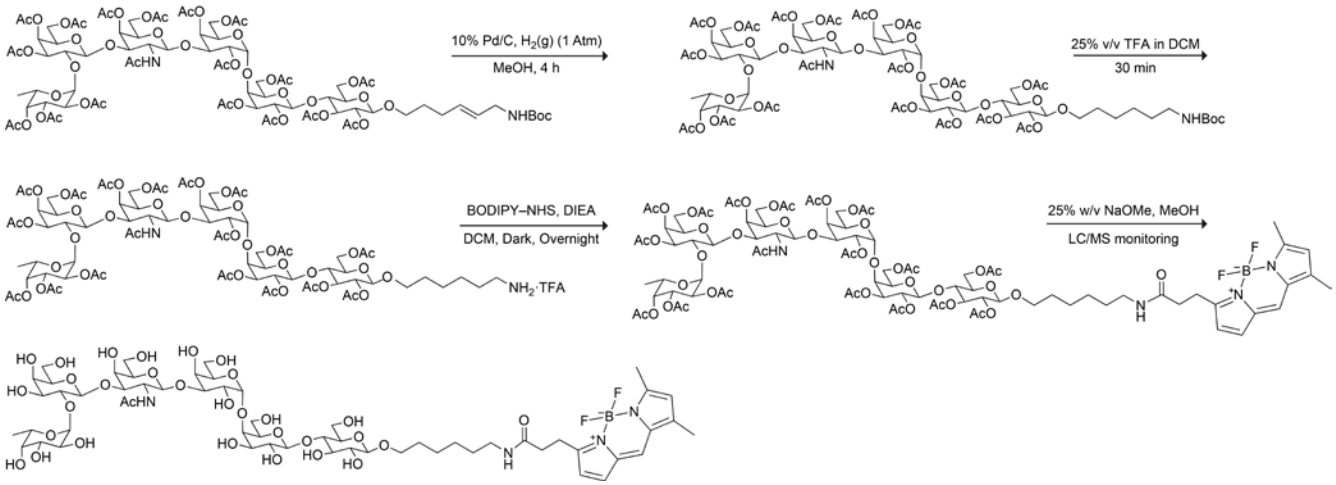
10% Pd/C, H2(g) (1 Atm)
MeOH, 4 h
25% v/v TFA in DCM
30 min
BODIPY–NHS, DIEA
DCM, Dark, Overnight
25% w/v NaOMe, MeOH
LC/MS monitoring
NHBoc
NH2·TFA
AcHN
AcO
OAc
HO
OH

Scheme S4.2 Route for the synthesis of Globo H–BODIPY

Scheme S4.3

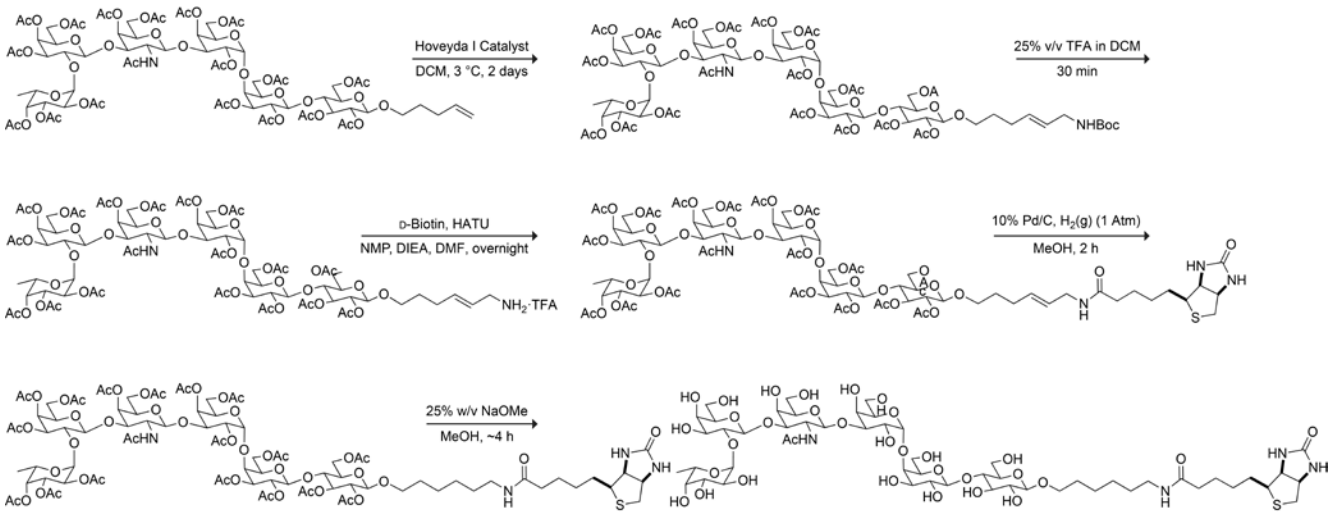
Hoveyda I Catalyst
DCM, 3 °C, 2 days
25% v/v TFA in DCM
30 min
D-Biotin, HATU
NMP, DIEA, DMF, overnight
10% Pd/C, H2(g) (1 Atm)
MeOH, 2 h
25% w/v NaOMe
MeOH, ~4 h

Scheme S4.3 Route for the synthesis of Globo H–biotin

Figure S4.1

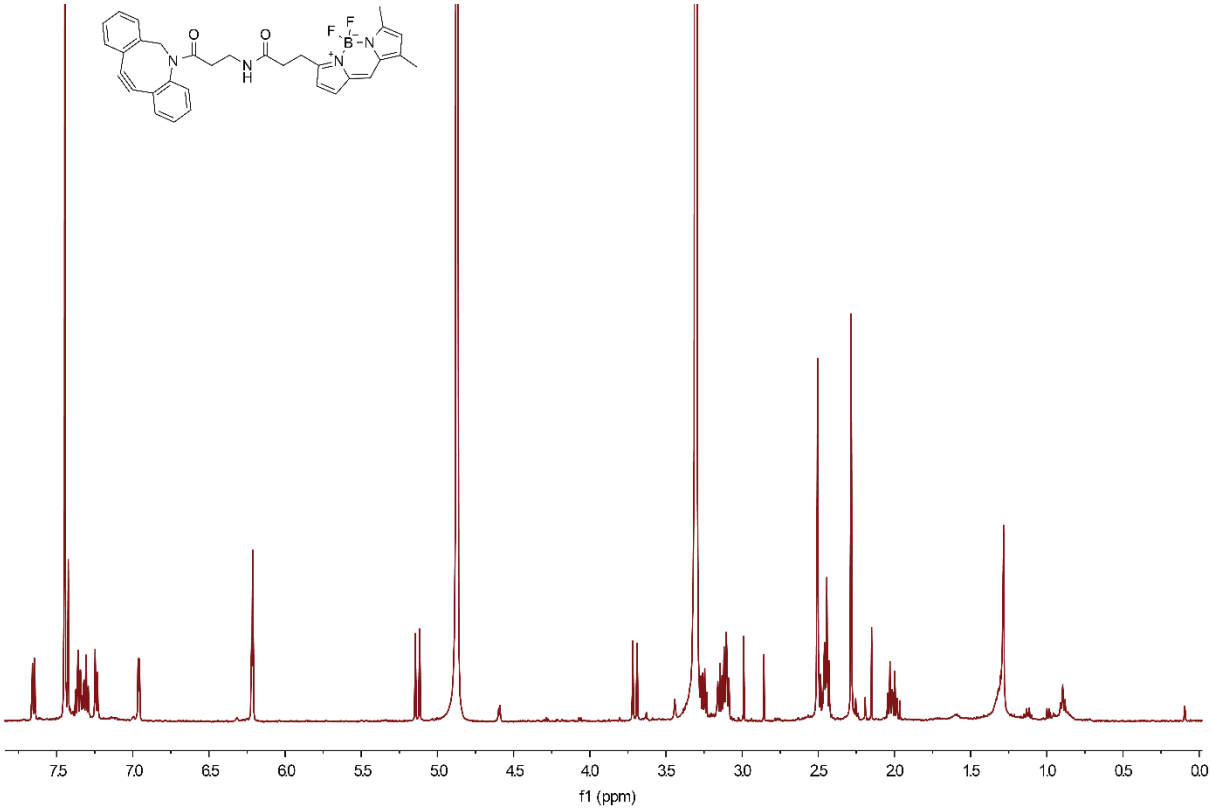

Figure S4.1 ^{1}H NMR spectrum of cyclooctyne–BODIPY

Figure S4.2

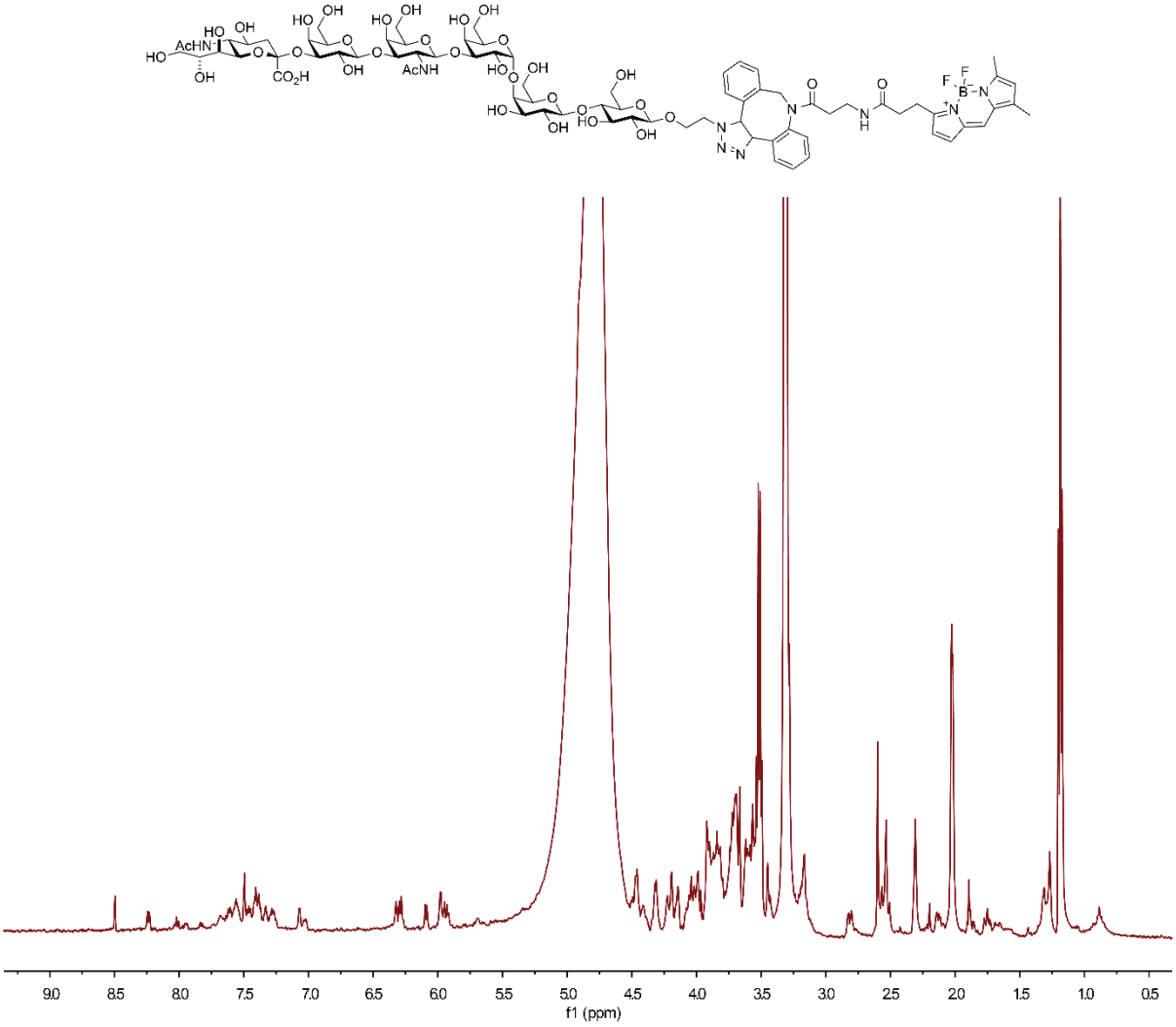

Figure S4.2 ^{1}H NMR spectrum of SSEA-4–BODIPY

Figure S4.3

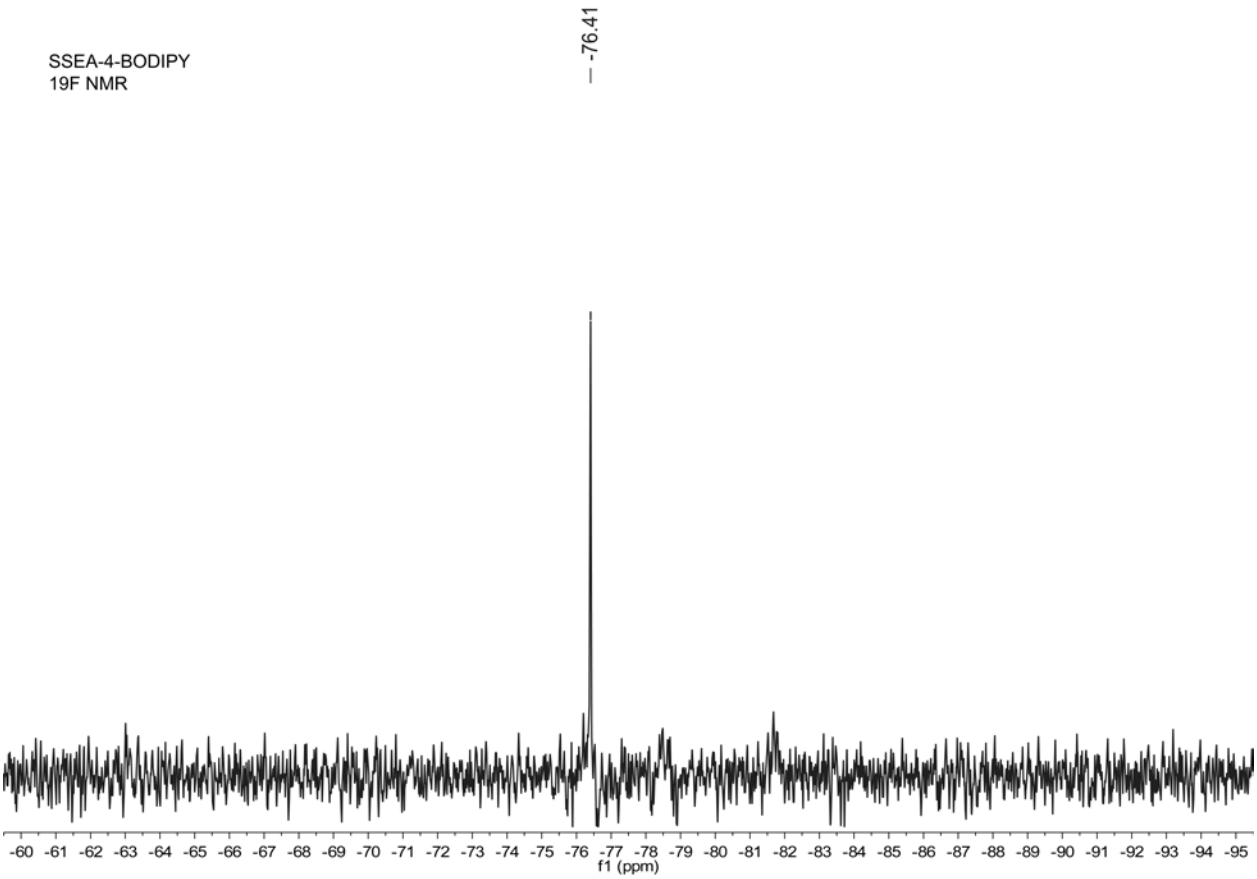
SSEA-4-BODIPY
19F NMR
-76.41
-60 -61 -62 -63 -64 -65 -66 -67 -68 -69 -70 -71 -72 -73 -74 -75 -76 -77 -78 -79 -80 -81 -82 -83 -84 -85 -86 -87 -88 -89 -90 -91 -92 -93 -94 -95
f1 (ppm)

Figure S4.3 ^{19}F NMR spectrum of Globo H–BODIPY

Figure S4.4

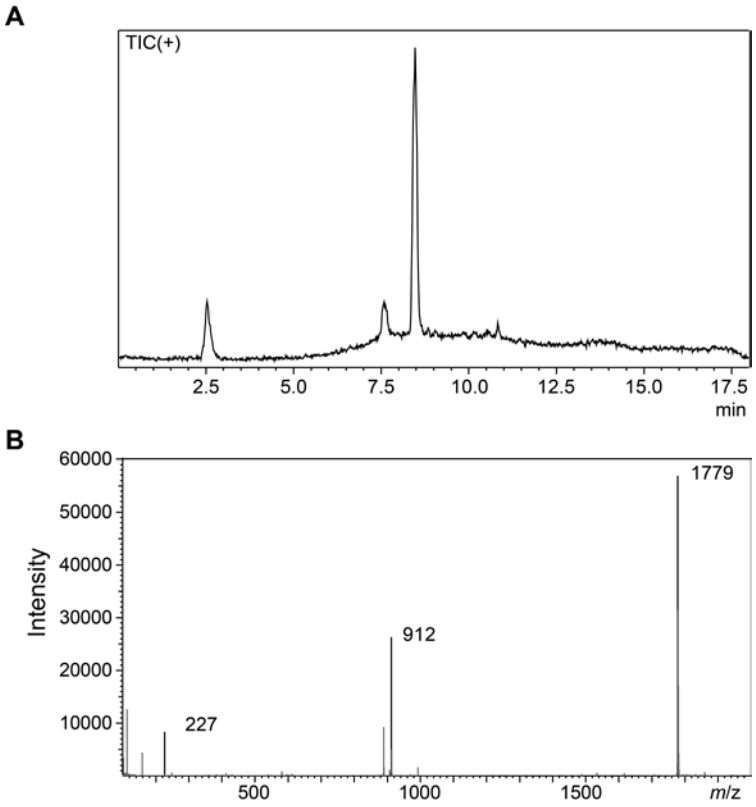
A
TIC(+)
2.5
5.0
7.5
10.0
12.5
15.0
17.5
min
B
Intensity
60000
50000
40000
30000
20000
10000
1779
912
227
500
1000
1500
m/z

Figure S4.4 LC/MS chromatogramw of SSEA-4–BODIPY

Sample was applied to a C5 column and eluted with a gradient of 5–95% v/v H_2O in CH_3CN containing formic acid (0.1% v/v). *A*. Time course monitoring ionizable molecules eluting from the column. *B*. Mass spectrum of the predominant peak eluting at 8.5 min in panel *A*. LC/MS *m*/*z* 1779 [calc'd for $C_{77}H_{104}BF_2N_9O_{36}$ (M+H) 1781].

Figure S4.5

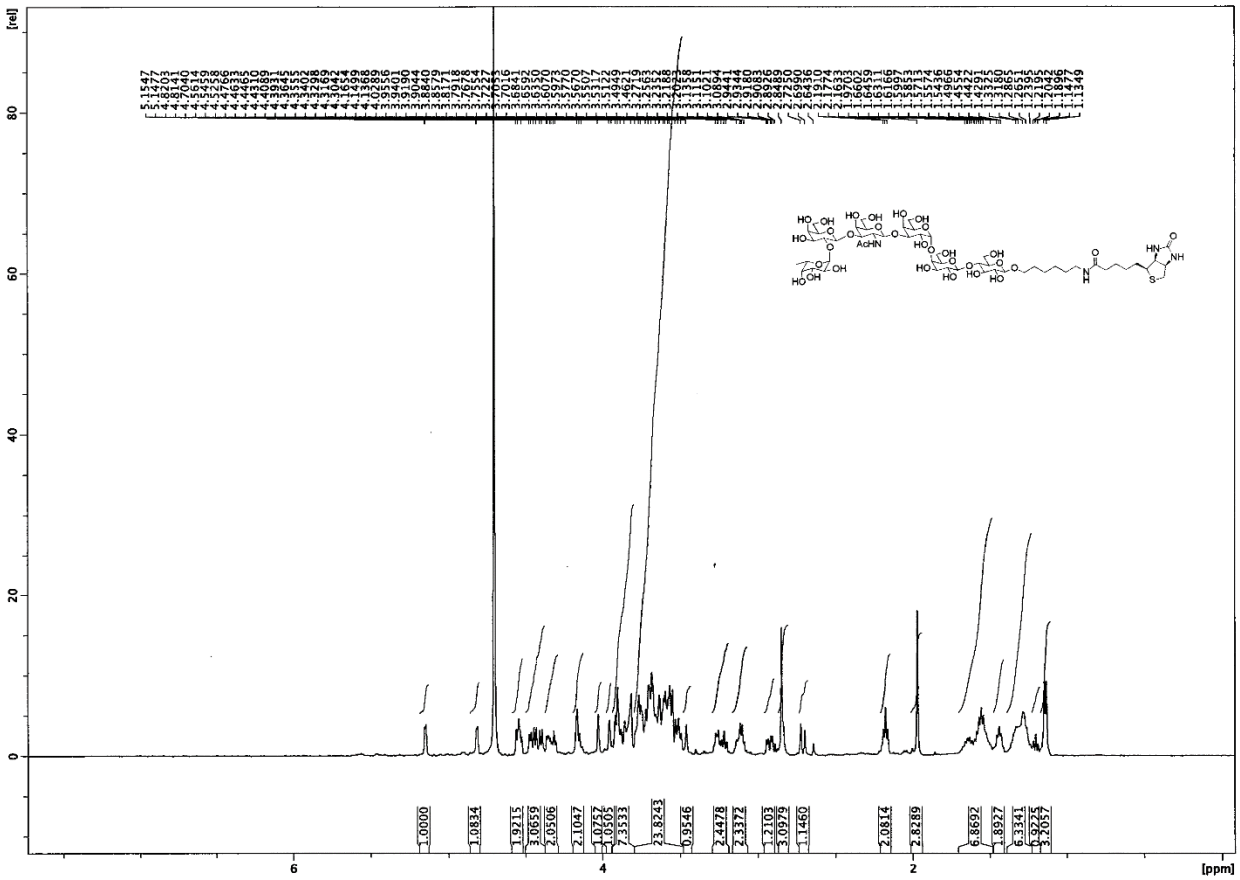
[rel]
[ppm]
1.0000
1.0834
1.9215
3.0659
2.0506
2.1047
1.0757
1.0505
7.3533
23.8243
0.9546
2.4478
2.3372
1.2103
3.0979
1.1460
2.0814
2.8289
6.8692
1.8927
6.3341
6.9275
3.2057

Figure S4.5 ^{1}H NMR spectrum of Globo H–biotin

Figure S4.6

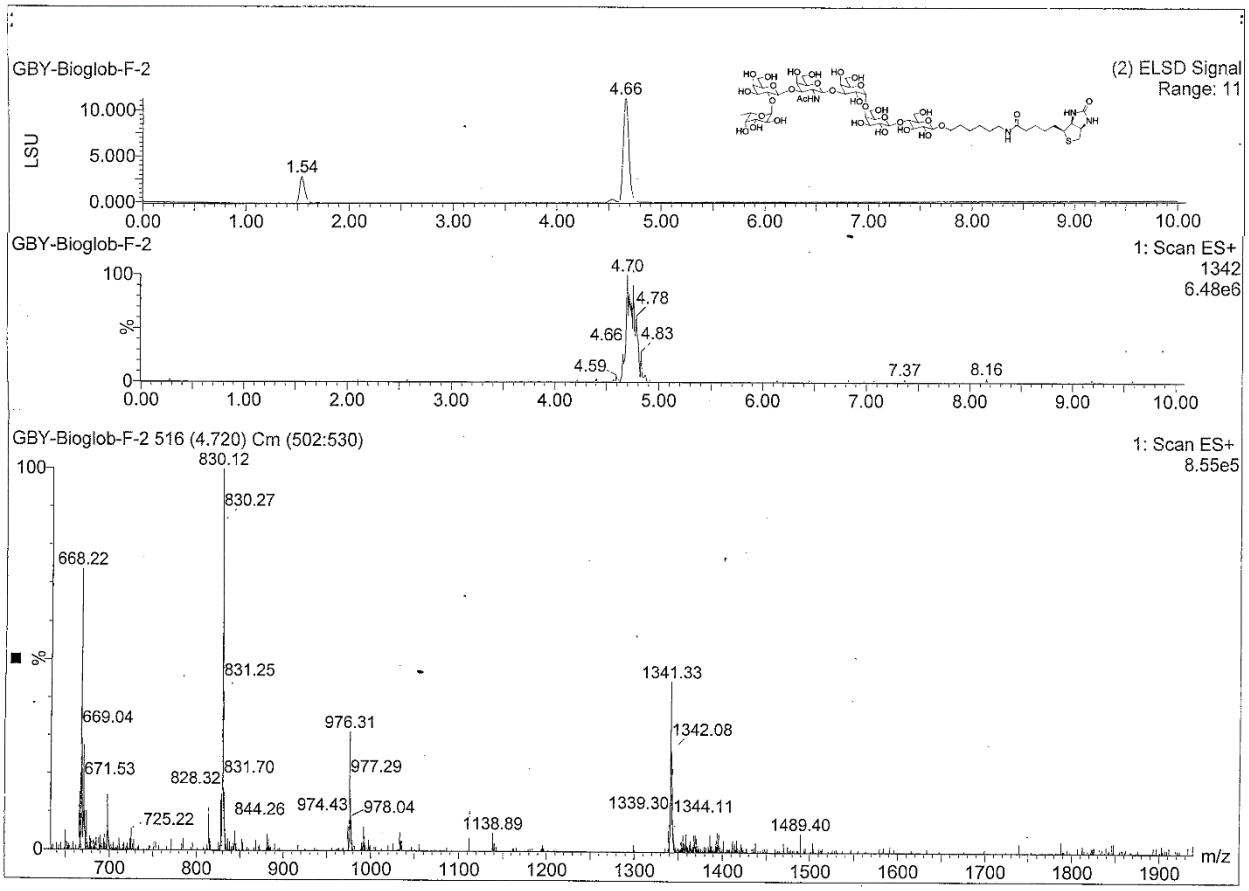
GBY-Bioglob-F-2
(2) ELSD Signal
Range: 11
LSU
10.000
5.000
0.000
1.54
4.66
0.00 1.00 2.00 3.00 4.00 5.00 6.00 7.00 8.00 9.00 10.00
GBY-Bioglob-F-2
1: Scan ES+
1342
6.48e6
100
%
0
4.70
4.78
4.66
4.83
4.59
7.37
8.16
GBY-Bioglob-F-2 516 (4.720) Cm (502:530)
1: Scan ES+
8.55e5
830.12
830.27
668.22
831.25
1341.33
669.04
976.31
1342.08
671.53
828.32
831.70
977.29
725.22
844.26
974.43
978.04
1138.89
1339.30
1344.11
1489.40
700 800 900 1000 1100 1200 1300 1400 1500 1600 1700 1800 1900
m/z

Figure S4.6 LC/MS chromatogram of Globo H–biotin

Figure S4.7

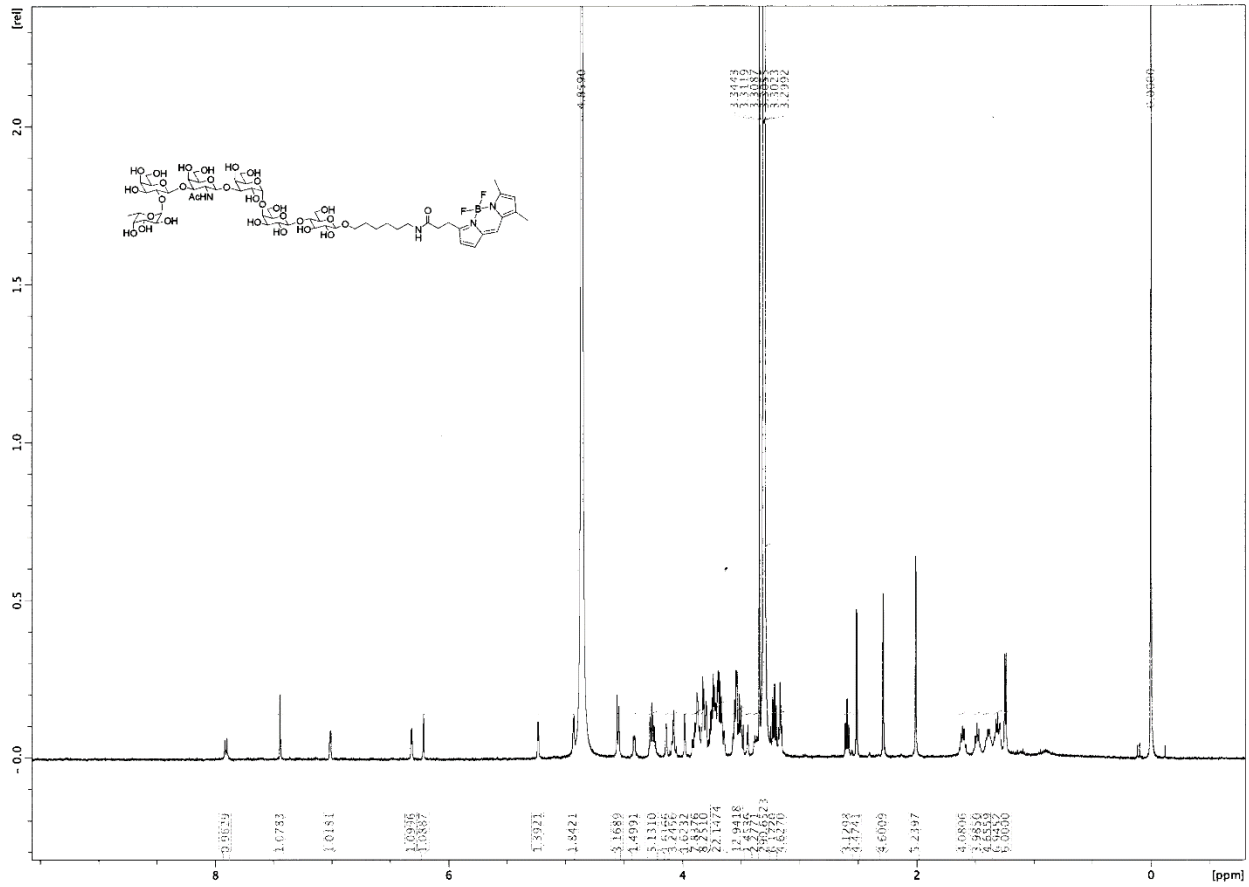

Figure S4.7 ^{1}H NMR spectrum of Globo H–BODIPY

Figure S4.8

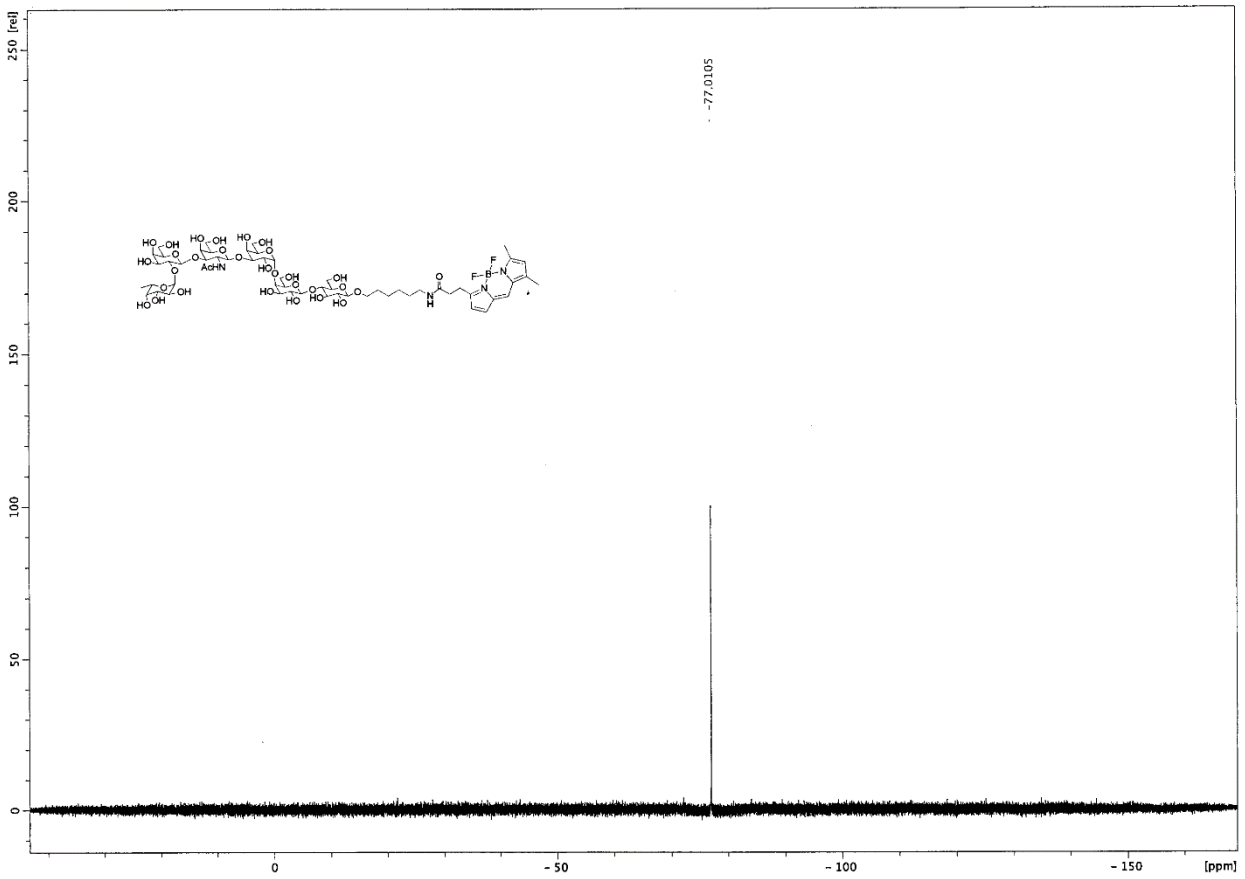

Figure S4.8 ^{19}F NMR spectrum of Globo H–BODIPY

Figure S4.9

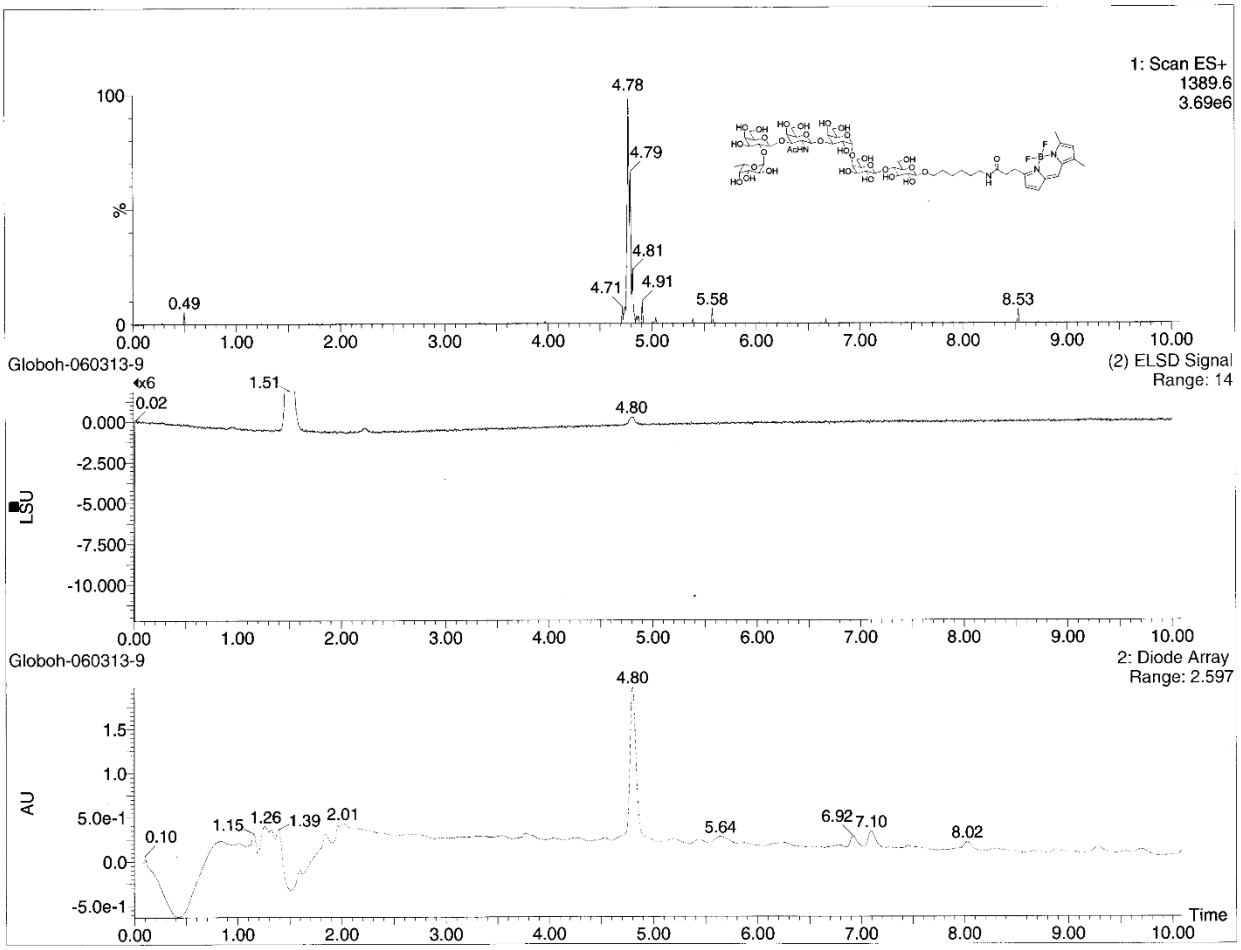
1: Scan ES+
1389.6
3.69e6
100
%
0
4.78
4.79
4.81
4.71
4.91
0.49
5.58
8.53
0.00
1.00
2.00
3.00
4.00
5.00
6.00
7.00
8.00
9.00
10.00
Globoh-060313-9
(2) ELSD Signal
Range: 14
x6
0.02
1.51
4.80
0.000
-2.500
-5.000
-7.500
-10.000
LSU
Globoh-060313-9
2: Diode Array
Range: 2.597
4.80
1.5
1.0
5.0e-1
0.0
-5.0e-1
AU
0.10
1.15
1.26
1.39
2.01
5.64
6.92
7.10
8.02
Time

Figure S4.9 LC/MS chromatogram of Globo H–BODIPY

Chapter 5

Conclusions and Future Studies

5.1 Conclusion

While over 60 years of expansive studies using RNase A brought a wealth of method development and biochemical knowledge, little effort has been expended to examine the properties specific to that of the human homolog, RNase 1. Indeed, the biological role was assigned as a digestive one. It has, however, become clear that RNase 1 diverges from its bovine homolog in many regards. Particularly, its wide tissue expression and presence in blood suggested a more systemic role. The work herein focused on characterizing the biochemical properties distinct to RNase 1. Further, as a secreted endogenous protein or a circulating therapeutic agent, RNases interact with the cell surface. Therefore, understanding the interactions with cell-surface carbohydrates may illuminate localized function and biological roles. To address these questions, I have probed the biochemistry and cell biology of RNase 1 in comparison to that of RNase A.

In CHAPTER 2, I described some key biochemical differences between RNase 1 and RNase A that likely indicates an evolving function. Most strikingly, RNase 1 exhibits ribonucleolytic activity on dsRNA and a pronounced pH optimum closer to that of physiological blood pH. RNase 1 also binds more tightly to cell-surface mimics and becomes internalized to a greater extent than does RNase A. Further, glycosylated RNase 1 is secreted from cells upon stimulation of viral dsRNA. Potentially RNase 1exerts this specific activity to degrade dsRNA and plays a likely role in viral immunity. Indeed, another bovine homolog, BRB, appears to shares these properties with RNase 1 and leads us to speculate that *it* is the true functional homolog, rather than RNase A.

In CHAPTER 3, I expand my search for cell-surface interactions with RNases. I find that RNase 1 interacts tightly with the cancer antigen, Globo H. This glycan interacts more tightly

with RNase 1 compared to RNase A. When Globo H biosynthesis is reduced and cell-surface localization is diminished, cytotoxicity mediated by RNase treatment is diminished. Structurally, RNase 1 binds Globo H in a distributed manner at neutral pH and these interactions cluster in acidic buffers. Potentially, this process could contribute to endosomal escape or be an endogenous target for RNases.

In CHAPTER 4, I characterize the interactions between Globo H and a related globo-series glycan, SSEA-4, toward their cognate monoclonal antibodies. These antibodies are currently used in the clinic and research laboratories, and understanding the affinity and potential cross-reactivity is thus important. I show that, indeed, these monoclonal antibodies exhibit nanomolar affinities to their cognate glycans with little cross reactivity.

5.2 Future studies

My work corroborates that RNase 1 displays some interesting biology and suggests that this function is likely motivated by its diverging biochemical properties. Indeed, I show major differences between homologs: human RNase 1 and bovine RNase A. While experiments within an organism will ultimately determine the role of RNase 1, I propose additional analyses that could tease out the biochemical differences discovered in my work. These experiments included determining the basis of the pH optimum, multivalent binding affinity, properties contributing to lipid bilayer disruption, new involvement in innate antimicrobial immunity, and finally exploration of the evolving properties of the RNase 1 family.

5.2.1 Determining the basis of the pH optimum of RNase 1 using NMR spectroscopy

Based on the high degree of similarity between RNase 1 and RNase A, I was surprised to see such a significant shift in pH optimum, as discussed in CHAPTER 2. Although Gaussian fit of activity assay over a pH range is acceptable for estimation of the active-site pK_a values, a more definitive determination requires a pH titration using NMR spectroscopy. This pioneering analysis was performed on RNase A in the 1970's to determine the pK_a values of the active-site residues His12 and His119 as 5.8 and 6.2, respectively.[231] This analysis monitors the protonation state of the C(2) (second carbon) of the side chain of histidine residues via the movement of the ^{1}H chemical shift. The resulting plot of pH versus chemical shift is then fitted to the Henderson–Hasselbalch equation. The chemical shift of the C(2)–H of histidine is particularly distinct—residing between 8.7 and 7.4 ppm—due to the environment between the nitrogen atoms of the imidazole ring. Still, unlabeled protein requires incubation in D_2O in order to remove peaks from exchangeable amino groups (*e.g.*, the protons on acidic and basic residues). RNase 1 has a total of five histidine residues—two of which are involved in catalysis. The other residues include two that are exposed to solvent and one that resides within the interior of the protein structure. The solvent-exposed residues would be predicted to exhibit a pK_a value around 6.5 and the interior residue would be non-titrateable. Computational analysis of crystal structures does not accurately predict the pK_a values of RNase A.[v] Still, the same analysis on both RNase A and RNase 1 predicts that the active-site residues of RNase 1 have more basic pK_a values due to increased charged. Based on this observation as well as the experimental pH optimum of 7.2, we hypothesize that the pK_a values of RNase 1 would be around 7.0 and 7.4.

[v] Determined from the Propka server, http://www.pymolwiki.org/index.php/Propka. The PROPKA method is developed by the Jensen Research Group, Department of Chemistry, University of Copenhagen.

5.2.1.1 Methods: Preparation of D_2O-exchanged RNase 1

Wild-type RNase 1 (15 mg) was lyophilized 3 times with reconstitution into 100% D_2O. After the final resuspension, protein was incubated in the dark at 4 °C for 1 month to allow for amine proton exchange with D_2O. Subsequently, protein was aliquoted into 3–5 mg samples and lyophilized. DSS (4,4-dimethyl-4-silapentane-1-sulfonic acid) was added at 0.5 mM to all samples as an NMR reference. Phosphate buffer (200 mM) at pH 5 and pH 8 were made in D_2O, and the pH was adjusted using DCl. Protein was resuspended in both buffers, pH 5 and 8. Small amount of the protein were mixed together to make samples at an intermediate pH and measured using a pH probe. Samples (30 µl) were injected into 1.7 mm NMR sample tubes (Bruker). Proton chemical shift was recorded on the 600 MHz Varian NMR spectrometer (NMR FAM) and overlay created in MestReNova (Mestrelab Research).

5.2.1.2 Results: RNase 1 chemical shift perturbations upon pH titration

RNase 1 contains five histidine residues. Preliminary data indicated that several proton chemical peaks shift upon pH titration (black arrows in Figure 5.1). The multiple peaks in the 8.6–7.5 ppm chemical shift range suggest that potentially not all the N–H protons exchanged and that a longer incubation time is needed. However, due to broadening of the exchanging protons, several peaks appear—some indicated with red arrows. Further, a contaminant appears in the samples at 8.4 ppm (blue arrow), which unfortunately masks the peaks in several spectra. This sharp peak is likely due to a small molecule in the glass that can be avoided by washing and drying the NMR tubes prior to sample preparation. While this experiment indicates the technique is possible, these preliminary experiments need repeating.

5.2.1.3 Future studies: Repeat RNase 1 pH gradient

In order to clarify the peak assignments, several options exist. Using a larger protein concentration, a lower strength magnetic field (*i.e.*, 400 MHz) spectrometer could be employed to lessen the broadening effect. This would also increase the intensity of the peaks for ease in detection. Further, washing of the glassware thoroughly should remove contaminants. Additionally, RNase 1 could be labeled with ^{14}C or ^{15}N as described in APPENDIX 1. This would allow for less protein sample while retaining a strong signal-to-noise ratio. Compared to a ^{1}H spectra, a 2D-NMR spectra would allow for greater separation of peaks and clear monitoring of the residues. Regardless of the technique use, specific identification of the active-site residues could be determined by addition of a substrate analog such as cytidine 3´-monophosphate, CMP. As shown with RNase A,[232] CMP would perturbed the chemical shifts of the active-site residues and allow for the direct identification.

5.2.2 Characterizing multivalent binding affinities of RNase 1

As many binding sites exist on a cell surface, it is unclear how RNase 1 binds to multiple sites. I identified and quantified binding of RNase 1 to heparan sulfate, chondroitin sulfate (CHAPTER 2), Globo H (CHAPTER 3), and phosphatidylserine liposomes (APPENDIX 3). However, it is unknown how all these binding events might act together. Measurement of this effect requires the controlled re-assembling of cell-surface molecules. These experiments typically require large amounts of compounds, and glycan synthesis or isolation is difficult. Particularly, Globo H synthesis is extremely challenging, and heterogeneous GAG molecules are commercial only as soluble compounds. To simplify the system, I attempted to determine and

compare the binding affinities of RNase 1 to liposomes containing phosphatidylserine (PS) and/or mono-sulfated glycosphingolipid (sulfatide).

5.2.2.1 Methods: Liposomal binding assays

Liposomal binding experiments were performed as described in APPENDIX 3 using phosphatidylcholine (PC) as a vehicle for liposomes. Liposomes contained 3 mM PC and 2 mM PS, 2 mM mono-sulfo galactosyl(ß) ceramide (sulfatide), or 1 mM PS plus 1 mM sulfatide. All lipids were obtained from Avanti Lipids, and liposomes were formed via extrusion with a diameter of ~130 nm. Fluorescence polarization of RNase 1–BODIPY monitored binding as the concentration of liposomes was increased in PBS, pH 7.4. Percent binding was normalized to protein unbound and saturated, and curves were fitted by nonlinear regression.

5.2.2.2 Results: Sulfatide binds to RNase 1 tighter than does phosphatidylserine

I found that RNase 1 bound to sulfatide with an affinity of 15 μM—tighter than to phosphatidylserine liposomes, 27 μM (Figure 5.2 and Table 5.1). I assessed multivalent binding by producing liposomes of 1:1 PS and sulfatide. However, as shown in Table 5.1, RNase 1 affinity to this combination of lipids (90 μM) more weakly than to either individually. Potentially, the binding sites for sulfate and phosphate are competing and, therefore, results in a weaker overall affinity.

5.2.2.3 Future studies: Characterizing multivalent binding affinities of RNase 1

It is possible that the sulfatide does not sufficiently mimic the binding we anticipate for heparan sulfate and other GAGs. Indeed, the affinity 15 μM is much weaker than the observed

nanomolar affinity for larger heparin molecules. Heparin is more negatively charged (~2.5/monomer) and the sulfatide charges might be too sparse in the liposomes. Yet, future analyses could incorporate the ever-expanding selection of accessible lipids, including gangliosides and di-sulfo sulfatides. Additionally, cell-surface compounds could be biotinylated and attached onto an avidin surface as described in CHAPTER 3.

5.2.3 Determining contributions of RNase 1 bilayer translocation

The pathway of RNase-mediated cytotoxicity relies on internalization and, more specifically, translocation from endosomes into the cytosol. This process is extremely difficult to monitor and current estimates predict that only 7% of the total RNases taken-up by cells enters the cytosol.[233] As RNases are extremely efficient enzymes, mere picomolar amounts of an RI-evasive enzyme are likely sufficient to cause cell death.

Current efforts are underway to quantify and improve the amount of protein leaving the endosomes within a cell. Meanwhile, several *in vitro* liposomal disruption assays could illuminate some of the properties that allow RNases to cross lipid bilayers. Understanding this process could aid in the engineering more efficient translocation for therapeutic delivery.

5.2.3.1 Methods: Liposomal disruption assays

RNase 1 and variants were purified as described.[40] Residues, R39, N67, N88, G89, and R91 were mutated to Leu, Ala, Arg, or Asp. The variant name indicates the amino acid to which that position was mutated. Liposome production (3:2 PC:PS) and dye/quencher incorporation was performed as described in CHAPTER 2.[195] RNase 1 and variants were added at 25 μM to a

liposome concentration of 750 μM (1:30 ratio). Disruption was normalized to untreated (0%) and to complete disruption with 0.1% (v/v) Triton X-100 (100%).

5.2.3.2 Results: Charged residues improve RNase 1 disruption of bilayers

Based on computational prediction in APPENDIX 3, the lobe face of RNase 1 preferentially docks to anionic membranes.[92] This region also contains the RI-binding interface. Particularly, mutation of residues R39, N67, N88, G89, and R91 have been shown to evade RI and exhibit cytotoxicity (Figure 5.3A).[40] RNase 1 exhibits little disruption on liposomes comprised of PC, a zwitterionic lipid. However, the disruption increases as the affinity to the liposome increases—the addition of anionic PS into the liposomes or the lowering of the buffer pH (Figure 5.3B). I assessed the contribution of charged and polar residues of this region of RNase 1 by measuring disruption of the variants. Analysis of RNase 1 and variants indicates that installation of charged residues increases the ability to disrupt membranes (Figure 5.3C). Indeed, mutations of these residues to nonpolar side chains, as in variant LLALL, exhibited reduced ability to disrupt liposomes. However, reinsertion of two arginine residues, along with anionic residues like aspartic acid, improved the disruption capability of RNase 1. Potentially, this disruption results from an increase in interactions with the PC lipids to allow for protein insertion into the membrane.

5.2.3.3 Future studies: Determining contributions of RNase 1 on bilayer translocation

Further mutagenesis could illuminate the mechanistic contributions of residues to translocation. In addition I hypothesize that sulfatide or more complex liposome compositions

(described in section 5.2.2) that exhibit greater affinity for RNases would also yield greater disruption.

5.2.4 Determining synergistic antimicrobial effect of RNase 1 with peptide LL-37

Some members of the ptRNase family including RNase 2, 3, 6, and 7 have been shown to inhibit the growth of microbes.[234-236] This property has not, however, been observed with RNase 1. Yet based on the high degree of gene evolution, RNase 1 has been speculated to serve a role in innate immune function.[237] Further, RNase 1 stimulated cytokine production in white blood cells, indicating some role in immunity.[51] Although RNase 1 is not known to have antimicrobial activity, many antimicrobial agents do exist in the human body. One class of agents involved in the innate immune response of vertebrates are antimicrobial peptides (AMP). The human AMP, known as LL-37 of the family of cathelicidin AMP, is a 37-residue alpha-helical cationic peptide. The peptide is secreted from various tissues and cells, including the epithelia, and is found in several bodily fluids including breast milk, seminal fluid, plasma, and mucosa.[238] The method of antimicrobial defense is thought to be a result of forming pores in the membrane of microbes, but LL-37 has also been effective against fungi, virus, and parasites. LL-37 has been shown to act synergistically with other AMPs such as protegrin-1 and lysozyme.[239,240] As both compounds are found in the body, I was prompted to determine if LL-37 could act synergistically with RNase 1.

5.2.4.1 Methods: Bacterial minimum inhibitory concentration assays

E. coli strain RP437 was diluted 10,000-fold from a saturated overnight growth, and a 200μL aliquot was added to the wells of a 96-well round-bottom plate (Evergreen Scientific). LL-37

(AnaSpec) or RNase 1 in PBS was added in increasing concentration to determine a minimum inhibitory concentration (MIC). To determine synergy, a checkerboard assay was employed. LL-37 was diluted in the rows down the plate at concentrations of 7.5, 10, 15, 20, 25, 30, and 40 μg/mL. RNase 1 was added at 200 nM and diluted 5-fold across the plate. For all assays, *E. coli* cells were allowed to grow for 18 h at 37 °C with shaking. Cell concentration was measured by reading the OD at 600 nm. Percent viability was determined by normalizing with wells containing added PBS (100%) or chloramphenicol (0%). To quantify synergy, a fractional inhibitory concentration (FIC) value was determined with the equation:

$$FIC = \frac{[A]}{MIC_A} \tag{5.1}$$

The FIC value is the ratio of the concentration of compound when used in combination over the MIC of the compound alone. These values are plotted as an isobologram to determine the extent of synergy. A linear line represents an additive effect, a concave line indicates synergy, and a convex line represents antagonism. Summing the individual FIC values gives the FIC index which is an overall indication of the extent of synergy.

$$FIC = \frac{[A]}{MIC_A} + \frac{[B]}{MIC_B} \tag{5.2}$$

An FIC index below 0.5 is considered significant synergy.

5.2.4.2 Methods: Cytotoxicity on human cells

The same concentrations of LL-37 and RNase 1 were tested on a human cell line, HeLa. Briefly, 5000 cells/well were plated in DMEM (Invitrogen). After surface adhesion, the cells were treated with LL-37 and RNase 1 as stated above. After 24 h at 37 °C, the medium was removed and replaced with Cell Titer (Promega) in DMEM. After a 2-h incubation, the plate was monitored by 490 nm. The percent of metabolically active cells was calculated by normalizing with PBS-treated and H_2O_2-treated cells.

5.2.4.3 Methods: Bacterial binding assay

A bacterial binding experiment was performed by incubating 300 μL of *E. coli* culture (OD ~0.8) with 1 μM RNase 1–BODIPY, 4 μM BSA (negative control), or 4 μM lysozyme (positive control) in 20 mM Tris-HCl buffer, pH 7.2, containing NaCl (50 mM). After a 30-min incubation at 37 °C, cells were pelleted by centrifugation, the supernatant was collected, and the pellet was washed in binding buffer. Supernatant and pellet were analyzed with SDS–PAGE. RNase 1–BODIPY was imaged by fluorescence scanning using excitation at 470 nm and emission at 530 nm. Total protein was visualized with Coomassie staining, and the gel image was scanned.

5.2.4.4 Results: RNase 1 exhibits synergy with antimicrobial peptide, LL-37

Using our method, we confirmed an MIC for LL-37 of ~20–40 μg/mL (or ~5–10 μM) against *E. coli*, falling within the published range (Figure 5.4A).[239,241] Incubation of RNase 1 with *E. coli* was not toxic even at concentrations up to 50 μM—well above physiological concentrations of ~30 nM (Figure 5.4B).[43] However, treating *E. coli* with sub-MIC concentrations of LL-37 and extremely low (pM) RNase 1 concentrations were sufficient to kill and inhibit bacterial growth (Figure 5.5A). Measurement of synergy (determined by FIC values)

of four checkerboard assays is represented as an isobologram (Figure 5.5B). The concave line indicates synergy between RNase 1 and LL-37. Indeed, the best FIC index was 0.167, and values <0.5 indicate synergistic effects. Further, this synergistic antimicrobial effect is due to ribonucleolytic activity (Figure 5.5C). Incubating *E. coli* with an active-site mutant H12A does not cause microbial toxicity.

Moreover, this cytotoxicity is specific to microbes, as treatment of these compounds had no synergistic effect on human cell line, HeLa (Figure 5.6). This result is expected as mammalian RI would bind and sequester RNase 1. LL-37 did, however, exhibit some toxicity towards HeLa cells. LL-37 has previously exhibited toxicity against cancerous cells.[242]

5.2.4.5 Results: RNase 1 binds to bacterial cells

The efficacy of low picomolar concentrations of RNase 1 suggest that RNase is effective at locating and entering the pores formed by LL-37 in bacteria cells. Using a bacterial binding assay, I found that RNase 1 associated with the bacterial membrane (Figure 5.7). BSA is known not to interact with bacterial membranes and was employed as a negative control. Conversely, lysozyme, a glycoside hydrolase, is known to bind to bacterial proteoglycans.

5.2.4.6 Future studies: Extent and mechanism of RNase 1 immune function

These results indicate, for the first time, that RNase 1 exhibits innate immune function to kill pathogenic microbes. Additional tests need to be further performed to determine the extent of antimicrobial toxicity and mechanism. For example, while *E. coli* is a gram-negative bacterium, assay with a gram-positive bacterium would indicate whether or not the presence of a proteoglycan increases or decreases efficacy. LL-37 is, in fact, more toxic to gram-positive

bacteria,[238] so potentially this effect could be amplified further. Additionally, it would be interesting to determine the molecules of the bacteria that interact with RNase 1. Potentially, a microbial glycan array (similar to the technique used in CHAPTER 3) would illuminate specific interactions that target RNase 1 to particular pathogens. Additionally, I wonder if this synergism could be effective toward viruses. LL-37 has been observed to decrease viral replication of small pox and slightly inactivate herpes simplex virus.[243,244] Further, I note that the experiments described in sections 5.2.2 and 5.2.3 could be amended to determine the properties of RNase 1 that contribute to antimicrobial activity.

5.2.5 Tracing the biochemical properties of the highly evolving RNase 1 family

Few enzyme families offer the opportunity for both genetic and biochemical analysis. The pancreatic-type ribonucleases have been a model for both disciplines. These enzymes are a rapidly evolving family—thus far only found in vertebrates—with high occurrence of gene duplication and gene loss. The number of RNase gene copies in mammals is quite large (13-20) whereas chicken and amphibian lack such diversity.[245,246] This coincides with adaptive radiation of mammalian diversity occurring during the Cenozoic era.[14]

In fact, different genes in this superfamily exhibit a variety of sequence identities ranging from 20–99%. Genetic analysis of this family has indicated that the most conserved member of the family is angiogenin—potentially indicating some essential function. Indeed, angiogenin has been found to alter transcription resulting in cellular proliferation.[247] Conversely, the eosinophil-associated proteins demonstrate the greatest sequence divergence—a property often observed in immunity genes.[18] The figurehead of the family, bovine RNase A, has been extremely well studied biochemically. Some of its properties—high non-specific activity and thermostability—

have contributed to speculation of a cellular role in digestion and clearance of cell debris. Presumably, the RNASE1 gene evolved for the purpose of foregut fermentation.[135] Yet, analysis of 52 RNASE1 genes from 24 different bat species found no correlation between the diet of herbivorous and carnivorous species and the rapidly expanding family.[248] Further, some evidence supports that the biochemical properties of this enzyme specifically evolved in ruminants and differ from that of human pancreas RNase 1.[195]

To address the effect of rapid gene evolution, we performed rigorous biochemical analysis as described in CHAPTER 2 on RNases from eleven different species. We illuminate key evolutionary functionality that has evolved from amphibians, reptiles, and birds to mammals. Indeed, dsRNA activity, neutral pH optimum, and tighter cell-surface interactions appear to be more prevalent in the mammals than is observed with amphibian, frog, and chicken species (Figure 5.8). Future experiments include determining which of these RNases exhibit antimicrobial activity as described in section 5.2.4. This may indicate that the rapid expansion of RNASE1 genes in mammals led to selection of host immune function.

Table 5.1 Binding affinity of RNase 1 for liposomes

Liposomes	K_d (μM)	Hill slope
Phosphatidylserine	26.9 ± 7.13	0.62 ± 0.05
PS/Sulfatide	90.5 ± 31.4	0.93 ± 0.17
Sulfatide	14.7 ± 2.75	1.2 ± 0.20

Values monitored by polarization at 25 °C after 30 min of equilibration in PBS, pH 7.4.

Figure 5.1

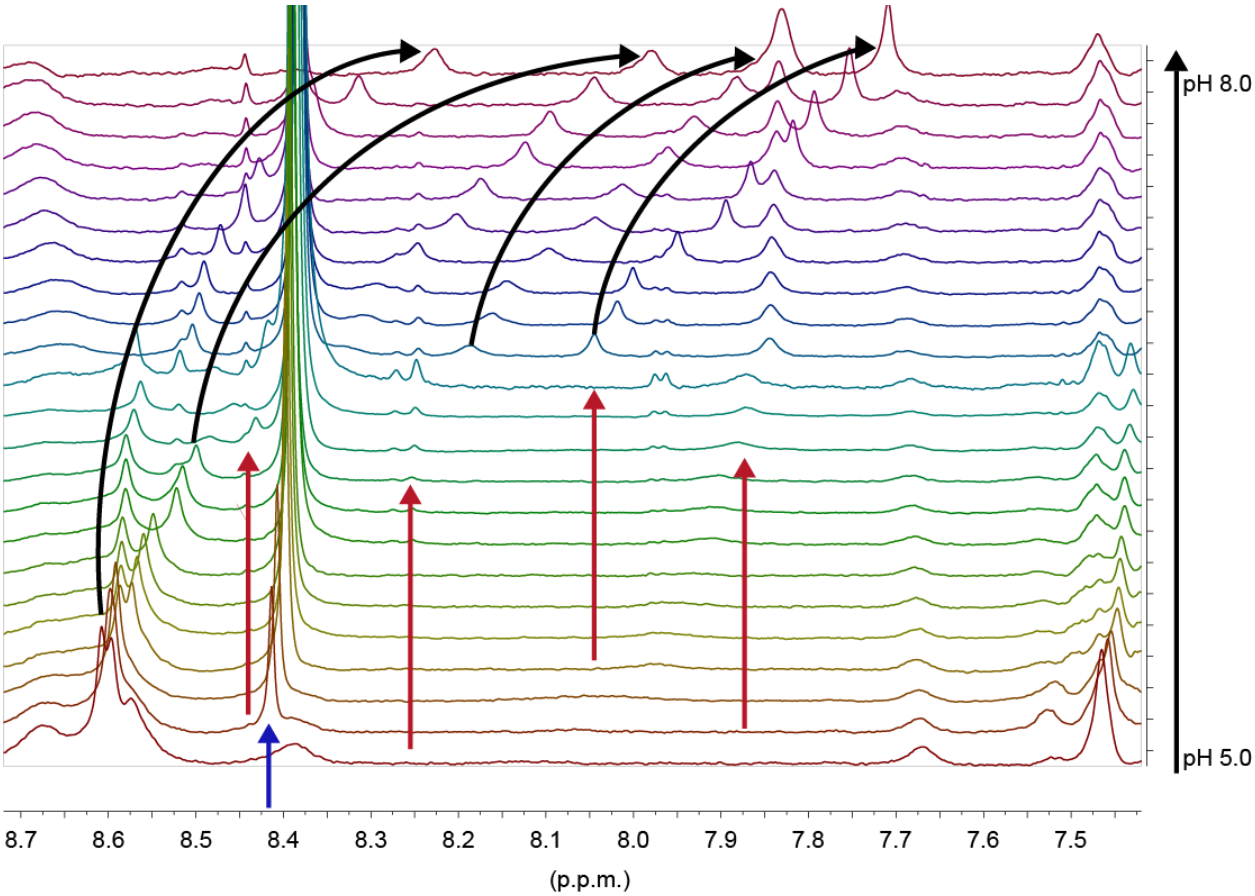

Figure 5.1 Perturbation of the ^{1}H chemical shift of RNase 1 upon pH titration

RNase 1 exchanged in D_2O, and samples prepared across a pH range of 5–8. Chemical shifts were recorded on a 600 MHz NMR spectrometer. Curved arrows indicate several examples of the shifting of peaks upon protonation. Red arrows indicate emerging peaks that were lost. A contaminating small-molecule peak (blue arrow) arises in some samples around 8.4 ppm.

Figure 5.2

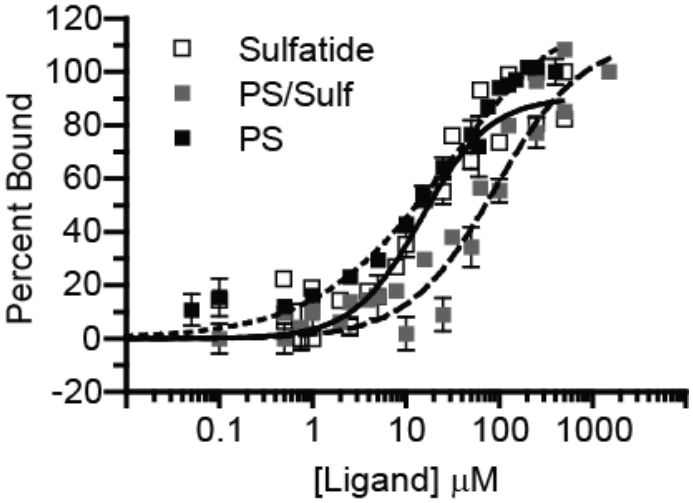
Sulfatide
PS/Sulf
PS
Percent Bound
120
100
80
60
40
20
0
-20
0.1
1
10
100
1000
[Ligand] μM

Figure 5.2 RNase 1 binds liposomes containing phosphatidylserine and sulfatide

Liposomes constructed of phosphatidylcholine with either phosphatidylserine and/or sulfatide are added to 50 nM RNase 1–BODIPY. Binding was monitored by fluorescence polarization and normalized to protein alone and complete saturation.

Figure 5.3

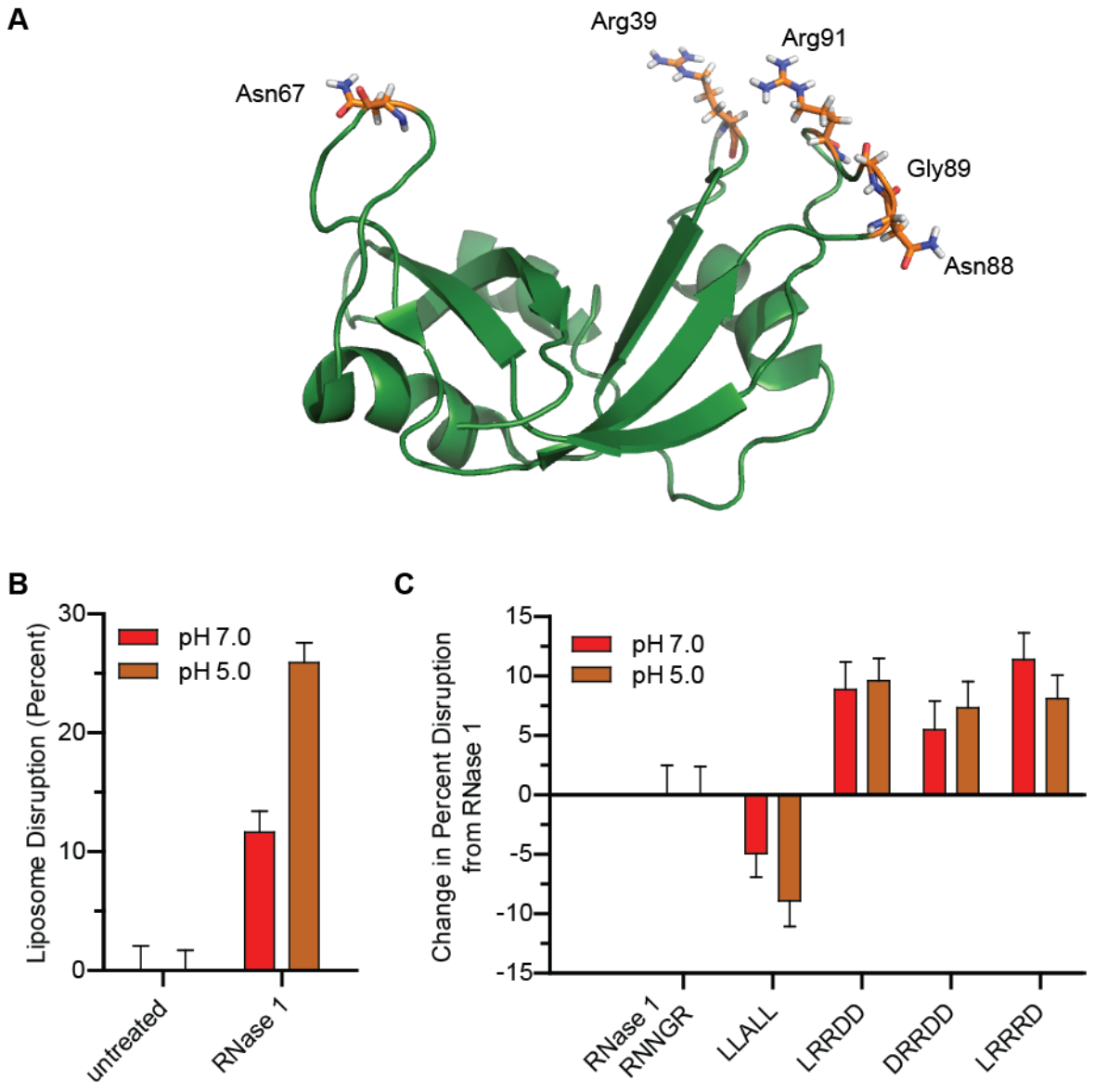
A
Arg39
Arg91
Asn67
Gly89
Asn88
B
Liposome Disruption (Percent)
30
20
10
0
pH 7.0
pH 5.0
untreated
RNase 1
C
Change in Percent Disruption from RNase 1
15
10
5
0
-5
-10
-15
pH 7.0
pH 5.0
RNase 1
RNNGR
LLALL
LRRDD
DRRDD
LRRRD

Figure 5.3 Liposomal disruption of RNase 1 and variants

A. Residues of RNase 1 that are involved in RI binding. *B*. RNase 1 disrupts liposomes constructed of an anionic lipid, phosphatidylserine (PS), at neural and acidic pH. *C*. Analysis of RNase 1 variants indicates that the importance of charged residues on the lobes for liposomal disruption as compared to wild-type RNase 1. Abbreviations indicate the residues inserted at positions 39, 67, 88, 89, and 91.

Figure 5.4

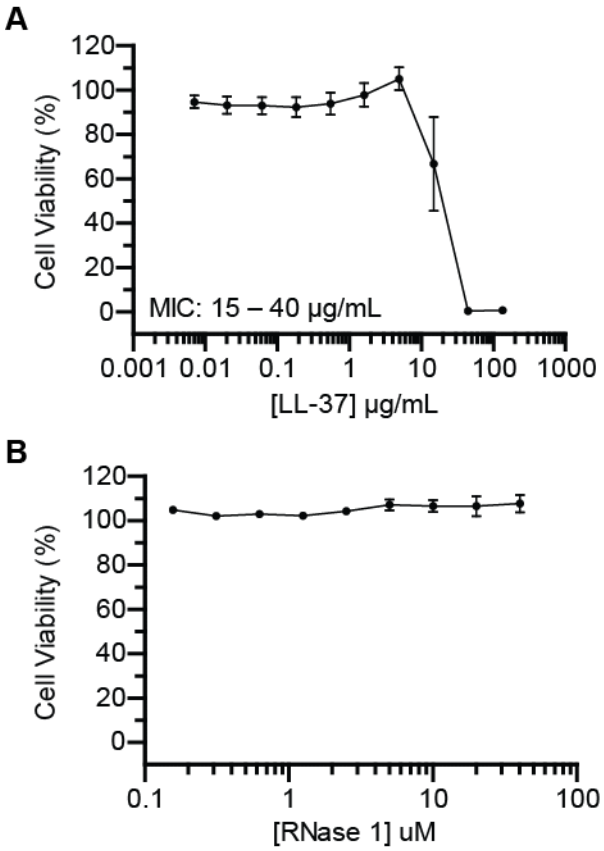
A
Cell Viability (%)
120
100
80
60
40
20
0
MIC: 15 – 40 µg/mL
0.001 0.01 0.1 1 10 100 1000
[LL-37] µg/mL
B
Cell Viability (%)
120
100
80
60
40
20
0
0.1 1 10 100
[RNase 1] uM

Figure 5.4 Antimicrobial activity of LL-37 and RNase 1 on *E. coli*

E. coli in LB medium were treated with increasing concentrations of *A.* LL-37 or *B.* RNase 1. Cells were incubated for 18 h at 37 °C while shaking. Cell viability was measured via absorbance at 600 nm and normalized using cells treated with PBS (100%) and chloramphenicol (0%).

Figure 5.5

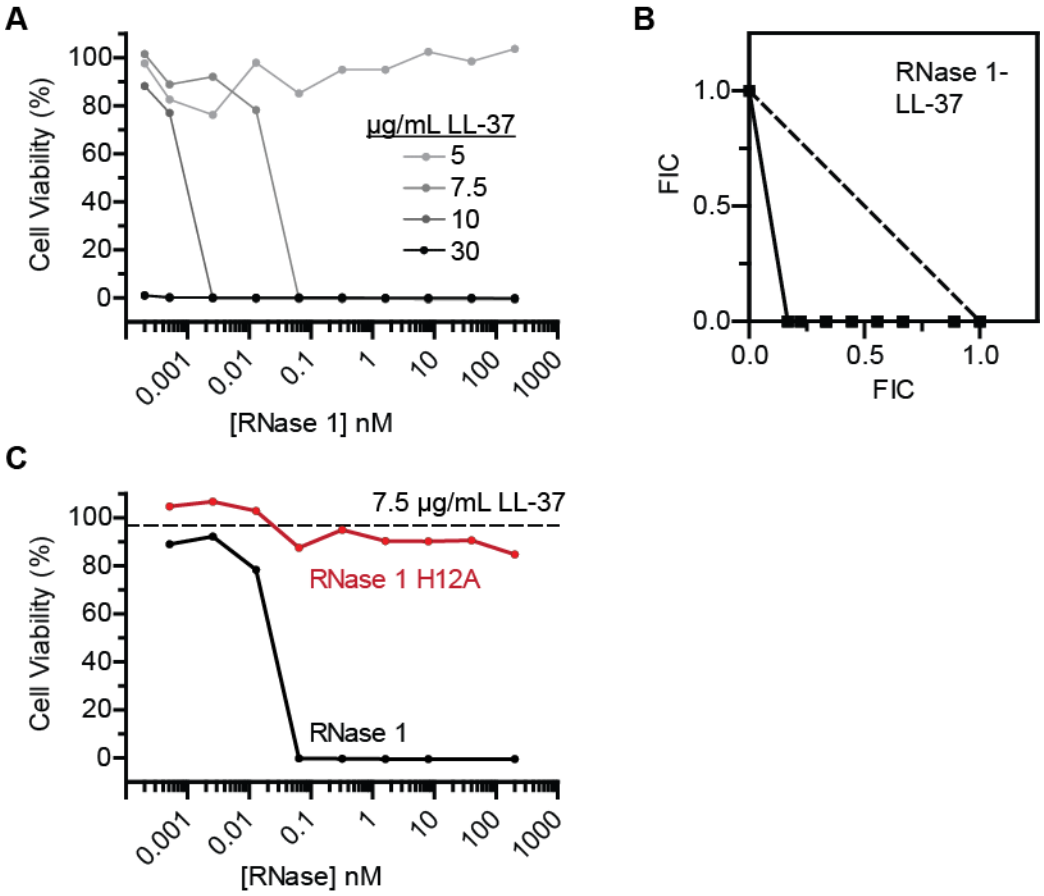
A
Cell Viability (%)
100
80
60
40
20
0
μg/mL LL-37
5
7.5
10
30
0.001
0.01
0.1
1
10
100
1000
[RNase 1] nM
B
RNase 1-
LL-37
FIC
1.0
0.5
0.0
0.0
0.5
1.0
FIC
C
7.5 μg/mL LL-37
RNase 1 H12A
RNase 1
Cell Viability (%)
100
80
60
40
20
0
0.001
0.01
0.1
1
10
100
1000
[RNase] nM

Figure 5.5 Synergistic effect of antimicrobial activity of LL-37 and RNase 1 on *E. coli*

A. E. coli were treated with concentrations of LL-37 (above and below the MIC, 20 μg/mL) with increasing amounts of RNase 1. *B.* Visualization of synergy as represented as an isobologram. The y-axis represents the FIC value (Eq 5.1) of RNase 1, and the x-axis represents the FIC value of LL-37. The dashed line indicates additive synergy, while a concave line is considered synergistic. *C.* RNase-mediated cytotoxicity is a result of ribonucleolytic activity. Bacteria exposed to LL-37 (7.5 μg/mL) were combined with increasing concentrations of RNase 1 or its active-site variant, H12A. Cell viability was measured via absorbance at 600 nm and normalized using cells treated with PBS (100%) and chloramphenicol (0%).

Figure 5.6

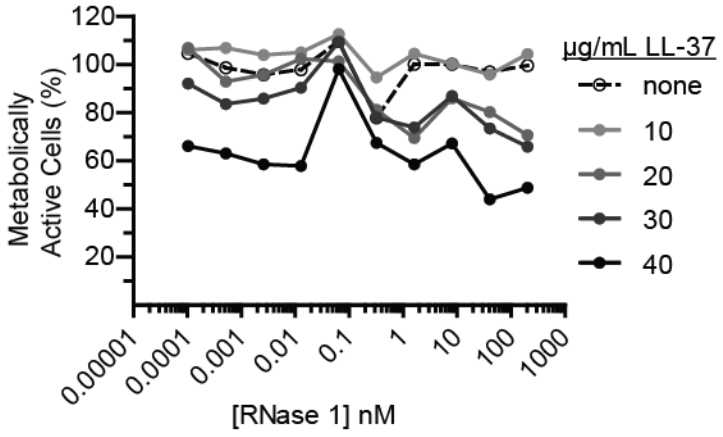
120
100
80
60
40
20
Metabolically
Active Cells (%)
0.00001
0.0001
0.001
0.01
0.1
1
10
100
1000
[RNase 1] nM
µg/mL LL-37
none
10
20
30
40

Figure 5.6 No synergy observed with LL-37 and RNase 1 on human cell line

RNase 1 was added to HeLa cells in increasing concentrations and treated with various amounts of LL-37 (indicated by color) for 24 h. Metabolically active cells were measured via a cell-titer assay and normalized using PBS vehicle control (100%) and H_2O_2 (0%).

Figure 5.7

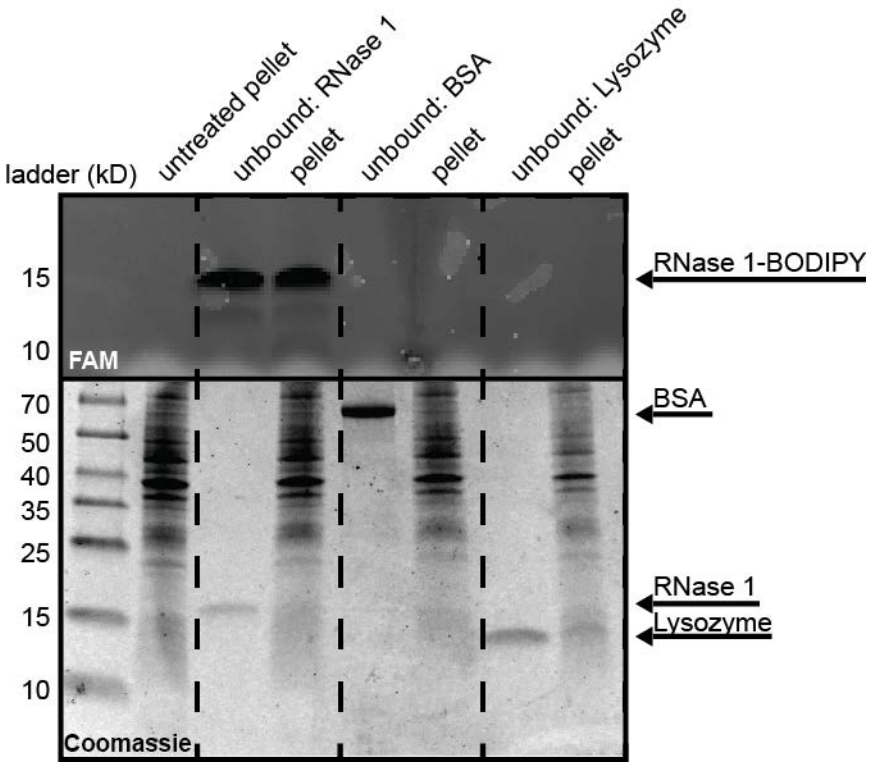
ladder (kD)
untreated pellet
unbound: RNase 1
pellet
unbound: BSA
pellet
unbound: Lysozyme
pellet
15
10
FAM
70
50
40
35
25
15
10
Coomassie
RNase 1-BODIPY
BSA
RNase 1
Lysozyme

Figure 5.7 RNase 1 associates with bacterial cells

RNase 1–BODIPY (1 μM), BSA (4 μM), or lysozyme (4 μM) was incubated with *E. coli* for 30 min at 37 °C. Unbound supernatant and bound pellet were subjected to SDS–PAGE. RNase 1–BODIPY (14.7 kD) was visualized by scanning fluorescence at 488 nm, (top panel), and total protein subsequently stained using Coomassie (bottom panel). BSA (66.5 kD) serves as a negative control, as it does not interact with the bacteria. Lysozyme (14.4 kD), as a positive control, binds to bacterial membranes and is captured in the cell pellet.

Figure 5.8

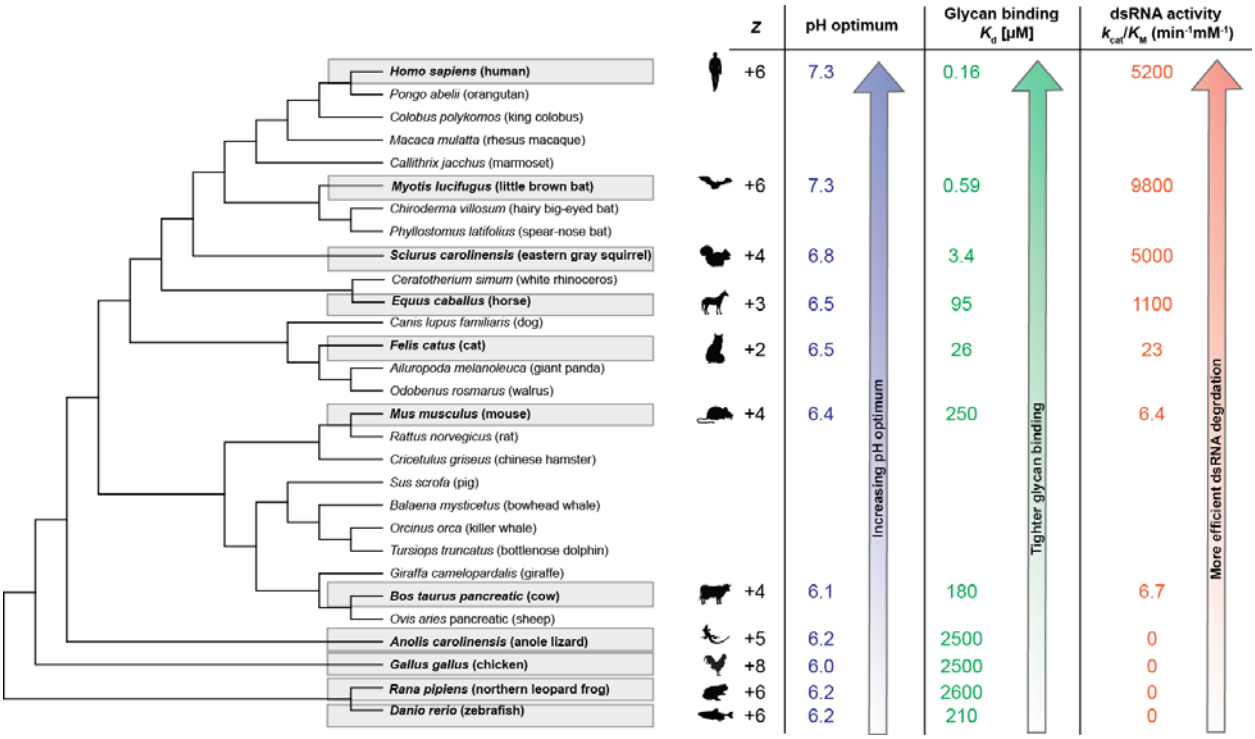
z
pH optimum
Glycan binding K_d [μM]
dsRNA activity k_{cat}/K_M (min⁻¹mM⁻¹)
Homo sapiens (human) +6 7.3 0.16 5200
Pongo abelii (orangutan)
Colobus polykomos (king colobus)
Macaca mulatta (rhesus macaque)
Callithrix jacchus (marmoset)
Myotis lucifugus (little brown bat) +6 7.3 0.59 9800
Chiroderma villosum (hairy big-eyed bat)
Phyllostomus latifolius (spear-nose bat)
Sciurus carolinensis (eastern gray squirrel) +4 6.8 3.4 5000
Ceratotherium simum (white rhinoceros)
Equus caballus (horse) +3 6.5 95 1100
Canis lupus familiaris (dog)
Felis catus (cat) +2 6.5 26 23
Ailuropoda melanoleuca (giant panda)
Odobenus rosmarus (walrus)
Mus musculus (mouse) +4 6.4 250 6.4
Rattus norvegicus (rat)
Cricetulus griseus (chinese hamster)
Sus scrofa (pig)
Balaena mysticetus (bowhead whale)
Orcinus orca (killer whale)
Tursiops truncatus (bottlenose dolphin)
Giraffa camelopardalis (giraffe)
Bos taurus pancreatic (cow) +4 6.1 180 6.7
Ovis aries pancreatic (sheep)
Anolis carolinensis (anole lizard) +5 6.2 2500 0
Gallus gallus (chicken) +8 6.0 2500 0
Rana pipiens (northern leopard frog) +6 6.2 2600 0
Danio rerio (zebrafish) +6 6.2 210 0
Increasing pH optimum
Tighter glycan binding
More efficient dsRNA degrdation

Figure 5.8 Evolutionary tree of the RNASE1 gene family and evolving biochemical properties Protein sequence alignments were made using MUSCLE [132] with manual adjustments. Boxes indicate the species of RNases that were biochemically purified and studied. Analysis is summarized in arrow bars indicating a shift in pH optimum, tighter glycan binding, and higher dsRNA activity in mammals.

Appendix 1

Assignments of RNase A by ADAPT-NMR and Enhancer

Contribution:

I purified and labeled RNase A for NMR, assisted in data analysis, and prepared portions of the manuscript.

This chapter was prepared for publication as:
Tonelli, M., **Eller, C.H.**, Bahrami, A., Singarapu, K.K., Westler, W.M., Raines, R.T., Markley, J.L. Assignments of RNase A by ADAPT-NMR and Enhancer. *Biomolecular NMR Assignments* (2014) In Press.

Abstract

We report here backbone ^{1}H and ^{15}N assignments for RNase A obtained by using ADAPT-NMR, a fully-automated approach for combined data collection, spectral analysis and resonance assignment. ADAPT-NMR was able to assign 98% of the resonances with 93% agreement with traditional data collection and assignment. Further refinement of the automated results with ADAPT-NMR Enhancer led to complete (100%) assignments with 96% agreement with assignments by the traditional approach.

A1.1 Introduction

Bovine pancreatic ribonuclease (RNase A) is a 124-residue protein that has served as a model for much landmark work on protein structure and function. RNase A is the third enzyme whose structure was determined by x-ray crystallography and is now the subject of more than 30 PDB entries. In addition, RNase A played a crucial role in the early development of NMR spectroscopy, leading to the determination of its solution structure. (for a review, see: [28]) RNase A catalyzes the cleavage of the P–O$^{5'}$ bond of RNA with a k_{cat}/K_M value that can exceed 10^9 $M^{-1}s^{-1}$ and exhibits high thermostability (T_m 62 °C). (For a review, see: [126]) The presumed biological function of RNase A is catalysis of the depolymerization of ingested RNA. Yet, high levels of RNase A and its human homologue (RNase 1) in many different tissues are consistent with additional roles.[16,249]

Recently, homologs and variants of RNase A have shown potential as cancer chemotherapeutic agents. [126] Enabling RNase A to achieve its clinical potential is likely to require a thorough understanding of its interactions with cellular molecules, including cell-surface glycans and the cytosolic ribonuclease inhibitor protein. Structural and dynamic aspects of these interactions can be probed by NMR spectroscopy. While characterizing these interactions, we found that our ^{1}H–^{15}N backbone assignments did not match with those reported previously.[250] In particular, assignments to several amide peaks in flexible loop regions varied, despite the use of identical buffer conditions. We used the ADAPT–NMR method [251,252] to assign the backbone amide resonances. Then, we confirmed these assignments by a more traditional manual approach. The ensuing information adds to the history of RNase A and provides the basis for further analyses.

A1.2 Materials and methods

A1.2.1 Production of [^{13}C,^{15}N]RNase A

[^{13}C,^{15}N]-RNase A was produced by heterologous expression in *Escherichia coli* strain BL21(DE3) as described previously,[40] with the exception of a double growth protocol in minimal medium. Induction medium contained 0.13% w/v [^{15}N]-NH_4Cl and 0.4% w/v [U-^{13}C6]-D-glucose (Cambridge Isotope Laboratories, Andover, MA) for isotope incorporation upon addition of IPTG (Sigma–Aldrich, St. Louis, MO) to 0.5 mM. Protein purification was monitored with SDS–PAGE. The mass of the final purified product was determined with matrix-assisted laser desorption/ionization (MALDI) mass spectroscopy at the University of Wisconsin Biotechnology Center. RNase A has the molecular formula $C_{575}H_{901}N_{171}O_{193}S_{12}$ and a molecular mass of 13,682 Da. The observed mass of 14,317 Da indicated a level of isotope incorporation of (14,317 – 13,682)/(575 + 171) = 85%.

To confirm that protein function was not compromised upon labeling, RNase A was assayed for ribonucleolytic activity by using a fluorogenic substrate, 6-FAM–dArUdGdA–6-TAMRA (Integrated DNA Technologies, Coralville, IA).[126] Upon cleavage of this substrate at ambient temperature, excitation at 492 nm elicits fluorescence at 515 nm. Assays were performed in oligo(vinylsulfonic acid)-free 0.10 M MES–NaOH buffer, pH 6.0 containing NaCl (0.10 M). The catalytic activity of the labeled RNase A [k_{cat}/K_M = (14.5 ± 3.5) $\mu M^{-1}s^{-1}$] was indistinguishable from that of unlabeled RNase A [k_{cat}/K_M = (21.6 ± 7.9) $\mu M^{-1}s^{-1}$].

A1.2.2 Preparation of NMR samples

For chemical shift assignments, freshly prepared RNase A was dialyzed into water, lyophilized, and dissolved in 100 mM potassium phosphate buffer, pH 4.7, containing 10% D_2O

(Sigma–Aldrich) to a final protein concentration of 1.7 mM. Another sample of RNase A dissolved in 90:10 H_2O:D_2O at pH 4.7 to reproduce conditions from previously determined assignments.[250] This sample was used to carry out a titration experiment with potassium phosphate also at pH 4.7. Samples used for NMR spectroscopy were enclosed in 5-mm susceptibility-matched Shigemi NMR tubes (Shigemi, Allison Park, PA).

A1.2.3 NMR data collection

All NMR spectra were acquired on Varian VNMRS spectrometers (Agilent Technologies, Santa Clara, CA) equipped with cryogenic triple-resonance probes. Two types of data collection and analysis were performed: traditional and fully automated using ADAPT-NMR.[251] For the traditional assignment approach, 2D ^{1}H,^{15}N-HSQC, 3D HNCACB and 3D NOESY ^{15}N-HSQC spectra were collected at 900 MHz (^{1}H) with the temperature of the sample regulated at 293 K (Table A1.1). Peak lists generated from 2D ^{1}H,^{15}N-HSQC and 3D HNCACB spectra were fed to the PINE server,[253] and the assignments obtained were further refined by hand by reference to a 3D ^{15}N-resolved ^{1}H-^{1}H NOESY spectrum viewed with Sparky.[254]

For fully automated backbone assignments with ADAPT-NMR, in addition to a 2D ^{1}H-^{15}N HSQC spectrum, six 3D spectra were collected as 2D planes: HNCO, HN(CA)CO, HN(CO)CA, HNCA, CBCA(CO)NH and HN(CA)CB. All spectra were collected at 600 MHz (^{1}H) at 308 K (Table A1.2). The pulse programs for these experiments were taken from BioPack (Varian/Agilent) and adapted for reduced dimensionality data collection as previously described.[251] All orthogonal and tilted planes were processed automatically by ADAPT-NMR with NMRpipe software.[255] The fully automated assignments were visualized, validated and further refined by using the ADAPT-NMR Enhancer package.[252] To reconcile assignments from

the manual and ADAPT-NMR approaches, a series of 2D $^{1}H,^{15}N$-HSQC spectra were collected at temperatures ranging from 293 K to 308 K at 2.5 K intervals (Table A1.3). An in-house written macro was used to collect these experiments in an automated fashion.

Finally, potassium phosphate was titrated into a solution of 0.25 mM ^{15}N-labeled RNase A dissolved in 90:10 H_2O:D_2O at pH 4.7, and 2D ^{1}H-^{15}N HSQC spectra were collected after each addition. These spectra were acquired on a Varian VNMRS spectrometer operating at 800 MHz (^{1}H) equipped with a conventional triple-resonance, triple-axis gradient probe (Table A1.4) with the temperature of the sample regulated at 293 K. Including the starting point, a total of 9 spectra were acquired at increasing phosphate concentrations: 0, 0.250, 0.750, 1.25, 2.50, 6.25, 11.3, 21.3 and 40.0 mM, corresponding to phosphate:RNase A molar ratios of 0:1, 1:1, 3:1, 5:1, 10:1, 25:1, 45:1, 85:1 and 160:1, respectively. All 2D spectra were processed by NMRPipe and analyzed with Sparky.

A1.3 Results and discussion

A1.3.1 NMR backbone assignments: ADAPT-NMR versus traditional

In our aim to study the interaction of potential cancer chemotherapeutic agents to cell-surface moieties by NMR, we prepared an ^{15}N-labeled sample of RNase A and planned to use the assignments deposited in BMRB (BMRB ID 4031) to identify the peaks in the 2D $^{1}H,^{15}N$-HSQC spectra. However, even though we adjusted the sample conditions to match those reported in BMRB (H_2O, pH 4.6 293 K), the deposited assignments did not agree with the peaks in our spectra. Thus, we prepared a doubly labeled ($^{15}N,^{13}C$) sample and assigned the protein backbone signals by using ADAPT-NMR, the fully automated approach for data collection, processing and analysis developed in our laboratory. The ADAPT-NMR approach made use of six 3D

experiments collected as 2D tilted planes: HNCO, HN(CA)CO, HN(CO)CA, HNCA, CBCA(CO)NH and HN(CA)CB. The tilted angles and experiments selected on-the-fly by ADAPT-NMR for data collection and other experimental details are provided in Table A1.2. Of these experiments, HN(CA)CB is the least sensitive and the most complicated spectrum to analyze, and, not surprisingly, it is also the one that took the longest time to collect. Thus, whereas data collection for the first five 3D experiments in the list took 32 hours, the HN(CA)CB experiment alone required 17 tilted planes and an additional 48 hours to collect. In the end, without any intervention by the user, ADAPT-NMR succeeded in assigning 117 of the 119 assignable residues (124 total residues minus the N-terminal residue and 4 prolines) for an assignment completion of 98% (only V63 and K66 were not assigned by ADAPT-NMR). Of these 117 residues, 113 were assigned with a probability score of above 80%.

Subsequently, in order to gather better and more complete assignments, the results of ADAPT-NMR were visualized and validated by using the ADAPT-NMR Enhancer package.[252] Using this package following the procedure described in the supplementary material, we generated new and improved peak lists and reran ADAPT-NMR. The program automatically detected the user-modified peak lists, and tried to find better assignments without collecting any additional NMR spectra. In the end, all 119 possible amino acids were identified by ADAPT-NMR, and the assignments for 8 residues, E2, S16–S18, S22–S23, G112-N113, were changed relative to those obtained by the automated approach prior to refinement with Enhancer (Table A1.5).

As a means of verifying the assignments made by ADAPT-NMR, we submitted peak lists generated with Sparky from 2D ^{1}H-^{15}N HSQC and 3D HNCACB spectra to the PINE server,[253] and refined the resulting assignments by hand with reference to the ^{15}N-resolved ^{1}H-^{1}H NOESY

3D spectrum as displayed by Sparky.[254] Using this approach, we were able to assign signals to 112 residues (out of 119 assignable residues – 94% completion). The remaining residues could not be identified because of ambiguities that we could not resolve using the spectra at our disposal.

To reconcile the automated assignments by ADAPT-NMR carried out at 308 K with the traditional assignments from 3D spectra collected at 293 K, we collected a series of 2D ^{1}H-^{15}N HSQC spectra at 2.5 degrees intervals between 293 K and 208 K. For residues identified by both methods, this analysis yielded 93% agreement between the assignments made by ADAPT-NMR and those from our limited traditional approach (102 out of the 110 commonly assigned residues). The agreement with the manual assignments increased to 96% (107 out of 112 common assignments) after the Enhancer package was used to refine the ADAPT-NMR results. In the end, only the ADAPT-NMR assignments for A19, S22, C84, G112 and N113 were inconsistent with those from the manual method. The Enhancer treatment left those for A19 and C84 unchanged and reconciled the assignments for S16–S18 and S23 with the manual ones, but its change in the assignment for S22 continued to be different from the manual assignment. Careful inspection of the peak connectivities for A19 and C84 suggested that the assignments found for these residues by ADAPT-NMR are more likely correct than the manual ones. In particular, C84 follows a string of residues that were not identified by the traditional method, thus rendering its assignment by ADAPT-NMR more reliable. On the other hand, the assignment for S22 was changed to a peak located within the ADAPT-NMR chemical shift tolerance of the peak assigned by the manual approach. Finally, the Enhancer treatment also altered the ADAPT-NMR assignments for residues G112 and N113 that initially agreed with the manual ones. It is

likely that the expanded peak lists generated after using the Enhancer package provided ADAPT-NMR with more probable assignments for these residues.

In any case, ADAPT-NMR was able to assign signals to 7 more residues (I81-D83, Q101-A102, H119-F120) than the manual approach (Table A1.5). The temperature titration spectra with both ADAPT-NMR and traditional assignments are shown in Figure A1.1. We have deposited the assignments made by ADAPT-NMR/Enhancer and by the traditional approach along with the assigned ^{1}H-^{15}N peak lists determined as a function of temperature (BMRB ID number 19065).

A1.3.2 Effect of phosphate on RNase A

To investigate the effect of phosphate on RNase A, we added increasing amounts of potassium phosphate to a solution of RNase A at 293 K and pH=4.7. At each titration point, we collected a 2D ^{1}H-^{15}N HSQC spectrum and used these spectra, along with the our ADAPT-NMR assignments obtained at 308 K in the presence of phosphate buffer and extrapolated to the same temperature by means of the temperature titration data, to extract the assignments for RNase A in the absence of phosphate. We observed that, whereas most peaks shifted upon the addition of phosphate, some shifted much more than others. As shown in Figure A1.2, peaks from residues V43, S80, C84, R85, E86, H119 and D121 showed the largest chemical shift changes upon the addition of phosphate, followed by Q11, N44, T45, K66, T87, T100 and A122. The majority of these peaks are in discrete regions of the protein, located near residues that are known to bind phosphate (Q11, H12, K41, H119, F120) or nucleotide phosphate (K7, R10, K66, R85).[256] These residues are in general agreement with residues perturbed by sodium phosphate buffer.[257] Furthermore, with the addition of phosphate, ^{1}H-^{15}N HSQC cross peaks generally sharpened, in

particular those that exhibited the largest chemical shift perturbations. Peaks from residues E2, S21, N27, F46–H48, I81–D83, Q101-A102 and F120 were too broad to be observed in the absence of phosphate. This broadening suggests the presence of conformational dynamic processes on the intermediate NMR time scale that are reduced upon binding of phosphate. The assigned backbone ^{1}H and ^{15}N chemical shifts for RNase A extrapolated to zero phosphate have been deposited at BMRB along with assigned peak lists at each phosphorus concentration (ID 19065). Our assignments at the end of the titration (40 mM phosphate) were still slightly different from those we obtained with the sample dissolved in 100 mM phosphate buffer (average $\Delta\Delta\delta$ of 0.0227 ± 0.0119 ppm).

A1.3.3 Comparison with assignments deposited in BMRB

The previous assignments for RNase A[250] were determined with a protein sample in the absence of phosphate. Thus, it is not surprising that our assignments for RNase A in the presence of 100 mM phosphate differed, particularly for residues known to bind phosphate (V43–T45 and C84–T87) (Figure A1.3A). Still, to our surprise, we found that many of our assignments in the absence of phosphate also did not match the deposited ones, although the discrepancies were fewer (Figure A1.3B). The origin of these differences is unclear. Because previous reports had suggested that deamidation of Asn and Gln side chains at multiple sites could be a possible source of variability in RNase A,[258,259] we inspected the 2D ^{1}H-^{15}N HSQC peaks from the side-chain NH_2 groups of Asn and Gln. We found the correct number of peaks for RNase A, suggesting that deamidation had not taken place in our sample. Deamidation of the previous sample seems unlikely, as N67, the more predominant site of modification,[259] or neighboring residues 66–69 were not major sites of discrepancy. Still, changes between assignments were

observed at N113 and neighboring residue, G112. The sample preparation from Shimotakahara exposed RNase A to disodium 2-nitro-5-(sulfothio)benzoate, and subsequent refolding occurred in a buffer of pH 8.2.[260] Current methods of RNase A purification do not subject the protein to such harsh and basic conditions. It is possible, for example, that the oxidizing agent intended for cysteine residues resulted in covalent modification of the side chains of serines, threonines, or lysines. Indeed, sites of changes that were observed in both the ADAPT-NMR and manually assigned assignments to BMRB 4031 were residues positioned within serine-rich loop region S15–S23 and S80. The previously referenced method also measured catalytic activity using an insensitive assay that might not have detected damage to the enzyme.

In conclusion, fully automated ADAPT-NMR achieved an assignment level of 98% for RNase A in the presence of 100 mM phosphate buffer; the assignments were refined and brought to a level of 100% by use of the ADAPT-NMR Enhancer package. These levels of assignment were greater than that achieved by a more traditional approach, albeit with a more limited set of data. As described previously,[250] spectra of RNase A contain signals from minor conformational states. It appears that these additional peaks, which can be linked together in data from triple-resonance backbone experiments, misled somewhat the automated assignments carried out by ADAPT-NMR. These errors could be rectified by use of the Enhancer package to achieve complete assignments.

Acknowledgments

This study was supported by NIH grant R01 CA073808 (NCI) and made use of the National Magnetic Resonance Facility at Madison, with support from NIH grants P41 RR02301 (BRTP/ NCRR) and P41 GM66326 (BRTP / NIGMS). Additional equipment was purchased with funds

from the University of Wisconsin, the NIH (RR02781, RR08438), the NSF (DMB-8415048, OIA-9977486, BIR-9214394), and the USDA.

Table A1.1 Experimental details for all 2D spectra collected by ADAPT-NMR

Experiment	Tilt Angles of Collected Planes	Spectral Window (KHz) $^{1}H \times ^{13}C \times ^{15}N$	# Scans	Complex Points	Time / tilted plane	Time / 0° plane
HNCO	25, 60, 69	10×2.2×2.2	4	1024×96	32 min	16 min
HN(CA)CO	28, 34, 41, 53, 69	10×2.2×2.2	16	1024×96	2 h 6 min	1 h 3 min
HN(CO)CA	28, 40, 64	10×4.8×2.2	8	1024×96	1 h 3 min	32 min
HNCA	26, 40, 51, 58, 56	10×4.8×2.2	8	1024×96	1 h 2 min	31 min
CBCA(CO)NH	25, 32, 43, 50, 57	10×11.2×2.2	16	1024×55	1 h 10 min	33 min
HN(CA)CB	12, 14, 15, 17, 18, 19, 22, 26, 29, 31, 32, 34, 37, 38, 47, 58, 66	10×11.2×2.2	16	1024×128	2 h 47min	1 h 24 min

All spectra were collected at 600 MHz with a cryogenic probe at 308 °K. A 2D ^{1}H-^{15}N HSQC spectrum was used as the 90° tilted plane in each experiment.

Table A1.2 Experimental details for 3D spectra collected for conventional assignments

Experiment	**Spectral Window (KHz)** $^{1}H\times^{13}C(^{1}H^{*})\times^{15}N$	**# Scans**	**Complex Points**	**Time**
HNCACB	14.5×18.1×2.7	4	1024×96×48	23 h 5 min
^{1}H-^{1}H NOESY ^{15}N-HSQC	14.5×12*×2.7	8	1024×96×48	49 h 4 min

All spectra were collected with a cryogenic probe at 900 MHz (^{1}H) at a temperature of 293 K

Table A1.3 Experimental details for 2D spectra acquired as a function of temperature at 600 MHz with a cryogenic probe

Experiment	**Temperature (K)**	**Spectral Window (KHz) $^{1}H\times^{15}N$**	**# Scans**	**Complex points**	**Time**
^{1}H-^{15}N HSQC	293,295.5,298, 300.5,303,305.5,308	10×2.2	8	1024× 256	1h 29min

Table A1.4 Experimental details for 2D spectra collected at 800 MHz with a conventional probe as a function of added potassium phosphate

Experiment	**Potassium Phosphate Concentration (mM)**	**Spectral Window (kHz) $^{1}H \times ^{15}N$**	**# Scans**	**Complex Points**	**Time / spectrum**
^{1}H-^{15}N HSQC	0, 0.25, 0.75, 1.25, 2.5, 3.75, 6.75, 11.25, 21.25, 40	13×2.8	8	512×256	1 h 20 min

Table A1.5 Comparison between manual assignments and automated assignments made by ADAPT-NMR before and after use of the ADAPT-NMR enhancer package

	Manual Assignments	**ADAPT-NMR Assignments**	**ADAPT-NMR Enhancer Assignments**
Manual Assignments	94% (I81-D83, Q101-Q102, H119-F120)	E2, S16-A19, S23-S23, C84	A19, S22, C84, G112, N113
ADAPT-NMR Assignments	93%	98% (V63, K66)	E2 S16-S18, S23-S23 G112, N113
ADAPT-NMR Enhancer Assignments	96%	93%	100%

The diagonal cells (dark shading) show the percent assigned residues achieved by each of the three methods, along with a list (in parentheses) of the residues that were not assigned. The top/right portion of the table (no shading) lists the residues whose assignments differed between the methods at each intersection. The bottom/left portion (light shading) reports the percent agreement between the methods at each intersection.

Figure A1.1

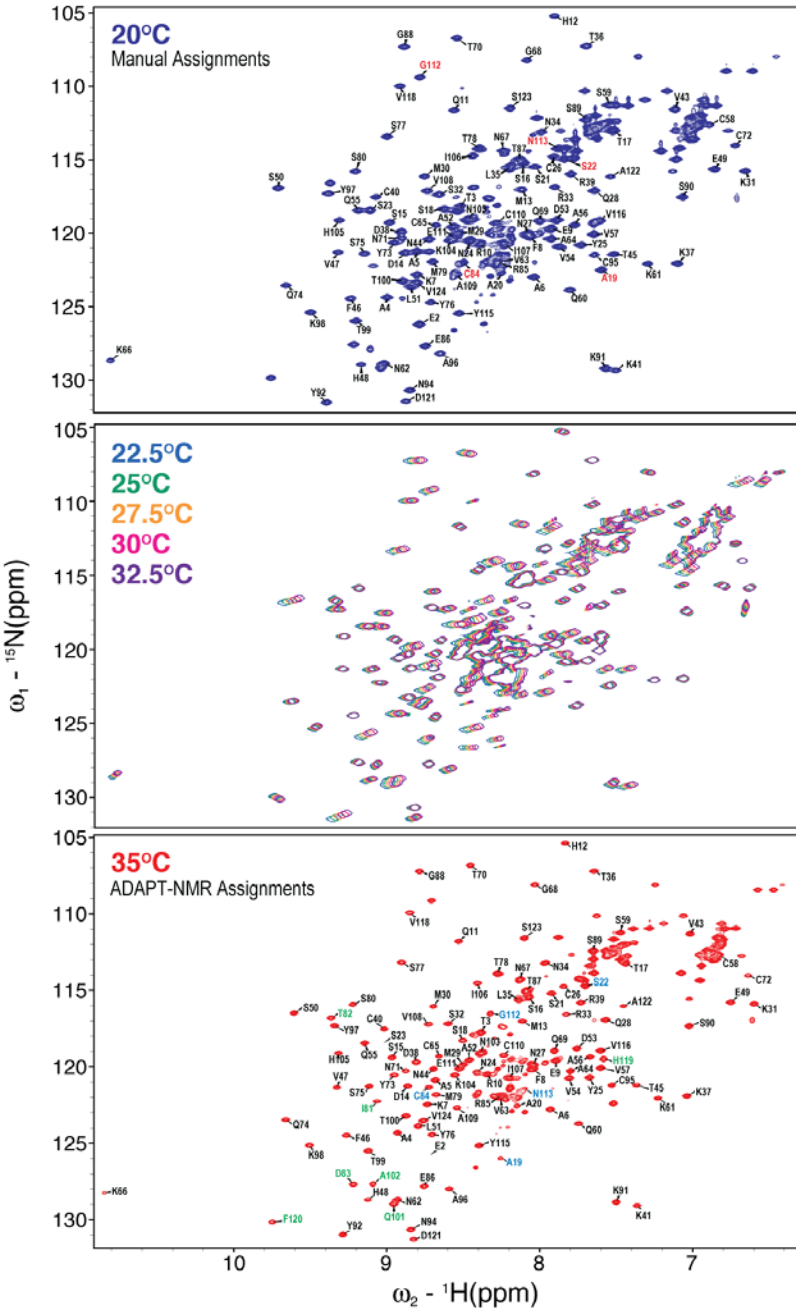
20°C
Manual Assignments
22.5°C
25°C
27.5°C
30°C
32.5°C
35°C
ADAPT-NMR Assignments
ω1 - 15N(ppm)
ω2 - 1H(ppm)

Figure A1.1 Temperature dependence of 2D ^{1}H-^{15}N HSQC spectra of RNase A

The spectrum recorded at 293 K is shown in the top panel. Peaks are labeled with the backbone assignments obtained by the traditional approach (residues whose assignment is different from the automated approach are labeled in red). Bottom panel shows the spectrum recorded at 308 K with Enhancer-refined ADAPT-NMR assignments (residues that were assigned by ADAPT-NMR but not the traditional approach are labeled in green; residues whose assignment is different from the traditional one are labeled in cyan). In the middle panel the 2D ^{1}H-^{15}N HSQC spectra recorded at temperatures ranging from 295.5 to 305.5 K are shown color-coded. As reported in Table A1.3, the spectra were collected on a Varian VNMRS spectrometer, operating at 600 MHz, equipped with a cryogenic *z*-axis gradient probe.

Figure A1.2

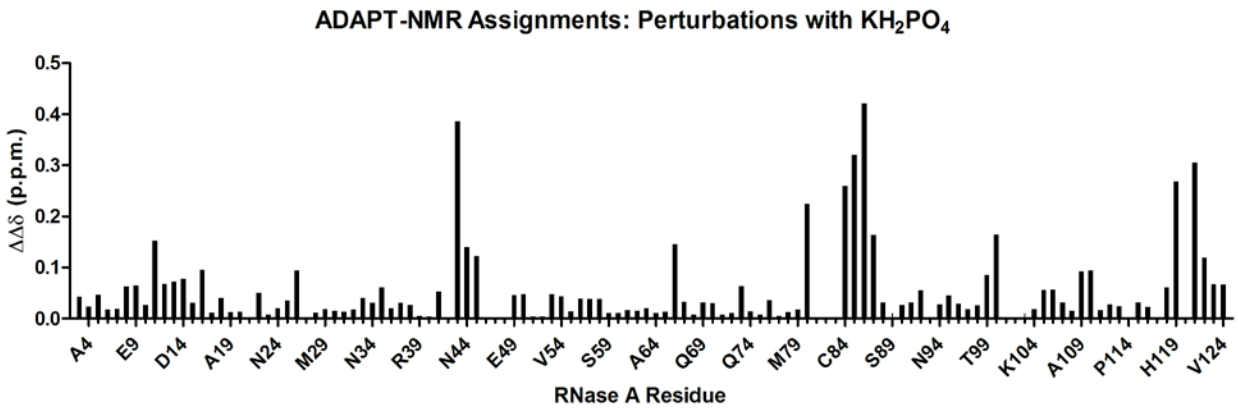
ADAPT-NMR Assignments: Perturbations with KH_2PO_4
ΔΔδ (p.p.m.)
0.5
0.4
0.3
0.2
0.1
0.0
A4
E9
D14
A19
N24
M29
N34
R39
N44
E49
V54
S59
A64
Q69
Q74
M79
C84
S89
N94
T99
K104
A109
P114
H119
V124
RNase A Residue

Figure A1.2 Effect of phosphate on the backbone ^{1}H-^{15}N chemical shifts of RNase A

Data were collected from RNase A samples at pH=4.7 in the absence of phosphate and in the presence of 40 mM potassium phosphate. 2D ^{1}H-^{15}N HSQC spectra were collected at 273 K on a Varian VNMR 800 MHz spectrometer equipped with a triple-axis gradient conventional probe. Differences in the backbone ^{1}H-^{15}N chemical shifts of RNase A in the absence of phosphate and in the presence of 40 mM potassium phosphate. Chemical shift differences ($\Delta\Delta\delta$) were calculated from the equation $(\Delta\Delta\delta) = ((\Delta\delta^{1}H)^{2} + 1/5(\Delta\delta^{15}N)^{2})^{1/2}$. Known nucleotide phosphate binding residues are K7, R10, K66, R85, while phosphate binding residues are Q11, H12, K41, H119, F120.

Figure A1.3

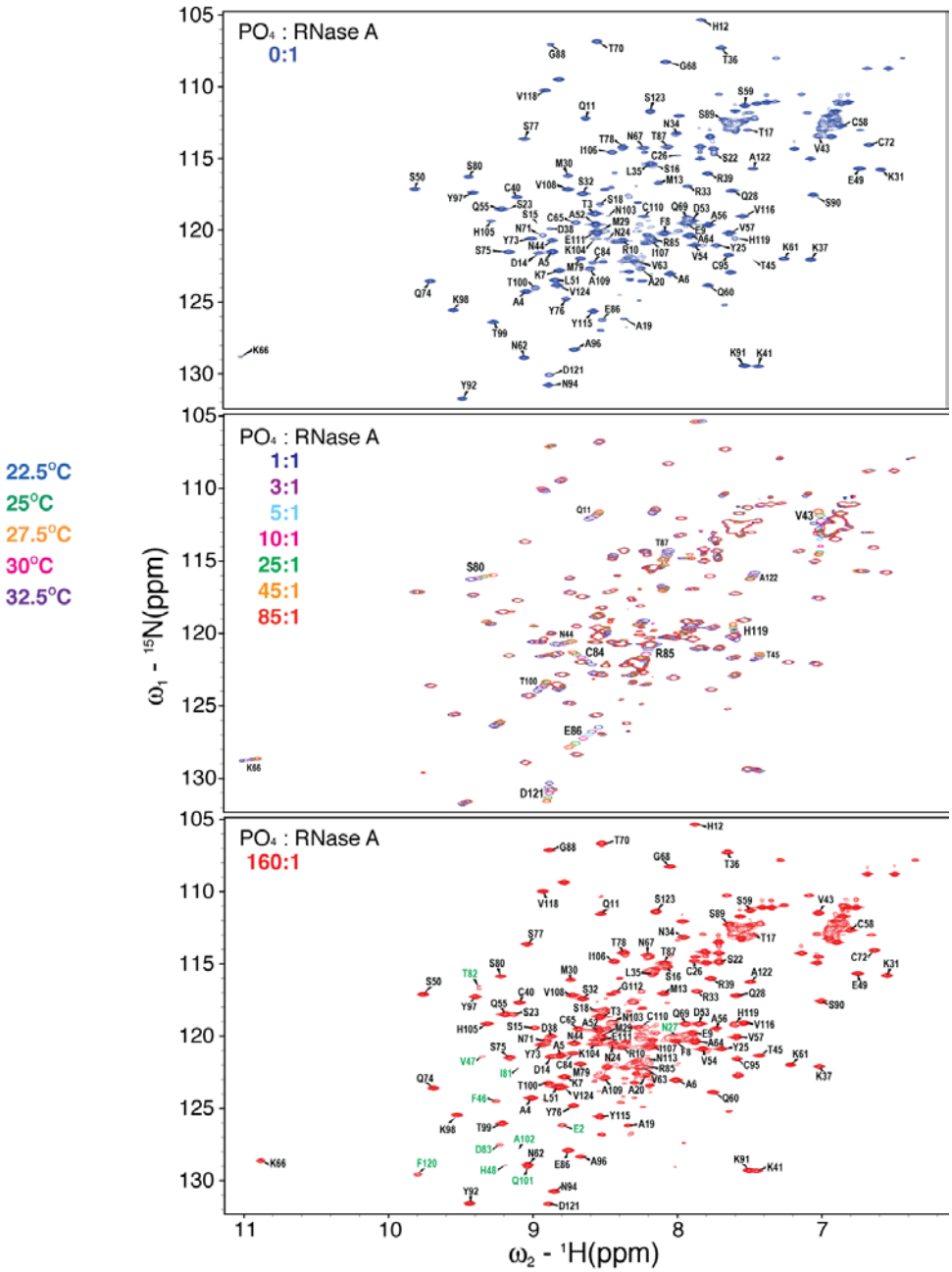
PO₄ : RNase A
0:1
PO₄ : RNase A
1:1
3:1
5:1
10:1
25:1
45:1
85:1
PO₄ : RNase A
160:1
22.5°C
25°C
27.5°C
30°C
32.5°C
ω₁ - ¹⁵N(ppm)
ω₂ - ¹H(ppm)

Figure A1.3 Phosphate titration spectra

The top panel shows a 2D ^{1}H-^{15}N HSQC spectrum recorded in the absence of phosphate. The bottom panel reports the spectrum recorded at the end of the phosphate titration. Peaks that were too broad to be visible in the absence of phosphate are labeled in green. The middle panel shows shown color-coded and overlapped spectra from the intermediate phosphate titration points. Residues that undergo the largest chemical shift changes upon the addition of phosphate are labeled (with a bigger font for those with the largest shifts).

Figure A1.4

A

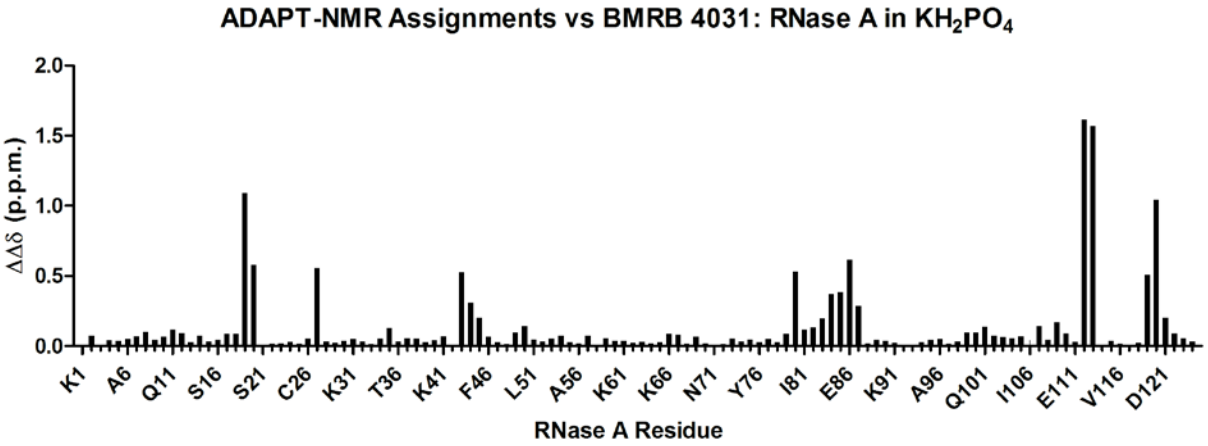

B

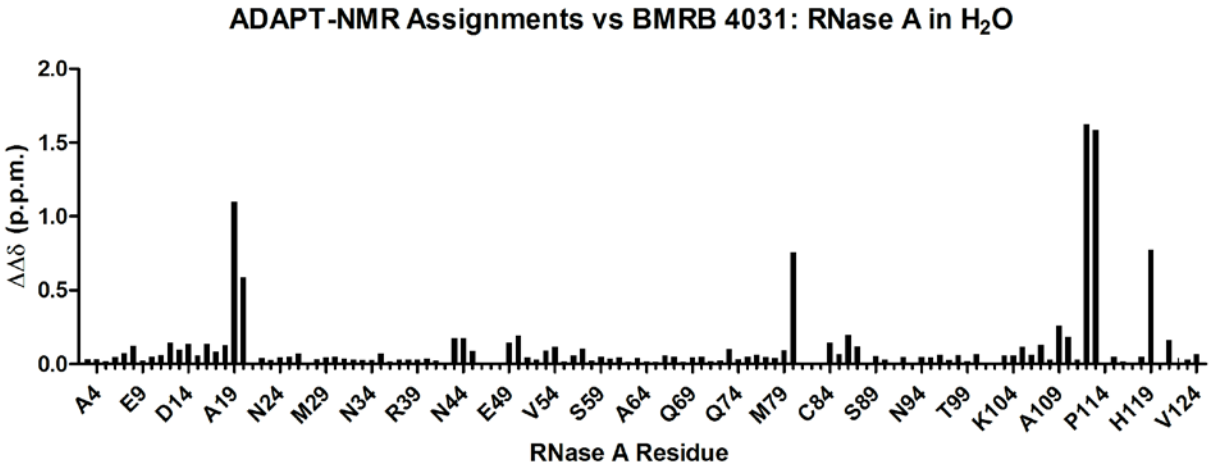

Figure A1.4 Comparison between RNase A assignments

A. Comparison between RNase A assignments by ADAPT-NMR in the presence of 40 mM phosphate (160:1 molar ratio to RNase A) and assignments deposited in BMRB (BMRB ID 4031). ***B*.** Comparison between RNase A assignments in the absence of phosphate and BMRB ID 4031 assignments. All chemical shift perturbations ($\Delta\Delta\delta$) were calculated from the equation $(\Delta\Delta\delta) = ((\Delta\delta^{1}H)^{2} + 1/5(\Delta\delta^{15}N)^{2})^{1/2}$.

Appendix 2

Rational Design and Evaluation of Mammalian Ribonuclease Cytotoxins

Contribution:
I assisted in the writing of this book chapter review.

This chapter was prepared for publication as:
Lomax, J.E., **Eller, C.H.**, and Raines, R.T. The Rational Design and Evaluation of Mammalian Ribonuclease Cytotoxins. *Methods in Enzymology* (2012) 502, 273 - 290.

Abstract

Mammalian pancreatic-type ribonucleases (ptRNases) comprise an enzyme family that is remarkably well suited for therapeutic exploitation. ptRNases are robust and prodigious catalysts of RNA cleavage that can naturally access the cytosol. Instilling cytotoxic activity requires endowing them with the ability to evade a cytosolic inhibitor protein (RI) while retaining other key attributes. These efforts have informed our understanding of ptRNase-based cytotoxins, as well as the action of protein-based drugs with cytosolic targets. Further, we have gained particular insight into the mechanisms governing the extremely tight interaction between ptRNases and RI. Here, we address the most pressing problems encountered in the design of cytotoxic ptRNases, along with potential solutions. In addition, we describe assays that can be used to evaluate a successful design *in vitro*, *in cellulo*, and *in vivo*. The emerging information validates the continuing development of ptRNases as chemotherapeutic agents.

A2.1 Introduction

Once, the utility of recombinant DNA technology in generating drugs was limited to producing wild-type human proteins in heterologous hosts. Now, protein engineering is being used to tailor proteins for specific clinical applications. The resulting biologic drugs can provide a level of target-specificity not achievable with small molecules.[261]

The mammalian pancreatic-type ribonucleases (ptRNases) are especially well suited for exploitation as chemotherapeutic agents. These enzymes circumvent the pitfalls that plague many other protein-based drugs, such as high molecular mass, instability, and immunogenicity. ptRNases comprise a highly conserved family of small (~13 kDa), secreted proteins that catalyze the degradation of RNA with extremely high efficiency.[28,262] Incredibly, mammalian cells internalize these enzymes readily (Figure A2.1); thus, ptRNases are not restricted to the extracellular or cell-surface targets of most other protein-based agents.[263] Moreover, whereas many promising proteins never achieve success in the clinic because they are hampered by problems with production, storage, and administration,[261] ptRNases are produced readily in microbial hosts, have unusually high conformational stability, and maintain their integrity in extracellular fluids and tissues.

Recently, ptRNases have garnered much attention because several, including the dimeric bovine seminal ribonuclease (BS-RNase) and an amphibian ortholog, Onconase (ONC), have proven to be natural cytotoxins for human cancer cells. ONC is currently in a Phase IIIb confirmatory clinical trial as a second-line chemotherapeutic agent for malignant mesothelioma and has been granted both orphan-drug and fast-track status by the U.S. Food and Drug Administration.[264,265] Despite their inherent cytotoxicity, both BS-RNase and ONC are of limited clinical utility. For example, ONC is compromised by dose-limiting renal toxicity and high

immunogenicity relative to mammalian ribonucleases.[266,267] Moreover, cytotoxic variants of mammalian ptRNases have greater specificity than ONC for cancer cells.[32] Efforts to exploit naturally occurring microbial and fungal ribotoxins have been plagued by similar immunogenicity and low specificity. (For reviews, see: [268,269]) Hence, the future of ptRNases as chemotherapeutic agents appears to rely on the strategic development of the mammalian homologues.[270]

Although mammalian ptRNases possess the necessary stability, catalytic activity, and non-immunogenicity to warrant consideration as potential chemotherapeutic agents, their success is limited by two substantial barriers: internalization into the cytosol of target cells and inhibition by the cytosolic ribonuclease inhibitor protein (RI), which binds with femtomolar affinity to most ptRNases but not BS-RNase or ONC (Figure A2.2).[271] To design ptRNase-based agents, we have sought to understand the underlying biophysical and biochemical basis for their mechanism of action, and then to translate that knowledge into optimized proteins.

A useful ptRNase-based cytotoxin must catalyze the degradation of RNA within target cells. To do so, it must gain entry to the cytosol, evade RI there, and retain its catalytic activity throughout the process. Here, we report on our current understanding of these requirements and our strategies for engineering ptRNases that achieve maximal therapeutic efficacy. We also provide details on the assays that we use to evaluate relevant attributes of putative ptRNase cytotoxins. Although we focus on the well-known enzymes from cow (RNase A) and human (RNase 1), the methodologies are applicable to other ptRNases as well.

A2.2 Attributes of cytotoxic ptRNases

A2.2.1 Catalytic activity and proteolytic stability

Two important attributes of a cytotoxic ptRNase are its ability to catalyze RNA cleavage and to resist proteolysis. Mammalian ptRNases can catalyze the cleavage of the P–$O^{5'}$ bond of RNA on the 3′ side of pyrimidine nucleosides with a second-order rate constant ($k_{cat}/K_M = 3.3 \times 10^9\ M^{-1}s^{-1}$)[272] that is among the highest known for an enzyme-catalyzed reaction. This activity leads to cellular apoptosis,[273] and is essential for ptRNase-mediated cytotoxicity.[274] Proteins with high thermostability tend to have low susceptibility to proteolytic degradation.[275] This premise holds true for ptRNases, as installing an additional disulfide bond in RNase A significantly increases its thermostability, resistance to proteolysis, and cytotoxicity.[276] Accordingly, when choosing residues to alter within ptRNases, care must be taken to avoid interference with active-site residues, cysteine residues that participate in disulfide bonds, and other residues critical to structure and function (Figure A2.3).[277] Although no consensus exists regarding the minimal requirements for either parameter, decreasing catalytic activity or thermostability leads to decreases in cytotoxicity.[66,276] Catalytic activity can be measured by using a fluorogenic substrate, such as 6-carboxyfluorescein–dArUdAdA–6-carboxytetramethylrhodamine;[127,278] thermostability can be monitored by ultraviolet or circular dichroism spectroscopy.

A2.2.2 Cellular internalization

ptRNases are especially well suited as biologic drugs due to their endogenous ability to enter cells without requiring any additional delivery strategy. Still, ptRNase internalization remains an inefficient process, and could limit cytotoxicity. To design a ptRNase-based drug that is equipped for more efficient internalization, it is important to understand the pathway by which ptRNases enter cells (Figure A2.1).

Mammalian ptRNases undergo endocytosis through an adsorptive process that is non-saturable, non-receptor-mediated, and dynamin-independent.[84] Certain anionic cell-surface molecules facilitate Coulombic interactions with cationic ptRNases, which are highly positively charged (Table A.1). Analyses *in vitro* and *in cellulo* reveal that RNase A interacts tightly with abundant anionic cell-surface glycosaminoglycans such as heparan sulfate and chondroitin sulfate, as well as sialic acid-containing glycoproteins. The uptake of RNase A correlates with cell-surface anionicity and could endow mammalian ptRNases with selective cytotoxicity for cancerous cells.[88] Following endocytosis, a very small fraction of the endosomal ptRNase is able to translocate into the cytosol and catalyze RNA degradation.

Specific modifications to a ptRNase can exploit the Coulombic interactions that likely facilitate RNase internalization. (For a review, see: [108]) Recent work has demonstrated that the amount of positive charge, as well as the distribution of that charge, can affect ptRNase adsorption.[91] For example, replacing two anionic surface residues, Glu49 and Asp53 (Figure A2.3), with arginines ("arginine grafting") results in enhanced internalization and cytotoxicity of an RNase A variant.[87] Similarly, chemical cationization of ptRNases by amidation of carboxyl groups with either ethylenediamine or polyethylenimine leads to enhanced internalization and cytotoxicity.[279] ptRNases can also be fused to cationic cell-penetrating peptides (CPPs) such as nonaarginine to increase internalization.[87,280] These cationic moieties need not be appended to ptRNases, as the addition of a cationic poly(aminoamine) dendrimer in trans increases the internalization and cytotoxicity of a ptRNase.[281] We note, however, that increasing the positive charge of a ptRNase can have the adverse effect of increasing its affinity for RI, which is highly anionic.[282]

A2.2.3 Evading the ribonuclease inhibitor protein

Ribonuclease inhibitor (RI) is a ~50-kDa protein found exclusively in the cytosol of mammalian cells. Multiple biological roles for RI have been proposed, including protecting cells from internalized secretory ptRNases and maintaining cellular redox homeostasis.[271,283] Despite the uncertainty surrounding its precise physiological role(s), RI binds to members of the mammalian ptRNase superfamily with a 1:1 stoichiometry, completely inhibiting their catalytic activity by steric occlusion of the enzymic active site (Figure A2.2). Because ribonucleolytic activity is necessary to induce cellular apoptosis, a cytotoxic ptRNase must evade RI. Nevertheless, as the noncovalent complexes formed between RI and its ligands are among the tightest known in biology, instilling RI-evasion is a difficult task.

The goal of RI-evasion strategies is to modify the ptRNase so as to perturb only its interaction with RI. Many strategies are possible. (For a review, see: [108]) Recent analyses of various crystallized RI·ptRNase complexes indicate that although the interaction of RI with various ptRNases is similar, evasion strategies should be optimized to recognize the subtle differences that exist in the binding interfaces. Computational analyses can be used to identify which residues of a ptRNase make the most contacts with RI.[32] These residues can then be targeted for substitution through site-directed mutagenesis. We have found that introducing electrostatic and steric incompatibilities in these regions destabilize the RI·RNase complex, and that disruption is often best achieved by replacing small neutral or anionic residues in a ptRNase with arginine (Figure A2.3). Arginine, as the most polar and second largest amino acid, can generate electrostatic repulsion and steric strain while increasing positive molecular charge, thereby enhancing internalization.

Our initial engineering efforts yielded a prototype ptRNase cytotoxin, G88R RNase A. The

modification of a single residue imbued native RNase A with 10 thousand-fold lower affinity for RI and cytotoxicity.[284] Guided by computational algorithms, we have designed second-generation variants of RNase A and RNase 1 that evade RI more efficiently. For example, D38R/R39D/N67R/G88R RNase A demonstrates 20 million-fold lower affinity for RI than does native RNase A with little change to catalytic activity or thermostability (Table A2.1). This variant is more toxic to human cancer cells than ONC.[32] In addition to mutating the RI-binding interface of RNase A, we find that appending a folate moiety to glycine 88 can engender RI-evasion through steric repulsion. The pendant folate molecule can additionally provide enhanced targeting and uptake to cells overexpressing the cell surface folate receptor, as is common with many types of cancer cells.[285] A similar phenomenon is observed by attaching a pendant poly(ethylene glycol) (PEG) moiety to RNase A at the same position. Beyond RI-evasion, an RNase A–PEG conjugate displayed markedly lower renal clearance and increased tumor growth inhibition in mouse models of human tumors.[77]

Human RNase 1 proved to be a greater challenge, as it binds to RI with 10^2-fold higher affinity than does RNase A. Although R39D/N67D/N88A/G89D/R91D RNase 1 has 6 billion-fold lower affinity for RI[89] than does wild-type RNase 1, this variant is not as cytotoxic as D38R/R39D/N67R/G88R RNase A. An alternative strategy to engender RI-evasion is to bypass RI contact altogether. The human ptRNase variant PE5 carries a non-contiguous nuclear localization signal and has been shown to possess potent cytotoxicity that is dependent upon its nuclear uptake.[286]

BS-RNase is a naturally dimeric homologue of RNase A that evades RI. But upon entry into the cytosol, the dimer dissociates and the resulting monomers are inhibited by RI.[123] Recently, the endogenous properties of BS-RNase have been recapitulated by creating genetically encoded

or chemically conjugated multimers of ptRNases that are unable to dissociate *in cellulo*.[75,287,288] Still, aspects of the mechanism of action of these multimers remain unclear. Multimeric ptRNases can be more cytotoxic than BS-RNase despite being less RI-evasive. Hence, the enhanced cytotoxicity demonstrated could be due, in part, to improved interaction of the multimers with the negatively charged cell membrane, thereby favoring endocytosis.[75,287,289] High cytosolic localization of tandem RNase A dimers supports this hypothesis.[288]

A2.3 Assays to evaluate the cytotoxicity of ptRNases

Just as effort has gone into the rational design of cytotoxic ptRNases, so too has substantial work been done to develop assays to measure and characterize the cytotoxicity of ptRNase-based chemotherapeutic agents. Cytotoxic ptRNases should be characterized thoroughly *in vitro* before being tested *in vivo*. Below, we describe the state-of-the-art in quantifying important parameters of ptRNase-mediated cytotoxicity, including cellular internalization, evasion of RI, inhibition of tumor cell proliferation *in vitro*, and inhibition of tumor growth *in vivo*. Several of these assays involve the use of fluorophores that can be tethered to ptRNases in a site-specific, non-perturbative manner.

A2.3.1 Utility of small molecule fluorophores

The constitutive fluorescence of traditional fluorophores (*e.g.*, fluorescein) can lead to high background that obscures valuable information. To overcome this limitation, we designed fluorogenic label **1** (Figure A2.4), which consists of a rhodamine 110 core enshrouded by an esterase-inducible “trimethyl lock” and a maleimido group for conjugation. Fluorescence is

unmasked only in the presence of intracellular esterases. Hence, the endocytic uptake of ptRNase–**1** conjugates can be monitored by either fluorescence microscopy or flow cytometry.[290]

We designed a second fluorescent label that is likewise amenable to thiol-reactive, site-specific conjugation. We had observed that the fluorescence of fluorescein-labeled RNase A decreases upon binding to RI because the protonated, non-fluorescent form of fluorescein is stabilized by the anionic RI.[39]

The discrepancy between the phenolic pK_a = 6.30 of fluorescein and physiological pH diminishes the sensitivity of this assay. To address this problem, we synthesized 2′,7′-diethylfluorescein, which has two electron-donating ethyl groups and a phenolic pK_a of 6.61. Fluorescent probe **2** (2′,7′-diethylfluorescein-5-iodoacetamide; Figure A2.4), which contains an iodoacetamido group for conjugation, enables a highly sensitive assay for the interaction of RI and ptRNases.[121]

A2.3.1.1 Site-specific conjugation of ptRNases to fluorophores

Fluorescently labeled ptRNases have proven to be remarkably adaptable tools for a variety of assays. Nonetheless, as mammalian ptRNases contain multiple amino groups—including an essential one for catalysis in an active-site lysine residue[291]—using amine-reactive reagents to cross-link or conjugate ptRNases can result in heterogeneity and inactivation. To overcome this problem, we install cysteine residues at inconsequential positions in ptRNases, allowing for site-specific conjugation to fluorophores.

Both RNase A and RNase 1 contain eight cysteine residues that form four disulfide bonds in the native enzyme. To enable attachment of a thiol-reactive fluorophore, we introduce a cysteine residue at position 19 using site-directed mutagenesis. Position 19 is an optimal location because

attachment of fluorophore groups there does not interfere with catalytic activity, RI binding, or cell-surface interactions (Figure A2.3). Further, this residue is in a solvated loop that is inconsequential for protein stability.[39] Free-cysteine variants are produced and purified by methods described previously for other ptRNase variants,[284] with the following modifications.

To ensure that the free cysteine residue does not suffer irreversible oxidation to a sulfinic or sulfonic acid, O_2(g) must be removed from the buffers used in the purification process. Following initial purification, the free thiol group at position 19 is protected as a mixed disulfide by reaction with a 4-fold molar excess of 5,5′-dithiobis(2-nitrobenzoic acid) (DTNB). Immediately following purification by gel-filtration chromatography, pooled protein fractions are adjusted to become 8% (w/v) in 1.0 M Tris–HCl buffer, pH 8.0, containing EDTA (10 mM). DTNB was dissolved in a small quantity of ethanol, then brought to 5 mM with 20 mM HEPES–NaOH buffer, pH 8.0. Upon addition of DTNB to the protein solution, a yellow color is observed due to the production of 2-nitro-5-thiobenzoic acid (NTB). The resulting mixture is dialyzed against several liters of 20 mM sodium acetate buffer, pH 5.0, overnight at 4 °C to remove unreacted NTB. NTB-protected ribonucleases are then purified further with cation-exchange chromatography and stored at 4 °C until needed for conjugation.

Immediately prior to fluorophore attachment, NTB-protected ptRNases are deprotected with a 4-fold molar excess of dithiothreitol and desalted by chromatography. Deprotected ptRNases are incubated for 6 h at 25 °C with a 10-fold molar excess of fluorophore in phosphate-buffered saline (PBS). *N*,*N*-Dimethylformamide (≤10% v/v) can be added to the reaction mixture to increase fluorophore solubility. Following the conjugation reaction, the solution is dialyzed against 20 mM sodium acetate buffer, pH 5.0, and then purified again with reverse-phase HPLC

to separate labeled and unlabeled protein. The molecular mass of each conjugate is verified by mass spectrometry prior to its use in assays.

A2.3.1.2 Assessing cellular internalization with fluorescence spectroscopy

The internalization of a ptRNase–**1** conjugate into live cells can be visualized with fluorescence microscopy. The rate of ptRNase internalization can be quantified with flow cytometry. These analyses can be used with both adherent and nonadherent cell lines.

To quantify internalization, mammalian cells from nearly confluent flasks are collected by centrifugation and resuspended at a density of 10^6 cells/mL in fresh medium that is appropriate to the cell type. A ptRNase–**1** conjugate is added (to 10 μM) to 250 μL of medium containing 10^6 cells/mL of cells. An unlabeled ptRNase can serve as a negative control. The cells are incubated at 37 °C for known times, typically ≤2 h. During this timeframe, we have observed that only a small fraction of labeled ptRNases are taken up by cells; therefore, we assume that the rate of internalization is not limited by substrate concentration. Further, we do not observe any significant exocytosis of labeled ptRNases by confocal microscopy.[290] To quench internalization, cells are collected by centrifugation at 1000 rpm for 5 min at 4 °C, washed once with ice-cold PBS, and resuspended in 250 μL of PBS. Samples are kept on ice until their analysis. The fluorescence of unmasked **1** can be detected by flow cytometry using a 530/30-nm band-pass filter. Total cell viability can be determined by staining with propidium iodide, which can be detected through a 660-nm long-pass filter. The mean channel fluorescence intensity of 20,000 viable cells are determined for each sample and used for subsequent analyses. To determine the steady-state rate constant (k_I) for ptRNase internalization, fluorescence intensity data is fitted to Eq. (A2.1), where F_{max} is the fluorescence intensity upon reaching the steady state and k_I is the

first-order rate constant for ptRNase internalization into cells.

$$F = Fmax(1 - e^{k_1 t}) \tag{A2.1}$$

A2.3.1.3 Evaluating RI evasion with fluorescence spectroscopy

Traditionally, the stability of a RI·RNase complex has been determined by measuring the inhibition of catalytic activity. The K_i values obtained by this method are lower than the concentration of wild-type RNase 1 used in the experiment itself. Accordingly, these values can only be an upper limit for the true K_d value. To more accurately measure the binding of ptRNases to RI, the dissociation rate of an RI·ptRNase complex is determined by monitoring the release of a ptRNase–**2** conjugate over time (Figure A2.5). To calculate the value of K_d of a RI·ptRNase complex, the value of k_a is assumed to be similar to that for the association of hRI with angiogenin or RNase A. These k_a values are within twofold of each other and are close to the diffusion limit.[292] Thus, the k_a value of homologous ptRNases is assumed to be equivalent to RNase A.

The dissociation rate of the complex between RI and a ptRNase–**2** conjugate can be determined by following the increase in fluorescence upon complex dissociation (Figure A2.5). A ptRNase–**2** conjugate (100 nM) in PBS containing tris(2-carboxyethyl)phosphine (100 μM) and bovine serum albumin (0.10 mg/mL; Sigma Chemical) is added to a 96-well microtiter plate, and the initial fluorescence is measured with a plate reader. RI is then added at equimolar concentrations and incubated with labeled ptRNase at 25 °C for 5 min. A 50-fold molar excess of human angiogenin or RNase 1 (5 μM) is added to scavenge dissociated complex, and the change

in fluorescence is measured at various time points. To insure that the proteins maintain their folded conformation for the duration of the experiment, additional data points should be monitored under the same conditions, only without the addition of the 50-fold molar excess of angiogenin. To account for indeterminant error, data are the mean (± SE) from six solutions normalized for the fluorescence of four solutions of labeled ptRNase (100 nM) in the absence of RI. Fluorescence data are fitted to Eq. (A2.2) to determine the dissociation rate constant (k_d), wherein F_0 is the fluorescence before the addition of angiogenin, and F_∞ is the fluorescence before RI addition. The equilibrium dissociation constant (K_d) for the RI·ptRNase complex can be determined with Eq. (A2.3) and the known value for the association rate constant of RNase A ($k_a = 3.4 \times 10^8\ M^{-1}s^{-1}$).[292]

$$F = F_0 + (F_\infty - F_0)(1 - e^{k_d t}) \tag{A2.2}$$

$$K_d = \frac{k_d}{k_a} \tag{A2.3}$$

A2.3.2 Measuring inhibition of tumor-cell proliferation *in vitro*

Multiple assays exist for measuring the effects of RNases on cultured cells *in vitro*. We choose to use the following cell proliferation assay because we find that it produces the most consistent results. Cytotoxicity is evaluated by measuring the incorporation of [methyl-^{3}H]thymidine into newly synthesized DNA. We have demonstrated that results obtained *in vitro* with this assay correlate well to reduced tumor volume *in vivo*.[75] This assay is amenable for use with either adherent or non-adherent cells. Cells should be grown in whatever medium is

optimal. Herein, we describe our procedure for assaying the cytotoxicity of ptRNases against the continuous human erythroleukemia line K-562 (ATCC; Manassas, VA).

Cells are grown in Roswell Park Memorial Institute (RPMI) 1640 medium (Mediatech, Herndon, VA) supplemented with fetal bovine serum (10% v/v), penicillin (100 units/ml), and streptomycin (100 μg/ml) and maintained at 37 °C in a humidified atmosphere containing CO_2 (g; 5% v/v). Aliquots (95 μl) of cultured K-562 cells (5 x 10^4 cells/ml) are placed in a microtiter plate and sterile solutions (5 μl) of ribonucleases in PBS are added to the aliquots. Cells are incubated in the presence or absence of ribonucleases for 44 h, followed by a 4-h pulse with [methyl-^{3}H]thymidine (0.2 μCi per well). Cells are then harvested onto glass fiber filters by using a PHD cell harvester (Cambridge Technology, Watertown, MA) and lysed by the passage of several milliliters of water through the filters. The filter retains DNA and other cellular macromolecules, while small molecules, including unincorporated label, pass through. After washing extensively with water, the filters should be dried with methanol and counted by using a liquid scintillation counter. Results from the cytotoxicity assays are expressed as the percentage of [methyl-^{3}H]thymidine incorporation into the DNA of PBS-treated control cells (Eq. A2.4). All assays should be repeated at least three times for maximum statistical power.

$$y = \frac{100\%}{1 + 10^{(\log(\mathrm{IC}_{50}) - \log[\mathrm{ribonuclease}])h}} \qquad \text{(A2.4)}$$

A2.3.3 Measuring the inhibition of tumor-cell proliferation *in vivo*

The most compelling method to measure the therapeutic effects of a cytotoxic ptRNase comes from *in vivo* analysis of tumor growth inhibition. This assay utilizes human tumor

xenografts grown in the flanks of nude mice. Here, we describe our method for analyzing the effect on the growth of these tumors. We use the human tumor cell lines DU145 (prostate cancer) and A549 (non-small cell lung cancer) for their ability to proliferate in mice, their low rate of spontaneous regression, and their known sensitivity to RI-evasive variants of RNase A.[32] Moreover, each line represents a clinically relevant target that is used often in the testing of new chemotherapeutic agents.

DU145 cells are grown in Dulbecco's modified Eagle's medium (ATCC) containing FBS (10% v/v); A549 cells are grown in F12K medium (ATCC) containing FBS (10% v/v). Cells (~10^6) are implanted into a rear flank of 5−6 week old male homozygous (*nu*/*nu*) nude mice. Tumors are allowed to grow to a volume of ≥75 mm^3 before the initiation of treatment. All test compounds are diluted in sterile PBS. All treatments are administered either by intraperitoneal injection (i.p.) or orally with a gavage needle (p.o.) for comparator chemotherapeutics, with the volume of administered solution based upon the body weight of the animal (10 μL/g). It is important to establish a dose and administration schedule that is effective with a specific cytotoxic ptRNase and tumor cell type. We have found that for mice bearing DU145 prostate carcinoma tumors, a dose of 15 mg/kg (i.p., qd × 5) of several monomeric ptRNase variants is optimal for eliciting maximum inhibition of tumor growth while minimizing off-target effects, as monitored by change in body weight. Similarly, we have found that frequent administration (qd × 5) achieves maximal tumor growth inhibition as compared to a single large dose (1 × wk). On the other hand, trimeric conjugates of cytotoxic RNase A variants can be administered less frequently and at a lower dose with comparable effect.[75] We speculate that the increased hydrodynamic radii of these trimeric conjugates results in enhanced persistence in circulation, as is observed with ptRNase-PEG.[77] Animal body weight should be monitored continually

throughout the experiment as an indicator of drug tolerance.

Treatment with all agents should be ongoing throughout the entire experiment, with a control set of animals treated with vehicle alone. Comparators can include approved chemotherapeutic agents, such as docetaxel (15 mg/kg; i.p., 1 × wk), cisplatin (6 mg/kg; i.p., 1 × wk), and erlotinib (100 mg/kg; p.o., 2 × wk). Tumor size should be measured twice-weekly using calipers, and tumor volume (mm^3) can be estimated by using the formula for a spheroid (Eq. A2.5). The percent tumor growth inhibition (%*TGI*) is then calculated with Eq. (A2.6).

$$volume = \frac{l \times w^2}{2} \tag{A2.5}$$

$$\%TGI = \left(1 - \left(\frac{(volume_{\text{final}} - volume_{\text{initial}})_{\text{treated}}}{(volume_{\text{final}} - volume_{\text{initial}})_{\text{control}}}\right)\right) \times 100 \tag{A2.6}$$

A2.4 Discussion

We have engineered mammalian ptRNases into useful cytotoxins. Through the use of novel, sensitive assays, we have been able to reveal the contribution of various parameters toward cytotoxicity. Still, mechanistic issues remain unclear, involving ptRNase translocation from endosomes to the cytosol and the specific RNA targets of ptRNases. Novel assays to illuminate these issues—and exploit them therapeutically—are being developed in our laboratory. Further work is directed at enhancing the circulating half-life of ptRNases *in vivo* using pegylation or glycosylation.

ptRNases have shown exceptional applicability as model proteins for multi-faceted drug design. The potential therapeutic value of ptRNases has been extended beyond cancer with the

creation of zymogens that can be engineered to be disease-specific. To date, protease-activatable ptRNase zymogens have been developed to combat malaria, hepatitis C, and HIV.[293-295] Another member of the ptRNase family, angiogenin, has been designed as a hyperactive variant capable of enhanced neovascularization.[296] Continued efforts to engineer this remarkable family of proteins will no doubt add even more therapeutic value.

Acknowledgements

J.E.L. is supported by an NSF Graduate Research Fellowship. Research on ribonucleases as cancer chemotherapeutic agents in the authors' laboratory is supported by Grant R01 CA073808 (NIH).

Table A2.6 Salient modifications of ptRNases that enhance cytotoxicity

Ribonuclease	T_m **(°C)**[a]	**Ribonucleolytic Activity (%)**[b]	K_i **or** K_d **(n*M*)**[c]	IC_{50} **(μ*M*)**[d]	Z[e]	**Ref.**
Wild-type RNase A	64	100	44×10^{-6}	>25	+4	32
G88R RNase A	60	142	2.8	6.2	+5	284
A4C/G88R/V188C RNase A	69	94	0.65	3	+5	276
D38R/R39D/N67R/G88R RNase A	56	75	1.4×10^{3}	0.19	+6	32
E49R/D53R/G88R RNase A	54	5	2.6	1.9	+9	87
E49R/D53R/G88R RNase A–R_9	49	7	3.0	0.58	+18	87
$(RNase\ A)_2$ [SGRSGRSG linker]	61	1.2	ND	12.9	+10	287
$(D38R/R39D/N67R/G88C\ RNase\ A)_3$	ND	17	ND	1.0	+16	75
Wild-type RNase 1	57	100	29×10^{-8}	>25	+6	89
R39D/N67R/N88R/G89D/R91D RNase 1	53	81	28	5.69	+3	89
PE5 (RNase 1–NLS)	46	ND	ND	4.6	+6	286
Onconase	90	100	$\geq 10^{3}$	0.27	+5	32

[a] Values of T_m are the temperature at the midpoint of thermal denaturation, which can be monitored by ultraviolet or circular dichroism spectroscopy.
[b] Values of ribonucleolytic activity are relative to the wild-type enzyme.
[c] Values of the equilibrium dissociation constant (or inhibition constant) are for the complex with human RI.
[d] Values of IC_{50} are for the incorporation of [*methyl*-^{3}H]thymidine into the DNA of K-562 human leukemia cells.
[e] Values of Z refer to the net molecular charge: Arg + Lys – Asp – Glu – Pyr (where "Pyr" refers to a pyroglutamate residue, which is found at the N-terminus of Onconase).

Figure A2.1

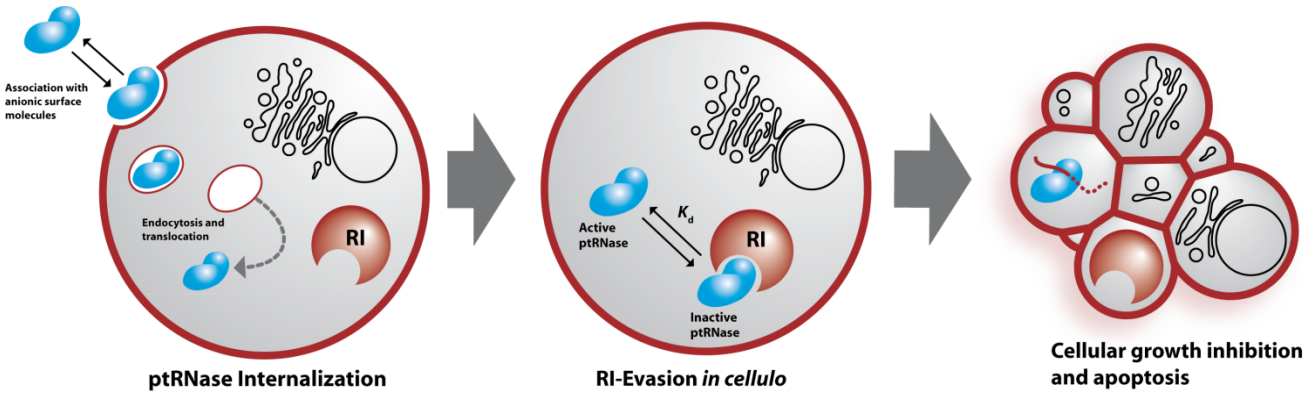
Association with anionic surface molecules
Endocytosis and translocation
RI
ptRNase Internalization
Active ptRNase
K_d
RI
Inactive ptRNase
RI-Evasion *in cellulo*
Cellular growth inhibition and apoptosis

Figure A2.1 Putative mechanism of ribonuclease cytotoxicity

The internalization pathway of ptRNases involves association with glycans on the cell membrane, absorptive endocytosis, and interaction with cytosolic RI. Upon evasion of RI, cytotoxic ptRNases can degrade cellular RNA and induce apoptosis.

Figure A2.2

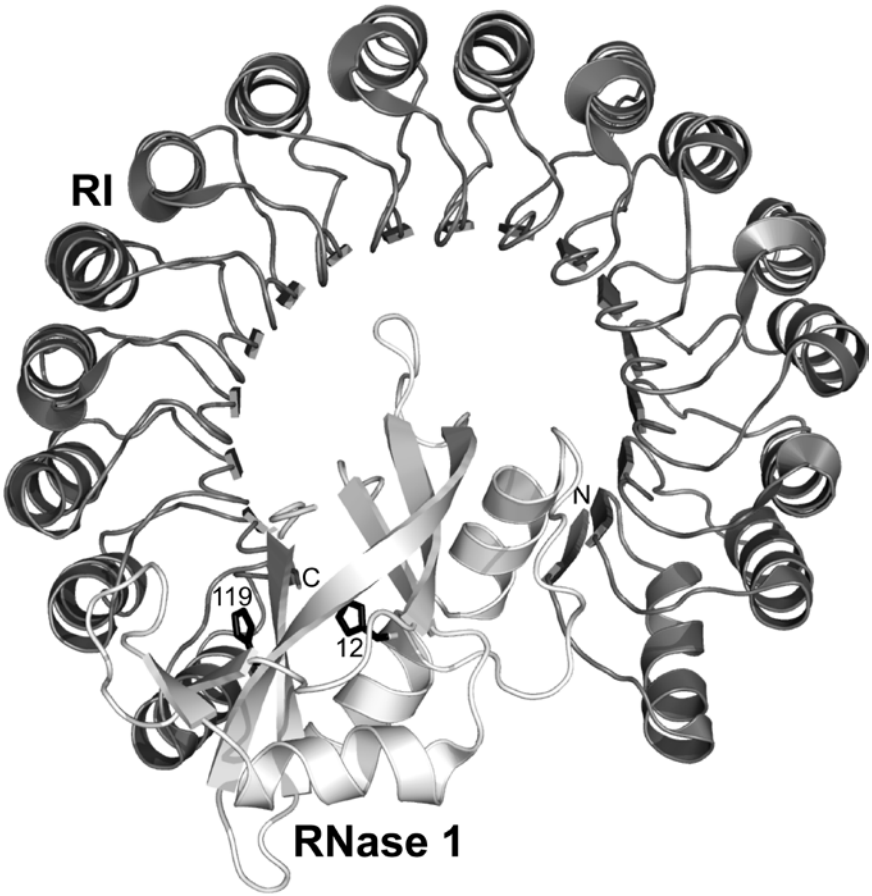

Figure A2.2 The structure of human RI complexed with human RNase 1

Three-dimensional structure of the human RI·RNase 1 complex (Protein Data Bank entry 1Z7X). The active-site histidine residues 12 and 119 of RNase 1 are depicted explicitly, and the N and C termini of RI are labeled. The complex has $K_d = 2.9 \times 10^{-16}$ M.[40]

Figure A2.3

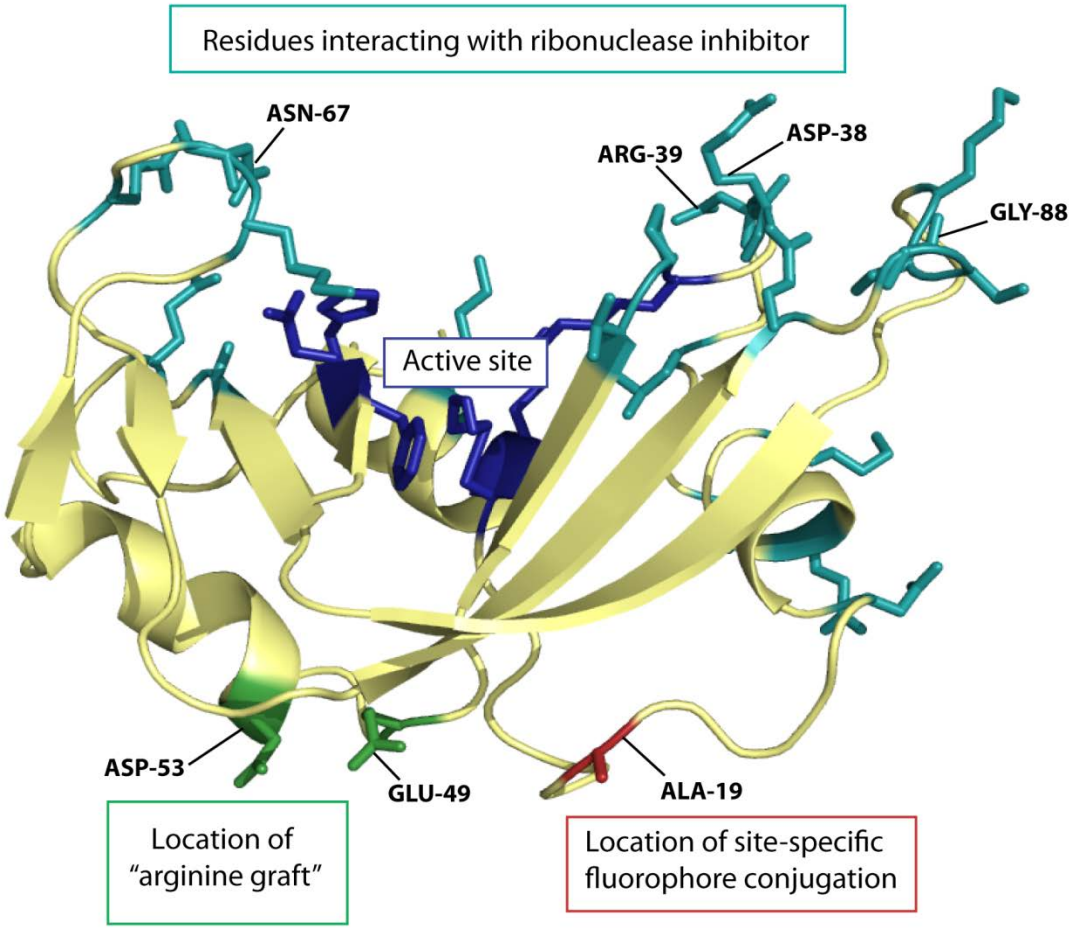
Residues interacting with ribonuclease inhibitor
ASN-67
ARG-39
ASP-38
GLY-88
Active site
ASP-53
GLU-49
ALA-19
Location of "arginine graft"
Location of site-specific fluorophore conjugation

Figure A2.3 Key functional residues in RNase A

Three-dimensional structure of RNase A showing residues important in the design and evaluation of an RNase A-based cytotoxin.

Figure A2.4

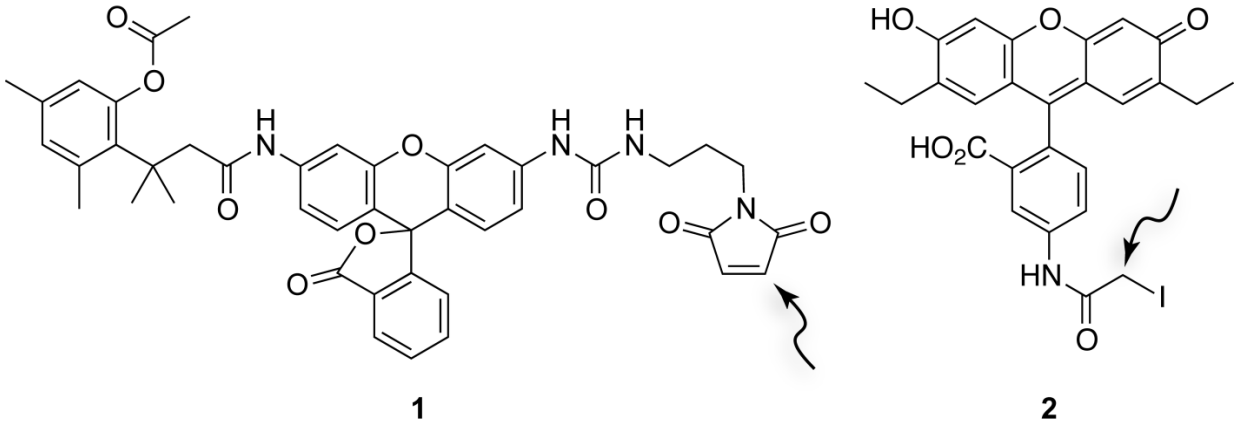

Figure A2.4 Chemical structures of fluorescent probes used in RNase conjugations

Structures of fluorogenic label **1** for monitoring endocytosis [290] and fluorescent probe **2** for monitoring protein–ligand interactions.[121] The arrows indicate electrophilic carbons that can form thioether linkages with cysteine residues.

Figure A2.5

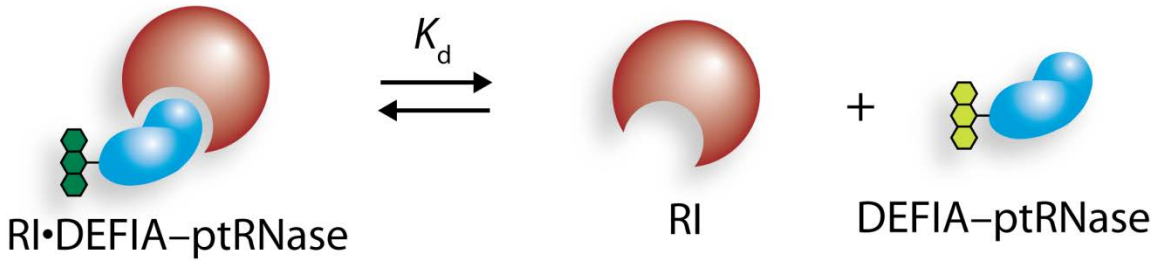

Figure A2.5 Mechanism of fluorescent probe quenching

Assay for evaluating K_d, which is the equilibrium dissociation constant of an RI·ptRNase complex.[121] Dissociation of the complex leads to an increase in fluorescence. The assay can also be used to evaluate the affinity of an unlabeled competitor ptRNase with a K_d value that is higher than the labeled ptRNase.

Appendix 3

Contribution of Electrostatics to the Binding of Pancreatic Ribonucleases to Membranes

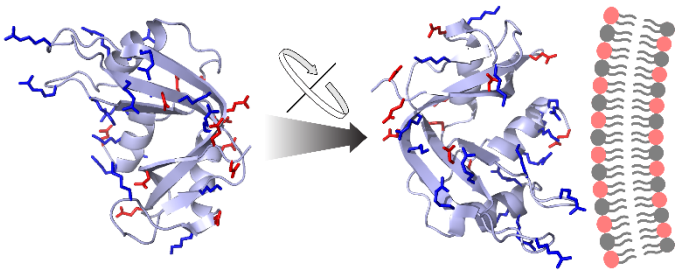

Contribution:

I purified and fluorescently-labeled RNases, designed and performed the binding experiments, and prepared portions of the manuscript.

This chapter was prepared for publication as:
Sundlass, N.K., **Eller, C.H.**, Qiang, C., Raines, R.T. Contribution of Electrostatics to the Binding of Pancreatic Ribonucleases to Membranes *Biochemistry* (2013) 52, 6304 - 6312.

Abstract

Pancreatic-type ribonucleases show clinical promise as chemotherapeutic agents, but are limited in efficacy by the inefficiency of their uptake by human cells. Cellular uptake can be increased by the addition of positive charges to the surface of ribonucleases, either by site-directed mutagenesis or by chemical modification. This observation has led to the hypothesis that ribonuclease-uptake by cells depends on electrostatics. Here, we use a combination of experimental and computational methods to ascertain the contribution of electrostatics to the cellular uptake of ribonucleases. We focus on three homologous ribonucleases: Onconase (frog), ribonuclease A (cow), and ribonuclease 1 (human). Our results support the hypothesis that electrostatics are necessary for the cellular uptake of Onconase. In contrast, specific interactions with cell-surface components likely contribute more to the cellular uptake of ribonuclease A and ribonuclease 1 than do electrostatics. These findings provide insight for the design of new cytotoxic ribonucleases.

A3.1 Introduction

Bovine pancreatic ribonuclease (RNase A; E.C. 3.1.27.5) has been the object of much seminal research in biochemistry and related fields.[28,141,142] The impact of this small secretory enzyme expanded when some members of the pancreatic-type ribonuclease superfamily were found to be natural toxins for tumor cells,[73,265,268,297,298] and others were engineered to be cytotoxic.[108,126] Notably, a ribonuclease from the Northern leopard frog (*Rana pipiens*), known as "Onconase®" (ONC or Ranpirnase), was granted both fast track and orphan drug status from the FDA for the treatment of malignant mesothelioma. Ultimately, however, dose-limiting renal toxicity limited its clinical utility.[73] More promising are cytotoxic variants of mammalian ribonucleases, such as RNase A and its human homolog (RNase 1), which demonstrate selective cytotoxicity without renal accumulation.[298,299]

A cytotoxic ribonuclease must be internalized by tumor cells, translocate across the endosomal membrane to the cytosol, evade the cytosolic ribonuclease inhibitor protein (RI), and catalyze the degradation of RNA.[108] RI is a 50-kDa cytosolic protein that binds to some ribonucleases, inhibiting their ribonucleolytic activity.[271] ONC does not bind to human RI under physiological conditions[300] and is naturally cytotoxic to human cells. Conversely, wild-type RNase A and wild-type RNase 1 bind to RI with femtomolar affinity and are not cytotoxic.[40,301] Variants engineered to evade RI do, however, demonstrate cytotoxicity.[40,89,108,126,284,302]

Inefficient cellular internalization can limit the cytotoxic activity of a pancreatic-type ribonuclease.[108] For example, ribonucleases exhibit picomolar IC_{50} values when injected directly into the cytosol, but micromolar IC_{50} values when simply incubated with cells.[303] Although ONC has been proposed to bind to two saturable sites on 9L glioma cells with K_d values of 0.25 μM and 62 nM,[83] ONC demonstrates non-saturable binding to HeLa, K-562, and CHO cells.[84,91,304]

ONC and its homologs are highly cationic proteins (Figure A3.1), and their endocytosis occurs via non–receptor-mediated pathways[84] similar to those used by cationic cell-penetrating peptides.[90]

Increasing the endocytosis of a ribonuclease can increase its cytotoxicity. For example, the covalent conjugation of RNase A to transferrin, which does have a cell-surface receptor, increases both its cellular uptake and cytotoxic activity.[305] In addition, increasing the net positive charge of RNase A and RNase 1 through either site-directed mutagenesis or chemical modification increases endocytosis.[87,198,279] Likewise, decreasing the net negative charge of mammalian cells decreases the uptake of RNase A and ONC.[304] Accordingly, the endocytosis of ribonucleases is likely mediated by electrostatic forces.[282] In addition to providing affinity, electrostatic forces could also contribute to the therapeutic index of pancreatic-type ribonucleases because cancer cells tend to be more anionic than analogous noncancerous cells.[78,98,306]

Ribonuclease cytotoxicity relies on translocation into the cytosol.[265] RNase A is found in lysosomes 100 h after endocytosis, consistent with inefficient translocation to the cytosol.[288] Indeed, only ~7% of the RNase A molecules that enter a cell reach the cytosol in 24 h.[233] Neutralization of the pH in endosomes results in an increase in ONC cytotoxicity, presumably due to increased translocation.[307] Cytotoxicity has also been found to correlate with the ability of a ribonuclease to disrupt synthetic anionic membranes.[308]

We suspected that theoretical approaches could provide insight on the interaction between ribonucleases and cellular membranes. In particular, we reasoned that a numerical solution of the Poisson–Boltzmann (PB) equation could be used to calculate the interaction energy between molecules using continuum electrostatics. The PB approach has been used to

calculate the binding energy between rigid proteins and model membranes and to identify energetically favorable orientations for binding.[309] Of special relevance was the use of PB calculations to predict the orientation of membrane-bound dimeric ribonucleases.[308] These calculations indicated that the ensuing electrostatic energy correlates with both the ability to disrupt membranes and cytotoxicity. The PB-based computational framework does not describe effects due to the atomic nature of solvent and lipid molecules, but is particularly useful in the current study, which aims to probe the contribution from generic electrostatic effects to the binding of a protein to anionic membranes.

Here, we use computational and experimental approaches to measure the contribution of electrostatics to the binding of RNase 1, RNase A, and ONC to anionic membranes. We report on the effect of salt concentration on the formation of a protein·membrane complex. We then use computational analysis to reveal favorable orientations for those complexes and to highlight differences caused by the differential distribution of charges on the surface of RNase 1, RNase A, and ONC. Finally, we compare experimental binding measurements to PB calculations and simulations using an implicit membrane model supplemented with a Gouy–Chapman term (IMM1–GC), which is another electrostatics-driven approach. The comparison highlights the advantages of each computational method and the quality of their predictions. Together, the experimental and computational data indicate that, despite similar structures and net charges, homologous ribonucleases have distinct affinities for anionic surfaces.

A3.2 Materials and methods

A3.2.1 Materials

BODIPY® FL *N*-(2-aminoethyl)maleimide (catalog number B-10250) was from Molecular Probes (Carlsbad, CA). 1,2-Dioleoyl-*sn*-glycero-3-phospho-L-serine (DOPS) and 1,2-dioleoyl-*sn*-glycero-3-phosphocholine (DOPC) were from Avanti Polar Lipids (Alabaster, AL). All other chemicals used were of commercial grade or better, and were used without further purification.

A3.2.2 Analytical instruments

Molecular mass was measured by MALDI–TOF mass spectrometry using a Voyager-DE-PRO Biospectrometry Workstation from Applied Biosystems (Foster City, CA). Fluorescence was quantified with an Infinite M1000 plate reader from Tecan (Männedorf, Switzerland).

A3.2.3 Production of fluorescently labeled ribonucleases

P19C RNase 1,[282] A19C RNase A,[290] and S61C ONC,[91] which are variants with an orphan cysteine residue, were prepared as described previously. The free cysteine residue in these variants was protected as a mixed disulfide by reaction with 5,5′-dithio-bis(2-nitrobenzoic acid). Prior to fluorophore attachment, each mixed disulfide was reduced with dithiothreitol (5 equiv), then desalted by using a PD-10 desalting column from GE Biosciences (Piscataway, NJ). Deprotected proteins were reacted for 4–6 h at 25 °C in PBS with BODIPY® FL *N*-(2-aminoethyl)maleimide (10 equiv) in DMSO. The reaction was quenched by rapid dilution into 50 mM sodium acetate buffer at pH 5.0. Conjugates were purified by chromatography using a HiTrap SPHP column, and concentrations of conjugates were determined with a bicinchoninic acid assay kit from Pierce (Rockford, IL).

A3.2.4 Liposome formation

Large unilamellar vesicles (*i.e.*, liposomes) were formed by mixing DOPC and DOPS solvated by chloroform in a 3:2 molar ratio at a 5 mM concentration of total lipid. The lipids were dried under N_2(g) to remove the chloroform, then dried further under vacuum overnight. The lipids were resuspended in 20 mM Tris–HCl buffer at pH 7.0, containing NaCl (50 or 80 mM), by vortexing, and were then allowed to hydrate for 1 h at 37 °C. The vesicles were then extruded 19 times through a 100-nm filter to form liposomes that were ~130 nm in diameter according to dynamic light scattering data obtained with an N4-Plus instrument from Beckman Coulter (Brea, CA).

A3.2.5 Protein–liposome binding assay

Fluorescence polarization was used to measure the binding affinity of the fluorescently labeled ribonucleases to liposomes. A concentration range (4.5 mM→2.25 nM; 2-fold dilutions) of liposomes was incubated with BODIPY-labeled ribonuclease (50 nM) in 20 mM Tris–HCl buffer at pH 7.0, containing NaCl (50 or 80 mM) for 1 h at 23 °C while shaking. Then, fluorescence polarization was measured with excitation at 470 nm and emission at 530 nm, and the value of the equilibrium dissociation constant (K_d) was calculated with the equation:

$$R = \frac{(R_{\max} - R_{\min})[\text{lipid}]}{K_d + [\text{lipid}]} \quad \text{(A3.1)}$$

where R refers to the observed polarization, R_{max} refers to the polarization when the ribonuclease is bound fully, R_{min} refers to the polarization when the ribonuclease is free, and [lipid] refers to the concentration of DOPS.

A3.2.6 Poisson-Boltzmann calculations

Electrostatic calculations were performed with the program APBS 1.2.1.[310] For the calculations presented herein, the free energy of binding, $\Delta\Delta G_{bind}$, between the protein and membrane was calculated with the equation:

$$\Delta\Delta G_{\mathrm{bind}} = \Delta\Delta G_{\mathrm{solv}} + \Delta\Delta G_{\mathrm{Coul}} \tag{A3.2}$$

where $\Delta\Delta G_{solv}$ refers to the contribution of solvation to binding and $\Delta\Delta G_{Coul}$ refers to the Coulombic contribution to binding. The solvation contribution to binding was calculated as

$$\Delta\Delta G_{\mathrm{solv}} = \Delta G_{\mathrm{solv,complex}} - \Delta G_{\mathrm{solv,protein}} - \Delta G_{\mathrm{solv,membrane}} \tag{A3.3}$$

where the terms refer to the solvation free energy of the protein·membrane complex, the protein, and the model membrane, respectively. The individual free energy terms were calculated by numerical solution of the Poisson–Boltzmann equation:

$$-\nabla \cdot \varepsilon(\bar{r})\nabla V(\bar{r}) = \rho_{\mathrm{f}}(\bar{r}) - 2qn_{\infty}\sinh\left(\frac{qV(\bar{r})}{k_{\mathrm{B}}T}\right) \tag{A3.4}$$

The Coulombic contribution was calculated in analogy to Eq. A3.3 as

$$\Delta\Delta G_{\mathrm{Coul}} = \Delta G_{\mathrm{Coul,complex}} - \Delta G_{\mathrm{Coul,protein}} - \Delta G_{\mathrm{Coul,membrane}} \quad \text{(A3.5)}$$

where the terms are the summation of all pairwise Coulombic interactions between all atoms within the protein·membrane complex, the protein, and the model membrane, respectively.

The structures of RNase 1, RNase A, and ONC were derived from PDB entries 1Z7X,[40] 1KF5,[311] and 1ONC,[312] respectively. All water molecules were removed from the PDB file prior to the addition of hydrogen atoms and atomic charges based on the CHARMM 27 force field with PDB2PQR.[313-315] The model membrane was approximated by an 80 × 80 Å plane of spheres (r = 3 Å; q = –1; ε = 78.50) with a charge density of 1 sphere/130 Å^2. The solvation free energy of the protein was calculated with 2 levels of focusing calculations in a 400 × 400 × 400 Å box with a 0.5-Å spacing at the finest level. Dielectric maps of the system were outputted and altered such that the dielectric constant below the charged plane of spheres was ε = 2.0. These dielectric maps were used to calculate the solvation free energies of the membrane and the protein·membrane complex. The model membrane was placed 5 Å below the bottom of the protein. Conformations of the protein relative to the membrane were sampled by applying a rotation matrix based on Euler's angles (θ = 0; ϕ = 0–2π; ψ = 0–π) in 15°-increments on the protein coordinates.

A3.2.7 IMM1-GC calculations

The IMM1-GC model was used to model an anionic membrane in CHARMM. IMM1-GC is based on the IMM1 model with the addition of a Gouy–Chapman (GC) term to describe the interaction between charged amino acids and the charged bilayer.[316] The IMM1 models the membrane as a low dielectric slab with a smooth transition to the high dielectric solvent. The IMM1 model is based on the EEF1 model for water-soluble proteins,[317] which neutralizes ionic side chains and uses a linear distance-dependent dielectric constant. The solvation free energy for a protein, ΔG_{solv}, is assumed to be the sum of the solvation free energy for individual atoms within the protein. The effective energy of the protein in the presence of the membrane is given by

$$W_{\mathrm{IMM1-GC}} = E_{\mathrm{intra}} + \Delta G_{\mathrm{solv}} + E_{\mathrm{GC}} \tag{A3.6}$$

where E_{intra} is the intramolecular energy of the protein and E_{GC} is the interaction between the charged amino acids and the charged lipid bilayer based on the Gouy–Chapman theory for a diffuse electrical bilayer.[318]

The initial coordinates were taken from the same PDB entries used in PB calculations. Six different initial orientations were generated with each one corresponding to the face of a cube containing the ribonuclease. The membrane was placed 3 Å below the bottom of the protein perpendicular to the *z*-axis. The salt concentration was set to 0.1 M, the area per lipid to 32 Å^2, and the anionic fraction of the membrane to 40% to match the experimental fluorescence polarization conditions. Molecular dynamic simulations were performed with CHARMM (c35a1).[319] The backbone atoms were constrained using an rmsd constraint. The structures were equilibrated for 100 ps at 298 K and then run for another 2000 ps. The conformations were

stored every 0.5 ps and used to calculate the effective energy of the protein in solvent and in the presence of a membrane. A total of 12 simulations were run for each protein. The average binding energy was calculated as the mean binding energy over the last 2 ns of the simulation and a trajectory was said to bind if the binding free energy is more favorable than –0.8 kcal/mol.

A3.3 Results

A3.3.1 Production of labeled ribonucleases

Ribonucleases were labeled with BODIPY in regions with few cationic residues (residue 19 in both RNase 1 and RNase A, and residue 61 in ONC), as these areas were deemed unlikely to interfere with the binding of the ribonucleases to the lipid vesicles. Moreover, the fluorescence of BODIPY is insensitive to pH. The expected mass of purified, labeled proteins was confirmed with MALDI–TOF mass spectrometry, and a properly folded structure was confirmed with measurements of enzymatic activity.[127]

A3.3.2 Liposome-ribonuclease interactions

The contribution of electrostatics to the cytotoxicity of ribonucleases has been difficult to study. To isolate the first step in the process, we studied the binding of RNase 1, RNase A, and ONC to large unilamellar vesicles containing 40% phosphatidylserine at various salt concentrations. Phosphatidylserine has a net negative charge and normally resides in the cytoplasmic leaflet of the lipid bilayer; in cancerous cells, however, phosphatidylserine relocates to the extracellular leaflet.[306] Cancer cells also display changes in glycosaminoglycans that lead to a more negatively charged surface.[78,98,306] Hence, we used phosphatidylserine liposomes to mimic the anionic cell surface, providing a comparator for our computational data.

Equilibrium binding isotherms for ribonucleases and liposomes are depicted in Figure A3.2, and values of K_d are listed in Table 1. RNase A did not bind to the liposomes at either salt concentration. ONC demonstrated some binding in the low salt condition. RNase 1 bound to the liposomes with a K_d value of 27 μM in the low salt condition and with much lower affinity in the high salt condition.

A3.3.3 Poisson–Boltzmann calculations

Poisson–Boltzmann calculations were performed to determine the most favorable orientation for ribonucleases to bind to a model membrane and the binding energy of that orientation (Figures A3–A5). The electrostatic map for RNase 1 reveals that the most energetically favorable orientation has its active site facing the membrane (Figures A3.3A–C). The predicted values of ΔG_{bind} are in gratifying agreement with the experimental ones (Table A3.1).

Similar to RNase 1, RNase A orients itself so that its active site faces the membrane (Figures A3.4A–C). This orientation, however, yields a relatively low affinity (Table A3.1), and is consistent with experiments showing that the binding of RNase A to phosphatidylserine liposomes is not detectable (Figure A3.2). Interestingly, for both RNase 1 and RNase A, the loops that mediate binding to RI (which is a highly anionic protein[271]) also seem to be important for binding to the model membrane.

In contrast to RNase 1 and RNase A, PB calculations predict that ONC can bind favorably either with its active site facing the membrane or in the opposite orientation (Figures A3.5A–C), which is a highly repulsive orientation for the mammalian ribonucleases. Moreover, ONC appears to be weakly attractive in any orientation, and the most favorable orientation for ONC is only 3-fold more likely than a random orientation. Like RNase A, however, ONC is predicted to

bind with low overall affinity in the high salt condition, consistent with experimental data (Table A3.1).

In general, the PB calculations were more predictive of the affinity of ribonucleases for membranes in the high salt condition than in the low salt condition. For example, the calculated binding free energy for RNase 1 in the low salt condition corresponds to a K_d value of 350 μM, but the experimental K_d value was 27 μM (Table A3.1). Similarly, ONC is calculated to have a K_d value of ~8 mM in low salt conditions, but the experimental K_d value was 0.7 mM. Lastly, although RNase A should display affinity only slightly less than that of ONC, its binding was not detectable by experiment. Nevertheless, the predicted trends in the affinity of the proteins for the model membrane: RNase 1 >> ONC > RNase A, were qualitatively consistent with experiment in the low salt condition.

A3.3.4 IMM1-GC simulations

Whereas the PB calculation results compared well overall with experimental values, especially in the high salt condition, they did not allow for side-chain rearrangements or measure hydrophobic interactions. Hence, we performed multiple short molecular dynamic simulations using the IMM1–GC model. In the simulations, the main chain was constrained, but side chains were unconstrained and the protein was allowed to rotate and translate. For ONC, because the PB calculation did not predict a favorite or an unfavorable orientation, we were surprised to see that only 7 of the 12 trajectories resulted in binding, although the average binding free energies were comparable to those from the PB calculations. The standard deviations reported in Table 3A.2 report on the amount of protein movement during the simulation, with larger variations reflecting a varied trajectory. Coarse-grained representations for the trajectories of simulations

that result in bound and unbound ONC are shown in Figures A3.5B and A3.5E, respectively. The bound trajectory remains in the areas that are most energetically favorable, as seen in Figure A3.5A. The unbound trajectory was started in a less energetically favorable area, where the binding free energy was insufficient to keep ONC on the membrane long enough for it to rotate to a more energetically favorable orientation. The two simulations starting from orientation $\theta = 270°$, $\psi = 90°$ also demonstrate this phenomenon. They both move away from the membrane due to a lack of favorable interactions. Nevertheless, in simulation 1, ONC does not rotate into a conformation allowing it to return to the membrane; whereas, in simulation 2, ONC rotates so that its most favorable surface faces the membrane, enabling it to bind, ultimately, with an energy of –2 kcal/mol. In contrast to ONC, RNase A and RNase 1 bound to the membrane in 9 of the 12 trajectories. The energies are similar to those from the PB calculations, and the trajectory snapshots follow the energetics predicted by the PB calculations. Lastly, none of the proteins inserted into the membrane, though they remained close to the membrane according to the average predictive binding energy.

A3.4 Discussion

A major factor that limits the efficacy of many putative protein chemotherapeutic agents is their delivery to the cytosol.[320] Lacking a receptor, cytotoxic ribonucleases undergo endocytosis and escape from endosomes.[108] Here, we use a combination of experimental and computational techniques to compare and contrast the effect of electrostatics on the interaction of RNase 1, RNase A, and ONC with lipid bilayers.

Our data suggest that electrostatic forces are sufficient to cause a weak association of ONC with the cell surface, where the protein remains until internalized via bulk-rate endocytosis.[304] Although computational results predict a weak affinity for a negatively charged surface, ONC spent most of its simulation time associated with the surface. Because bulk endocytosis occurs constitutively, time spent near the cell surface is critical for internalization. We suggest that the low experimental rate of ONC cellular uptake[91,304] is explicable by its low binding energy combined with the lack of a cell-surface binding partner.

Comparing the cellular uptake to the calculated binding energies reveals unusual disparities for RNase A compared to ONC and RNase 1. Calculations predict that RNase A has a cell-surface affinity similar to that of ONC[304]. Yet, RNase A is internalized by cells at a rate that is 10^2-fold greater than that of ONC.[304] The absence of heparan sulfate and chondroitin sulfate on the cell surface reduces the internalization rate of an RI-evasive variant of RNase A by 4-fold but does not affect that of ONC. We propose that the presence of these and other cell-surface moieties with specific affinity for RNase A but not ONC explains the discrepancy between predicted and experimental results. RNase A and RNase 1 display similar levels of cellular uptake,[282] even though RNase 1 has a higher net charge (Figure A3.1), demonstrates a salt-dependence in its membrane affinity (Figure A3.2), and has a much higher predicted binding free energy (Table A3.1). These data are consistent with RNase A having a greater affinity for specific cell-surface moieties than does RNase 1.

Poisson–Boltzmann calculations were used to predict the affinity of the three homologous cationic proteins for an anionic membrane. Although explicit lipid-based membrane simulations are becoming increasingly powerful,[321] computing the binding free energy of a protein to a multi-component lipid bilayer with atomistic models remains as a significant challenge. Given

the simplicity of the lipid bilayer model, which consists of an implicit solvent and a plane of negatively charged spheres above a low-dielectric slab, its correspondence with experimental data is encouraging. The simplicity of the lipid bilayer model decreases computational cost compared to explicit lipid models. Most importantly, the PB calculations directly address the contribution of *electrostatics* to the binding affinity of the cationic proteins to an anionic membrane.

IMM1–GC simulation results were consistent with the PB calculations and with experimental results. They provided additional insight by clarifying the necessary strength of an interaction for a long-lasting stable interaction to occur in the protein·membrane complex and by showing that hydrophobic interactions are involved only minimally. The lack of ribonuclease penetration of the membrane suggests that, in contrast to cell-penetrating peptides,[316] ribonucleases require more than electrostatic or hydrophobic forces to penetrate a lipid bilayer. IMM1–GC simulations required much less computational resources compared to the PB calculations and provided additional information, making them an attractive option for identifying energetically favorable orientations of proteins at the membrane surface and for estimating the binding free energy. We propose that the results of IMM1-GC simulations could be refined further by explicit membrane simulations starting from the predicted binding orientations, though gaining quantitative insights requires novel simulation methods that allow an efficient sampling of local lipid (de)mixing upon protein binding.

Our future efforts will focus on identifying residues in pancreatic-type ribonucleases that mediate their affinity for those glycans that are upregulated in cancer cells.[78] Manipulations that enhance such interactions could increase the clinical utility of chemotherapeutic agents based on RNase 1 and its homologs.

Acknowledgements

We are grateful to S. Yang for technical expertise, and I. C. Tanrikulu, G. A. Ellis, and E. Smith for contributive discussions. Mass spectrometry and dynamic light scattering were performed at the Biophysics Instrumentation Facility, which was established with grants BIR-9512577 (NSF) and S10 RR013790 (NIH)

Table A3.1 Experimental and calculated affinity of ribonucleases for a phosphatidylserine membrane

		Experimental		Calculated
Ribonuclease	**[NaCl] (mM)**	**K_d (mM)**	**ΔG_{bind} (kcal/mol)**	**ΔG_{bind} (kcal/mol)**
RNase 1	50	0.027 ± 0.002	–6.23 ± 0.02	–4.7
RNase 1	80	0.5 ± 0.1	–4.5 ± 0.1	–3.6
RNase A	50	>1.8	>–3.7	–2.8
RNase A	80	>1.8	>–3.7	–2.2
ONC	50	0.7 ± 0.2	–4.3 ± 0.2	–3.1
ONC	80	>1.8	>–3.7	–2.5

Experimental data were determined by fluorescence polarization in 20 mM Tris–HCl buffer at pH 7.0. Calculated data were determined by Poisson–Boltzmann analysis.

Table A3.2 Summary of IMM1–GC simulations

	Starting Orientation	Binding Energy(kcal/mol)
RNase 1	$\theta = 0;\ \psi = 0$	0.0
		0.0
	$\theta = 180;\ \psi = 0$	–3.9 ± 0.9
		–4.4 ± 0.7
	$\theta = 270;\ \psi = 0$	–0.1 ± 0.6
		–2.2 ± 1.5
	$\theta = 270;\ \psi = 90$	–3.4 ± 0.9
		–3.4 ± 0.7
	$\theta = 90;\ \psi = 0$	–3.3 ± 0.9
		–4.0 ± 0.8
	$\theta = 90;\ \psi = 90$	–3.2 ± 1.0
		–3.0 ± 1.2
RNase A	$\theta = 0;\ \psi = 0$	–0.6 ± 0.9
		–2.2 ± 0.7
	$\theta = 180;\ \psi = 0$	–2.9 ± 0.5
		–2.6 ± 0.6
	$\theta = 270;\ \psi = 0$	0.0
		–0.1 ± 0.3
	$\theta = 270;\ \psi = 90$	–1.1 ± 1.3
		–2.5 ± 0.6
	$\theta = 90;\ \psi = 0$	–2.1 ± 0.7
		–1.6 ± 1.0
	$\theta = 90;\ \psi = 90$	–1.8 ± 0.8
		–1.3 ± 0.9
ONC	$\theta = 0;\ \psi = 0$	–2.0 ± 0.5
		–2.5 ± 0.7
	$\theta = 180;\ \psi = 0$	–1.5 ± 0.7
		–2.0 ± 0.6
	$\theta = 270;\ \psi = 0$	–1.5 ± 1.2
		–2.6 ± 0.4
	$\theta = 270;\ \psi = 90$	–0.2 ± 0.4
		–0.8 ± 0.8
	$\theta = 90;\ \psi = 0$	0.0
		–0.1 ± 0.3
	$\theta = 90;\ \psi = 90$	–0.2 ± 0.5

Each RNase was rotated using Euler angles to obtain 6 starting orientations. Two independent 2-ns simulations were run for each orientation. The binding energy reports on the average energy over the duration of a simulation and its standard deviation arises from variation in the trajectory.

Figure A3.1

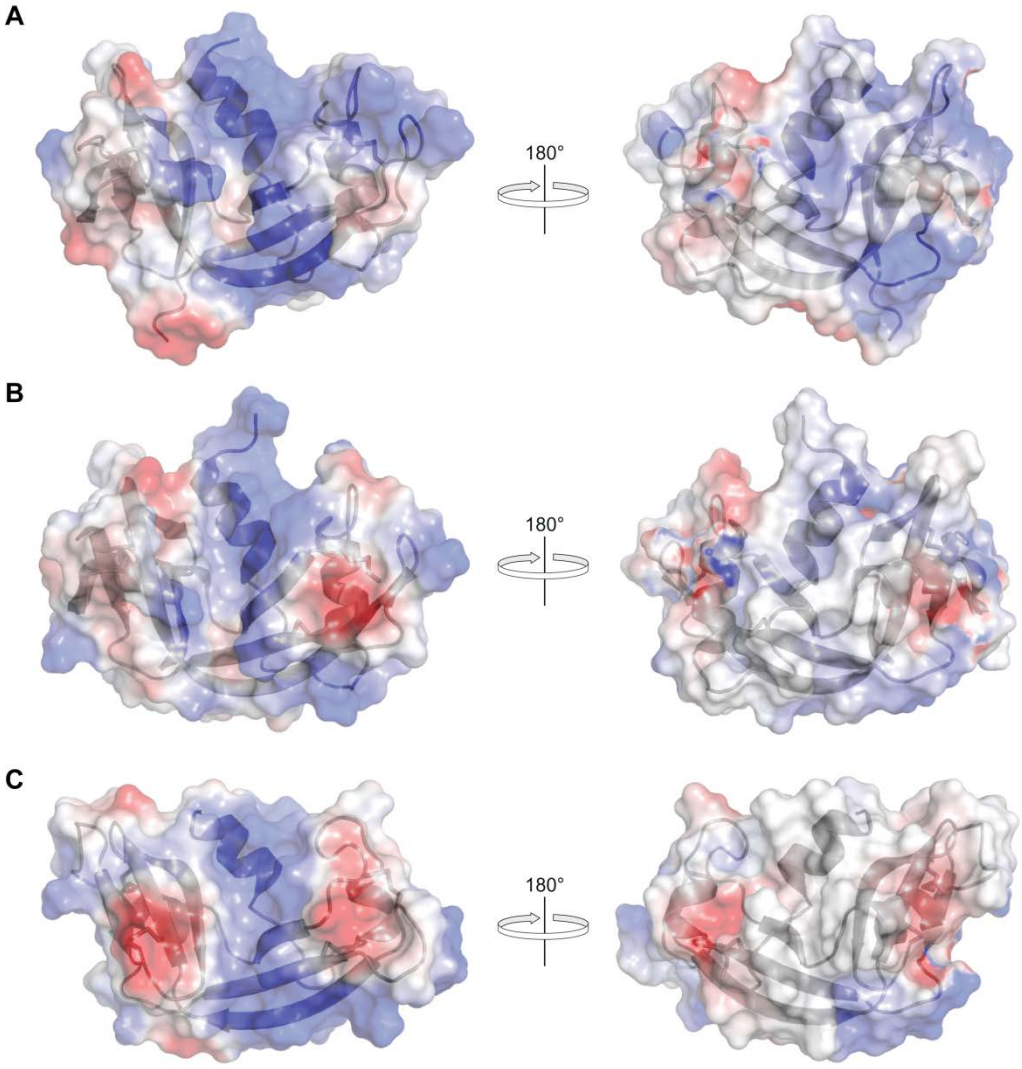

Figure A3.1 Electrostatic surface potential of pancreatic-type ribonucleases

A. RNase 1 (1Z7X), which has a net charge (Arg + Lys – Asp – Gly) of $Z = +6$. *B*. RNase A (1KF5), which has $Z = +4$ and 68% sequence identity with RNase 1. *C*. ONC (1ONC), which has $Z = +5$ and 23% sequence identity with RNase 1. Images were made with the program PyMOL from Schrödinger (Portland, OR).

Figure A3.2

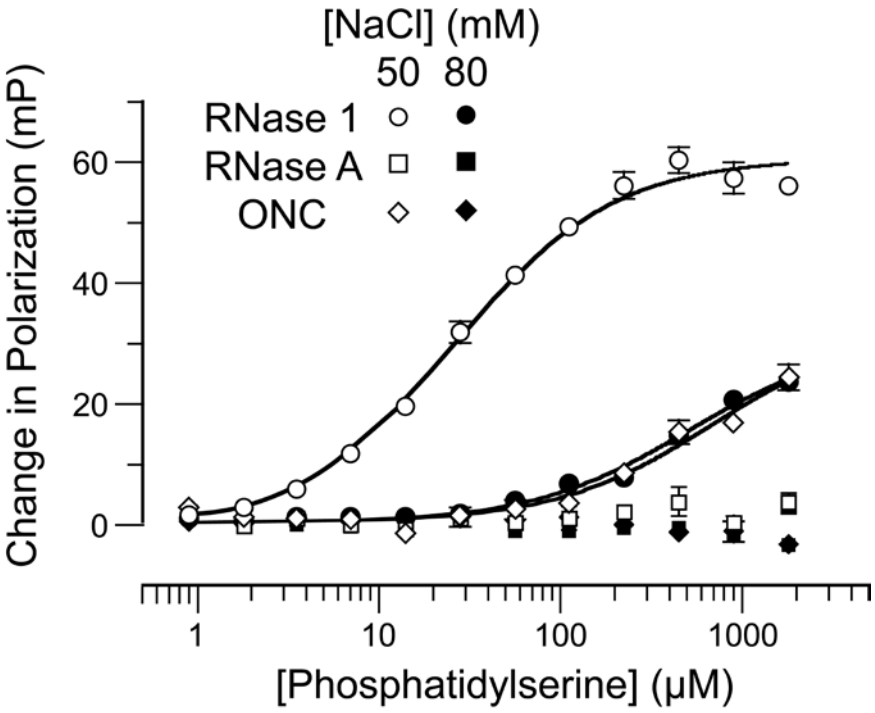
[NaCl] (mM)
50 80
RNase 1
RNase A
ONC
Change in Polarization (mP)
60
40
20
0
1
10
100
1000
[Phosphatidylserine] (μM)

Figure A3.2 Ribonuclease binding isotherms toward phosphatidylserine liposomes

Binding was measured by fluorescence polarization using fluorescently-labeled ribonucleases and increasing concentration of liposomes containing DOPC and DOPS at a ratio of 3:2 in 20 mM Tris–HCl buffer at pH 7.0, containing NaCl (50 or 80 mM). Data were fitted by a non-linear regression analysis.

Figure A3.3

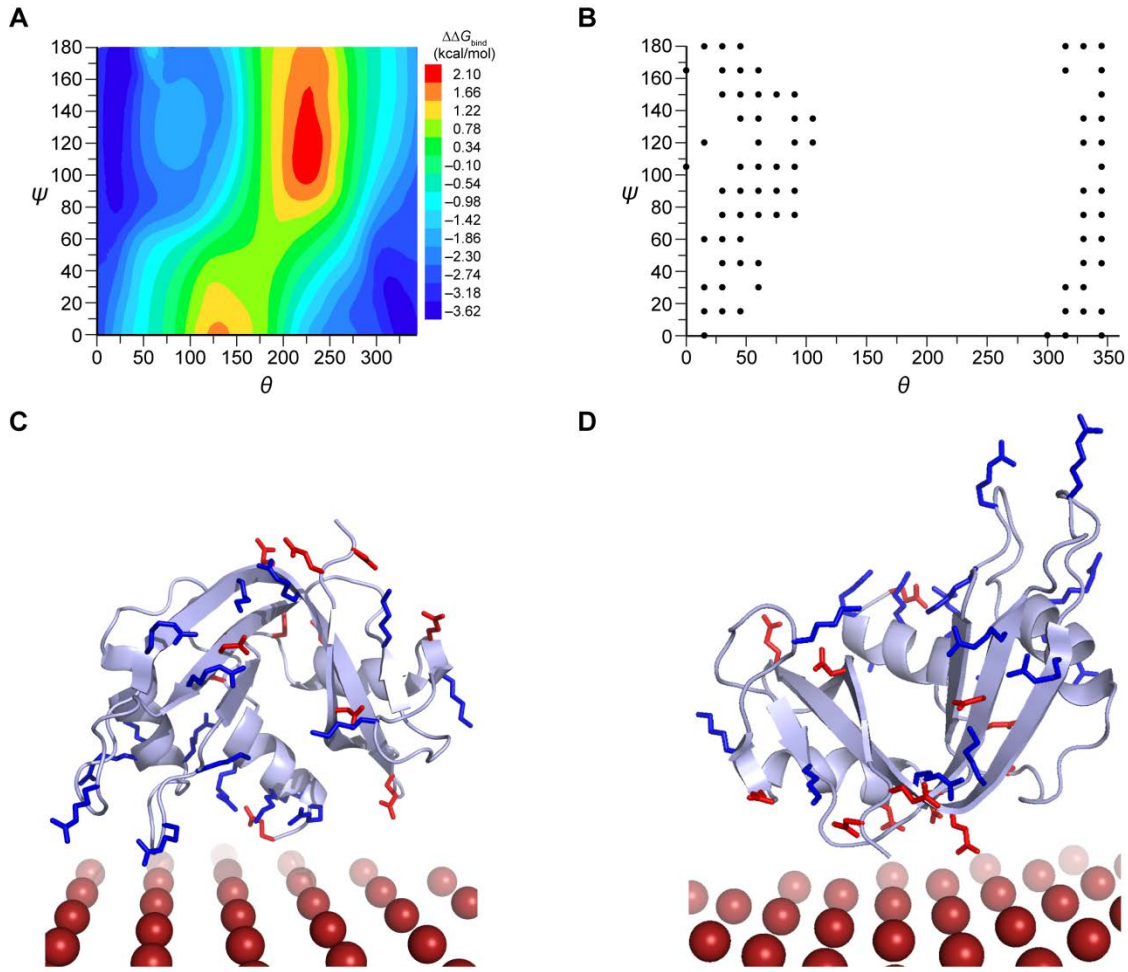
A
B
C
D
ΔΔG_bind (kcal/mol)
2.10
1.66
1.22
0.78
0.34
−0.10
−0.54
−0.98
−1.42
−1.86
−2.30
−2.74
−3.18
−3.62
ψ
θ

Figure A3.3 Computational calculation of the binding of RNase 1 to model membranes *A*. Poisson–Boltzmann calculations of the electrostatic free energy of interaction between RNase 1 (PDB entry 1Z7X), rotated using Euler angles (θ = 0–360°; ψ = 0–180°; increments of 15°), with a model membrane with an anionic fraction of 1 electron per 130 $Å^2$. *B*. A coarse-grained representation of trajectories from a 2-ns IMM1–GC simulation that result in a protein·membrane complex. Each point represents a snapshot from the trajectory. *C*. Depiction of RNase 1 with a model membrane in the most energetically favorable orientation from PB calculations. In the images of Figures 3–5, the N-terminal helix is shown in the center-rear; and Arg and Lys (blue), and Asp and Glu (red) side chains are shown explicitly. *D*. Depiction of RNase 1 with model membrane in the least energetically favorable orientation from PB calculations.

Figure A3.4

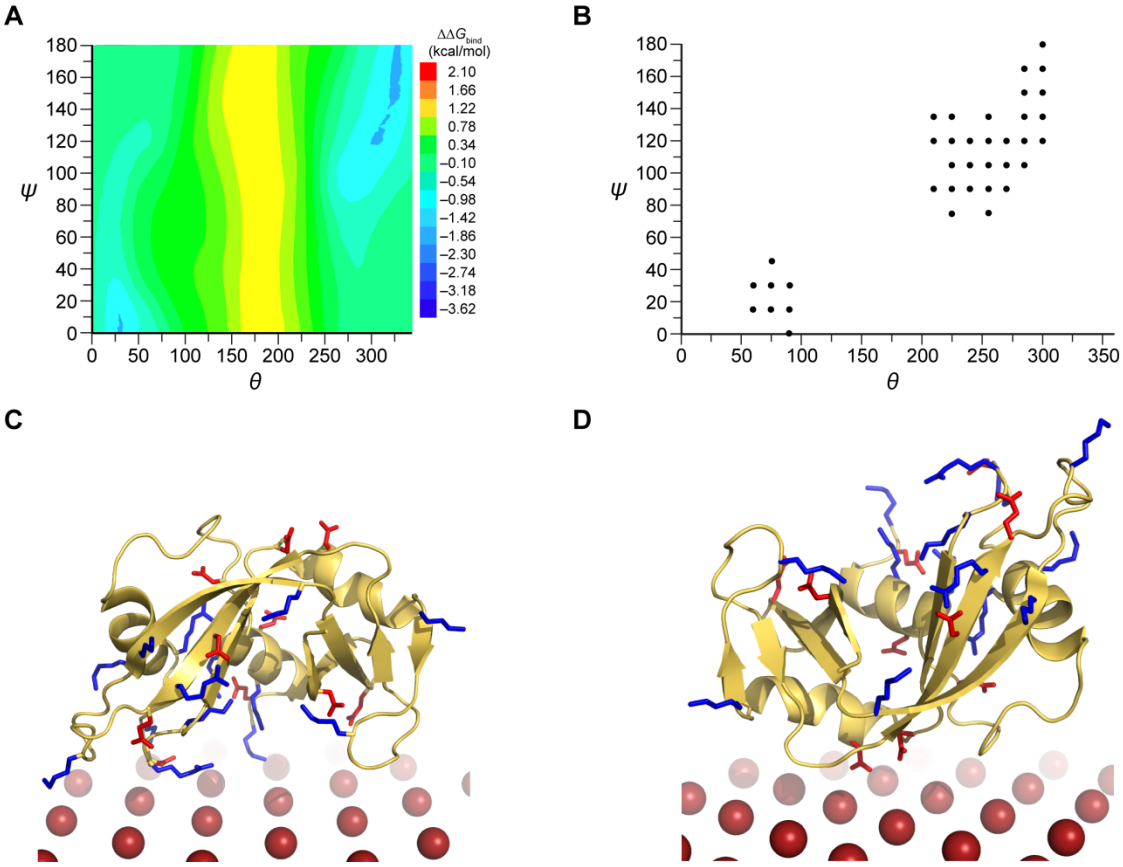
A
B
C
D
ΔΔG_bind (kcal/mol)
2.10
1.66
1.22
0.78
0.34
−0.10
−0.54
−0.98
−1.42
−1.86
−2.30
−2.74
−3.18
−3.62
ψ
θ

Figure A3.4 Computational calculation of the binding of RNase A to model membranes *A*. Poisson–Boltzmann calculations of the electrostatic free energy of interaction between RNase A (PDB entry 1KF5), rotated using Euler angles (θ = 0–360°; ψ = 0–180°; increments of 15°), with a model membrane with an anionic fraction of 1 electron per 130 $Å^2$. *B*. A coarse-grained representation of trajectories from a 2-ns IMM1–GC simulation that result in a protein·membrane complex. *C*. Depiction of RNase A with a model membrane in the most energetically favorable orientation from PB calculations. *D*. Depiction of RNase A with a model membrane in the least energetically favorable orientation from PB calculations.

Figure A3.5

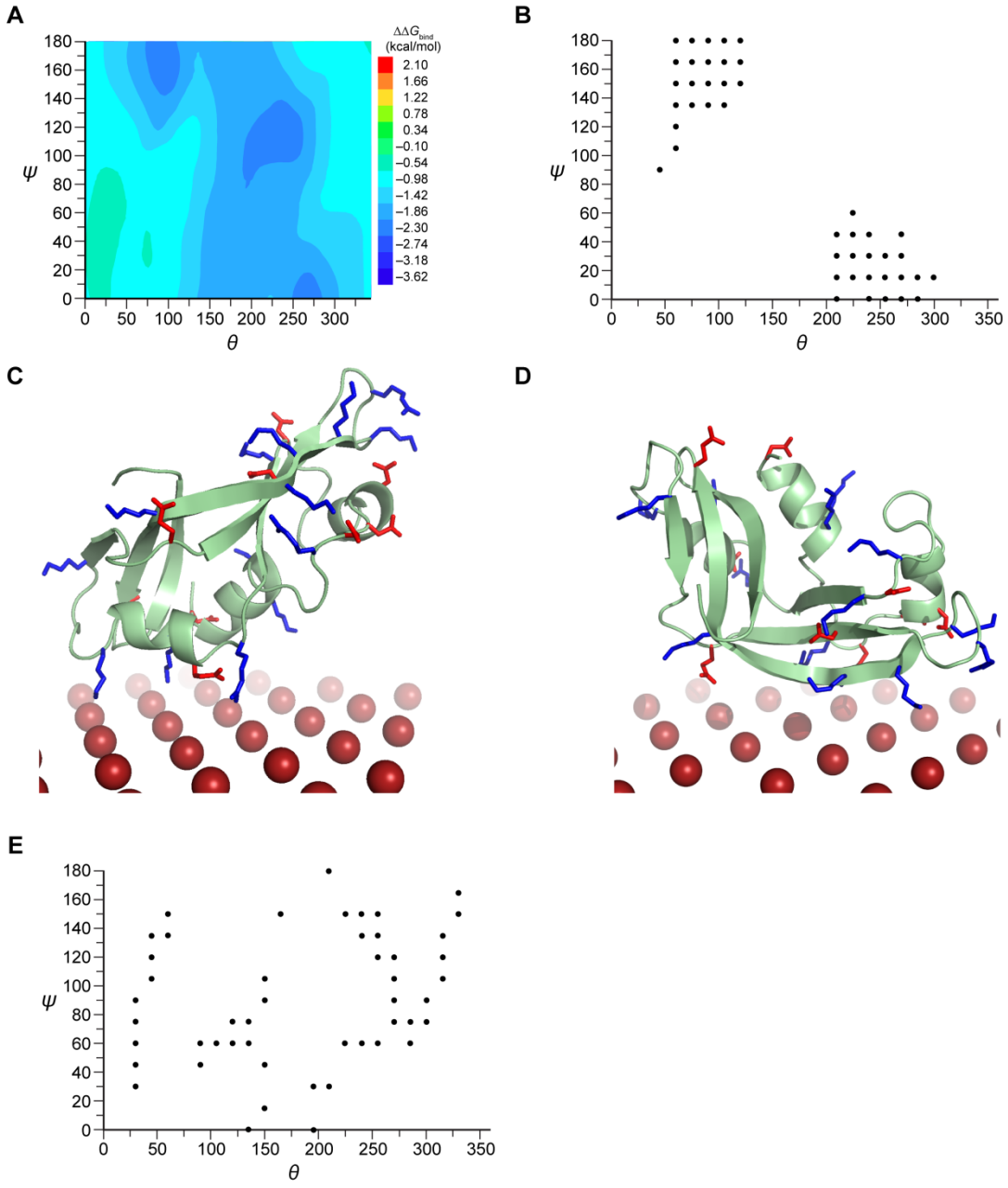
A
B
C
D
E
ΔΔG_bind (kcal/mol)
2.10
1.66
1.22
0.78
0.34
−0.10
−0.54
−0.98
−1.42
−1.86
−2.30
−2.74
−3.18
−3.62
ψ
θ

Figure A3.5 Computational calculation of ONC binding to model membranes

A. Poisson–Boltzmann calculations of the electrostatic free energy of interaction between ONC (PDB entry 1ONC), rotated using Euler angles (θ = 0–360°; ψ = 0–180°; increments of 15°), with a model membrane with an anionic fraction of 1 electron per 130 $Å^2$. *B*. A coarse-grained representation of trajectories from a 2-ns IMM1–GC simulation that result in a protein·membrane complex. *C*. Depiction of ONC with a model membrane in the most energetically favorable orientation from PB calculations. *D*. Depiction of ONC with a model membrane in the least energetically favorable orientation from PB calculations. *E*. A coarse-grained representation of trajectories from a 2-ns IMM1–GC simulation that do not result in a protein·membrane complex.

References

1. Central dogma of molecular biology. Crick, F. *Nature* **1970**, *227*, 561-563.

2. The noncoding RNA revolution-trashing old rules to forge new ones. Cech, T. R.; Steitz, J. A. *Cell* **2014**, *157*, 77-94.

3. Large-scale transcriptional activity in chromosomes 21 and 22. Kapranov, P.; Cawley, S. E.; Drenkow, J.; Bekiranov, S.; Strausberg, R. L.; Fodor, S. P.; Gingeras, T. R. *Science* **2002**, *296*, 916-919.

4. Finishing the euchromatic sequence of the human genome. International Human Genome Sequencing, C. *Nature* **2004**, *431*, 931-945.

5. The transcriptional landscape of the mammalian genome. Carninci, P.; Kasukawa, T.; Katayama, S.; Gough, J.; Frith, M. C.; Maeda, N.; Oyama, R.; Ravasi, T.; Lenhard, B.; Wells, C.; Kodzius, R.; Shimokawa, K.; Bajic, V. B.; Brenner, S. E.; Batalov, S.; Forrest, A. R.; Zavolan, M.; Davis, M. J.; Wilming, L. G.; Aidinis, V.; Allen, J. E.; Ambesi-Impiombato, A.; Apweiler, R.; Aturaliya, R. N.; Bailey, T. L.; Bansal, M.; Baxter, L.; Beisel, K. W.; Bersano, T.; Bono, H.; Chalk, A. M.; Chiu, K. P.; Choudhary, V.; Christoffels, A.; Clutterbuck, D. R.; Crowe, M. L.; Dalla, E.; Dalrymple, B. P.; de Bono, B.; Della Gatta, G.; di Bernardo, D.; Down, T.; Engstrom, P.; Fagiolini, M.; Faulkner, G.; Fletcher, C. F.; Fukushima, T.; Furuno, M.; Futaki, S.; Gariboldi, M.; Georgii-Hemming, P.; Gingeras, T. R.; Gojobori, T.; Green, R. E.; Gustincich, S.; Harbers, M.; Hayashi, Y.; Hensch, T. K.; Hirokawa, N.; Hill, D.; Huminiecki, L.; Iacono, M.; Ikeo, K.; Iwama, A.; Ishikawa, T.; Jakt, M.; Kanapin, A.; Katoh, M.; Kawasawa, Y.; Kelso, J.; Kitamura, H.; Kitano, H.; Kollias, G.; Krishnan, S. P.; Kruger, A.; Kummerfeld, S. K.; Kurochkin, I. V.; Lareau, L. F.; Lazarevic, D.; Lipovich, L.; Liu, J.; Liuni, S.; McWilliam, S.; Madan Babu, M.; Madera, M.; Marchionni, L.; Matsuda, H.; Matsuzawa, S.; Miki, H.; Mignone, F.; Miyake, S.; Morris, K.; Mottagui-Tabar, S.; Mulder, N.; Nakano, N.; Nakauchi, H.; Ng, P.; Nilsson, R.; Nishiguchi, S.; Nishikawa, S. *Science* **2005**, *309*, 1559-1563.

6. Antisense transcription in the mammalian transcriptome. Katayama, S.; Tomaru, Y.; Kasukawa, T.; Waki, K.; Nakanishi, M.; Nakamura, M.; Nishida, H.; Yap, C. C.; Suzuki, M.; Kawai, J.; Suzuki, H.; Carninci, P.; Hayashizaki, Y.; Wells, C.; Frith, M.; Ravasi, T.; Pang, K. C.; Hallinan, J.; Mattick, J.; Hume, D. A.; Lipovich, L.; Batalov, S.; Engstrom, P. G.; Mizuno, Y.; Faghihi, M. A.; Sandelin, A.; Chalk, A. M.; Mottagui-Tabar, S.; Liang, Z.; Lenhard, B.; Wahlestedt, C.; Group, R. G. E. R.; Genome Science, G.; Consortium, F. *Science* **2005**, *309*, 1564-1566.

7. Landscape of transcription in human cells. Djebali, S.; Davis, C. A.; Merkel, A.; Dobin, A.; Lassmann, T.; Mortazavi, A.; Tanzer, A.; Lagarde, J.; Lin, W.; Schlesinger, F.; Xue, C.; Marinov, G. K.; Khatun, J.; Williams, B. A.; Zaleski, C.; Rozowsky, J.; Roder, M.; Kokocinski, F.; Abdelhamid, R. F.; Alioto, T.; Antoshechkin, I.; Baer, M. T.; Bar, N. S.; Batut, P.; Bell, K.; Bell, I.; Chakrabortty, S.; Chen, X.; Chrast, J.; Curado, J.; Derrien, T.; Drenkow, J.; Dumais, E.; Dumais, J.; Duttagupta, R.; Falconnet, E.; Fastuca, M.; Fejes-Toth, K.; Ferreira, P.; Foissac, S.; Fullwood, M. J.; Gao, H.; Gonzalez, D.; Gordon, A.; Gunawardena, H.; Howald, C.; Jha, S.; Johnson, R.; Kapranov, P.; King, B.; Kingswood, C.; Luo, O. J.; Park, E.; Persaud, K.; Preall, J. B.; Ribeca, P.; Risk, B.; Robyr, D.; Sammeth, M.; Schaffer, L.; See, L. H.; Shahab, A.; Skancke, J.; Suzuki, A. M.; Takahashi, H.; Tilgner, H.; Trout, D.; Walters, N.; Wang, H.; Wrobel, J.; Yu, Y.; Ruan, X.; Hayashizaki, Y.; Harrow, J.; Gerstein, M.; Hubbard, T.; Reymond, A.; Antonarakis, S. E.; Hannon, G.; Giddings, M. C.; Ruan, Y.; Wold, B.; Carninci, P.; Guigo, R.; Gingeras, T. R. *Nature* **2012**, *489*, 101-108.

8. The many pathways of RNA degradation. Houseley, J.; Tollervey, D. *Cell* **2009**, *136*, 763-776.

9. Ribonucleases P/MRP and the expanding ribonucleoprotein world. Hernandez-Cid, A.; Aguirre-Sampieri, S.; Diaz-Vilchis, A.; Torres-Larios, A. *IUBMB Life* **2012**, *64*, 521-528.

10. T2 Family ribonucleases: Ancient enzymes with diverse roles. Luhtala, N.; Parker, R. *Trends Biochem Sci* **2010**, *35*, 253-259.

11. Ribonuclease H: The enzymes in eukaryotes. Cerritelli, S. M.; Crouch, R. J. *FEBS J* **2009**, *276*, 1494-1505.

12. Secondary structures involving the poly(A) tail and other 3' sequences are major determinants of mRNA isoform stability in yeast. Moqtaderi, Z.; Geisberg, J. V.; Struhl, K. *Microb Cell* **2014**, *1*, 137-139.

13. A day in the life of the spliceosome. Matera, A. G.; Wang, Z. *Nat Rev Mol Cell Biol* **2014**, *15*, 108-121.

14. The RNase A superfamily: Generation of diversity and innate host defense. Dyer, K. D.; Rosenberg, H. F. *Mol Divers* **2006**, *10*, 585-597.

15. The ribonuclease A superfamily of mammals and birds: Identifying new members and tracing evolutionary histories. Cho, S.; Beintema, J. J.; Zhang, J. *Genomics* **2005**, *85*, 208-220.

16. Mapping, phylogenetic and expression analysis of the RNase (RNaseA) locus in cattle. Wheeler, T. T.; Maqbool, N. J.; Gupta, S. K. *J Mol Evol* **2012**, *74*, 237-248.

17. Characterization of ribonucleases and ribonuclease inhibitor in subcellular fractions from rat adrenals. Girija, N. S.; Sreenivasan, A. *Biochem J* **1966**, *98*, 562-566.

18. Recombinant human eosinophil-derived neurotoxin/RNase 2 functions as an effective antiviral agent against respiratory syncytial virus. Domachowske, J. B.; Dyer, K. D.; Bonville, C. A.; Rosenberg, H. F. *J Infect Dis* **1998**, *177*, 1458-1464.

19. Eosinophil-derived neurotoxin (EDN), an antimicrobial protein with chemotactic activities for dendritic cells. Yang, D.; Rosenberg, H. F.; Chen, Q.; Dyer, K. D.; Kurosaka, K.; Oppenheim, J. J. *Blood* **2003**, *102*, 3396-3403.

20. Eosinophil-derived neurotoxin acts as an alarmin to activate the TLR2-MyD88 signal pathway in dendritic cells and enhances Th2 immune responses. Yang, D.; Chen, Q.; Su, S. B.; Zhang, P.; Kurosaka, K.; Caspi, R. R.; Michalek, S. M.; Rosenberg, H. F.; Zhang, N.; Oppenheim, J. J. *J Exp Med* **2008**, *205*, 79-90.

21. Isolation of angiogenin from normal human plasma. Shapiro, R.; Strydom, D. J.; Olson, K. A.; Vallee, B. L. *Biochemistry* **1987**, *26*, 5141-5146.

22. Specific binding of angiogenin to calf pulmonary artery endothelial cells. Badet, J.; Soncin, F.; Guitton, J. D.; Lamare, O.; Cartwright, T.; Barritault, D. *Proc Natl Acad Sci USA* **1989**, *86*, 8427-8431.

23. Antimicrobial RNases of human skin. Zasloff, M. *J Invest Dermatol* **2009**, *129*, 2091-2093.

24. RNase 8, a novel RNase A superfamily ribonuclease expressed uniquely in placenta. Zhang, J.; Dyer, K. D.; Rosenberg, H. F. *Nucleic Acids Res* **2002**, *30*, 1169-1175.

25. Molecular cloning and characterization of a novel human ribonuclease (RNase k6): Increasing diversity in the enlarging ribonuclease gene family. Rosenberg, H. F.; Dyer, K. D. *Nucleic Acids Res* **1996**, *24*, 3507-3513.

26. Impaired sperm maturation in RNase9 knockout mice. Westmuckett, A. D.; Nguyen, E. B.; Herlea-Pana, O. M.; Alvau, A.; Salicioni, A. M.; Moore, K. L. *Biol Reprod* **2014**, *90*, 1-10.

27. Epididymal protein RNase10 is required for post-testicular sperm maturation and male fertility. Krutskikh, A.; Poliandri, A.; Cabrera-Sharp, V.; Dacheux, J. L.; Poutanen, M.; Huhtaniemi, I. *FASEB J* **2012**, *26*, 4198-4209.

28. Ribonuclease A. Raines, R. T. *Chem Rev* **1998**, *98*, 1045-1066.

29. Tertiary structure of ribonuclease. Kartha, G.; Bello, J.; Harker, D. *Nature* **1967**, *213*, 862-865.

30. The nuclear magnetic resonance spectrum of ribonuclease. Saunders, M.; Wishnia, A.; Kirkwood, J. G. *J Am Chem Soc* **1957**, *79*, 3289-3290.

31. Principles that govern the folding of protein chains. Anfinsen, C. B. *Science* **1973**, *181*, 223-230.

32. Disruption of shape-complementarity markers to create cytotoxic variants of ribonuclease A. Rutkoski, T. J.; Kurten, E. L.; Mitchell, J. C.; Raines, R. T. *J Mol Biol* **2005**, *354*, 41-54.

33. Catalysis by ribonuclease A is limited by the rate of substrate association. Park, C.; Raines, R. T. *Biochemistry* **2003**, *42*, 3509-3518.

34. Structural determinants of enzymatic processivity. delCardayre, S. B.; Raines, R. T. *Biochemistry* **1994**, *33*, 6031-6037.

35. A residue to residue hydrogen bond mediates the nucleotide specificity of ribonuclease A. delCardayré, S. B.; Raines, R. T. *J Mol Biol* **1995**, *252*, 328-336.

36. The extent to which ribonucleases cleave ribonucleic acid. delCardayré, S. B.; Raines, R. T. *Anal Biochem* **1995**, *225*, 176-178.

37. Correlation proton magnetic resonance studies at 250 MHz of bovine pancreatic ribonuclease. I. Reinvestigation of the histidine peak assignment. Markley, J. L. *Biochemistry* **1975**, *14*, 3546-3553.

38. Biological function of pancreatic ribonuclease. Barnard, E. A. *Nature* **1969**, *221*, 340-344.

39. Fluorescence assay for the binding of ribonuclease A to the ribonuclease inhibitor protein. Abel, R. L.; Haigis, M. C.; Park, C.; Raines, R. T. *Anal Biochem* **2002**, *306*, 100-107.

40. Inhibition of human pancreatic ribonuclease by the human ribonuclease inhibitor protein. Johnson, R. J.; McCoy, J. G.; Bingman, C. A.; Phillips, G. N., Jr.; Raines, R. T. *J Mol Biol* **2007**, *368*, 434-449.

41. Cytotoxic potential of ribonuclease and ribonuclease hybrid proteins. Rybak, S.; Saxena, S.; Ackerman, E.; Youle, R. *J Biol Chem* **1991**, *266*, 21202-21207.

42. Glycosylation of serum ribonuclease 1 indicates a major endothelial origian and reveals an increase in core fucosylation in pancreatic cancer. Barrabés, S.; Pagès-Pons, L.; Radcliffe, C. M.; Tabarés, G.; Fort, E.; Royle, L.; Harvey, D. J.; Moenner, M.; Dwek, R. A.; Rudd, P. M.; De Llorens, R.; Peracaula, R. *Glycobiology* **2007**, *17*, 388-400.

43. Immunological assay of pancreatic ribonuclease in serum as an indicator of pancreatic cancer. Weickmann, J. L.; Olson, E. M.; Glitz, D. G. *Cancer Res* **1984**, *44*, 1682-1687.

44. Expression and localisation of vascular ribonucleases in endothelial cells. Fischer, S.; Nishio, M.; Dadkhahi, S.; Gansler, J.; Saffarzadeh, M.; Shibamiyama, A.; Kral, N.; Baal, N.; Koyama, T.; Deindl, E.; Preissner, K. T. *Thromb Haemost* **2011**, *105*, 345-355.

45. The amino acid sequence of human pancreatic ribonuclease. Beintema, J. J.; Wietzes, P.; Weickmann, J. L.; Glitz, D. G. *Anal Biochem* **1984**, *136*, 48-64.

46. Muscle protein catabolism in the septic patient as measured by 3-methylhistidine excretion. Long, C. L.; Schiller, W. R.; Blakemore, W. S.; Geiger, J. W.; O'Dell, M.; Henderson, K. *Am J Clin Nutr* **1977**, *30*, 1349-1352.

47. Effect of disease states on the ribonuclease concentration of body fluids. Levy, A. L.; Rottino, A. *Clin Chem* **1960**, *6*, 43-51.

48. Serum ribonuclease in patients with malignant disease. Zytko, J.; Cantero, A. *Can Med Assoc J* **1962**, *86*, 482-485.

49. Changes in serum and urinary ribonuclease activity in surgically treated cases of digestive organ tumors and various other diseases. Hisada, T. *Iryo* **1969**, *23*, 613-625.

50. Effects of recombinant leukocyte interferon on ribonuclease activities in serum in chronic hepatitis B. Tsuji, H.; Murai, K.; Akagi, K.; Fujishima, M. *Clin Chem* **1990**, *36*, 913-916.

51. Human ribonuclease A superfamily members, eosinophil-derived neurotoxin and pancreatic ribonuclease, induce dendritic cell maturation and activation. Yang, D.; Chen, Q.; Rosenberg, H.; Rybak, S.; Newton, D.; Wang, Z.; Fu, Q.; Tchernev, V.; Wang, M.; Schweitzer, B. *J Immunol* **2004**, *173*, 6134-6142.

52. Human pancreatic ribonuclease presents higher endonucleolytic activity than ribonuclease A. Rodriguez, M.; Moussaoui, M.; Benito, A.; Cuchillo, C. M.; Nogues, M. V.; Vilanova, M. *Arch Biochem Biophys* **2008**, *471*, 191-197.

53. Degradation of double-stranded RNA by human pancreatic ribonuclease: crucial role of noncatalytic basic amino acid residue. Sorrentino, S.; Naddeo, M.; Russo, A.; D'Alessio, G. *Biochemistry* **2003**, *42*, 10182-10190.

54. Circulating microRNAs as stable blood-based markers for cancer detection. Mitchell, P. S.; Parkin, R. K.; Kroh, E. M.; Fritz, B. R.; Wyman, S. K.; Pogosova-Agadjanyan, E. L.; Peterson, A.; Noteboom, J.; O'Briant, K. C.; Allen, A.; Lin, D. W.; Urban, N.; Drescher, C. W.; Knudsen, B. S.; Stirewalt, D. L.; Gentleman, R.; Vessella, R. L.; Nelson, P. S.; Martin, D. B.; Tewari, M. *Proc Natl Acad Sci USA* **2008**, *105*, 10513-10518.

55. A robust methodology to study urine microRNA as tumor marker: microRNA-126 and microRNA-182 are related to urinary bladder cancer. Hanke, M.; Hoefig, K.; Merz, H.;

Feller, A. C.; Kausch, I.; Jocham, D.; Warnecke, J. M.; Sczakiel, G. *Urol Oncol* **2010**, *28*, 655-661.

56. Salivary microRNA: Discovery, characterization, and clinical utility for oral cancer detection. Park, N. J.; Zhou, H.; Elashoff, D.; Henson, B. S.; Kastratovic, D. A.; Abemayor, E.; Wong, D. T. *Clin Cancer Res* **2009**, *15*, 5473-5477.

57. Extracellular 'communicator RNA'. Benner, S. A. *FEBS Lett* **1988**, *233*, 225-228.

58. Exosome-mediated transfer of mRNAs and microRNAs is a novel mechanism of genetic exchange between cells. Valadi, H.; Ekstrom, K.; Bossios, A.; Sjostrand, M.; Lee, J. J.; Lotvall, J. O. *Nat Cell Biol* **2007**, *9*, 654-659.

59. Extracellular RNA liberates tumor necrosis factor-alpha to promote tumor cell trafficking and progression. Fischer, S.; Gesierich, S.; Griemert, B.; Schanzer, A.; Acker, T.; Augustin, H. G.; Olsson, A. K.; Preissner, K. T. *Cancer Res* **2013**, *73*, 5080-5089.

60. Host-derived extracellular nucleic acids enhance innate immune responses, induce coagulation, and prolong survival upon infection in insects. Altincicek, B.; Stotzel, S.; Wygrecka, M.; Preissner, K. T.; Vilcinskas, A. *J Immunol* **2008**, *181*, 2705-2712.

61. Circulating microRNAs as biomarkers and potential paracrine mediators of cardiovascular disease. Gupta, S. K.; Bang, C.; Thum, T. *Circ Cardiovasc Genet* **2010**, *3*, 484-488.

62. Circulating microRNAs, potential biomarkers for drug-induced liver injury. Wang, K.; Zhang, S.; Marzolf, B.; Troisch, P.; Brightman, A.; Hu, Z.; Hood, L. E.; Galas, D. J. *Proc Natl Acad Sci USA* **2009**, *106*, 4402-4407.

63. Human traumatic brain injury alters plasma microRNA levels. Redell, J. B.; Moore, A. N.; Ward, N. H., 3rd; Hergenroeder, G. W.; Dash, P. K. *J Neurotrauma* **2010**, *27*, 2147-2156.

64. Extracellular RNA constitutes a natural procoagulant cofactor in blood coagulation. Kannemeier, C.; Shibamiya, A.; Nakazawa, F.; Trusheim, H.; Ruppert, C.; Markart, P.; Song, Y.; Tzima, E.; Kennerknecht, E.; Niepmann, M.; von Bruehl, M. L.; Sedding, D.; Massberg, S.; Gunther, A.; Engelmann, B.; Preissner, K. T. *Proc Natl Acad Sci USA* **2007**, *104*, 6388-6393.

65. Extracellular RNA is a natural cofactor for the (auto-)activation of Factor VII-activating protease (FSAP). Nakazawa, F.; Kannemeier, C.; Shibamiya, A.; Song, Y.; Tzima, E.; Schubert, U.; Koyama, T.; Niepmann, M.; Trusheim, H.; Engelmann, B.; Preissner, K. T. *Biochem J* **2005**, *385*, 831-838.

66. A synapomorphic disulfide bond is critical for the conformational stability and cytotoxicity of an amphibian ribonuclease. Leland, P. A.; Staniszewski, K. E.; Kim, B.-M.; Raines, R. T. *FEBS Lett* **2000**, *477*, 203-207.

67. Cytostatic and cytotoxic effects of Pannon (P-30 Protein), a novel anticancer agent. Darzynkiewicz, Z.; Carter, S. P.; Mikulski, S. M.; Ardelt, W. J.; Shogen, K. *Cell Tissue Kinet* **1988**, *21*, 169-182.

68. Enhancement of activation-induced apoptosis of lymphocytes by the cytotoxic ribonuclease Onconase (Ranpirnase). Halicka, D. H.; Pozarowski, P.; Ita, M.; Ardelt, W. J.; Mikulski, S. M.; Shogen, K.; Darzynkiewicz, Z. *Int J Oncol* **2002**, *21*, 1245-1250.

69. Enhancement of vincristine cytotoxicity in drug-resistant cells by simultaneous treatment with Onconase, an antitumor ribonuclease. Rybak, S. M.; Pearson, J. W.; Fogler, W. E.; Volker, K.; Spence, S. E.; Newton, D. L.; Mikulski, S. M.; Ardelt, W.; Riggs, C. W.; Kung, H. F.; Longo, D. L. *J Natl Cancer Inst* **1996**, *88*, 747-753.

70. Antitumor efficacy of the cytotoxic RNase, Ranpirnase, on A549 human lung cancer xenografts of nude mice. Lee, I.; Kalota, A.; Gewirtz, A. M.; Shogen, K. *Anticancer Res* **2007**, *27*, 299-307.

71. Phase I human clinical trial of Onconase (P-30 Protein) administered intravenously on a weekly schedule in cancer patients with solid tumors. Mikulski, S. M.; Grossman, A. M.; Carter, P. W.; Shogen, K.; Costanzi, J. J. *Int J Oncol* **1993**, *3*, 57-64.

72. Functional evolution of ribonuclease inhibitor: insights from birds and reptiles. Lomax, J. E.; Bianchetti, C. M.; Chang, A.; Phillips, G. N., Jr.; Fox, B. G.; Raines, R. T. *J Mol Biol* **2014**, *426*, 3041-3056.

73. Ribonucleases as a novel pro-apoptotic anticancer strategy: review of the preclinical and clinical data for Ranpirnase. Costanzi, J.; Sidransky, D.; Navon, A.; Goldsweig, H. *Cancer Invest* **2005**, *23*, 643-650.

74. Reversible nephrotoxicity of Onconase and effect of lysine pH on renal Onconase uptake. Vasandani, V. M.; Burris, J. A.; Sung, C. *Cancer Themother Pharmacol* **1999**, *44*, 164-169.

75. Antitumor activity of ribonuclease multimers created by site-specific covalent tethering. Rutkoski, T. J.; Kink, J. A.; Strong, L. E.; Schilling, C. I.; Raines, R. T. *Bioconjugate Chemistry* **2010**, *21*, 1691-1702.

76. Human ribonuclease with a pendant poly(ethylene glycol) inhibits tumor growth in mice. Rutkoski, T. J.; Kink, J. A.; Strong, L. E.; Raines, R. T. *Transl Oncol* **2013**, *6*, 392-397.

77. Site-specific PEGylation endows a mammalian ribonuclease with antitumor activity. Rutkoski, T. J.; Kink, J. A.; Strong, L. E.; Raines, R. T. *Cancer Biology & Therapy* **2011**, *12*, 208-214.

78. Glycans in cancer and inflammation--potential for therapeutics and diagnostics. Dube, D. H.; Bertozzi, C. R. *Nat Rev Drug Discovery* **2005**, *4*, 477-488.

79. Fluorogenic probe for constitutive cellular endocytosis. Levine, M. N.; Hoang, T. T.; Raines, R. T. *Chem Biol* **2013**, *20*, 614-618.

80. Increased N-glycosylation of Asn(88) in serum pancreatic ribonuclease 1 is a novel diagnostic marker for pancreatic cancer. Nakata, D. *Sci Rep* **2014**, *4*, 6715-6723.

81. The solution structure of a cytotoxic ribonuclease from the oocytes of *Rana catesbeiana* (bullfrog). Chang, C. F.; Chen, C.; Chen, Y. C.; Hom, K.; Huang, R. F.; Huang, T. H. *J Mol Biol* **1998**, *283*, 231-244.

82. Isolation and characterization of *Rana catesbeiana* lectin and demonstration of the lectin-binding glycoprotein of rodent and human tumor cell membranes. Nitta, K.; Takayanagi, G.; Kawauchi, H.; Hakomori, S. *Cancer Res* **1987**, *47*, 4877-4883.

83. A cytotoxic ribonuclease. Study of the mechanism of Onconase cytotoxicity. Wu, Y.; Mikulski, S. M.; Ardelt, W.; Rybak, S. M.; Youle, R. J. *J Biol Chem* **1993**, *268*, 10686-10693.

84. Secretory ribonucleases are internalized by a dynamin-independent endocytic pathway. Haigis, M. C.; Raines, R. T. *J Cell Sci* **2003**, *116*, 313-324.

85. Expression of receptors for human angiogenin in vascular smooth muscle cells. Hatzi, E.; Badet, J. *Eur J Biochem* **1999**, *260*, 825-832.

86. Basic fibroblast growth factor (FGF-2) internalization through the heparan sulfate proteoglycans-mediated pathway: an ultrastructural approach. Gleizes, P. E.; Noaillac-Depeyre, J.; Amalric, F.; Gas, N. *Eur J Cell Biol* **1995**, *66*, 47-59.

87. Increasing the potency of a cytotoxin with an arginine graft. Fuchs, S. M.; Rutkoski, T. J.; Kung, V. M.; Groeschl, R. T.; Raines, R. T. *Protein Eng Des Sel* **2007**, *20*, 505-509.

88. Cellular uptake of ribonuclease A relies on anionic glycans. Chao, T. Y.; Lavis, L. D.; Raines, R. T. *Biochemistry* **2010**, *49*, 10666-10673.

89. Cytotoxic ribonucleases: the dichotomy of Coulombic forces. Johnson, R. J.; Chao, T. Y.; Lavis, L. D.; Raines, R. T. *Biochemistry* **2007**, *46*, 10308-10316.

90. Mechanism of Ribonuclease A endocytosis: analogies to cell-penetrating peptides. Chao, T. Y.; Raines, R. T. *Biochemistry* **2011**, *50*, 8374-8382.

91. Onconase cytotoxicity relies on the distribution of its positive charge. Turcotte, R. F.; Lavis, L. D.; Raines, R. T. *FEBS J* **2009**, *276*, 3846-3857.

92. Contribution of electrostatics to the binding of pancreatic-type ribonucleases to membranes. Sundlass, N. K.; Eller, C. H.; Cui, Q.; Raines, R. T. *Biochemistry* **2013**, *52*, 6304-6312.

93. Localization of the permeability barrier to solutes in isolated arteries by confocal microscopy. van Haaren, P. M.; VanBavel, E.; Vink, H.; Spaan, J. A. *Am J Physiol Heart Circ Physiol* **2003**, *285*, 2848-2856.

94. The endothelial glycocalyx: composition, functions, and visualization. Reitsma, S.; Slaaf, D.; Vink, H.; van Zandvoort, M.; oude Egbrink, M. *Pflüeg Arch Eur J Physiol* **2007**, *454*, 345-359.

95. The structure of glycosaminoglycans and their interactions with proteins. Gandhi, N. S.; Mancera, R. L. *Chem Biol Drug Des* **2008**, *72*, 455-482.

96. Neutrophil cell surface receptors and their intracellular signal transduction pathways. Futosi, K.; Fodor, S.; Mocsai, A. *Int Immunopharmacol* **2013**, *17*, 638-650.

97. Integrin signaling. LaFlamme, S. E.; Auer, K. L. *Semin Cancer Biol* **1996**, *7*, 111-118.

98. Cellular electrophoretic mobility data: A first approach to a database. Slivinsky, G. G.; Hymer, W. C.; Bauer, J.; Morrison, D. R. *Electrophoresis* **1997**, *18*, 1109-1119.

99. The eight human "canonical" ribonucleases: molecular diversity, catalytic properties, and special biological actions of the enzyme proteins. Sorrentino, S. *Febs Lett* **2010**, *584*, 2194-2200.

100. Pathways of clathrin-independent endocytosis. Mayor, S.; Pagano, R. E. *Nat Rev Mol Cell Biol* **2007**, *8*, 603-612.

101. Ruminal temperature may aid in the detection of subacute ruminal acidosis. AlZahal, O.; Kebreab, E.; France, J.; Froetschel, M.; McBride, B. *J Dairy Sci* **2008**, *91*, 202-207.

102. Dietary regulation of pancreatic enzyme synthesis, secretion and inactivation in the rat. Snook, J. T. *J Nutr* **1965**, *87*, 297-305.

103. Serum RNase in the diagnosis of pancreatic carcinoma. Peterson, L. M. *Proc Natl Acad Sci USA* **1979**, *76*, 2630-2634.

104. Glycosylation of serum ribonuclease 1 indicates a major endothelial origin and reveals an increase in core fucosylation in pancreatic cancer. Barrabés, S.; Pagès-Pons, L.; Radcliffe, C. M.; Tabarés, G.; Fort, E.; Royle, L.; Harvey, D. J.; Moenner, M.; Dwek, R. A.; Rudd, P. M.; De Llorens, R.; Peracaula, R. *Glycobiology* **2007**, *17*, 388-400.

105. Increased ribonuclease expression reduces inflammation and prolongs survival in TLR7 transgenic mice. Sun, X.; Wiedeman, A.; Agrawal, N.; Teal, T. H.; Tanaka, L.; Hudkins, K. L.; Alpers, C. E.; Bolland, S.; Buechler, M. B.; Hamerman, J. A.; Ledbetter, J. A.; Liggitt, D.; Elkon, K. B. *J Immunol* **2013**, *190*, 2536-2543.

106. RNase therapy assessed by magnetic resonance imaging reduces cerebral edema and infarction size in acute stroke. Walberer, M.; Tschernatsch, M.; Fischer, S.; Ritschel, N.; Volk, K.; Friedrich, C.; Bachmann, G.; Mueller, C.; Kaps, M.; Nedelmann, M.; Blaes, F.; Preissner, K. T.; Gerriets, T. *Curr Neurovasc Res* **2009**, *6*, 12-19.

107. Role of extracellular RNA in atherosclerotic plaque formation in mice. Simsekyilmaz, S.; Cabrera-Fuentes, H. A.; Meiler, S.; Kostin, S.; Baumer, Y.; Liehn, E. A.; Weber, C.; Boisvert, W. A.; Preissner, K. T.; Zernecke, A. *Circulation* **2014**, *129*, 598-606.

108. Evasion of ribonuclease inhibitor as a determinant of ribonuclease cytotoxicity. Rutkoski, T. J.; Raines, R. T. *Curr Pharm Biotechnol* **2008**, *9*, 185-189.

109. Effects of a second-generation human anti-ErbB2 immunoRNase on trastuzumab-resistant tumors and cardiac cells. D'Avino, C.; Paciello, R.; Riccio, G.; Coppola, M.; Laccetti, P.; Maurea, N.; Raines, R. T.; De Lorenzo, C. *Protein Eng Des Select* **2014**, *27*, 83-88.

110. Strong, L. E.; Kink, J. A.; Pensinger, D; Mei, B.; Shahan, M.; Raines, R. T. (2012) Efficacy of ribonuclease QBI-139 in combination with standard of care therapies. *Cancer Res.* **72** (Suppl. 1), 1838

111. Strong, L. E.; Kink, J. A.; Mei, B.; Shahan, M. N.; Raines, R. T. (2012) First in human phase I clinical trial of QBI-139, a human ribonuclease variant, in solid tumors. *J. Clin. Oncol.* **30** (Suppl.), TPS3113.

112. Inclusion of cetaceans within the order Artiodactyla based on phylogenetic analysis of pancreatic ribonuclease genes. Kleineidam, R. G.; Pesole, G.; Breukelman, H. J.; Beintema, J. J.; Kastelein, R. A. *J Mol Evol* **1999**, *48*, 360-368.

113. Molecular evolution of genes encoding ribonucleases in ruminant species. Confalone, E.; Beintema, J. J.; Sasso, M. P.; Carsana, A.; Palmieri, M.; Vento, M. T.; Furia, A. *J Mol Evol* **1995**, *41*, 850-858.

114. Ribonucleases in ruminants. Beintema, J. J. *Science* **2002**, *297*, 1121-1122.

115. Seminal RNase: A unique member of the ribonuclease superfamily. D'Alessio, G.; Di Donato, A.; Parente, A.; Piccoli, R. *Trends Biochem Sci* **1991**, *16*, 106-108.

116. Ribonucleases and their antitumor activity. Matoušek, J. *Comp Biochem Physiol* **2001**, *129C*, 175-191.

117. Primary structure of a ribonuclease from bovine brain. Watanabe, H.; Katoh, H.; Ishii, M.; Komoda, Y.; Sanda, A.; Takizawa, Y.; Ohgi, K.; Irie, M. *J Biochem* **1988**, *104*, 939-945.

118. Characterization of a ribonuclease from bovine brain. Elson, M.; Glitz, D. G. *Biochemistry* **1975**, *14*, 1471-1476.

119. A gene atlas of the mouse and human protein-encoding transcriptomes. Su, A. I.; Wiltshire, T.; Batalov, S.; Lapp, H.; Ching, K. A.; Block, D.; Zhang, J.; Soden, R.; Hayakawa, M.; Kreiman, G.; Cooke, M. P.; Walker, J. R.; Hogenesch, J. B. *Proc Natl Acad Sci USA* **2004**, *101*, 6062-6067.

120. Parallel functional changes in the digestive RNases of ruminants and colobines by divergent amino acid substitutions. Zhang, J. *Mol Biol Evol* **2003**, *20*, 1310-1317.

121. Tuning the pK_a of fluorescein to optimize binding assays. Lavis, L. D.; Rutkoski, T. J.; Raines, R. T. *Anal Chem* **2007**, *79*, 6775-6782.

122. Intraspecies regulation of ribonucleolytic activity. Johnson, R. J.; Lavis, L. D.; Raines, R. T. *Biochemistry* **2007**, *46*, 13131-13140.

123. Cytotoxicity of bovine seminal ribonuclease: Monomer versus dimer. Lee, J. E.; Raines, R. T. *Biochemistry* **2005**, *44*, 15760-15767.

124. High-throughput melting-temperature analysis of a monoclonal antibody by differential scanning fluorimetry in the presence of surfactants. Menzen, T.; Friess, W. *J Pharm Sci* **2013**, *102*, 415-428.

125. The use of differential scanning fluorimetry to detect ligand interactions that promote protein stability. Niesen, F. H.; Berglund, H.; Vedadi, M. *Nat Protoc* **2007**, *2*, 2212-2221.

126. Rational design and evaluation of mammalian ribonuclease cytotoxins. Lomax, J. E.; Eller, C. H.; Raines, R. T. *Methods in Enzymology* **2012**, *502*, 273-290.

127. Hypersensitive substrate for ribonucleases. Kelemen, B. R.; Klink, T. A.; Behlke, M. A.; Eubanks, S. R.; Leland, P. A.; Raines, R. T. *Nucleic Acids Res* **1999**, *27*, 3696-3701.

128. Degradation of double-stranded RNA by mammalian pancreatic-type ribonucleases. Libonati, M.; Sorrentino, S. *Methods Enzymol* **2001**, *341*, 234-248.

129. Membrane binding of pH-sensitive influenza fusion peptides. positioning, configuration, and induced leakage in a lipid vesicle model. Esbjörner, E.; Oglecka, K.; Lincoln, P.; Gräslund, A.; Norden, B. *Biochemistry* **2007**, *46*, 13490-13504.

130. Mechanism of leakage of contents of membrane vesicles determined by fluorescence requenching. Ladokhin, A. S.; Wimley, W. C.; Hristova, K.; White, S. H. *Methods Enzymol* **1997**, *278*, 474-486.

131. A versatile negative-staining ribonuclease zymogram. Bravo, J.; Fernández, E.; Ribó, M.; de Llorens, R.; Cuchillo, C. M. *Anal Biochem* **1994**, *219*, 82-86.

132. MUSCLE: multiple sequence alignment with high accuracy and high throughput. Edgar, R. C. *Nucleic Acids Res* **2004**, *32*, 1792-1797.

133. The rapid generation of mutation data matrices from protein sequences. Jones, D. T.; Taylor, W. R.; Thornton, J. M. *Comput Appl Biosci* **1992**, *8*, 275-282.

134. Molecular cloning of the gene encoding the bovine brain ribonuclease and its expression in different regions of the brain. Sasso, M. P.; Carsana, A.; Confalone, E.; Cosi, C.; Sorrentino, S.; Viola, M.; Palmieri, M.; Russo, E.; Furia, A. *Nucleic Acids Res* **1991**, *19*, 6469-6474.

135. Ruminant brain ribonucleases: expression and evolution. Zhao, W.; Confalone, E.; Breukelman, H. J.; Sasso, M. P.; Jekel, P. A.; Hodge, E.; Furia, A.; Beintema, J. J. *Biochim Biophys Acta* **2001**, *1547*, 95-103.

136. Antitumor action of seminal ribonuclease, its dimeric structure, and its resistance to the cytosolic ribonuclease inhibitor. Antignani, A.; Naddeo, M.; Cubellis, M. V.; Russo, A.; D'Alessio, G. *Biochemistry* **2001**, *40*, 3492-3496.

137. Adaptive evolution of a duplicated pancreatic ribonuclease gene in a leaf-eating monkey. Zhang, J.; Zhang, Y. P.; Rosenberg, H. F. *Nat Genet* **2002**, *30*, 411-415.

138. Role of unique basic residues of human pancreatic ribonuclease in its catalysis and structural stability. Dey, P.; Islam, A.; Ahmad, F.; Batra, J. K. *Biochem Biophys Res Commun* **2007**, *360*, 809-814.

139. Human endothelial cells selectively express large amounts of pancreatic-type ribonuclease (RNase 1). Landre, J.; Hewett, P.; Olivot, J.; Friedl, P.; Ko, Y.; Sachinidis, A.; Moenner, M. *J Cell Biochem* **2002**, *86*, 540-552.

140. Immune regulation by microvascular endothelial cells: directing innate and adaptive immunity, coagulation, and inflammation. Danese, S.; Dejana, E.; Fiocchi, C. *J Immunol* **2007**, *178*, 6017-6022.

141. Bovine pancreatic ribonuclease: Fifty years of the first enzymatic reaction mechanism. Cuchillo, C. M.; Nogués, M. V.; Raines, R. T. *Biochemistry* **2011**, *50*, 7835-7841.

142. Back to the future: Ribonuclease A. Marshall, G. R.; Feng, J. A.; Kuster, D. J. *Biopolymers* **2008**, *90*, 259-277.

143. Reconstructing the evolutionary history of the artiodactyl ribonuclease superfamily. Jermann, T. M.; Opitz, J. G.; Stackhouse, J.; Benner, S. A. *Nature* **1995**, *374*, 57-59.

144. Planetary biology—paleontological, geological, and molecular histories of life. Benner, S. A.; Caraco, M. D.; Thomson, J. M.; Gaucher, E. A. *Science* **2002**, *296*, 864-868.

145. Respiratory syncytial virus infection, TLR3 ligands, and proinflammatory cytokines induce CD161 ligand LLT1 expression on the respiratory epithelium. Satkunanathan, S.; Kumar, N.; Bajorek, M.; Purbhoo, M. A.; Culley, F. J. *J Virol* **2014**, *88*, 2366-2373.

146. The interferon response circuit: induction and suppression by pathogenic viruses. Haller, O.; Kochs, G.; Weber, F. *Virology* **2006**, *344*, 119-130.

147. Pathogen recognition and innate immunity. Akira, S.; Uematsu, S.; Takeuchi, O. *Cell* **2006**, *124*, 783-801.

148. Recognition of double-stranded RNA and activation of NF-kappaB by Toll-like receptor 3. Alexopoulou, L.; Holt, A. C.; Medzhitov, R.; Flavell, R. A. *Nature* **2001**, *413*, 732-738.

149. Recognition of single-stranded RNA viruses by Toll-like receptor 7. Lund, J. M.; Alexopoulou, L.; Sato, A.; Karow, M.; Adams, N. C.; Gale, N. W.; Iwasaki, A.; Flavel, R. A. *Proc Natl Acad Sci USA* **2004**, *101*, 5598-5603.

150. Molecular modeling of protein–glycosaminoglycan interactions. Cardin, A. D.; Weintraub, H. J. *Arteriosclerosis* **1989**, *9*, 21-32.

151. Glycosaminoglycan-protein interactions: definition of consensus sites in glycosaminoglycan binding proteins. Hileman, R. E.; Fromm, J. R.; Weiler, J. M.; Linhardt, R. J. *Bioessays* **1998**, *20*, 156-167.

152. The BBXB motif of RANTES is the principal site for heparin binding and controls receptor selectivity. Proudfoot, A. E.; Fritchley, S.; Borlat, F.; Shaw, J. P.; Vilbois, F.; Zwahlen, C.; Trkola, A.; Marchant, D.; Clapham, P. R.; Wells, T. N. *J Biol Chem* **2001**, *276*, 10620-10626.

153. Kinetic and equilibrium studies of the ribonuclease-catalyzed hydrolysis of uridine 2′,3′-cyclic phosphate. del Rosario, E. J.; Hammes, G. G. *Biochemistry* **1969**, *8*, 1884-1889.

154. Composite active sites in bovine seminal ribonuclease. Mazzarella, L.; Mattia, C. A.; Capasso, S.; Di Lorenzo, G. *Gaz Chim Ital* **1987**, *117*, 91-97.

155. The dual-mode quaternary structure of seminal RNase. Piccoli, R.; Tamburrini, M.; Piccialli, G.; Di Donato, A.; Parente, A.; D'Alessio, G. *Proc Natl Acad Sci USA* **1992**, *89*, 1870-1874.

156. The influence of management, breed and season upon the pH of bull semen. Raps, G.; Cannon, C. Y. *J Dairy Sci* **1947**, *30*, 933-938.

157. Heterogeneity in the glycosylation pattern of human pancreatic ribonuclease. Ribó, M.; Beintema, J. J.; Osset, M.; Fernández, E.; Bravo, J.; de Llorens, R.; Cuchillo, C. M. *Biol Chem Hoppe Seyler* **1994**, *375*, 357-363.

158. The structure of the asparagine-linked sugar chains of bovine brain ribonuclease. Katoh, H.; Ohgi, K.; Irie, M.; Endo, T.; Kobata, A. *Carbohydr Res* **1990**, *195*, 273-293.

159. The importance of being proline: the interaction of proline-rich motifs in signaling proteins with their cognate domains. Kay, B. K.; Williamson, M. P.; Sudol, M. *FASEB J* **2000**, *14*, 231-241.

160. Role of extracellular RNA and TLR3-Trif signaling in myocardial ischemia-reperfusion injury. Chen, C.; Feng, Y.; Zou, L.; Wang, L.; Chen, H. H.; Cai, J. Y.; Xu, J. M.; Sosnovik, D. E.; Chao, W. *J Am Heart Assoc* **2014**, *3*, e000683.

161. Enforcing the positive charge of N-termini enhances membrane interaction and antitumor activity of bovine seminal ribonuclease. D'Errico, G.; Ercole, C.; Lista, M.; Pizzo, E.; Falanga, A.; Galdiero, S.; Spadaccini, R.; Picone, D. *Biochim Biophys Acta* **2011**, *1808*, 3007-3015.

162. Organogenesis and angiogenin. Vallee, B. L.; Riordan, J. F. *Cell Mol Life Sci* **1997**, *53*, 803-815.

163. Ribonuclease A variants with potent cytotoxic activity. Leland, P. A.; Schultz, L. W.; Kim, B. M.; Raines, R. T. *Proc Natl Acad Sci USA* **1998**, *95*, 10407-10412.

164. Endowing human pancreatic ribonuclease with toxicity for cancer cells. Leland, P. A.; Staniszewski, K. E.; Kim, B. M.; Raines, R. T. *J Biol Chem* **2001**, *276*, 43095-43102.

165. Working group report: the roles of glycans in hemostasis, inflammation and vascular biology. Varki, A. P.; Baum, L. G.; Bellis, S. L.; Cummings, R. D.; Esko, J. D.; Hart, G. W.; Linhardt, R. J.; Lowe, J. B.; McEver, R. P.; Srivastava, A.; Sarkar, R. *Glycobiology* **2008**, *18*, 747-749.

166. Glycan arrays for functional glycomics. Drickamer, K.; Taylor, M. E. *Genome Biol* **2002**, *3*, 1034-1038.

167. Immunohistochemical reactivity of a monoclonal antibody prepared against human breast carcinoma. Mariani-Costantini, R.; Colnaghi, M. I.; Leoni, F.; Menard, S.; Cerasoli, S.; Rilke, F. *Virchows Arch A Pathol Anat Histopathol* **1984**, *402*, 389-404.

168. Reactivity of a monoclonal antibody with tissues and tumors from the human breast. Immunohistochemical localization of a new antigen and clinicopathologic correlations. Mariani-Costantini, R.; Barbanti, P.; Colnaghi, M. I.; Menard, S.; Clemente, C.; Rilke, F. *Am J Pathol* **1984**, *115*, 47-56.

169. Selection of tumor antigens as targets for immune attack using immunohistochemistry: I. Focus on gangliosides. Zhang, S.; Cordon-Cardo, C.; Zhang, H. S.; Reuter, V. E.; Adluri, S.; Hamilton, W. B.; Lloyd, K. O.; Livingston, P. O. *Int J Cancer* **1997**, *73*, 42-49.

170. Study of the expression and function of the tumour-associated antigen CaMBr1 in small cell lung carcinomas. Martignone, S.; Menard, S.; Bedini, A.; Paccagnella, A.; Fasolato, S.; Veggian, R.; Colnaghi, M. I. *Eur J Cancer* **1993**, *29A*, 2020-2025.

171. Prognostic significance of the CaMBr1 antigen on breast carcinoma: relevance of the type of recognised glycoconjugate. Perrone, F.; Menard, S.; Canevari, S.; Calabrese, M.; Boracchi, P.; Bufalino, R.; Testori, S.; Baldini, M.; Colnaghi, M. I. *Eur J Cancer* **1993**, *29A*, 2113-2117.

172. Evaluation of toxic effects following administration of monoclonal antibody MBr1 in patients with breast cancer. Cascinelli, N.; Doci, R.; Belli, F.; Nava, M.; Marolda, R.; Costa, A.; Menard, S.; Terno, G. *Tumori* **1986**, *72*, 267-271.

173. Affinity of monoclonal antibodies to Globo-series glycans. Eller, C. H., Yang, G., Ouerfelli, O., Raines, R.T. *Carbohydr Res* **2014**, *Epub.*

174. Defining the molecular recognition of Globo-H (human breast-cancer) antigen through probe structures prepared by total synthesis. Kim, I. J.; Park, T. K.; Hu, S. H.; Abrampah, K.; Zhang, S. L.; Livingston, P. O.; Danishefsky, S. J. *J Org Chem* **1995**, *60*, 7716-7717.

175. From synthesis to biologics: preclinical data on a chemistry derived anticancer vaccine. Zhu, J.; Wan, Q.; Lee, D.; Yang, G.; Spassova, M. K.; Ouerfelli, O.; Ragupathi, G.; Damani, P.; Livingston, P. O.; Danishefsky, S. J. *J Am Chem Soc* **2009**, *131*, 9298-9303.

176. Printed covalent glycan array for ligand profiling of diverse glycan binding proteins. Blixt, O.; Head, S.; Mondala, T.; Scanlan, C.; Huflejt, M. E.; Alvarez, R.; Bryan, M. C.; Fazio, F.; Calarese, D.; Stevens, J.; Razi, N.; Stevens, D. J.; Skehel, J. J.; van Die, I.; Burton, D. R.; Wilson, I. A.; Cummings, R.; Bovin, N.; Wong, C. H.; Paulson, J. C. *Proc Natl Acad Sci USA* **2004**, *101*, 17033-17038.

177. Alexa dyes, a series of new fluorescent dyes that yield exceptionally bright, photostable conjugates. Panchuk-Voloshina, N.; Haugland, R. P.; Bishop-Stewart, J.; Bhalgat, M. K.; Millard, P. J.; Mao, F.; Leung, W. Y. *J Histochem Cytochem* **1999**, *47*, 1179-1188.

178. Assignments of RNase A by ADAPT-NMR and enhancer. Tonelli, M.; Eller, C. H.; Singarapu, K. K.; Lee, W.; Bahrami, A.; Westler, W. M.; Raines, R. T.; Markley, J. L. *Biomol NMR Assign* **2014**.

179. Hypersensitive substrate for ribonucleases. Kelemen, B.; Klink, T.; Behlke, M.; Eubanks, S.; Leland, P.; Raines, R. *Nucleic Acids Res* **1999**, *27*, 3696.

180. A practical total synthesis of Globo-H for use in anticancer vaccines. Jeon, I.; Iyer, K.; Danishefsky, S. J. *J Org Chem* **2009**, *74*, 8452-8455.

181. Development of orally active inhibitors of protein and cellular fucosylation. Okeley, N. M.; Alley, S. C.; Anderson, M. E.; Boursalian, T. E.; Burke, P. J.; Emmerton, K. M.; Jeffrey, S. C.; Klussman, K.; Law, C. L.; Sussman, D.; Toki, B. E.; Westendorf, L.; Zeng, W. P.; Zhang, X. Q.; Benjamin, D. R.; Senter, P. D. *Proc Natl Acad Sci USA* **2013**, *110*, 5404-5409.

182. Global metabolic inhibitors of sialyl- and fucosyltransferases remodel the glycome. Rillahan, C. D.; Antonopoulos, A.; Lefort, C. T.; Sonon, R.; Azadi, P.; Ley, K.; Dell, A.; Haslam, S. M.; Paulson, J. C. *Nat Chem Biol* **2012**, *8*, 661-668.

183. The solution structure and dynamics of human pancreatic ribonuclease determined by NMR spectroscopy provide insight into its remarkable biological activities and inhibition. Kover, K. E.; Bruix, M.; Santoro, J.; Batta, G.; Laurents, D. V.; Rico, M. *J Mol Biol* **2008**, *379*, 953-965.

184. Amelioration of hyperglycemia in streptozotocin-induced diabetic mice with fetal pancreatic allografts: prevention of rejection by donor specific transfusion in conjunction with CTLA4Ig. Hirakawa, E.; Yasunami, Y.; Nakano, M.; Shiiba, M.; Takehara, M.; Uede, T.; Todo, S.; Ono, J.; Ikeda, S. *Pancreas* **2004**, *28*, 146-152.

185. Two-dimensional chromatography in the analysis of complex glycans from transferrin. Charlwood, J.; Birrell, H.; Tolson, D.; Camilleri, P. *Anal Chem* **1998**, *70*, 2530-2535.

186. The structures and microheterogeneity of the carbohydrate chains of human plasma ceruloplasmin. A study employing 500-MHz 1H-NMR spectroscopy. Endo, M.; Suzuki, K.; Schmid, K.; Fournet, B.; Karamanos, Y.; Montreuil, J.; Dorland, L.; van Halbeek, H.; Vliegenthart, J. F. *J Biol Chem* **1982**, *257*, 8755-8760.

187. Synthetic carbohydrate-based antitumor vaccines: Challenges and opportunities. Ouerfelli, O.; Warren, J. D.; Wilson, R. M.; Danishefsky, S. J. *Expert Rev Vaccines* **2005**, *4*, 677-685.

188. Stage-specific embryonic antigens (SSEA-3 and -4) are epitopes of a unique Globo-series ganglioside isolated from human teratocarcinoma cells. Kannagi, R.; Cochran, N. A.; Ishigami, F.; Hakomori, S.; Andrews, P. W.; Knowles, B. B.; Solter, D. *EMBO J* **1983**, *2*, 2355-2361.

189. Lectin binding profiles of SSEA-4 enriched, pluripotent human embryonic stem cell surfaces. Venable, A.; Mitalipova, M.; Lyons, I.; Jones, K.; Shin, S.; Pierce, M.; Stice, S. *BMC Dev Biol* **2005**, *5*, 15.

190. Expression profile of saccharide epitope CaMBr1 in normal and neoplastic tissue from dogs, cats, and rats: Implication for the development of human-derived cancer vaccines. Adobati, E.; Zacchetti, A.; Perico, M. E.; Cremonesi, F.; Rasi, G.; Vallebona, P. S.; Hagenaars, M.; Kuppen, P. J.; Pastan, I.; Panza, L.; Russo, G.; Colnaghi, M. I.; Canevari, S. *Histochem J* **1999**, *31*, 729-737.

191. Influence of proinflammatory stimuli on the expression of vascular ribonuclease 1 in endothelial cells. Gansler, J.; Preissner, K. T.; Fischer, S. *FASEB J* **2013**.

192. Expression of Globo H and SSEA3 in breast cancer stem cells and the involvement of fucosyl transferases 1 and 2 in Globo H synthesis. Chang, W. W.; Lee, C. H.; Lee, P.; Lin, J.; Hsu, C. W.; Hung, J. T.; Lin, J. J.; Yu, J. C.; Shao, L. E.; Yu, J.; Wong, C. H.; Yu, A. L. *Proc Natl Acad Sci USA* **2008**, *105*, 11667-11672.

193. Membrane lipids: Where they are and how they behave. van Meer, G.; Voelker, D. R.; Feigenson, G. W. *Nat Rev Mol Cell Biol* **2008**, *9*, 112-124.

194. Investigation of SSEA-4 binding protein in breast cancer cells. Hung, T. C.; Lin, C. W.; Hsu, T. L.; Wu, C. Y.; Wong, C. H. *J Am Chem Soc* **2013**, *135*, 5934-5937.

195. Bovine brain ribonuclease is the functional homolog of human ribonuclease 1. Eller, C. H.; Lomax, J. E.; Raines, R. T. *J Biol Chem* **2014**.

196. Contribution of plasma proteins, albumin and alpha 1-acid glycoprotein, to pharmacokinetics of a multi-targeted receptor tyrosine kinase inhibitor, sunitinib, in analbuminemic rats. Toyama, Y.; Ueyama, J.; Nomura, H.; Tsukiyama, I.; Saito, H.; Hisada, T.; Matsuura, K.; Hasegawa, T. *Anticancer Res* **2014**, *34*, 2283-2289.

197. PEGylation--a well-proven strategy for the improvement of recombinant drugs. Zundorf, I.; Dingermann, T. *Pharmazie* **2014**, *69*, 323-326.

198. Preparation of potent cytotoxic ribonucleases by cationization: Enhanced cellular uptake and decreased interaction with ribonuclease inhibitor by chemical modification of carboxyl groups. Futami, J.; Maeda, T.; Kitazoe, M.; Nukui, E.; Tada, H.; Seno, M.; Kosaka, M.; Yamada, H. *Biochemistry* **2001**, *26*, 7518-7524.

199. Effects of monomethoxypoly(ethylene glycol) modification of ribonuclease on antibody recognition, substrate accessibility and conformational stability. Caliceti, P.; Schiavon, O.; Veronese, F. M.; Chaiken, I. M. *J Mol Recognit* **1990**, *3*, 89-93.

200. Nomenclature of glycolipids. Chester, M. A. *Pure Appl Chem* **1997**, *69*, 2475-2487.

201. Glycosphingolipids: Synthesis and functions. D'Angelo, G.; Capasso, S.; Sticco, L.; Russo, D. *FEBS J* **2013**, *280*, 6338-63553.

202. Structure and function of glycosphingolipids and sphingolipids: Recollections and future trends. Hakomori, S. I. *Biochim Biophys Acta* **2008**, *1780*, 325-346.

203. A vital role for glycosphingolipid synthesis during development and differentiation. Yamashita, T.; Wada, R.; Sasaki, T.; Deng, C. X.; Bierfreund, U.; Sandhoff, K.; Proia, R. L. *Proc Natl Acad Sci USA* **1999**, *96*, 9142-9147.

204. Switching of the core structures of glycosphingolipids from globo- and lacto- to ganglio-series upon human embryonic stem cell differentiation. Liang, Y. J.; Kuo, H. H.; Lin, C. H.; Chen, Y. Y.; Yang, B. C.; Cheng, Y. Y.; Yu, A. L.; Khoo, K. H.; Yu, J. *Proc Natl Acad Sci USA* **2010**, *107*, 22564-22569.

205. Profiling of microRNA in human and mouse ES and iPS cells reveals overlapping but distinct microRNA expression patterns. Razak, S. R.; Ueno, K.; Takayama, N.; Nariai, N.; Nagasaki, M.; Saito, R.; Koso, H.; Lai, C. Y.; Murakami, M.; Tsuji, K.; Michiue, T.; Nakauchi, H.; Otsu, M.; Watanabe, S. *PLoS One* **2013**, *8*, 10.1371/journal.pone.0073532.

206. Differentiation antigens of human germ cell tumours: Distribution of carbohydrate epitopes on glycolipids and glycoproteins analyzed using PDMP, an inhibitor of glycolipid synthesis. Fenderson, B. A.; Radin, N.; Andrews, P. W. *Eur Urol* **1993**, *23*, 30-37.

207. Stem cell glycolipids. Yanagisawa, M. *Neurochem Res* **2011**, *36*, 1623-1635.

208. Staining embryonic stem cells using monoclonal antibodies to stage-specific embryonic antigens. Fenderson, B. A.; De Miguel, M. P.; Pyle, A. D.; Donovan, P. J. *Methods Mol Biol* **2006**, *325*, 207-224.

209. Plasticity of human menstrual blood stem cells derived from the endometrium. Lin, J.; Xiang, D.; Zhang, J. L.; Allickson, J.; Xiang, C. *J Zhejiang Univ Sci B* **2011**, *12*, 372-380.

210. A review of stem cell translation and potential confounds by cancer stem cells. Bibber, B.; Sinha, G.; Lobba, A. R.; Greco, S. J.; Rameshwar, P. *Stem Cells Int* **2013**, *2013*, 10.1155/2013/241048.

211. Surface marker antigens in the characterization of human embryonic stem cells. Wright, A. J.; Andrews, P. W. *Stem Cell Res* **2009**, *3*, 3-11.

212. Stage-specific embryonic antigen-4 as a potential therapeutic target in glioblastoma multiforme and other cancers. Lou, Y. W.; Wang, P. Y.; Yeh, S. C.; Chuang, P. K.; Li, S. T.; Wu, C. Y.; Khoo, K. H.; Hsiao, M.; Hsu, T. L.; Wong, C. H. *Proc Natl Acad Sci USA* **2014**, *111*, 2482-2487.

213. Expression of Globo H and SSEA-3 in breast cancer stem cells and the involvement of fucosyl transferases 1 and 2 in Globo H synthesis. Chang, W. W.; Lee, C. H.; Lee, P.; Lin, J.; Hsu, C. W.; Hung, J. T.; Lin, J. J.; Yu, J. C.; Shao, L. E.; Yu, J.; Wong, C. H.; Yu, A. L. *Proc Natl Acad Sci USA* **2008**, *105*, 11667-11672.

214. Carbohydrate-based vaccines with a glycolipid adjuvant for breast cancer. Huang, Y. L.; Hung, J. T.; Cheung, S. K. C.; Lee, H. Y.; Chu, K. C.; Li, S. T.; Lin, Y. C.; Ren, C. T.; Cheng, T. J. R.; Hsu, T. L.; Yu, A. L.; Wu, C. Y.; Wong, C. H. *Proc Natl Acad Sci USA* **2013**, *110*, 2517-2522.

215. New Globo-series glycosphingolipids in human teratocarcinoma reactive with the monoclonal antibody directed to a developmentally regulated antigen, stage-specific embryonic antigen 3. Kannagi, R.; Levery, S. B.; Ishigami, F.; Hakomori, S.; Shevinsky, L. H.; Knowles, B. B.; Solter, D. *J Biol Chem* **1983**, *258*, 8934-8942.

216. Immunochemical analysis of the determinant recognized by a monoclonal antibody (MBr1) which specifically binds to human mammary epithelial cells. Canevari, S.; Fossati, G.; Balsari, A.; Sonnino, S.; Colnaghi, M. I. *Cancer Res* **1983**, *43*, 1301-1305.

217. Characterization of a glycosphingolipid antigen defined by the monoclonal-antibody Mbr1 expressed in normal and neoplastic epithelial-cells of human mammary-gland. Bremer, E. G.; Levery, S. B.; Sonnino, S.; Ghidoni, R.; Canevari, S.; Kannagi, R.; Hakomori, S. I. *J Bio Chem* **1984**, *259*, 4773-4777.

218. Glycan microarray of Globo H and related structures for quantitative analysis of breast cancer. Wang, C. C.; Huang, Y. L.; Ren, C. T.; Lin, C. W.; Hung, J. T.; Yu, J. C.; Yu, A. L.; Wu, C. Y.; Wong, C. H. *Proc Natl Acad Sci USA* **2008**, *105*, 11661-11666.

219. Cancer vaccines and carbohydrate epitopes. Heimburg-Molinaro, J.; Lum, M.; Vijay, G.; Jain, M. T.; Almogren, A.; Rittenhouse-Olson, K. *Vaccine* **2011**, *29*, 8802-8826.

220. Pilot study of a heptavalent vaccine-keyhole limpet hemocyanin conjugate plus QS21 in patients with epithelial ovarian, fallopian tube, or peritoneal cancer. Sabbatini, P. J.; Ragupathi, G.; Hood, C.; Aghajanian, C. A.; Juertzka, M.; Lasonos, A.; Hensley, M. L.; Spassova, M. K.; Ouerfelli, O.; Spriggs, D. R.; Tew, W. P.; Konner, J.; Clausen, H.; Abu Rustum, N.; Dansihefsky, S. J.; Livingston, P. O. *Clin Cancer Res* **2007**, *13*, 4170-4177.

221. Pursuit of optimal carbohydrate-based anticancer vaccines: Preparation of a multiantigenic unimolecular glycopeptide containing the Tn, MBr1, and Lewis(y) antigens. Allen, J. R.; Harris, C. R.; Danishefsky, S. J. *J Am Chem Soc* **2001**, *123*, 1890-1897.

222. Carbohydrate recognition in the immune system: contributions of neoglycolipid-based microarrays to carbohydrate ligand discovery. Feizi, T. *Ann N Y Acad Sci* **2013**, *1292*, 33-44.

223. Bright ideas for chemical biology. Lavis, L.; Raines, R. *ACS Chemical Biology* **2008**, *3*, 142-155.

224. Structure of serum albumin. Carter, D. C.; Ho, J. X. *Adv Protein Chem* **1994**, *45*, 153-203.

225. On the attribution and additivity of binding energies. Jencks, W. P. *Proc Natl Acad Sci USA* **1981**, *78*, 4046-4050.

226. Entropic contributions to rate accelerations in enzymatic and intramolecular reactions and the chelate effect. Page, M. I.; Jencks, W. P. *Proc Natl Acad Sci USA* **1971**, *68*, 1678-1683.

227. *Multivalency in carbohydrate binding*. Wolfenden, M. L.; Cloninger, M. J.; John Wiley & Sons: New York, NY, 2011.

228. Strength in numbers: Non-natural polyvalent carbohydrate derivatives. Kiessling, L. L.; Pohl, N. L. *Chem Biol* **1996**, *3*, 71-77.

229. Monoclonal antibody to murine embryos defines a stage-specific embryonic antigen expressed on mouse embryos and human teratocarcinoma cells. Shevinsky, L. H.; Knowles, B. B.; Damjanov, I.; Solter, D. *Cell* **1982**, *30*, 697-705.

230. Stage-specific embryonic antigen-4 as a potential therapeutic target in glioblastoma multiforme and other cancers. Lou, Y. W.; Wang, P. Y.; Yeh, S. C.; Chuang, P. K.; Li, S. T.; Wu, C. Y.; Khoo, K. H.; Hsiao, M.; Hsu, T. L.; Wong, C. H. *Proc Natl Acad Sci USA* **2014**, *111*, 2482-2487.

231. Correlation proton magnetic resonance studies at 250 MHz of bovine pancreatic ribonuclease. III. Mutual electrostatic interaction between histidine residues 12 and 119. Markley, J. L.; Finkenstadt, W. R. *Biochemistry* **1975**, *14*, 3562-3566.

232. Coulombic effects of remote subsites on the active site of ribonuclease A. Fisher, B. M.; Schultz, L. W.; Raines, R. T. *Biochemistry* **1998**, *37*, 17386-17401.

233. Fluorogenic label to quantify the cytosolic delivery of macromolecules. Chao, T.-Y.; Raines, R. T. *Mol BioSyst* **2013**, *9*, 339-342.

234. Ribonucleases 6 and 7 have antimicrobial function in the human and murine urinary tract. Becknell, B.; Eichler, T. E.; Beceiro, S.; Li, B.; Easterling, R. S.; Carpenter, A. R.; James, C. L.; McHugh, K. M.; Hains, D. S.; Partida-Sanchez, S.; Spencer, J. D. *Kidney Int* **2014**.

235. Ribonuclease 7, an antimicrobial peptide upregulated during infection, contributes to microbial defense of the human urinary tract. Spencer, J. D.; Schwaderer, A. L.; Wang, H.; Bartz, J.; Kline, J.; Eichler, T.; DeSouza, K. R.; Sims-Lucas, S.; Baker, P.; Hains, D. S. *Kidney Int* **2013**, *83*, 615-625.

236. Antimicrobial activity of human eosinophil granule proteins. Chopra, A.; Batra, J. K. *Methods Mol Biol* **2014**, *1178*, 267-281.

237. Rapid evolution of a unique family of primate ribonuclease genes. Rosenberg, H. F.; Dyer, K. D.; Tiffany, H. L.; Gonzalez, M. *Nature Genet* **1995**, *10*, 219-223.

238. LL-37, the only human member of the cathelicidin family of antimicrobial peptides. Durr, U. H.; Sudheendra, U. S.; Ramamoorthy, A. *Biochim Biophys Acta* **2006**, *1758*, 1408-1425.

239. Synergistic interactions between mammalian antimicrobial defense peptides. Yan, H.; Hancock, R. E. *Antimicrob Agents Chemother* **2001**, *45*, 1558-1560.

240. Synergistic effect of antibacterial agents human beta-defensins, cathelicidin LL-37 and lysozyme against *Staphylococcus aureus* and *Escherichia coli*. Chen, X.; Niyonsaba, F.; Ushio, H.; Okuda, D.; Nagaoka, I.; Ikeda, S.; Okumura, K.; Ogawa, H. *J Dermatol Sci* **2005**, *40*, 123-132.

241. Cutaneous injury induces the release of cathelicidin anti-microbial peptides active against group A Streptococcus. Dorschner, R. A.; Pestonjamasp, V. K.; Tamakuwala, S.; Ohtake, T.; Rudisill, J.; Nizet, V.; Agerberth, B.; Gudmundsson, G. H.; Gallo, R. L. *J Invest Dermatol* **2001**, *117*, 91-97.

242. C-Terminal domain of human CAP18 antimicrobial peptide induces apoptosis in oral squamous cell carcinoma SAS-H1 cells. Okumura, K.; Itoh, A.; Isogai, E.; Hirose, K.; Hosokawa, Y.; Abiko, Y.; Shibata, T.; Hirata, M.; Isogai, H. *Cancer Lett* **2004**, *212*, 185-194.

243. Evaluation of the inactivation of infectious Herpes simplex virus by host-defense peptides. Yasin, B.; Pang, M.; Turner, J. S.; Cho, Y.; Dinh, N. N.; Waring, A. J.; Lehrer, R. I.; Wagar, E. A. *Eur J Clin Microbiol Infect Dis* **2000**, *19*, 187-194.

244. Selective killing of vaccinia virus by LL-37: Implications for eczema vaccinatum. Howell, M. D.; Jones, J. F.; Kisich, K. O.; Streib, J. E.; Gallo, R. L.; Leung, D. Y. *J Immunol* **2004**, *172*, 1763-1767.

245. Characterization of a ribonuclease gene and encoded protein from the reptile, *Iguana iguana*. Nitto, T.; Lin, C.; Dyer, K. D.; Wagner, R. A.; Rosenberg, H. F. *Gene* **2005**, *352*, 36-44.

246. Evolution and function of leukocyte RNase A ribonucleases of the avian species, *Gallus gallus*. Nitto, T.; Dyer, K. D.; Czapiga, M.; Rosenberg, H. F. *J Biol Chem* **2006**, *281*, 25622-25634.

247. The nuclear function of angiogenin in endothelial cells is related to rRNA production. Xu, Z. P.; Tsuji, T.; Riordan, J. F.; Hu, G. F. *Biochem Biophys Res Commun* **2002**, *294*, 287-292.

248. Multiple bursts of pancreatic ribonuclease gene duplication in insect-eating bats. Xu, H.; Liu, Y.; Meng, F.; He, B.; Han, N.; Li, G.; Rossiter, S. J.; Zhang, S. *Gene* **2013**, *526*, 112-117.

249. Tissue-specific expression of pancreatic-type RNases and RNase inhibitor in humans. Futami, J.; Tsushima, Y.; Murato, Y.; Tada, H.; Sasaki, J.; Seno, M.; Yamada, H. *DNA and Cell Biol* **1997**, *16*, 413-419.

250. NMR structural analysis of an analog of an intermediate formed in the rate-determining step of one pathway in the oxidative folding of bovine pancreatic ribonuclease A: Automated analysis of 1H, 13C, and 15N resonance assignments for wild-type and [C65S, C72S] mutant forms. Shimotakahara, S.; Rios, C. B.; Laity, J. H.; Zimmerman, D. E.; Scheraga, H. A.; Montelione, G. T. *Biochemistry* **1997**, *36*, 6915-6929.

251. Robust, integrated computational control of NMR experiments to achieve optimal assignment by ADAPT-NMR. Bahrami, A.; Tonelli, M.; Sahu, S. C.; Singarapu, K. K.; Eghbalnia, H. R.; Markley, J. L. *PLoS One* **2012**, *7*, e33173.

252. ADAPT-NMR Enhancer: Complete package for reduced dimensionality in protein NMR spectroscopy. Lee, W.; Bahrami, A.; Markley, J. L. *Bioinformatics* **2013**, *29*, 515-517.

253. Probabilistic interaction network of evidence algorithm and its application to complete labeling of peak lists from protein NMR spectroscopy. Bahrami, A.; Assadi, A. H.; Markley, J. L.; Eghbalnia, H. R. *Plos Comput Biol* **2009**, *5*, e1000307.

254. SPARKY 3. Goddard, T. D.; Kneller, D. G.; University of California, San Francisco: 2000.

255. NMRPipe - a multidimensional spectral processing system based on Unix Pipes. Delaglio, F.; Grzesiek, S.; Vuister, G. W.; Zhu, G.; Pfeifer, J.; Bax, A. *J Biomolecular NMR* **1995**, *6*, 277-293.

256. Comparison of 2 independently refined models of ribonuclease A. Wlodawer, A.; Borkakoti, N.; Moss, D. S.; Howlin, B. *Acta Crystallogr Sect B: Struct Sci* **1986**, *42*, 379-387.

257. What's in your buffer? Solute altered millisecond motions detected by solution NMR. Wong, M.; Khirich, G.; Loria, J. P. *Biochemistry* **2013**, *52*, 6548-6558.

258. The ultrahigh resolution crystal structure of ribonuclease A containing an isoaspartyl residue: Hydration and sterochemical analysis. Esposito, L.; Vitagliano, L.; Sica, F.; Sorrentino, G.; Zagari, A.; Mazzarella, L. *J Mol Bio* **2000**, *297*, 713-732.

259. Stepwise deamidation of ribonuclease A at five sites determined by top down mass spectrometry. Zabrouskov, V.; Han, X. M.; Welker, E.; Zhai, H. L.; Lin, C.; van Wijk, K. J.; Scheraga, H. A.; McLafferty, F. W. *Biochemistry* **2006**, *45*, 987-992.

260. Expression of wild-type and mutant bovine pancreatic ribonuclease A in *Escherichia coli*. Laity, J. H.; Shimotakahara, S.; Scheraga, H. A. *Proc Natl Acad Sci USA* **1993**, *90*, 615-619.

261. Longer action means better drug: Tuning up protein therapeutics. Szlachcic, A.; Zakrzewska, M.; Otlewski, J. *Biotechnol Adv* **2011**, *29*, 436-441.

262. *Ribonucleases: Structures and Functions*; D'Alessio, G.; Riordan, J. F., Eds.; Academic Press: New York, 1997.

263. Introduction to current and future protein therapeutics: A protein engineering perspective. Carter, P. J. *Exp Cell Res* **2011**, *317*, 1261-1269.

264. Phase II trial of a single weekly intravenous dose of Ranpirnase in patients with unresectable malignant mesothelioma. Mikulski, S. M.; Costanzi, J. J.; Vogelzang, N. J.; McCachren, S.; Taub, R. N.; Chun, H.; Mittelman, A.; Panella, T.; Puccio, C.; Fine, R.; Shogen, K. *J Clin Oncol* **2002**, *20*, 274-281.

265. Ribonucleases as novel chemotherapeutics: The Ranpirnase example. Lee, J. E.; Raines, R. T. *BioDrugs* **2008**, *22*, 53-58.

266. Ranpirnase—an antitumour ribonuclease: Its potential role in malignant mesothelioma. Pavlakis, N.; Vogelzang, N. J. *Expert Opin Biol Ther* **2006**, *6*, 391-399.

267. Comprehensive comparison of the cytotoxic activities of Onconase and bovine seminal ribonuclease. Matoušek, J.; Souček, J.; Slavík, T.; Tománek, M.; Lee, J. E.; Raines, R. T. *Comp Biochem Physiol* **2003**, *136C*, 343-356.

268. Ribonucleases as potential modalities in anticancer therapy. Ardelt, W.; Ardelt, B.; Darzynkiewicz, Z. *Eur J Pharmacol* **2009**, *625*, 181-189.

269. Ribonucleases of different origins with a wide spectrum of medicinal applications. Fang, E. F.; Ng, T. B. *Biochim Biophys Acta* **2011**, *1815*, 65-74.

270. Cancer chemotherapy--ribonucleases to the rescue. Leland, P. A.; Raines, R. T. *Chem Biol* **2001**, *8*, 405-413.

271. Ribonuclease inhibitor: Structure and function. Dickson, K. A.; Haigis, M. C.; Raines, R. T. *Prog Nucleic Acid Res Mol Bio* **2005**, *80*, 349-374.

272. Quantitative analysis of the effect of salt concentration on enzymatic catalysis. Park, C.; Raines, R. T. *J Am Chem Soc* **2001**, *123*, 11472-11479.

273. A ribonuclease A variant with low catalytic activity but high cytotoxicity. Bretscher, L. E.; Abel, R. L.; Raines, R. T. *J Biol Chem* **2000**, *275*, 9893-9896.

274. Catalytic activity of bovine seminal ribonuclease is essential for its immunosuppressive and other biological activities. Kim, J.-S.; Souček, J.; Matoušek, J.; Raines, R. T. *Biochem J* **1995**, *308*, 547-550.

275. The structural stability of a protein is an important determinant of its proteolytic susceptibilityin *Escherichia coli*. Parsell, D. A.; Sauer, R. T. *J Biol Chem* **1989**, *264*, 7590-7595.

276. Conformational stability is a determinant of ribonuclease A cytotoxicity. Klink, T. A.; Raines, R. T. *J Biol Chem* **2000**, *275*, 17463-17467.

277. Genetic selection for critical residues in ribonucleases. Smith, B. D.; Raines, R. T. *J Mol Biol* **2006**, *362*, 459-478.

278. Fast, facile, hypersensitive assays for ribonucleolytic activity. Park, C.; Kelemen, B. R.; Klink, T. A.; Sweeney, R. Y.; Behlke, M. A.; Eubanks, S. R.; Raines, R. T. *Methods Enzymol* **2001**, *341*, 81-94.

279. Design of cytotoxic ribonucleases by cationization to enhance intracellular protein delivery. Futami, J.; Yamada, H. *Current Pharmaceutical Biotechnology* **2008**, *9*, 180-184.

280. Polyarginine as a multifunctional fusion tag. Fuchs, S. M.; Raines, R. T. *Protein Science* **2005**, *14*, 1538-1544.

281. Potentiation of ribonuclease cytotoxicity by a poly(amidoamine) dendrimer. Ellis, G. A.; Hornung, M. L.; Raines, R. T. *Bioorg Med Chem Lett* **2011**, *21*, 2756-2758.

282. Cytotoxic ribonucleases: The dichotomy of Coulombic forces. Johnson, R. J.; Chao, T.-Y.; Lavis, L. D.; Raines, R. T. *Biochemistry* **2007**, *46*, 10308-10316.

283. The cytosolic ribonuclease inhibitor contributes to intracellular redox homeostasis. Monti, D. M.; Montesano Gesualdi, N.; Matoušek, J.; Esposito, F.; D'Alessio, G. *FEBS Lett* **2007**, *581*, 930-934.

284. Ribonuclease A variants with potent cytotoxic activity. Leland, P. A.; Schultz, L. W.; Kim, B.-M.; Raines, R. T. *Proc Natl Acad Sci USA* **1998**, *98*, 10407-10412.

285. Site-specific folate conjugation to a cytotoxic protein. Smith, B. D.; Higgin, J. J.; Raines, R. T. *Bioorg Med Chem Lett* **2011**, *21*, 5029-5032.

286. The nuclear transport capacity of a human-pancreatic ribonuclease variant is critical for its cytotoxicity. Tubert, P.; Rodriguez, M.; Ribo, M.; Benito, A.; Vilanova, M. *Invest New Drugs* **2011**, *29*, 811-817.

287. Tandemization endows bovine pancreatic ribonuclease with cytotoxic activity. Leich, F.; Köditz, J.; Ulbrich-Hofman, R.; Arnold, U. *J Mol Biol* **2006**, *358*, 1305-1313.

288. Endocytotic internalization as a crucial factor for the cytotoxicity of ribonucleases. Leich, F.; Stohr, N.; Rietz, A.; Ulbrich-Hofmann, R.; Arnold, U. *J Biol Chem* **2007**, *282*, 27640-27646.

289. Crystal structure of RNase A tandem enzymes and their interaction with the cytosolic ribonuclease inhibitor. Arnold, U.; Leich, F.; Neumann, P.; Lilie, H.; Ulbrich-Hofmann, R. *FEBS J* **2011**, *278*, 331-340.

290. Fluorogenic label for biomolecular imaging. Lavis, L. D.; Chao, T.-Y.; Raines, R. T. *ACS Chem Biol* **2006**, *1*, 252-260.

291. Ribonuclease A: Revealing structure–function relationships with semisynthesis. Messmore, J. M.; Fuchs, D. N.; Raines, R. T. *J Am Chem Soc* **1995**, *117*, 8057-8060.

292. Tryptophan fluorescence as a probe of placental ribonuclease inhibitor binding to angiogenin. Lee, F. S.; Auld, D. S.; Vallee, B. L. *Biochemistry* **1989**, *28*, 219-224.

293. Creation of a zymogen. Plainkum, P.; Fuchs, S. M.; Wiyakrutta, S.; Raines, R. T. *Nat Struct Mol Biol* **2003**, *10*, 115-119.

294. A ribonuclease zymogen activated by the NS3 protease of the hepatitis C virus. Johnson, R. J.; Lin, S. R.; Raines, R. T. *FEBS J* **2006**, *273*, 5457-5465.

295. Design and Characterization of an HIV-Specific Ribonuclease Zymogen. Turcotte, R. F.; Raines, R. T. *AIDS Res Hum Retroviruses* **2008**, *24*, 1357-1363.

296. Ribonuclease inhibitor regulates neovascularization by human angiogenin. Dickson, K. A.; Kang, D. K.; Kwon, Y. S.; Kim, J. C.; Leland, P. A.; Kim, B. M.; Chang, S. I.; Raines, R. T. *Biochemistry* **2009**, *48*, 3804-3806.

297. On the track of antitumor ribonucleases. Benito, A.; Ribó, M.; Vilanova, M. *Mol Biosyst* **2005**, *1*, 294-302.

298. Natural and engineered ribonucleases as potential cancer therapeutics. Arnold, U.; Ulbrich-Hofmann, R. *Biotechnol Lett* **2006**, *28*, 1615-1622.

299. Molecular determinants in the plasma clearance and tissue distribution of ribonucleases of the ribonuclease A superfamily. Vasandani, V. M.; Wu, Y.-N.; Mikulski, S. M.; Youle, R. J.; Sung, C. *Cancer Res* **1996**, *56*, 4180-4186.

300. Interaction of Onconase with the human ribonuclease inhibitor protein. Turcotte, R. F.; Raines, R. T. *Biochem Biophys Res Commun* **2008**, *377*, 512-514.

301. Tight-binding inhibition of angiogenin and ribonuclease A by placental ribonuclease inhibitor. Lee, F. S.; Shapiro, R.; Vallee, B. L. *Biochemistry* **1989**, *28*, 225-230.

302. Endowing human pancreatic ribonuclease with toxicity for cancer cells. Leland, P. A.; Staniszewski, K. E.; Kim, B.-M.; Raines, R. T. *J Biol Chem* **2001**, *276*, 43095-43102.

303. Comparison of RNases and toxins upon injection into *Xenopus* oocytes. Saxena, S. K.; Rybak, S. M.; Winkler, G.; Meade, H. M.; McGray, P.; Youle, R. J.; Ackerman, E. J. *J Biol Chem* **1991**, *266*, 21208-21214.

304. Cellular uptake of ribonuclease A relies on anionic glycans. Chao, T.-Y.; Lavis, L. D.; Raines, R. T. *Biochemistry* **2010**, *49*, 10666-10673.

305. Engineering receptor-mediated cytotoxicity into human ribonucleases by steric blockage of inhibitor interaction. Suzuki, M.; Saxena, S. K.; Boix, E.; Prill, R. J.; Vasandani, V. M.; Ladner, J. E.; Sung, C.; Youle, R. J. *Nat Biotechnol* **1999**, *17*, 265-270.

306. Increased exposure of anionic phospholipids on the surface of tumor blood vessels. Ran, S.; Downes, A.; Thorpe, P. E. *Cancer Res* **2002**, *62*, 6132-6140.

307. Intracellular pathway of Onconase that enables its delivery to the cytosol. Rodriguez, M.; Torrent, G.; Bosch, M.; Rayne, F.; Dubremetz, J.-F.; Ribó, M.; Benito, A.; Vilanova, M.; Beaumelle, B. *J Cell Sci* **2007**, *120*, 1405-1411.

308. The role of electrostatic interactions in the antitumor activity of dimeric RNases. Notomista, E.; Mancheño, J. M.; Crescenzi, O.; Di Donato, A.; Gavilanes, J.; D'Alessio, G. *FEBS J* **2006**, *273*, 3687-3697.

309. Prediction of protein orientation upon immobilization on biological and nonbiological surfaces. Talasaz, A.; Davis, R. *Proc Natl Acad Sci USA* **2006**, *103*, 14773-14778.

310. Electrostatics of nanosystems: Application to microtubules and the ribosome. Baker, N. A.; Sept, D.; Joseph, S.; Holst, M. J.; McCammon, J. A. *Proc Natl Acad Sci USA* **2001**, *98*, 10037-10041.

311. Atomic resolution structures of ribonuclease A at six pH values. Berisio, R.; Sica, F.; Lamzin, V. S.; Wilson, K. S.; Zagari, A.; Mazzarella, L. *Acta Crystallogr, Sect D* **2002**, *58*, 441-450.

312. Refined 1.7 Å X-ray crystallographic structure of P-30 protein, an amphibian ribonuclease with anti-tumor activity. Mosimann, S. C.; Ardelt, W.; James, M. N. G. *J Mol Biol* **1994**, *236*, 1141-1153.

313. All-atom empirical potential for molecular modeling and dynamics studies of proteins. MacKerell, A. D.; Bashford, D.; Bellott, M.; Dunbrack, R. L.; Evanseck, J. D.; Field, M. J.; Fischer, S.; Gao, J.; Guo, H.; Ha, S.; Joseph-McCarthy, D.; Kuchnir, L.; Kuczera, K.; Lau, F. T. K.; Mattos, C.; Michnick, S.; Ngo, T.; Nguyen, D. T.; Prodhom, B.; Reiher, W. E.; Roux, B.; Schlenkrich, M.; Smith, J. C.; Stote, R.; Straub, J.; Watanabe, M.; Wiorkiewicz-Kuczera, J.; Yin, D.; Karplus, M. *J Phys Chem B* **1998**, *102*, 3586-3616.

314. PDB2PQR: An automated pipeline for the setup, execution, and analysis of Poisson-Boltzmann electrostatics calculations. Dolinsky, T. J.; Nielsen, J. E.; McCammon, J. A.; Baker, N. A. *Nucleic Acids Res* **2004**, *32*, 665-667.

315. PDB2PQR: Expanding and upgrading automated preparation of biomolecular structures for molecular simulations. Dolinsky, T. J.; Czodrowski, P.; Li, H.; Nielsen, J. E.; Jensen, J. H.; Klebe, G.; Baker, N. A. *Nucleic Acids Res* **2007**, *35*, 522-525.

316. Implicit solvent simulations of peptide interactions with anionic lipid membranes. Lazaridis, T. *Proteins* **2005**, *58*, 518-527.

317. Effective energy function for proteins in solution. Lazaridis, T.; Karplus, M. *Proteins* **1999**, *35*, 133-152.

318. The electrostatic properties of membranes. McLaughlin, S. *Annu Rev Biophys Biophys Chem* **1989**, *18*, 113-136.

319. CHARMM: A program for macromolecular energy, minimization, and dynamics calculations. Brooks, B. R.; Bruccoleri, R. E.; Olafson, B. D.; States, D. J.; Swaminathan, S.; Karplus, M. *J Comput Chem* **1983**, *4*, 187-217.

320. Aspects of the cytotoxic action of ribonucleases. Arnold, U. *Curr Pharm Biotechnol* **2008**, *9*, 161-168.

321. Molecular dynamics simulations of membrane channels and transporters. Khalili-Araghi, F.; Gumbart, J.; Wen, P. C.; Sotomayor, M.; Tajkhorshid, E.; Schulten, K. *Curr Opin Struct Biol* **2009**, *19*, 128-137.